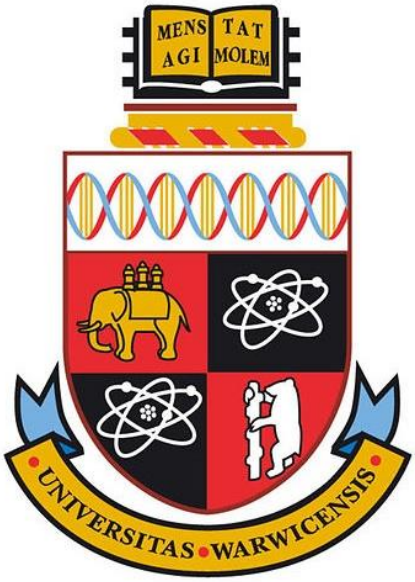

The On-Surface Self-Assembly, Reactions and Electronic Properties of PXX and Binol Derivatives

by

James Lawrence

A thesis submitted in partial fulfilment of the requirements for the degree of Doctor of Philosophy in Chemistry

Department of Chemistry, University of Warwick

November 2018

Table of Contents

List of Figures

List of Tables

Acknowledgements

I would firstly like to thank my PhD supervisor, Professor Giovanni Costantini, for allowing me to work with him on this project. I am very grateful for all of the support and advice that he has given to me throughout the last four years, as well as the help that he has given me with my future career. It has been a pleasure working with him and the rest of the group.

I would also like to thank:

Dr. Ada Della Pia, for teaching me how to use the LT-STM instrument in the first place, as well as guiding me through my first year in the laboratory.

Dr. Marc Walker, for teaching me how to use the XPS system, along with all of his help.

Rod Wesson, for the amazing amount of dedication and skill that he has shown in helping us with all of our electronics problems throughout the years. The LT-STM would not still be functioning without his assistance.

The rest of the Costantini group: Dan, Phil, Jon, Luis and Harry, for both entertaining and helping me throughout my PhD. Working in the lab would not be the same without hearing the same rap music and dark jokes on repeat.

My housemates, Glen and Dan, for both putting up with me over the last four years, as well as for providing many entertaining evenings. We'll take the lot!

Finally, I thank my family for their support and love over the years, as well as my partner, Nattakan. She has helped to keep me level and always believed in me, and I would not be the same without her love.

Declarations

This thesis has been submitted to the University of Warwick in partial fulfilment of the requirements for the degree of Doctor of Philosophy in Chemistry. All work presented is my own, unless otherwise explicitly stated. Some aspects of the work presented are a result of working with collaborators, and their contribution are stated in each relevant section. This work has been performed under the supervision of Professor Giovanni Costantini between September 2014 and October 2018. No work in this thesis has previously been submitted to any institution for a higher degree. Some of the work presented in this thesis will be published in the following articles:

J. Lawrence, G. Sosso, L. Đorđević, H. Pinfold, D. Bonifazi, G. Costantini, *Halogen or hydrogen Bonding? Structural elucidation via high resolution STM,* In preparation.

J. Lawrence, L. Đorđević, D. Bonifazi, G. Costantini, *On-surface reactions of binol at metallic substrates,* In preparation.

J. Lawrence, L. Đorđević, H. Pinfold, D. Bonifazi, G. Costantini, *Modifying the donor and acceptor strength of molecules via the formation of doped nanoribbons,* In preparation.

J. Lawrence, L. Đorđević, H. Pinfold, D. Bonifazi, G. Costantini, *On-surface 2D PXX/TCNQ charge transfer networks,* In preparation.

James Lawrence, November 2018.

Abstract

Peri-xanthenoxanthene (PXX) is an electron donor molecule that has been previously used as an active component in organic thin film transistors (OTFTs), exhibiting desirable properties such as high levels of stability, efficient charge injection and high mobility. Previous studies of PXX and related molecules have shown that small changes to its structure enable the adjustment (in energy) of its frontier orbitals, enabling precise tweaking of its energetic alignment with other materials in devices.

In this thesis, PXX and related molecules are studied at metallic interfaces via scanning tunnelling microscopy (STM), scanning tunnelling spectroscopy (STS) and x-ray photoelectron spectroscopy (XPS) in idealised conditions. In particular, on-surface reactions are used to form extended nanoribbons of PXX and related molecules, and the dependence of the donor/acceptor strength on the length of these structures is examined via STS.

The on-surface reactions of a related molecule, binol, were studied on Cu(111) and Au(111) via STM and XPS with the aim of forming PXX in an idealised analogous reaction to solution phase synthetic methods that involve metal catalysts. Binol was found to form metal-organic structures on Cu(111) with annealing, with disordered covalent structures forming at higher temperatures. Au(111) did not catalyse on-surface reactions of binol, with the addition of a co-deposited metal (Fe) required to initiate the formation of metal-organic structures and covalent products at higher temperatures.

PXX was found to adsorb onto metallic surfaces, with indications of molecule-metal decoupling on Au(111), such as the high levels of mobility exhibited and the clear signals in STM imaging that resemble its gas phase molecular orbitals. The addition of bromine atoms to its structure allowed for the formation of halogen bonded networks and enabled the on-surface synthesis of extended PXX nanoribbons via metal-catalysed on-surface Ullmann and dehydrogenation reactions. STS measurements on the PXX nanoribbons give a strong indication of an increased donor strength (higher HOMO energy) with increased length.

An acceptor analogue of brominated PXX, Vat Orange 3 (VO3), was also studied on Au(111). After the formation of halogen bonded networks upon its deposition,

annealing was found to yield extended nanoribbon structures that exhibited increased acceptor strength with increased length.

Finally, on-surface donor-acceptor (DA) type structures involving PXX were examined. Its deposition with a common acceptor molecule, tetracyanoquinodimethane (TCNQ) was found to lead to the formation of mixed assemblies that showed signs of increased levels of surface-mediated charge transfer to TCNQ. Similar results were found when instead using PXX nanoribbons, with any differences ascribed to the change in the stabilities of the mixed assemblies due to changes in intermolecular interactions. Covalently bonded DA nanoribbon structures, formed from PXX and VO3, were also examined via STM/STS, and the tweaking of the frontier energy levels and band gaps via co-polymerisation was demonstrated.

List of Abbreviations

1D	One-dimensional
2D	Two dimensional
3D	Three-dimensional
ADC	Analogue to digital converter
AFM	Atomic force microscopy
Br_2PXX	Di-bromo peri-xanthenoxanthene
CNL	Charge neutrality level
CT	Charge transfer
CV	Cyclic voltammetry
D-A	Donor-acceptor
DAC	Digital to analogue converter
DFT	Density functional theory
DOS	Density of states
fcc	Face-centred cubic
GNR	Graphene nanoribbon
hcp	Hexagonal close-packed
HOMO	Highest occupied molecular orbital
HR-SPM	High resolution scanning probe microscopy
HR-STM	High resolution scanning tunnelling microscopy
ICT	Integer charge transfer
IDIS	Induced density of states
IETS	Inelastic electron tunnelling spectroscopy
LDOS	Local density of states
LEED	Low energy electron diffraction
LL	Load-lock
LT-STM	Low-temperature scanning tunnelling microscope
LUMO	Lowest unoccupied molecular orbital
ML	Monolayer
MO	Metal-organic
MOF	Metal-organic framework
NC-AFM	Non-contact atomic force microscopy

NICS	Nucleus-independent chemical shift
NMR	Nuclear magnetic resonance
NR	Nanoribbon
OFET	Organic field-effect transistor
OLED	Organic light emitting diode
OMBE	Organic molecular beam epitaxy
OTFT	Organic thin-film transistors
PAH	Polyaromatic hydrocarbon
PTCDI	3,4,9,10-perylene-tetracarboxylic diimide
PXX	Peri-xanthenoxanthene
SC	Stabilising conditions
SOMO	Singly occupied molecular orbital
SPM	Scanning probe microscopy
STM	Scanning tunnelling microscopy
STS	Scanning tunnelling spectroscopy
SUMO	Singly unoccupied molecular orbital
TBP	Tetra[1,3-di(tert-butyl)phenyl]pyrene
TCNQ	Tetracyanoquinodimethane
TDA	4,1′,4′,1″-terphenyl-1,4″-dicarboxylic acid
TMA	Trimesic acid
TMLA	Trimellitic acid
TPA	Terephthalic acid
TTF	Tetrathiafulvalene
UHV	Ultra-high vacuum
UPS	Ultraviolet photoelectron spectroscopy
UV	Ultraviolet
vdW	Van der Waals
VL	Vacuum level
VO3	Vat Orange 3
XPS	X-ray photoelectron spectroscopy

1 Introduction: Molecules at Metallic Surfaces

In recent years, electronics based around small molecules have become increasingly more prevalent. Optoelectronic applications generally require tuneable semi-conducting materials[1,2] with controllable frontier orbital energies and HOMO-LUMO (highest occupied – lowest unoccupied molecular orbital) gaps. Polyaromatic hydrocarbons (PAH) showcase these properties in optoelectronics, with uses as chromophores[3,4] and emissive materials[5]. The frontier energy levels of PAHs may be tuned in a variety of ways, including: changing the size of the aromatic network[6]; changes to the edge states and functional groups at the peripheries[7]; and the replacement of carbon positions in the framework via heteroatom doping[8–12]. The effects of increasing the size of the aromatic network and doping are subjects of particular interest for this project.

Bottom-up synthetic methods are one potential way of further increasing the number and variety of these structures. There are an increasing number of demonstrations of the power of bottom-up synthetic techniques, one field of which involves the use of underlying substrates as both catalysts and frame-works for the formation and structure of the resulting products. The field of on-surface synthesis is an exciting and rapidly expanding one, with a steadily increasing number of synthetic pathways that can yield significantly different results to their solution-based counterparts[13–18].

Studying and exploiting the self-assembly of these molecules at interfaces also paves the way to smaller-scale devices that are not currently possible with top-down processing methods. Furthermore, understanding how these molecules interact with and assemble on electrode-type substrates is also essential for the creation of more efficient devices with good matches between molecular energy levels and the electrode Fermi level for charge transport in devices[19,20]. In particular, the structure of the first few layers of molecular material in devices has a significant effect on this energy level alignment.

In the following, the background to all of these aspects will be explored in the context of studying molecular systems at metallic surfaces. A particular focus of this project is on the molecule *peri*-xanthenoxanthene (PXX), an electron donor molecule, and

how its structure may be tweaked via on-surface synthesis in order to change its properties for potential future use in optoelectronic devices.

In this section, the basic concepts of molecular systems adsorbed at metallic surfaces will be discussed. In particular, the effects of molecular adsorption on interfacial dipoles, frontier molecular orbital shifts and charge transfer are presented. Finally, brief literature reviews on 2D self-assembly and on-surface reactions are set out.

1.1 Work Function and Interfacial Dipoles

The work function of a metal surface, ϕ, is defined as the energy required to remove an electron from the highest bound state (the electrochemical potential of the surface, μ, or the Fermi level, E_F, at low temperatures) to rest at the vacuum level (*VL(s)*), just beyond the surface at a point at which the image force can be neglected[21]:

$$\phi = VL(s) - \mu = VL(s) - E_F$$

Eq. 1.1

The difference between the vacuum level just outside the surface (*VL(s)*) and the vacuum level at an infinite distance (*VL(∞)*) can be mainly attributed to the effect of the surface dipole layer. Variations in measured work functions are found for different facets of the same material[22], and thus the corresponding changes in surface potential must clearly play a role in the work function value as the Fermi level is a common property of the bulk material. The work function can be related to the compactness of the surface, with the work function increasing for more compact facets of the same material[23]. As *VL(s)* is usually found to be higher than *VL(∞)*, it can be seen as an initial electron extraction barrier that must be overcome to bring an electron to rest at larger distances.

The surface dipole layer is a result of the spill-out of electrons that occurs at a metallic surface. This is because there is no repulsion felt with other electrons that would have been found in the 'missing' half of the crystal (where there is now a vacuum). A corresponding reduction in the density of electrons also occurs at the surface layer due to this 'spill out', leading to a dipole formation. A diagram, adapted from Ishii et al.[24] in **Fig. 1.1**, illustrates the change in potential felt by an electron as it moves further away from a surface. Initially at small distances, this can be modelled as an infinite plane capacitor. As the electron moves further away, the dipole layer of the surface

can be considered as a point dipole, so the potential decays with x^{-2} to the vacuum level at infinity.

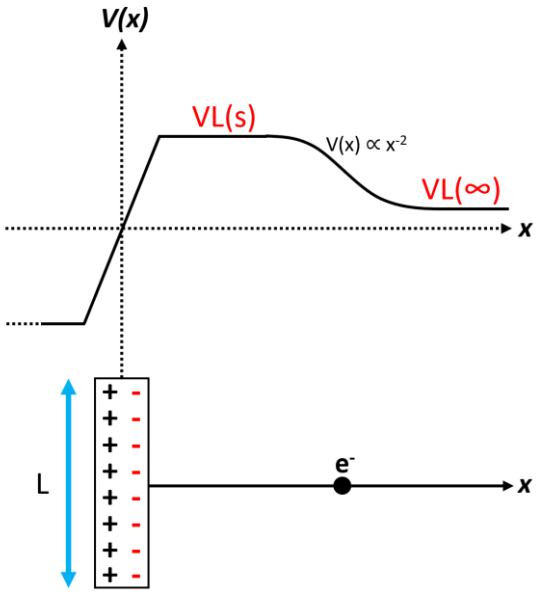

Figure 1.1. *An illustration, adapted from Ishii et al.*[24]*, of a model of the potential felt by an electron (V(x)) as it moves further (in x) from the surface dipole of a metal. The initial linear approximation only holds at shorter distances from the surface, as the system can be approximated as a plate capacitor.*

1.2 Molecular Adsorption

Adsorption of molecules can lead to a variety of changes to properties observed at interfaces, including the work function. There are two extremes of adsorption: physisorption and chemisorption. Physisorption is characterised by weak molecule-metal interactions (mostly van der Waals (vdW) forces) and a shallow adsorption potential well, with the adsorbate often found further from the surface plane, at a distance equal to the combined sum of the van der Waals radii of both systems. Chemisorption, on the other hand, is a closer, stronger binding between the molecule and substrate; hybridisation (the formation of new states) and broadening of the adsorbate and surface wavefunctions may occur, and the molecule sits more closely to the surface plane than the sum of the vdW radii[21]. In some cases, chemisorption may be associated with breaking intramolecular bonds in the adsorbate, with new bonds to the substrate formed. In general, many molecular systems sit somewhere between these two extremes. As is discussed later, the adsorption potential of molecules is also affected by the presence of other species on the surface; stabilising interactions between co-adsorbates may also change the adsorption potential well.

The adsorption of molecules at metallic surfaces can also have a significant impact on the interfacial dipole, and thus the work function of the surface. Several different situations leading to this are presented in **Fig. 1.2**.

A phenomenon that generally affects most adsorbate-metal interfaces is the so-called 'pillow' effect (**Fig. 1.2(a)**). Upon adsorption of a molecule at a metal surface, the 'spilled-out' electron density of the metal may be pushed back by Pauli repulsion with electrons in the molecule. As a result, the interfacial dipole is reduced underneath the molecule. This effect is shown throughout **Fig. 1.2**.

Charge transfer between the molecule and metal (and vice versa) also alters the interfacial dipole (**Fig. 1.2(c)**). A negatively charged adsorbate increases the size of the interfacial dipole - this is because the dipole formed between it and its 'image charge' in the underlying metal lies in the same direction as the initial surface dipole before adsorption[21]. As a result, increasing the coverage of such a negatively charged adsorbate also leads to an overall increase of the work function (in the macroscopic sense) of the surface. A positively charged adsorbate and its dipole (with its image charge) opposes the intrinsic surface dipole, leading to a reduction in the overall surface dipole and thus a reduction in the work function[25]. Whilst in both cases, an initial increase in coverage will either increase or reduce the work function, a maximum/minimum work function value may be reached before the surface is saturated with a full layer of the adsorbate[25]. This is because an increase in charged species at the interface also leads to adsorbate-adsorbate repulsion, thus eventually disfavouring charge transfer and reducing the overall transfer to/from the adsorbates, slightly reducing their effect on the work function.

Intrinsic molecular dipoles (depending on the conformation of the adsorbed molecule at the surface) may also add to/subtract from the intrinsic interfacial dipole (**Fig. 1.2(d)**).

Finally, in the case of chemisorbed species, there may also be a dipole associated with the bond/hybrid states between the molecule and the surface (**Fig. 1.2(e)**).

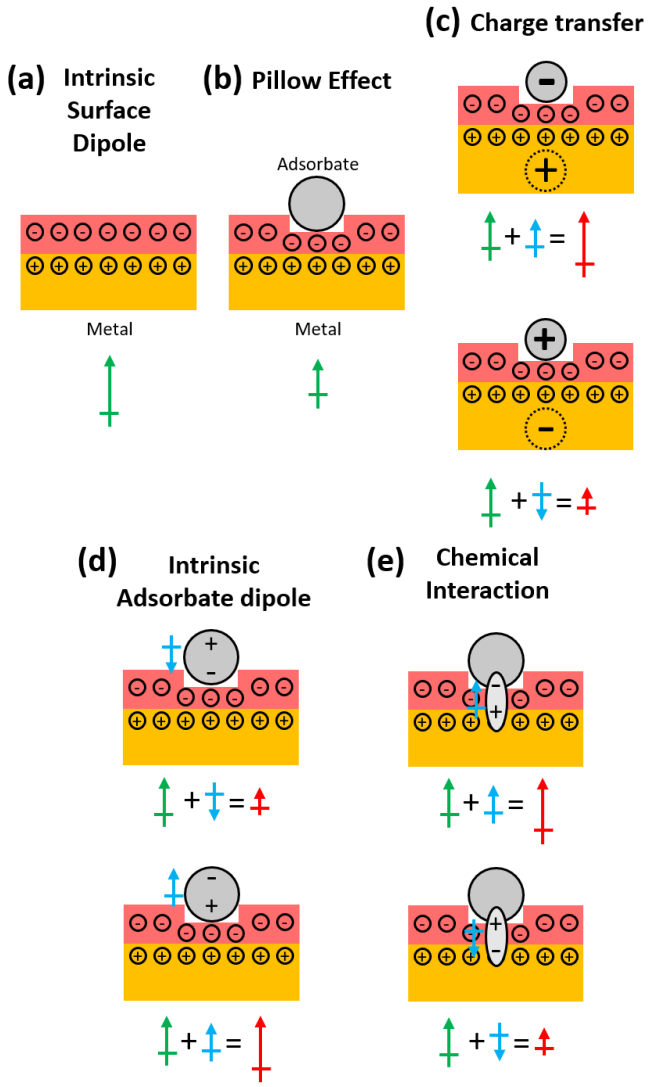

Figure 1.2. *(a) and (b) The intrinsic surface dipole due to electron spill out, and the effect that adsorbed molecules may have on it (the 'pillow effect'). The green dipole symbol refers to the intrinsic interfacial dipole. This is shown for all of the diagrams as it is omnipresent. (c) Dipoles due to charge transfer between adsorbate and surface (blue) may add to or oppose the intrinsic surface dipole, increasing or reducing the overall surface dipole (red). (d) Molecules may have intrinsic dipoles of their own due to their molecular structure or adsorption conformation. (e) Chemical bonds between molecule and substrate may also be polar.*

Assuming that there is not a significant level of hybridisation, the adsorption of molecules onto metallic surfaces can also have a notable effect on the energies of the adsorbate's HOMO (highest occupied molecular orbital) and LUMO (lowest unoccupied molecular orbital). In particular, a shrinking of the HOMO-LUMO gap occurs, with the effective HOMO being raised in energy relative to the gas phase molecule, and the effective LUMO being lowered in energy relative to the gas phase. This can be rationalised by considering the screening effects of the metal on charged

species via the image-charge effect; the energy of charged species is lowered via an interaction with an opposing image charge in the underlying metal. Less energy is required to extract an electron (i.e. the effective HOMO is increased) and more energy is gained from acquiring an electron (i.e. the effective LUMO is decreased). This effect is shown in **Fig. 1.3** and has an impact on charge transfer between metals and adsorbates[21]. The HOMO-LUMO gap may also be further reduced by a decreased molecule-metal distance when adsorbed[21].

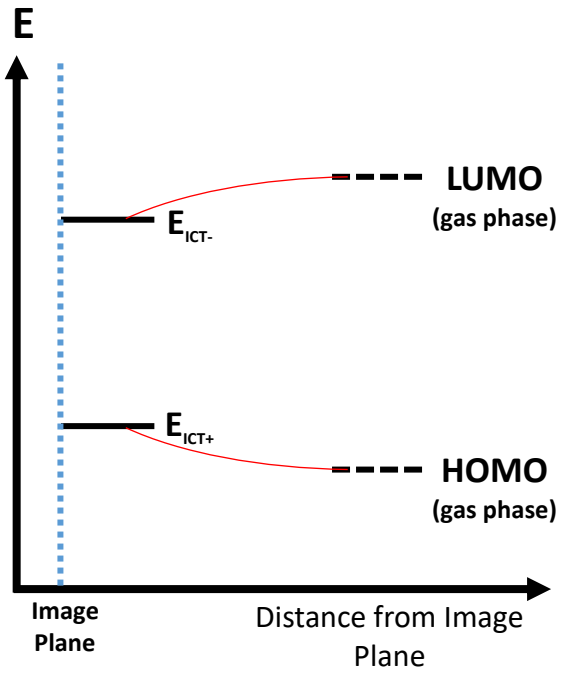

Figure 1.3. *The effect of metal substrates on the effective HOMO and LUMO energies, referred to here as E_{ICT+} and E_{ICT-}. A narrowing of the gap occurs upon the approach of the molecule to the image plane of the surface.*

1.3 Charge Transfer

Charge transfer (CT) between adsorbed molecules and an underlying metal may occur in two ways. In the case of weakly adsorbed or decoupled molecules, transfer of full charges may occur across the interface via tunnelling of electrons: this is known as the integer charge transfer (ICT) model, as described by Braun et al[26]. This relies on the relative alignment of the energy levels of both the molecule and the metal. **Fig. 1.4**, adapted from Braun et al.[26], shows three possible situations in the ICT model. If the energy of the effective molecular HOMO, referred to above as E_{ICT+} (the positive integer charge transfer state), is higher than the Fermi energy of the metal, then charge

is transferred from the molecule to the metal until an equilibrium is reached, where E_{ICT+} and the potential energy of the interface (Δ) is equal to the substrate work function. As a result, the Fermi level is pinned to E_{ICT+} at the interface. The opposite is also true for CT into the effective LUMO (E_{ICT-}); if the Fermi level is higher than E_{ICT-} then charge is spontaneously transferred from the metal to the molecule until an equilibrium is reached.

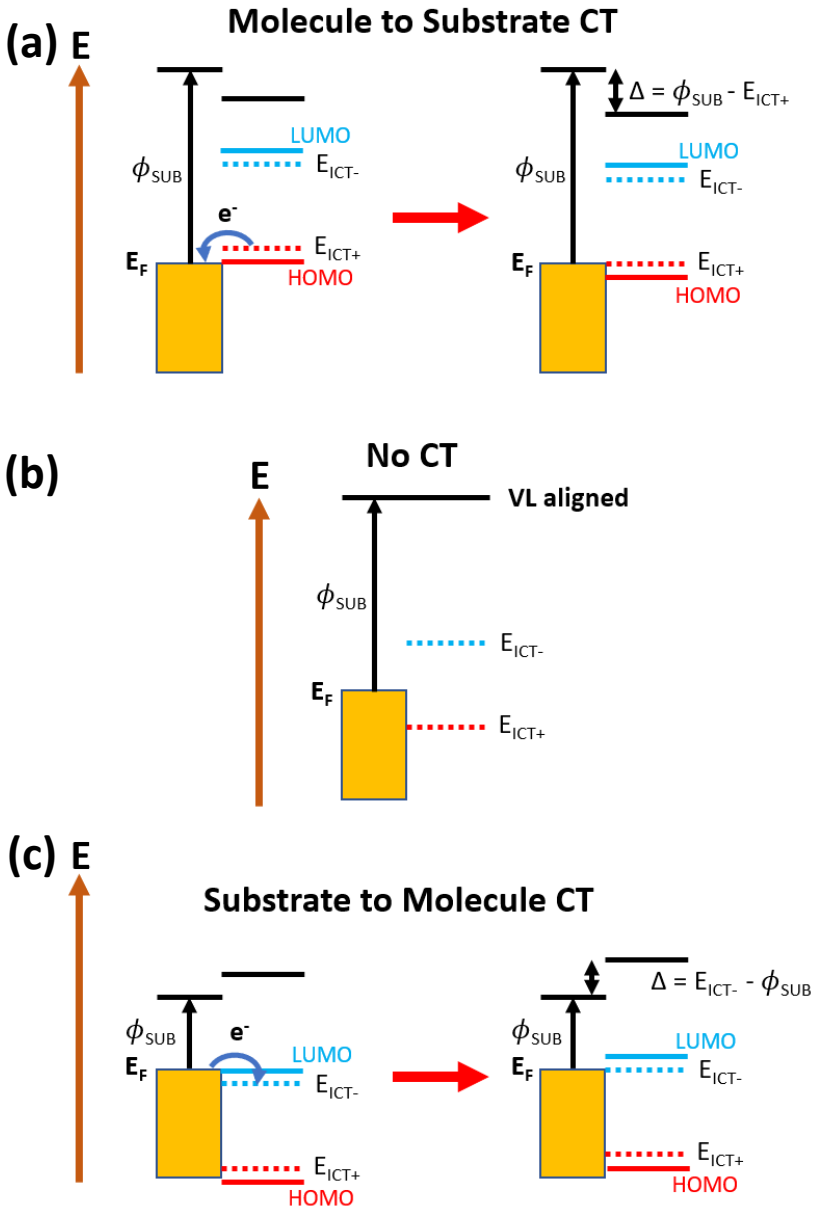

Figure 1.4. *Diagrams illustrating the ICT model, adapted from Braun et al.*[26] *In (a), the energy of the effective HOMO is higher than the Fermi energy of the surface, resulting in molecule to substrate CT. In (c), the effective LUMO is lower in energy than the Fermi level of the surface, resulting in substrate to molecule CT. The alignment in (b) is such that no CT may take place, with alignment of the vacuum levels shown.*

If the Fermi level lies between E_{ICT+} and E_{ICT-} then no charge is transferred, and the vacuum levels of both sides of the interface are aligned. The latter situation is an idealised one, and does not take into account possible dipoles that may form when molecules are adsorbed at surfaces but no charge transfer occurs[21].

The ICT model does not apply to interfaces in which more hybridisation is involved. When molecules are chemisorbed, the description of any charge transfer that takes place becomes considerably more complex. Whilst the general alignment of the molecular levels with the Fermi level may still dictate the general direction of charge transfer, chemical bonds between the molecule and metal can also result in a rearrangement of charge at the interface, and the energies of the HOMO and LUMO of the molecule may be significantly modified by hybridisation.

The induced density of states (IDIS) model may be used for molecules that exhibit a chemical interaction with the substrate (albeit a weak one, with no covalent bond). Hybridisation of the molecular and metal states leads to a continuum density of broadened states that are located both on and between the molecule and substrate atoms. As a result, the molecule may no longer be considered as purely a semiconductor, but instead has inherited some metallic character from the substrate. The direction of the charge transfer is dictated by the difference between the metal Fermi level and the charge neutrality level (CNL). This is modelled by taking the calculated induced density of states of the interface and filling it up with charge from the gas phase molecule – this dictates the position of the CNL[21].

Neither model may perfectly suit most systems – but many can be reasonably approximated as one or the other. In the case of strongly chemisorbed systems, such as those that exhibit significant charge transfer but not Fermi-level pinning (e.g. the filling of a molecular LUMO that is downshifted well below the Fermi level[27–30]), the IDIS model does not apply. In some cases, such a chemisorption via certain molecular bonding sites can result in a significantly more stable charged species when bound to the surface, through increased levels of aromaticity or conjugation length[31–33].

1.4 Supramolecular Self-Assembly at Surfaces

Supramolecular self-assembly can allow the precise formation of structures on the nanoscale that are not yet feasible with top-down methods. Careful control of molecular structure may yield a wide variety of possible geometries and structures,

with the reversibility of intermolecular bonding also giving structures self-healing properties. This control can be enacted by choosing the functional groups of the sub-units within the structure, as well as controlling their geometry via synthetic chemistry. Surface-based supramolecular assembly has several aspects that distinguish it from the more traditional three-dimensional supramolecular chemistry. The use of supporting substrates in 2D self-assembly allows for templating via surface structure; using substrates with a particular reconstruction or symmetry can also help to guide self-assembly[34]. Changing the reactivity of the substrate material can in turn also affect the type of bonding that takes place as well as determine the molecule-substrate binding strength[35]. Imperfections in surface structure such as step edges may also interfere with supramolecular structure, and often act as locations for the initial seeding and growth of structures.

There are several main types of intermolecular interaction that are often exploited for on-surface self-assembly. A list of these, with indications of their range and strength, is presented in **Table 1.1**. From this list, the only truly long-range type of interaction is electrostatic. Van der Waals (vdW) forces are omnipresent and are often weak relative to the other interactions listed, with the exception of some systems such as those in which long alkyl chains with extensive vdW contacts are involved[14,36,37]. Substrate-mediated interactions (not listed) can also play a role in a small amount of systems; adsorbed molecules may act as scattering centres for electrons in the substrate's surface state and change the adsorption potential for other molecules[21]. All of the interactions on this list play significant roles in the self-assembly of the various molecules described throughout this thesis.

Interaction	Strength	Range
vdW[38]	0.02 – 0.10 eV	<1 nm
H-bonding[21,39]	0.01 – 1.70 eV	1.2 – 3.0 Å
Halo-bonding[40]	0.1 – 1.6 eV	0.6 – 4.0 Å
Metal-organic[38,41]	0.1 – 3.5 eV	1.5 – 2.5 Å
Electrostatic[38]	0.05 – 2.5 eV	Long range

Table 1.1. *A list of the most important supramolecular interactions, along with ranges for their strength (energy) and distances.*

Hydrogen bonding is a particularly common interaction studied in on-surface supramolecular assembly. A hydrogen atom, referred to as the hydrogen bond *donor*, is covalently bound to a more electronegative atom (X), resulting in a polar bond. The donor hydrogen may then form a bond (that can have both electrostatic characteristics and some features of covalent bonding, depending on the system) to another atom (A) that is typically an electronegative element with a lone pair of electrons, known as the hydrogen bond *acceptor*[39]. A variety of functional groups have been shown to take part in H-bonding at surfaces[42]. Carboxylic acid moieties have been particularly extensively studied[43], with molecules such as trimesic acid[44] (TMA) and related structures[42,45,46] having been a particular focus. Structures consisting of multiple H-bonds for extra strength have been demonstrated, including co-assemblies such as the PTCDI-melamine network[47–49], in a similar fashion to DNA base pairs[50]. These assemblies involve nitrogen-based functional groups as the H-bond acceptor and donor, as well as ketone groups that may act as acceptors[51]. Hydrogen bonds may be classified into strong, moderate and weak bonds, based on their length, directionality and induced changes in the length of the X-H bond[21,39]. Whilst many of the above systems were designed for the formation of moderate to strong hydrogen bonds, weaker H-bonds may also occur in other systems that are designed for other purposes. For example, C-H bonds in adsorbed molecules can act as weak hydrogen bond donors[52–55].

Halogen bonding[40] is considerably less widely studied but has increasingly been a focus of research in supramolecular chemistry in recent years. A halogen bond consists of an attractive interaction felt between an electrophilic D-X (X = Cl, Br, I…) donor and a nucleophilic acceptor moiety. The interaction typically arises due to the polarisable nature of larger halogen atoms. Other groups in the same molecule can withdraw charge through the D-X sigma bond, resulting in a distribution in the electrostatic potential over the halogen atom. The so-called ‘sigma hole’, a region of positive electrostatic potential, is thus formed on the side of the halogen opposite to the sigma bond[40]. A band of negative electrostatic potential can also be found around the middle of the halogen atom. Halogen bonds are a result of the sigma hole being oriented towards regions of negative electrostatic potential, such as electronegative atoms on other molecules or the sides of other halogen atoms. There are three main

forms of halogen bond, illustrated in **Fig. 1.5**. A brief literature review of examples of halogen bonded systems can be found in the introduction to **Chapter 5**.

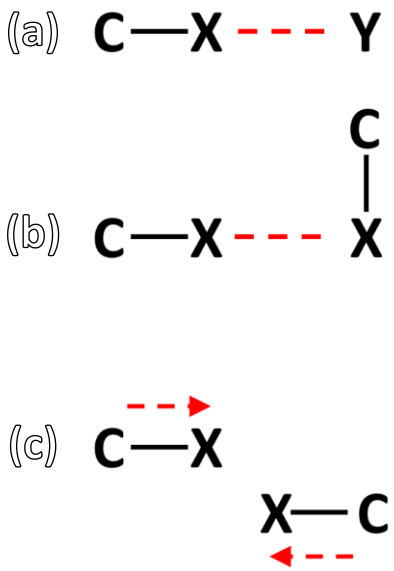

Figure 1.5. *(a) – (c) The three general types of halogen bonding seen with C-X groups. (a) and (b) involve the orientation of the sigma hole towards regions of negative electrostatic potential, whereas (c) is more of a dipolar interaction. X = halogen, Y = halogen bond acceptor.*

Metal-organic (MO) co-ordination provides another way of forming selective and directional bonds of intermediate strength[16] in the formation of supramolecular architectures. MO structures are both reversible and directional, and a wide variety of structures may be formed, such as 1D chains, 2D grids and 3D frameworks[56]. In these networks, ligand molecules are bound to shared metal co-ordination centres and arranged into an ordered array. This shows promise for future technological applications that may require regular arrays of metal atoms, such as catalysis[56,57] and information storage[58]. There is also the potential for other novel properties in 2D co-ordination networks that have been predicted by theory, such as topological insulation[59]. Additionally, the large surface area of some porous metal organic frameworks (MOFs) can be exploited for the storage of gases[60]. Surface-confined MOFs in general have fewer linkages per metal atom due to the nature of 2D surface confinement. In on-surface MOF formation, the metal atom may be sourced from the surface itself (as an adatom[61] or pulled-up substrate atom[62]) or co-deposited with the molecular linkers[34]. Carboxylic acid functionalities are commonly used in on-surface MOFs[56,63]; after deprotonation, often by atoms from the underlying metal substrate[64,65]

or co-deposited transition metal atoms[66], they may arrange into arrays that depend on the number and location of the binding groups within the molecular linkers. Molecules such as trimesic acid (TMA)[67], terephthalic acid (TPA)[66], trimellitic acid (TMLA)[68] and 4,1′,4′,1″-terphenyl-1,4″-dicarboxylic acid (TDA)[69] are commonly used as MOF building blocks. A wide variety of other molecular linkers have also been presented in the literature. A comprehensive list of these is presented in the review by Dong et al.[56], and includes other motifs such as carbonitrile groups[70], halogenated precursors[35], pyridine groups[71], thiols[61] and alcohols[70]. As with carboxylic acids, in some of these cases activation by the surface is required before MOFs may form – such as the deprotonation of SH or OH groups and the dehalogenation of C-X groups. In many examples of on-surface synthesis that involve Ullmann couplings (see later in this chapter), a metal-organic intermediate (also known as a 'protopolymer'[35,72] in some cases) is formed after the dehalogenation of the C-X bond in the precursor and the resulting formation of a radical carbon position[35,73–75].

The effects of electrostatic interactions on intermolecular assembly are less widely studied. There are several cases in the literature of dispersive assemblies that may be the result of repulsive interactions between adsorbates. It has been demonstrated that molecules such as tetrathiafulvalene[76,77] (TTF), rubrene[78], porphine[79], tetraphenyl porphyrins[80] and phthalocynanines[81] may become charged upon adsorption onto a metallic surface, leading to a dispersed repulsive assembly. The amount of molecule-molecule repulsion can depend on the substrate used[80,82], as such a charge transfer depends on the relative alignments of metallic and molecular states. Increasing the coverage of charged molecular species at surfaces may eventually lead to more compact assemblies at higher coverages, as is the case with TTF on Au(111)[77]. At lower coverages, long-range repulsive forces dominate the TTF/Au(111) assembly. At higher coverages, however, short range attractive forces (such as H-bonding, vdW) become more important. As shown by Fraxedas et al.[77], an increase in molecular coverage also leads to a decrease in the dipole moment per molecule at the surface due to a decrease in the amount of charge transfer. Because of this, the work function of the surface does not change linearly with increasing coverage, in a similar fashion to other charged systems at surfaces[25]. More complex structures may form when molecules that become oppositely charged when adsorbed at interfaces are co-deposited[83]. Della Pia et al.[84] showed via experimental results on the TBP/TCNQ

(tetra[1,3-di(tert-butyl)phenyl]pyrene/tetracyanoquinodimethane) system, along with Monte Carlo calculations, that the structure of electron donor/acceptor islands can be a result of a delicate combination of electrostatic interactions combined with other intermolecular forces. There are several other examples of mixed donor-acceptor type assemblies, many of which involve the acceptor TCNQ and other related molecules[85–89]. As will be discussed further in **Chapter 8**, the structure of these assemblies can depend quite significantly on not just electrostatics, but also other intermolecular interactions such as H-bonding, as well as the coverage of each species[90]. Another perspective on this is to consider that mixing molecules at surfaces affects the level of possible charge transfer with the substrate, due to the effects of the supramolecular surroundings on the stability of the resulting charged species[21].

1.5 On-Surface Reactions: Covalent Bond Formation

Stronger than any of the aforementioned intermolecular forces is, of course, the covalent bond. The study of on-surface reactions that result in the formation of covalent bonds is an area of rapidly increasing interest in the surface science community. On-surface synthesis opens new pathways to reactions that would not normally readily occur in traditional solution-based chemistry. Networks that are based around covalent bonds also have an inherently higher level of stability than those held together by intermolecular interactions, along with more effective charge transport properties through the bond[91]. Control over the reaction pathway on metallic surfaces is usually enacted via the precursor structure, substrate material/facet, and temperature. There are an increasing number of types of reactions that have been demonstrated in the literature[13,17]. In the following, a brief review of the more prevalent reactions is presented.

The most commonly utilised on-surface reaction is the Ullmann[92] coupling. It was first demonstrated in this context with iodobenzene on Cu(111) by Xi et al[93,94]; later, the STM tip-induced Ullmann coupling of the same molecule was also demonstrated[95]. The ground-breaking study of brominated (tetraphenyl)porphyrins by Grill et al.[96] first demonstrated the use of Ullmann coupling for the formation of 1D and 2D covalent networks, and since that time there have been a large amount of studies based on the formation of various structures at surfaces via Ullmann coupling[13,17].

The reaction proceeds thusly: a halogenated (usually Br or I) molecule is adsorbed onto a metallic surface. At a certain temperature (depending on the surface used), the C-X bond can undergo a surface-catalysed homolysis, leaving behind a radical carbon position and a halogen atom that is bound to the metal. The resulting molecular radicals may then diffuse and combine to form new molecules. The design of the precursor usually dictates the resulting structure; for example, a singly halogenated monomer may only form dimers after Ullmann coupling, whereas two or more C-X bonds may lead to 1D chains or 2D networks[96]. In some cases, other reactions may then proceed after an Ullmann coupling at similar or higher temperatures, such as dehydrogenation and cyclization[97].

The conditions required for Ullmann coupling, along with the morphology of the resulting covalently bound structures, significantly depend on the substrate used. More reactive surfaces generally dehalogenate precursors at lower temperatures – for example, dehalogenation often requires annealing on Au(111), whereas it readily occurs at room temperature on copper surfaces[98]. Differences may be found between substrates of the same material but different facets due to changes in the relative reactivity and the geometry of the surface[35]. It has also been shown that using different substrates can change the relative density and order of the resulting 2D covalent structures[99]; stronger binding between the surface and the molecules limits the diffusion of radicals and results in sparser, more dendritic assemblies. The surface geometry/reconstruction can also serve to direct and template the structures[100,101]. The choice of halogen for Ullmann coupling plays a significant role; iodine typically requires lower annealing temperatures for dissociation than bromine due its weaker bond to carbon – this can be exploited for the sequential addition of building blocks of different components[100]. As mentioned above, the formation of metal-organic proto-polymer intermediates after dehalogenation is also often seen on surfaces with higher surface adatom concentrations, such as Cu(111).

Alongside Ullmann coupling, there are a number of other reactions that have been demonstrated in on-surface studies. Surface-assisted C-H activation and dehydrogenation is commonly used in on-surface coupling reactions. Upon heating on metal surfaces, certain C-H positions in molecules are often found to more favourably react to form C-C linkages[102,103]. This is frequently used in the on-surface synthesis of graphene nanoribbons, in which an Ullmann coupling that forms a polymer is followed

by dehydrogenation that flattens the polymer into a nanoribbon[97]. Glaser coupling, in which a C-C bond is formed between terminal alkyne groups, has also been reported[104–106], as have reactions between terminal alkynes and halogen groups (Sonogashira couplings)[107]. Condensation reactions, using boronic acid groups to form boroxines or boronic esters[108] have been shown to occur readily at room temperature on Ag(111), and this has also been combined with Ullmann coupling to form networks consisting of boroxine and C-C linkages in two steps[109]. Other condensation reactions in the literature include those resulting in the formation of an imines[110] and imides[111]. More examples of on-surface couplings, such as several examples of different types of cyclisation reactions, can be found in comprehensive reviews on the subject[13,17].

1.6 Molecular Systems Used in this Work: PXX and Related Molecules

In this thesis, the self-assembly, on-surface reactions and electronic properties of *peri*-xanthenoxanthene (PXX) and several related molecules (**Fig. 1.6**) are investigated on metallic surfaces via scanning tunnelling microscopy (STM), scanning tunnelling spectroscopy (STS) and x-ray photoelectron spectroscopy (XPS).

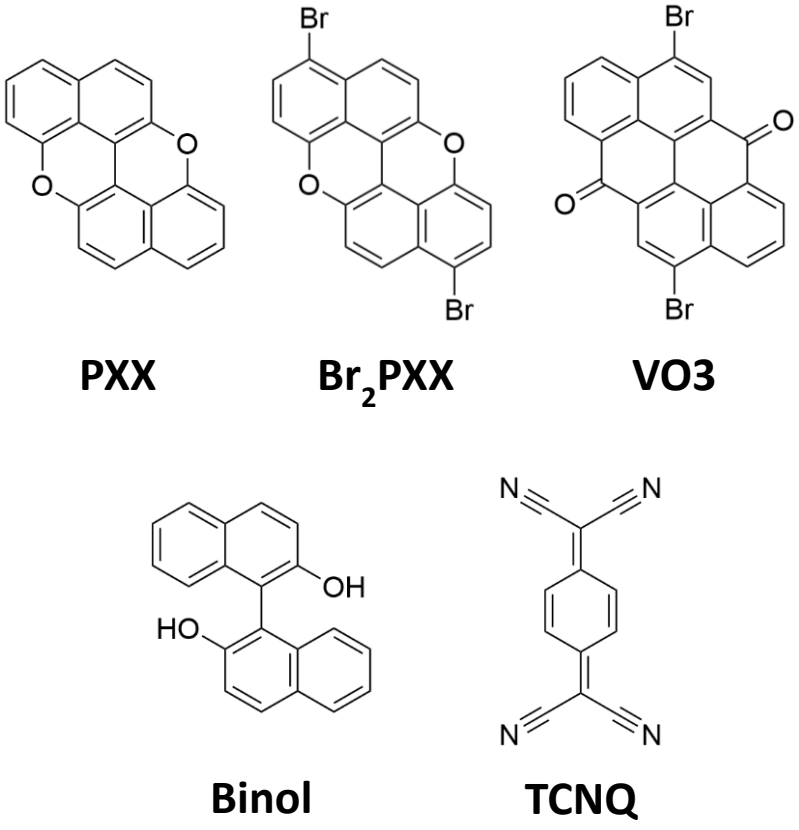

Figure 1.6. *The molecules worked with during this project. VO3 is short for Vat Orange 3, and TCNQ is short for tetracyanoquinodimethane.*

PXX is a chromophore that has previously been used as an active organic semiconductor in flexible organic light emitting diode (OLED) screens[112,113]. Structurally, PXX is the O-doped, more stable analogue of anthanthrene[114]. Substituted derivatives of PXX have been found to have good injection and carrier transport properties, along with high levels of chemical and thermal stability[114,115]. It has been shown that altering the structure of PXX by changing the size of the aromatic moieties can be used to tune the absorption properties of the molecule, with derivatives retaining the same high emission yields. As an electron donor, PXX's HOMO level can be raised (and thus its donor strength increased) by the addition of further aromatic structure, as shown by Miletić et al.[6] (**Fig. 1.7(a)**). Small zig-zag nanoribbons with PXX features (**Fig. 1.7(b)**) have also been synthesised up to three units in length, with a corresponding increase in the HOMO level, as measured by cyclic voltammetry and photophysical data[116]. In addition, it has been shown that the HOMO level of PXX may be further tweaked (and lowered) by the addition of alkyl-imide groups, producing a molecule that was found to be photoredox active[7].

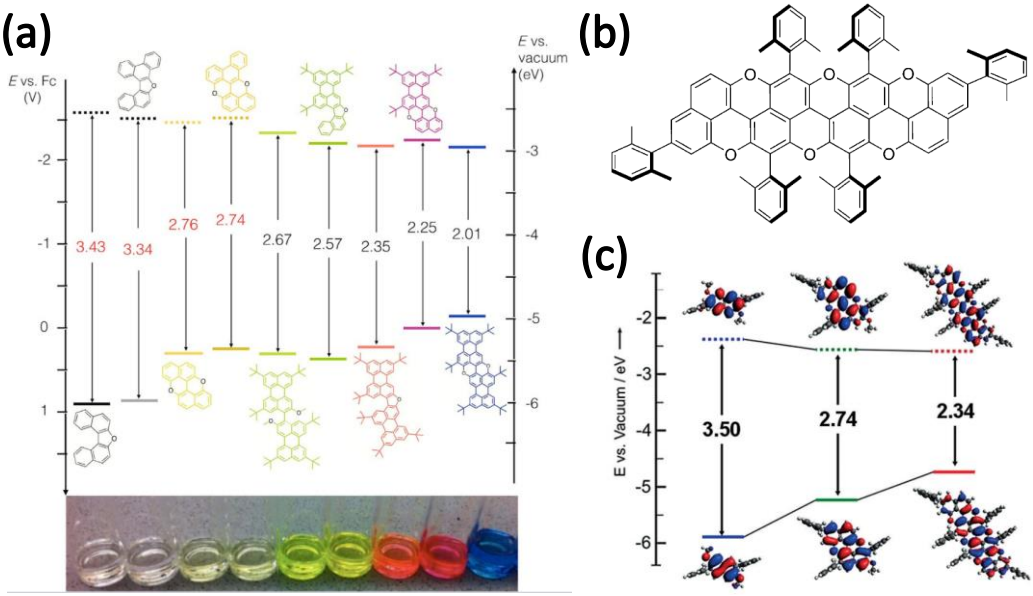

Figure 1.7. *(a) Figure adapted from Miletić et al.*[6] *showing the dependence of the HOMO-LUMO gap on the addition of aromatic features to the structure of PXX. (b) and (c) Figures adapted from Berezin et al.*[116]*, showing the structure and HOMO-LUMO gaps of PXX-type nanoribbons.*

The central oxygen-containing rings in PXX are also shown to be anti-aromatic by density functional theory (DFT) calculated nucleus-independent chemical shifts (NICS) (performed by Dr. Luka Đorđević, University of Trieste), and this is also

expected to be true of nanoribbon structures that may be formed from its derivatives (**Fig. 1.8**). Few examples of molecules studied/formed at surfaces for their anti-aromaticity exist[117], and it is not clear what effect adsorption onto a metallic surface may have in this case. The oxidation of PXX molecules or nanoribbons due to charge transfer with the surface could, however, result in a fully aromatic molecule.

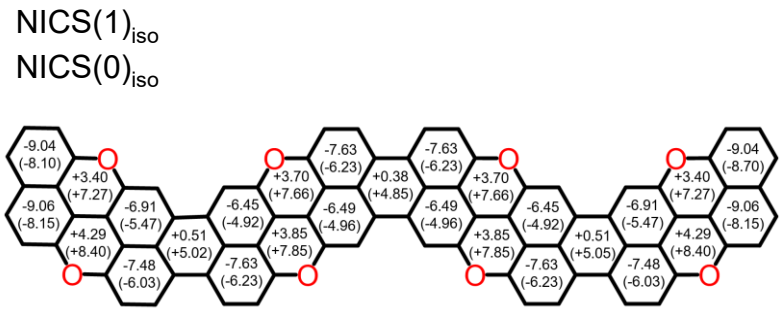

Figure 1.8. *A PXX nanoribbon with calculated NICS values for each ring. A large positive value indicates anti-aromaticity. NICS(0) is the value at the centre of the ring, NICS(1) is the value 1 Å above the centre. Calculations performed by Dr. Luka Đorđević, University of Trieste.*

In the following, PXX's behaviour as an electron donor molecule will be examined in the context of its adsorption on metal surfaces in idealised conditions (i.e. in vacuum), both alone and with an electron acceptor, tetracyanoquinodimethane (TCNQ). Its electronic properties and self-assembly behaviour at metallic surfaces will be characterised via scanning tunnelling microscopy and spectroscopy. Binol, a precursor to PXX in one solution-based synthetic protocol[118], will also be studied at surfaces with the aim of forming PXX via metal-catalysed on-surface ring-closing reactions. In addition, on-surface reactions involving a brominated derivative of PXX, Br_2PXX, will be investigated, with the aim of forming ultra-thin PXX nanoribbons at surfaces that are significantly longer than is possible in solution, with corresponding measurements to examine their potential properties as stronger electron donors than the PXX due to their increase in length[116,119–121]. An acceptor analogue of PXX, Vat Orange 3 (VO3), will also be examined in this context, with the aim of forming strong acceptor nanoribbons. Finally, the tuning of the properties of these nanoribbons via co-polymer formation will also be investigated.

In all of the above cases, the molecular systems will be characterised on single crystal metal surfaces in ultra-high vacuum ($<10^{-9}$ mbar). This allows the study of idealised interfaces, which can give greater insight into molecule-substrate and molecule-

molecule interactions without the interference of atmospheric gases/contaminants. It also enables the facile use of more reactive materials that would oxidise in air, such as copper surfaces. Furthermore, examining these systems at low temperatures in vacuum allows precise characterisation via the use of techniques such as scanning tunnelling spectroscopy and constant height scanning tunnelling microscopy imaging, both of which are discussed in more detail in **Chapter 2**.

This project is part of a collaboration with the group of Prof. Davide Bonifazi at Cardiff University and the University of Trieste. PXX and Br_2PXX were synthesised by Dr. Luka Đorđević, who also performed some of the DFT calculations shown. Other DFT calculations were also performed by Dr. Gabriele Sosso and Harry Pinfold at the University of Warwick. The collaborator that ran/analysed the calculations is indicated in the figure/table caption for each case. The rest of the molecules used throughout this project were purchased from chemical suppliers, with further purification performed in some cases.

1.7 Metallic Surfaces

Throughout this project, the (111) surfaces of gold and copper are utilised. Au(111) has been previously shown to enable the controllable study of Ullmann coupling reactions; the molecules may be easily characterised before and after reaction without de-bromination at room temperature[122]. Furthermore, it is generally seen as a more inert substrate – the trend in molecule-substrate interaction strength from Cu to Au can be attributed to the relative extent of the bonding d-orbitals, with the more extended Au 5d orbital resulting in a decreased coupling strength and thus a more repulsive interaction between molecule and metal[21]. As a result of this, molecules adsorbed onto Au(111) can sometimes be considered as relatively decoupled from the underlying metal surface, without the need for insulating layers such as NaCl. This may enable experiments in which molecular states with a resemblance to those seen in the gas phase can be observed by scanning tunnelling microscopy and spectroscopy. Cu(111) acts as a more reactive substrate in comparison to experiments on Au(111), with a significantly lower work function (The work function of Cu(111) is 4.98 eV and Au(111) is 5.31 eV)[123]. Copper surfaces can be useful for studying copper catalysed reactions in idealised conditions, as will be examined in the binol chapter of this thesis. Cu(111) also has a strong tendency to form metal-organic structures that

involve adatoms or pulled-up surface atoms[32,124–126], resulting in significantly different assemblies to those observed on Au(111).

Scanning tunnelling microscopy images of Au(111) and Cu(111) are shown in **Fig. 1.9**. The Cu(111) surface is unreconstructed, whereas Au(111) exhibits a 'herringbone' reconstruction. Pairs of parallel corrugation lines run along the equivalent [11$\bar{2}$] directions, with 120° bends at elbow points to form a zig-zag pattern. This reconstruction is due to the elastic strain that is a result of incorporating 23 surface atoms into 22 bulk sites; the surface contracts along the [1$\bar{1}$0] direction and forms the herringbone ridge lines to minimise its energy.

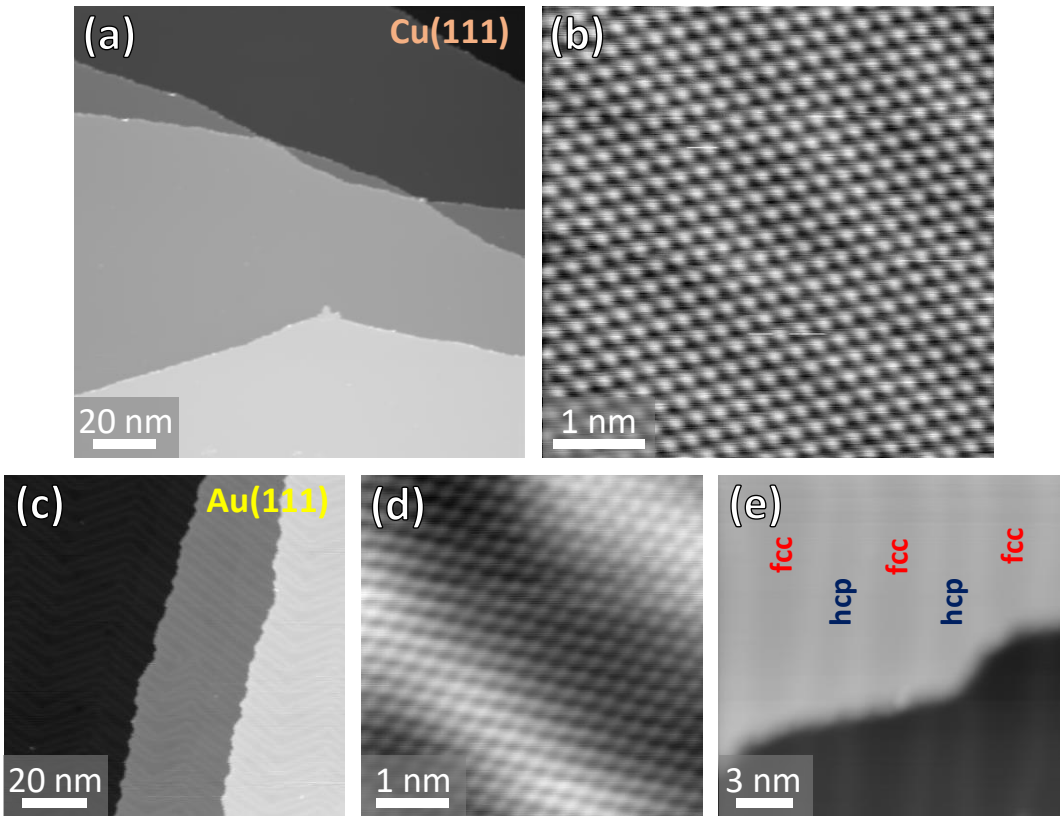

Figure 1.9. *(a) and (b) Overview and atomic resolution scanning tunnelling microscopy (STM) images of Cu(111). (b) – (d) STM images of Au(111), with the herringbone fcc and hcp regions indicated.*

The reconstructed surface has regions of fcc (face-centred cubic) and hcp (hexagonally closed packed) surface atoms[127], as indicated in **Fig. 1.9**. Adsorbates are often found to preferentially adsorb on the fcc regions and elbow sites due to their deeper potential well[76,128]. In some cases, strong binding to the Au(111) surface results in the lifting of the reconstruction – typically this can be seen in STM measurements when the

herringbone cannot be detected through molecular islands, or if there is a clear distortion of the ridge lines around adsorbates[129–131]. Atomic resolution of both surfaces is shown in **Fig. 1.9**. Two different Au(111) crystals were used during the course of this work, with different orientations relative to the STM scanning directions.

2 Experimental Methods: Background and Setup

2.1 Scanning Tunnelling Microscopy and Spectroscopy

2.1.1 Introduction

First demonstrated by Binnig and Rohrer in 1982[132], and later earning them the Nobel prize in physics in 1986, the scanning tunnelling microscope (STM) was a revolutionary invention that allowed unprecedented resolution when imaging conductive surfaces. Since that time, it has become a routine technique for studying systems at surfaces at the molecular and atomic level, revealing information about the geometrical and electronic characteristics of these systems. Due to the nature of the atomically sharp STM tip, precise manipulation of individual atoms and molecules has also been demonstrated[133,134] and has become increasingly sophisticated[135,136], giving scientists the ability to move closer to the ideas presented by Richard Feynman in his famous "There's Plenty of Room at the Bottom" lecture in 1959[137].

STM works on the principle of quantum tunnelling, which occurs when two conductive materials are held close together (at the nanometre scale) and a bias voltage is applied between them, leading to a tunnelling current[138]. In STM experiments, an atomically sharp metallic tip is brought close to a conductive sample of interest, with the bias voltage typically applied to the sample. A tunnelling current may then be detected, which can then be used to probe the surface by scanning the tip across it to form an image. In the following, a brief description of the theoretical background to quantum tunnelling will be provided, along with explanations of the different scanning modes employed to image surfaces with the STM. A related technique that can be used to investigate the electronic structure of the sample, scanning tunnelling spectroscopy (STS), will also be introduced. Finally, the experimental setup of the low temperature STM (LT-STM) used throughout this thesis will be presented.

2.1.2 Quantum Tunnelling: Theoretical Background

A schematic of the potential landscape experienced by an electron in a tunnelling junction is shown in **Fig 2.1**[139]. Three different situations are presented: zero bias, positive bias and negative bias (all applied to the sample). In the zero-bias situation, an electrical equilibrium is reached across the junction, with common Fermi levels

reached. No net transfer of electrons (i.e. a current) is seen in this situation. Applying a bias voltage, however, leads to the detection of a tunnelling current, the direction of which is determined by the polarity of the bias. In this situation, a positive voltage results in the transfer of electrons from the occupied states of the tip to the unoccupied states of the sample, and for a negative voltage the transfer occurs from the occupied states of the sample to the unoccupied states of the tip.

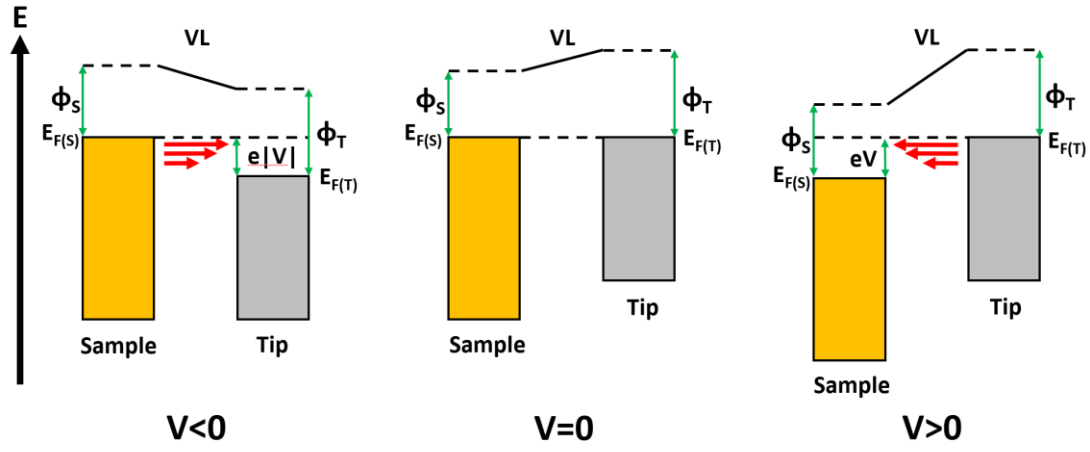

Figure 2.1. *Energy level diagrams for tunnelling junctions with different bias polarities. E_F refers to each electrode's Fermi level, V is the applied bias voltage (on the sample), e is the electron charge, ϕ_T and ϕ_S are the tip and sample work functions. For the negative bias situation (V<0), electrons flow from the occupied states of the sample to the unoccupied states of the tip. For the positive bias (V>0) situation, electrons flow from the occupied states of the tip to the unoccupied states of the sample. For both situations, there is exponentially decreasing current away from the Fermi level due to the increased potential barrier for electrons that are lower in energy, as shown by the decreasing size of the red arrows. When no bias is applied, there is no net current flow and the Fermi levels are aligned.*

The potential barrier in the gap region, shown by the size of both work functions (ϕ_T and ϕ_S for the tip and sample work functions, respectively) is typically much larger than k_BT (the thermal energy) of an electron, and thus no transfer of electrons between the two electrodes would be expected for a classical particle. However, as electrons can be described in terms of quantum mechanics with delocalised wave functions, a penetration through a large potential barrier may occur. This is referred to as quantum tunnelling.

A tunnelling current can be described in terms of time-dependent perturbation theory, shown in more detail elsewhere[139–141]. The current may be obtained by considering the transition probability per unit time, which is given by Fermi's golden rule when considering the isolated sample and tip as unperturbed systems. Summing the

transition probability per unit time over all states, and multiplying this by the electron charge, *e*, results in an energy integral equation for the tunnelling current (*I*) in terms of the density of states of the sample and tip (ρ_S and ρ_T, respectively), and the Fermi-Dirac distributions of each (f_S and f_T):

$$I = \frac{4\pi e}{\hbar}\int_{-\infty}^{\infty}[f_T(E_F^T - eV + \epsilon) - f_S(E_F^S + \epsilon)] \times \rho_T(E_F^T - eV + \epsilon)\rho_S(E_F^S + \epsilon)|M|^2 d\epsilon$$

Eq. 2.1

where *e* is the electron charge, $\hbar$ is the reduced Planck constant, E_F is the Fermi level, *V* is the applied bias voltage, and *M* is the tunnelling matrix element. At lower temperatures, $k_BT << eV$, and the Fermi-Dirac distributions can be approximated by step functions. This leads to a simplified equation for the tunnelling current when $V > 0$:

$$I = \frac{4\pi e}{\hbar}\int_0^{eV} \rho_T(E_F^T - eV + \epsilon)\rho_S(E_F^S + \epsilon)|M|^2 d\epsilon$$

Eq. 2.2

For negative bias voltages ($V < 0$), the integration limits become $-e|V|$ and 0. As shown by the above equation, only electrons between E_F and $E_F - eV$ may participate in the tunnelling current. Electrons with lower energies than this cannot tunnel across the junction due to the Pauli exclusion principle. The tunnelling matrix, *M*, is unknown - this is because the precise sample and tip wave functions are also unknown, and potentially very complex. At low bias voltages, $|M|^2$ may be approximated by a one-dimensional tunnelling probability, $D(\epsilon)$, that only accounts for the last atom of the tip and the atom of the sample underneath it[142]. Further simplifications, such as the approximation of the trapezoidal potential barrier as a square barrier of an average height of that in both tip and sample, result in a simple equation for the tunnelling probability:

$$D(\epsilon, V, s) = e^{-2ks}$$

Eq. 2.3

where:

$$k = \sqrt{\frac{2m}{\hbar^2}(\phi_{eff} - \epsilon)}$$

Eq. 2.4

s is the tip- sample distance, *m* is the mass of an electron, and ϕ_{eff} is the effective work function, as approximated by the average height of both barriers. This simple equation for the tunnelling probability exhibits the inverse exponential relationship with the tip-sample separation. As a result of this, small changes in the tip-sample distance result in large changes in the tunnelling probability, and thus the tunnelling current. For typical work function values, an increase of 1 Å in separation can result in an order of magnitude decrease of the tunnelling probability. This demonstrates the exceptional sensitivity of the tunnelling current to small changes in tip-sample distance that allows the high vertical resolution of STM. The lateral resolution in STM is determined by the tip geometry. This is extremely changeable in STM experiments, but in ideal cases (such as a single atom at the end of the tip) may be as low as sub-Ångstrom.

Combining the above equations yields an overall one for the simplified tunnelling current:

$$I = \frac{4\pi e}{\hbar}\int_0^{eV} \rho_T(E_F^T - eV + \epsilon)\rho_S(E_F^S + \epsilon)e^{-2ks}d\epsilon$$

Eq. 2.5

To summarise, this shows that, for a certain tunnelling junction with a tip fixed in position above the sample, the tunnelling current depends on the voltage, *V*, applied in the junction, the density of states of the last atom of the tip and the atom of the sample underneath it (ρ_T and ρ_S, respectively, where ρ_S is referred to as the local density of states or LDOS due to this approximation), and the tip-sample distance, *s*. Crucially, this dependence on the LDOS of the sample allows the use of the STM for studying the electronic states of the sample.

2.1.3 STM Scanning Modes

To exploit this tunnelling current for the imaging of conductive surfaces, an atomically sharp tip is brought close enough to the surface that a tunnelling current may be detected. This is achieved via control electronics with a feedback loop. After the tip is manually moved close to the surface, a current set point is entered, and the tip is automatically approached until the required tunnelling current is detected. The tip is

then raster-scanned across the surface to form an image. Precise control of the tip is achieved via the use of piezos that distort upon the application of a voltage. This allows fine movement on the sub-Ångström scale.

There are two main scanning modes that are employed for this purpose in STM experiments: constant current and constant height modes. These are both presented in **Fig. 2.2**.

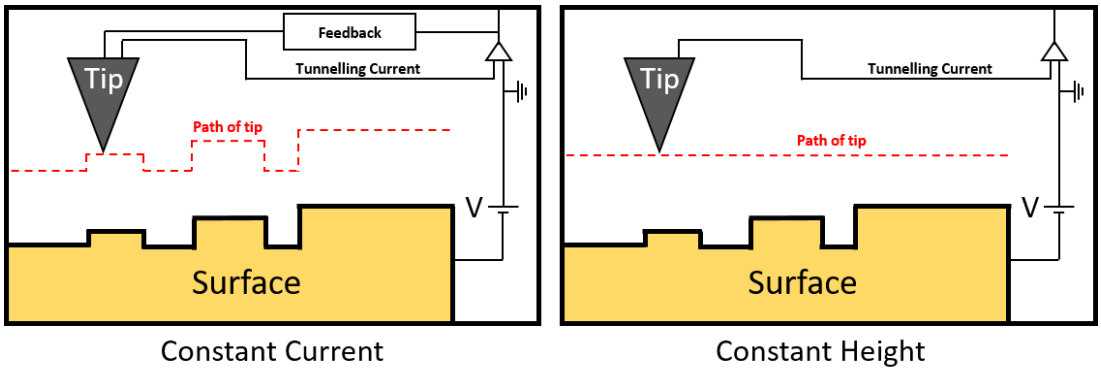

Figure 2.2. *Cross-sectional view of a single line of constant current and constant height imaging. The feedback mechanism is turned off in constant height mode, and ideally the tip does not move up and down during scanning.*

Constant current: As the tip is scanned across the surface, the feedback mechanism monitors the tunnelling current and adjusts the height of the tip relative to the surface in order to maintain the setpoint current. The output recorded whilst scanning is thus the vertical (z)-movement of the tip. This mode lets the user scan more three-dimensional features at a surface without the issue of tip-surface collision, as the height of the tip is constantly adjusted to avoid this. It also compensates for vertical thermal drift (due to temperature changes and thermal expansion/contraction of different materials in the scanner/sample) of the tip/sample that may lead to the tip drifting away from or into the surface.

Constant height: After approaching the tip to a certain height above the surface via the feedback mechanism/tunnelling current, the feedback is then turned off as the tip scans across the surface at a constant z-piezo position (or in a set plane). Changes in the tunnelling current as the tip raster scans across the surface are then recorded and output as an image. This mode is only suitable for very flat areas of the surface and low temperatures with low thermal drift, as it may otherwise lead to a tip/sample

collision. However, as no feedback is involved, the tip can be scanned much more quickly across the surface. It may also be a more reliable indicator of the relative intensity of features, e.g. for imaging the shape/intensity of a molecular electronic state in dI/dV imaging (see later).

It is important to point out that STM imaging, though often used as an indication of the topography, does not necessarily give a true representation of it. This is due to the dependence of the tunnelling current on the sample density of states, as shown in **eq. 2.5**. There are often situations, particularly with adsorbates on the surface, in which features that should be represented as a 'hill' feature in the topography are actually represented as a 'hole' relative to the surrounding surface, despite being adsorbed on top of it[143–145]. This is because it is possible to have a decrease in the sample density of states close to the Fermi level over some features, often as a result of charge transfer phenomena. To compensate for this, the tip moves closer to maintain the same current in constant current imaging, resulting in a decrease in apparent height. It should also be noted that the opposite can also be true – features may appear disproportionately brighter (with a larger apparent height than would be expected) due to a higher LDOS, localised on the feature, that is within the bias range of the scan. As such, the apparent height of objects (with the exception of comparing features with the same LDOS, such as step heights in metal surfaces) should not be trusted as an indicator of 'real' height.

2.1.4 High resolution STM (HR-STM)

In recent years, higher resolution forms of scanning probe microscopy (SPM) have become available[52,146–149] that make use of functionalised tips (such as CO, Xe, D_2, H_2, Br, and CuO)[146,148–151] to reveal the atomic structure of molecules adsorbed on surfaces with astounding clarity[147]. In particular, non-contact atomic force microscopy (NC-AFM) and high resolution STM (HR-STM) have been used to resolve the internal structures of molecules that are difficult to determine with other more traditional analytical methods such as NMR or mass spectrometry[152–154], as well as to identify the intermediates and products of reactions that have taken place on surfaces[155–157]. Both NC-AFM and HR-STM are now routinely employed for examining the internal structure of graphene nanostructures, as the number and type of molecular rings can be easily resolved[158–161]. There are also various examples of the use of these high resolution techniques for studying self-assembled molecular structures[51,162–165], but in

most cases the molecular arrangements within these structures are not ambiguous and can be clearly determined already with the standard forms of SPM.

The mechanism of the sub-molecular resolution in NC-AFM and HR-STM with functionalised tips has been the subject of multiple theoretical studies[166–170]. In the case of NC-AFM, sub-molecular contrast can be attributed to a combination of forces acting between the probe molecule and the sample: Pauli repulsion, van der Waals interactions, electrostatic forces, and the relaxation of the probe molecule[166,168]. The latter has in particular been identified as the origin for some anomalous intermolecular features that have been previously controversially attributed to hydrogen bonding[52], as well as amplified covalent bond lengths[171]. For HR-STM, it is thought that the observed contrast is a combination of the relaxation motions of the probe particle and of the variations in the local density of states (LDOS) of the molecule[167]. For HR-STM imaging, the probe molecule on the tip must be close enough to the underlying molecule to enter the repulsive regime. This leads to relaxation motions of the probe molecule that reflect the forces felt between it and the adsorbed molecule. As a result, the tunnelling current also changes. This can lead to sub-molecular resolution, as more repulsion is generally felt over the covalent bonds in the molecule (e.g. the rings of planar aromatic molecules).

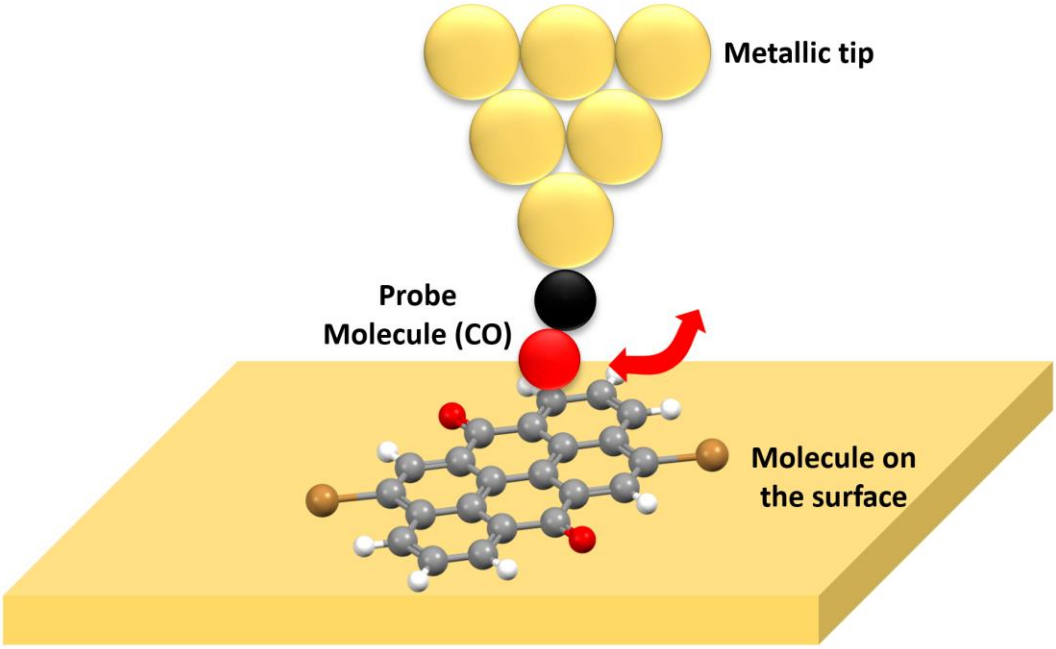

Figure 2.3. *Cartoon depicting a CO tip/molecule interface. The red arrow indicates the motion of the probe when it enters the repulsive regime in close proximity to the molecule.*

A simple cartoon illustrating the motions of the CO probe molecule when in the repulsive regime is shown in **Fig. 2.3**. A similar resolution can be achieved with both techniques, although the interpretation of HR-STM images may sometimes be complicated by the LDOS contribution, which is not an issue with NC-AFM. There are several approaches to performing HR-STM measurements; the quantity measured is usually either the tunnelling current (I), the dI/dV signal or the d^2I/dV^2 signal (inelastic tunnelling spectroscopy, IETS imaging) in constant height mode. There are also notable exceptions in which constant current mode is used, measuring the out of phase dI/dV signal to give a different contrast over the molecular rings[159]. In all of these cases, the tip is typically very close to the surface, with a bias voltage near to zero.

There are many examples of HR-STM performed with a CO tip throughout this thesis. Generally, the desired molecular system is first deposited onto the surface and allowed to self-assemble. The sample is then cooled down with liquid helium to 7 K in the low temperature STM chamber. After this, CO is leaked into the system to a pressure of approximately 10^{-7} mbar for a short time (in the range of 15-45 seconds). Due to the temperature of the sample, which is around 10-15 K during this process, the CO molecules adsorb onto the substrate, even if it would not normally do so at higher temperatures. Following initial tip preparation via controlled bias voltage pulses and tip 'dipping' into the metallic surface, a CO molecule is then picked up by the tip. This may occur during scanning, when the tip passes over a CO molecule, or may be done more controllably by adjusting the height of the tip and the bias voltage applied when over a CO molecule. In some cases, there is an obvious change in imaging resolution or observed features when the CO is adsorbed onto the tip. For example, the picking up a CO from Cu(111) results in other adsorbed CO molecules changing from a purely dark appearance to a dark circle with a bright central feature[144]. However, most of the HR-STM experiments in this work have been performed on Au(111), and there is not always an obvious change in the appearance of most objects after CO pickup. Unlike Cu(111), CO is found to still be mobile at 7 K on Au(111), resulting in semi-regular hexagonal clusters of molecules with a large deviation in their appearance. This deviation may be due to mobility of CO molecules that are confined to a small region. **Fig. 2.4(b)** and **(c)** show the same area before and after pickup of CO on Au(111) via the STM tip, along with an overview STM image showing groups of CO molecules in

clusters that are adjacent to an island of Vat Orange 3 molecules (see **Chapter 7** of this thesis) in **Fig. 2.4(a)**.

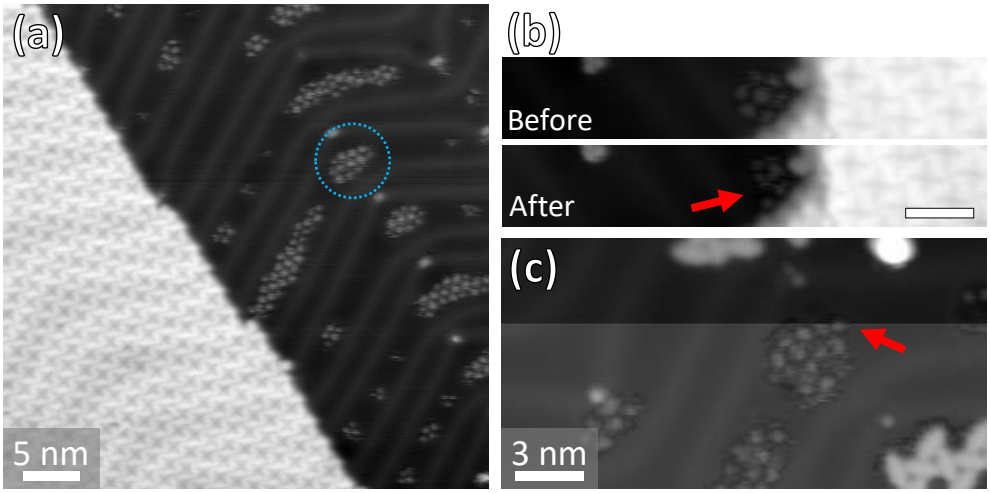

Figure 2.4. *(a) Overview STM image (1.8 V) of a molecular island of Vat Orange 3 (lower left) adjacent to an area of bare Au(111) with clusters of CO molecules arranged over it. One cluster is circled. (b) Before and after STM images (1.3 V) of a CO molecule pickup at the location indicated. More than one CO has disappeared in the 'after' image. (c) Example of picking up a CO molecule whilst scanning over it in constant current mode (1.1 V). The tip change observed at the position of the red arrow correlates well with the position of the CO island. The tip moves upwards in z to maintain the same current after CO pickup, hence why the lower half of the image appears brighter.*

Following this, the molecules of interest are scanned in constant height mode with the tip close to the surface and at low bias voltages (<50 mV applied). The bias is generally chosen so that it is not close in energy to any molecular resonances. This avoids the convolution of the sub-molecular structure and the spatial variation of the electronic state. This is not always possible, as seen later in this thesis. A lower voltage also helps to prevent damage to molecules that would be caused by a strong electric field when the tip is in close proximity (i.e. in the repulsive regime) for HR-STM measurements. All examples of HR-STM used in this work are constant height images in which only the tunnelling current is recorded.

2.1.5 Scanning Tunnelling Spectroscopy

The tunnelling current equation described in the previous section (**eq. 2.5**) clearly shows a relationship between the tunnelling current and the density of states of both the sample and the tip. This in turn implies that information about the density of states may be extracted from the tunnelling current. This is the main idea behind scanning

tunnelling spectroscopy. Furthermore, as the STM tip inherently probes the local density of states due to its size, this allows the user to examine the properties of individual atoms and molecules, as well as spatially map out the extent and structure of the states measured over these species.

Taking the derivative of **eq. 2.5** (but instead with the one-dimensional tunnelling probability left as *D*) and assuming that the tip density of states is constant and that a small bias voltage range is used results in the following expression:

$$\frac{dI(V)}{dV} \propto \rho_s(E_F^S + eV)D(eV, V, s)$$

Eq. 2.6

As *D* depends monotonously on *V*, the structure seen in the differential conductance when varying the voltage can thus be related to the sample density of states underneath the STM tip. The assumption that the density of states of the tip is constant is a good approximation for metallic tips, but often the tip structure is unknown, and there may be adsorbed molecules near or at the apex. To account for this, STS experiments often also involve recording a spectrum of a known species (e.g. the bare surface) to check for features in the dI/dV spectrum that relate to the tip and not the sample.

The typical procedure for recording a *dI/dV* point spectrum (as used throughout the work in this thesis) is the following: Firstly, the tip is moved to the position of interest (e.g. an adsorbed molecule) with the feedback loop closed. Once the tip has reached this point (with a height above the sample dictated by the set tunnelling conditions/feedback), the feedback is turned off, and the voltage is swept across a set range whilst the current (*I*) and *dI/dV* signals are recorded. This may be repeated multiple times, with an average formed in order to increase the signal:noise ratio. If at higher temperatures in which vertical (z) thermal drift is a significant factor, the tip may also be instructed to move towards/away from the surface to counter it. The total time taken for recording a spectrum may also be reduced to avoid this problem. The *dI/dV* signal, plotted against voltage, may then contain features such as peaks that may correspond to features in the local density of states of the sample underneath the tip. An example *dI/dV* spectrum of a bare Au(111) surface is shown below in **Fig. 2.5**. The *dI/dV* units are not shown – this is because the size of the signal depends significantly

on the stabilisation conditions used prior to the spectrum acquisition, and these conditions may vary between different spectra that are being compared.

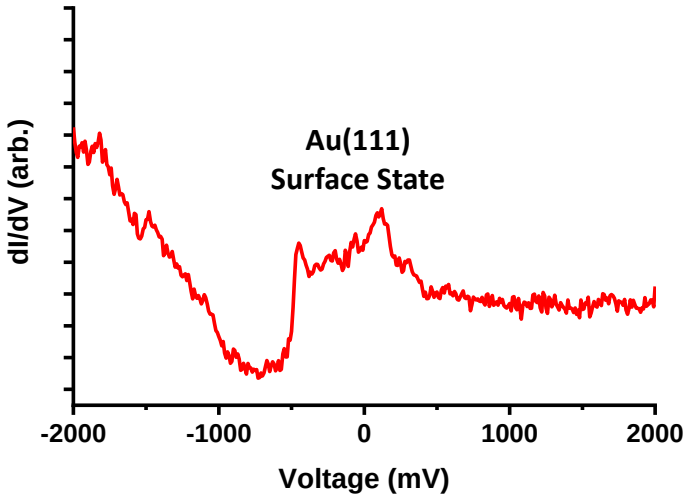

Figure 2.5. *Example of a Au(111) dI/dV spectrum, with the typical surface state feature that has an onset at around −500 mV.*

Whilst the *dI/dV* signal may be arrived at by numerically differentiating the current (*I*) signal, this typically results in a noisy spectrum. To avoid this, a lock-in amplifier is used to directly record a *dI/dV* signal. This is achieved by adding a small high frequency sinusoidal oscillation to the bias voltage. The resulting current signal is then amplified and multiplied by a sinusoidal reference signal and integrated over a time longer than the reference signal period. As the signal can be expanded into a power series due to the small amplitude of the sinusoidal oscillation, the *dI/dV* signal can thus be directly extracted by the lock-in amplifier. This enables the recording of the signal whilst scanning to create *dI/dV* maps, as well as spectra with a higher signal:noise ratio.

Typical oscillation frequencies used in the dI/dV spectra presented in this work range from 400 – 1100 Hz, with amplitudes of 5 – 50 mV. Stabilisation conditions prior to acquiring a spectrum varied, but the bias voltage was always within normal scanning conditions (±2.5 V) and the tunnelling current was usually in the range of 300 – 1000 pA. All dI/dV spectra shown in this thesis are acquired at a constant height.

After features of interest in *dI/dV* spectra have been identified, spatial maps of these features may also be acquired. This can help with identification of the source and

identity of the spectral feature; for example, certain states with distinct shapes may be recorded over adsorbed molecules and not elsewhere on the surface. These can in turn be related to theoretical calculations to assist with identification. In some cases, when molecules are decoupled from surfaces, states with a similar appearance to gas-phase calculations of frontier molecular orbitals may be observed in *dI/dV* maps[172,173].

dI/dV maps are created by recording an STM image whilst also measuring the *dI/dV* signal at a certain voltage (i.e. the voltage of the feature). This may be done in both constant current and constant height mode. Throughout this thesis, only constant height mode *dI/dV* maps are shown. This is because the vertical motion of the tip in constant current mode (which may be responding to tunnelling through other states that are not of interest) leads to a less reliable indicator of the relative intensity of features in *dI/dV* maps.

Recording *dI/dV* maps of molecules at surfaces with a CO tip leads to a significantly different contrast to similar maps recorded with metallic tips. The p-wave nature of the CO tip results in an increased signal at the *nodes* of the molecular orbitals of the adsorbed molecule[174]. This can be understood with a simple model in which the overlap of the p-orbitals of the CO molecule and the underlying molecular orbitals is considered. The most overlap occurs at the positions in which the phase of the orbital changes, i.e. the position at which the lateral gradient of the orbital is the greatest. This is in agreement with Chen's derivative rule[175]. The effects of the CO p-wave tip are demonstrated in more detail in the results shown in **Chapter 6**.

2.1.6 LT-STM Experimental Setup

The main instrument used throughout this thesis is a low temperature, ultra-high vacuum scanning tunnelling microscope, manufactured by CreaTec Fischer & Co. GmbH. Various custom parts have also been added to the system, in particular for the deposition of molecular species onto surfaces. Photographs of the system are shown in **Fig. 2.6**, with the main sections of the machine labelled.

Although STM may be performed under ambient conditions, the use of ultra-high vacuum allows the study of more reactive substrates (such as copper) and adsorbed molecular species in isolation. At higher pressures, oxidation of metallic surfaces may occur, and a film of water and other species from the atmosphere may also interfere with fundamental measurements. All of the work presented in this thesis has been

performed under ultra-high vacuum, at 10^{-9} mbar or lower. After any equipment has been exposed to atmosphere, it is usually baked at higher temperatures (393 – 423 K) to remove adsorbed species that may otherwise slowly outgas when placed under vacuum. As a result, lower pressures may be reached immediately after baking.

There are three main chambers that make up the bulk of the system: the STM analysis chamber, the sample preparation chamber, and the load-lock chamber.

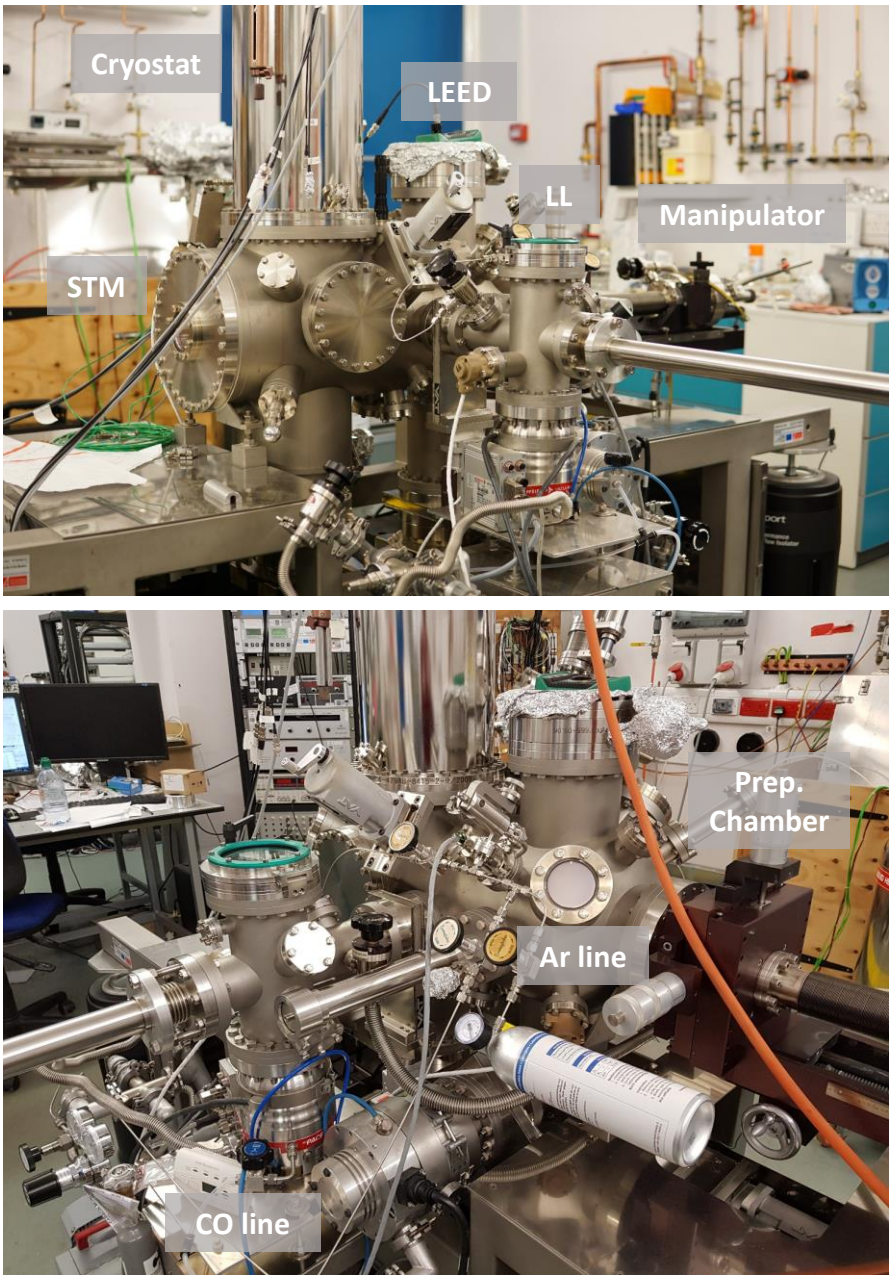

Figure 2.6. *Photographs of the LT-STM system with the main chambers/features labelled.*

The STM chamber contains the STM scanning head, encased in two layers of radiation shielding that help to maintain constant low sample temperatures, particularly when using liquid helium. On top of the chamber sits the cryostat, directly attached to the STM head. The cryostat contains two layers, which are both filled with cryogenic liquid when operating at low temperatures. For 77 K operation, the inner and outer cryostats are both filled with liquid nitrogen. For 7 K operation, the inner is filled with liquid helium and the outer is filled with liquid nitrogen. The inner cryostat may last up to four days before requiring re-filling with liquid helium, and seven days with liquid nitrogen. A rubber hose is attached to the outlet of the inner cryostat and connected to a helium reclamation line for the collection and re-use of helium boil-off. The outer cryostat is filled every two to three days. The STM chamber is pumped via an ion pump and held at a typical pressure of 5×10^{-11} mbar, as monitored by an ion gauge. This allows the study of even reactive samples for a week or more without significant levels of contamination/oxidation from gaseous species.

The preparation chamber is directly connected to the STM chamber via a gate valve. A manipulator arm allows the transfer of samples between the preparation and STM chambers through the valve. Samples are prepared whilst attached to the end of the manipulator. Two deposition sources are attached to the preparation chamber: the organic molecular beam epitaxy (OMBE) system for molecular deposition (see later, **Fig. 2.8**), and an e-beam metal deposition source. A low energy electron diffraction (LEED) system is also fitted on top of the chamber, but no results from this system are presented in this work as it is mostly unsuitable for delicate molecular films. Within the preparation chamber there is also a 'garage' arm for sample and tip storage. An ion gun is placed on the side of the preparation chamber, with an attached argon gas line; this is used for the preparation of samples. Adjacent to this is another gate valve that leads to the load lock chamber. The preparation chamber is pumped via an ion pump for the majority of the time and kept at pressures in the range of $1\text{-}5 \times 10^{-10}$ mbar; during sputtering, the ion pump is closed off via a gate valve and the chamber is instead pumped by a turbomolecular pump, which can also be shut off from the chamber via a pneumatic gate valve.

The load-lock (LL) chamber is pumped by another turbomolecular pump and can reach pressures as low as 5×10^{-10} mbar after baking. A hatch on top of the chamber allows the transfer of new samples into the system – the LL chamber is first vented,

then the hatch is opened and the new sample is placed on to the transfer arm. After pumping down again to high vacuum (10^{-8} mbar), the sample may then be transferred through the gate valve to the preparation chamber via the transfer arm and removed with the manipulator.

Samples are attached to a CreaTec sample holder, shown in **Fig. 2.7**. Single metal crystals, purchased from MaTecK (Au(111) and Cu(111) are used in this thesis), are clamped on top of a button heater via a molybdenum clamp and tantalum wire. A thermocouple is mounted onto the side of the crystal, and wires for sample connections and heating are connected to the button heater via spot welding. At the rear of the sample holder, metal pads allow the connections to the manipulator and the STM head to be made, with separate pads for heating and thermocouple readings. The sample is picked up by the manipulator via a T-bar clamping mechanism. Before being transferred to the STM chamber, samples are usually cooled to around 150 K by flowing liquid nitrogen through the manipulator. This avoids excessive wait times whilst the sample cools down after transfer.

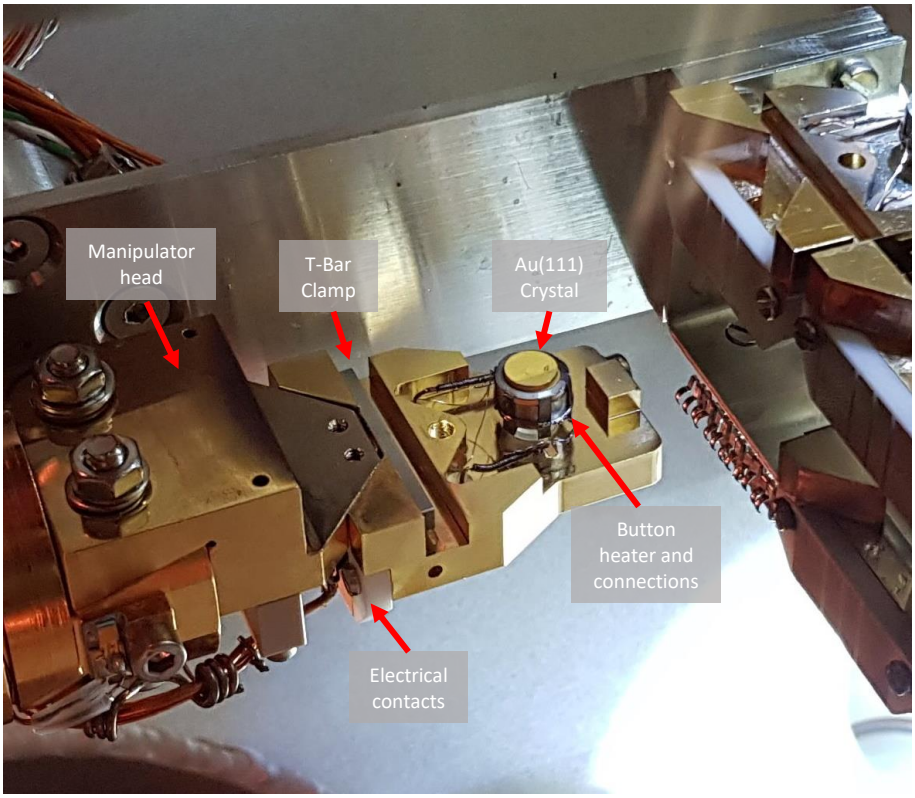

Figure 2.7. *Photograph of the Au(111) sample clamped onto the manipulator head, adjacent to the sample storage garage (right hand side of picture)*

Metal samples are cleaned via cycles of Ar^+ sputtering and annealing. During sputtering, argon (99.999% purity, purchased from Air Liquide) is leaked into the preparation chamber to a pressure of 1×10^{-5} mbar. The ion gun then ionises the argon and accelerates the resulting ions towards the sample at typical energies of around 1 keV. The ions bombard the crystal, removing material from the surface; samples are typically sputtered for 20-30 minutes. During this process, the chamber is pumped by the turbomolecular pumps to prevent argon contamination of the ion pumps.

Following the sputtering, the samples are annealed up to around 800 K for 5-10 minutes. This allows the atomically flat surface to reform and desorbs other species, including embedded argon from the sputtering. Depending on the sample, multiple sputtering and annealing cycles may be used.

Following the cleaning of the crystals, molecules are deposited via organic molecular beam epitaxy (OMBE). A photograph of the OMBE apparatus is shown in **Fig. 2.8**. Compounds in powder/crystal form are placed into crucibles. Four of these crucibles can then be placed into four heaters held at the end of the OMBE. The temperature of the crucibles is then increased via resistive heating of filaments inside the heaters – a thermocouple attached to each allows the regulation of the temperature, and the heating is regulated by a control box with a feedback loop. The molecules sublime in vacuum with sufficient heating and are directed into a beam by two holes above the crucible, one of which can be moved as part of a shutter that controls deposition time. The metal samples are held in front of the beam for the duration of this deposition time. Unless stated otherwise, the samples were held at room temperature (293-303 K) during depositions. In order to avoid cross-talk (i.e. undesired heating of other adjacent compounds), the OMBE can also be cooled with water or air.

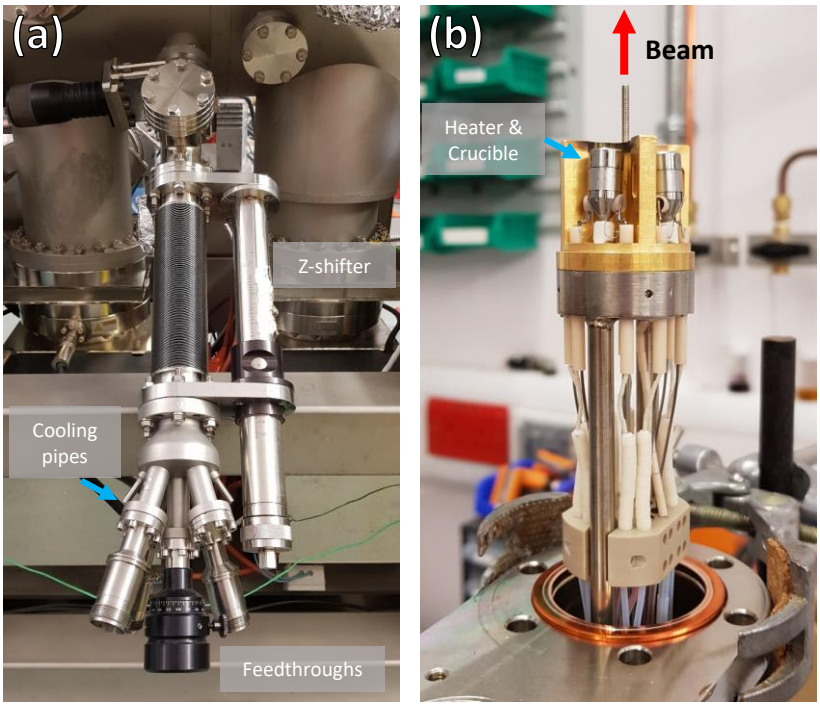

Figure 2.8. *(a) Exterior view of the OMBE attached to the side of the chamber. (b) The head of the OMBE with the cap and shutter removed, showing the heaters for the crucibles and the direction of the beam.*

A list of the molecules used throughout this work and their sublimation temperatures is presented in **Table 2.1**. The deposition times for these compounds at the stated temperatures are in the order of minutes for achieving a full monolayer.

Molecule	Sublimation Temperature /K
Binol	413
PXX	438
Br2PXX	483
Vat Orange 3	543
TCNQ	403

Table 2.1. *A list of the compounds used in this thesis, along with the sublimation temperature used during depositions.*

Samples may also be post-annealed after the deposition of molecules. Post-annealing temperatures are detailed in the results sections for each molecule. Typically, samples were post-annealed to the desired temperature for 5 minutes.

A metal evaporation source, mounted on the side of the preparation chamber, is used for the deposition of iron onto samples. Inside the source, an iron rod is surrounded at one end by a filament. A current is flowed through this filament and a voltage (700-1000 V) is applied between it and the iron rod, resulting in electron bombardment that in turn releases iron (neutral and charged) from the end of the rod. A shutter at the end of the source allows more precise deposition times.

Attached to the Ar line (used for sputtering) is a second gas line, used for CO deposition. A lecture bottle filled with 99.995% purity CO (CK Special Gases Ltd) is connected to the line via a regulator, and several valves along the line control the volumes that are filled with each gas. Prior to deposition, the line is purged with CO several times via a connection to the LL, then filled to a pressure of 1.5 bar. During the deposition, it is leaked into the preparation chamber (pumped by the turbomolecular pumps, ion pumps shut off) via the leak valve to 10^{-7} mbar. The ion pump in the STM chamber is then shut off, and the valve between the two chambers is opened. When samples are at liquid helium temperatures, the exposure time at this pressure is in the order of 15-45 s. The CO molecules also readily adsorb onto other cold surfaces in the chamber. As a result, when it is warmed to liquid nitrogen temperatures or higher, a significant amount of CO desorption occurs. Lower pressures/times are required for CO deposition at 77 K.

A photograph of the STM Beesocke-Beetle type scanner head is shown in **Fig. 2.9(a)**. The head may sit in two positions: pulled down, for sample transfer and cooling; and pulled up, for scanning. The head is moved between the two positions via a pulling mechanism that leads to a handle on the exterior of the cryostat. A stainless-steel tape is connected to the handle through a series of rollers and springs and attaches to the underside of the STM head. When in the scanning position, the sample is raised inside the head and pushed up against it for mechanical stability and a good thermal contact. The whole head hangs on three springs to reduce the effects of mechanical vibration, and a ring of magnets underneath the head allows for eddy current damping of any motion.

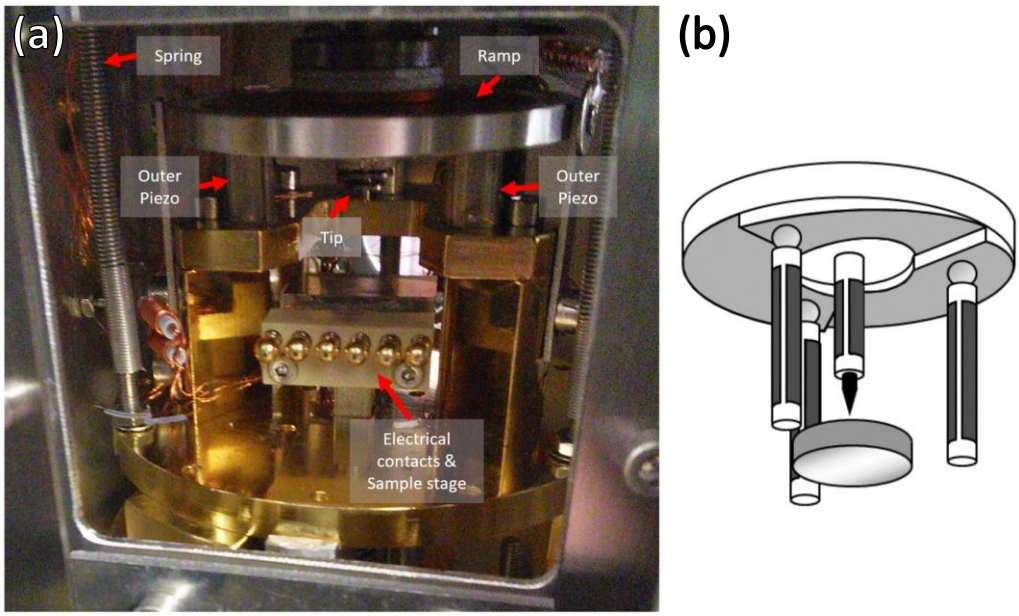

Figure 2.9. *(a) Photograph through the shutter in the inner radiation shield, showing the STM head without a sample inside. (b) Schematic of the Beesocke-Beetle type scanner piezo arrangement, adapted from the thesis of A. Della Pia*[38].

The scanner itself consists of four piezos. Three of these are mounted in a triangle around the sample, with a sapphire ball attached to the top of each. A disc with three ramps underneath (**Fig. 2.9(b)**) sits freely on top of the three outer piezos. At the centre of the underside of the disc sits the fourth piezo, with the STM tip magnetically attached to the bottom. Coarse movement of the tip in all directions is achieved with the three outer piezos. Large vertical movements are performed via the rotational slip-stick movement of the ramp up and down on top of the three piezos. When approaching the tip to the sample, it is first moved close via a series of coarse movements of the outer piezos. After this, an automatic approach may be performed, with the controls and feedback of the STM active. The automatic approach and scanning can be done with both sets of the piezos; the three outer piezos can control x, y and z when scanning, as can the central piezo. Normally a combination of both is used, with the outer piezos controlling lateral (x, y) movement and the central piezo controlling the vertical (z) movement of the tip. This allows the decoupling of the lateral and vertical motions.

STM and STS experiments are controlled by a computer that is interfaced with a CreaTec manufactured digital-to-analogue converter (DAC) and analogue-to-digital (ADC) converter control unit. The tunnelling parameters are set and monitored in the

computer software, as is the proportional-integral feedback control. The calibration of the piezos is also controlled via the software and is typically adjusted by comparing atomic resolution imaging with values from the literature. As a result of the relationship between temperature and the voltage required to distort the piezos, different calibration values are used for 77 K and 7 K measurements. These values were checked with Cu(111) atomic resolution every time the temperature was changed.

The STM tips used during this work were all made of tungsten, and electrochemically etched to form a sharp point. In some cases, after extensive use or time spent in the preparation chamber, the tips were re-prepared via Ar^+ sputtering, in a similar fashion to the sample preparation. Tip-forming was also undertaken during STM experiments; to create a cleaner or sharper tip, a voltage pulse can be applied, or the tip can be controllably crashed into the surface with a set z-movement. These procedures may remove material from the tip but can also result in the coating of the tip with substrate atoms. As such, after extensive tip forming, the apex of the tip is typically considered to consist of whatever metal is being scanned at the time.

Typical scanning conditions used during STM experiments for this thesis were bias voltages in the range ±2.5 V, with a tunnelling current in the range of 50-1000 pA. Acquisition times per image also varied between 40s and 300s. Quicker scanning was often utilised when in constant height mode to avoid vertical (z) drift – the lack of feedback mechanism also allows for faster scan rates. All image analysis was performed with the WSxM[176] and Gwyddion[177] software packages.

2.2 X-ray Photoelectron Spectroscopy

2.2.1 Introduction and Background

X-ray photoelectron spectroscopy (XPS) is a commonly used surface science technique that enables characterisation of the elemental composition of surfaces. XPS relies on the photoelectric effect[178,179]; absorption of photons of a sufficient energy may excite core-level electrons from atoms at a surface to an unbound state higher than the vacuum level. Different elements have characteristic sets of binding energies for their core-level electrons, resulting in a fingerprint when examining the resulting kinetic energies of electrons after they have been ejected from the solid. Slight variations in the kinetic energies (and thus the original binding energies) of core

electrons also provide an indication of their chemical environment, allowing the identification of different types of species on the surface[180,181].

A simple diagram of the process of photoelectron ejection is shown in **Fig. 2.10**. A photon of specific energy, *hv*, is absorbed by a core-level electron. The core-level electron is ejected from the sample, with enough energy to move beyond the vacuum level (VL). The remaining kinetic energy, E_k, is used as a measure of the original binding energy, E_b, when taking into account the work function of the surface, ϕ.

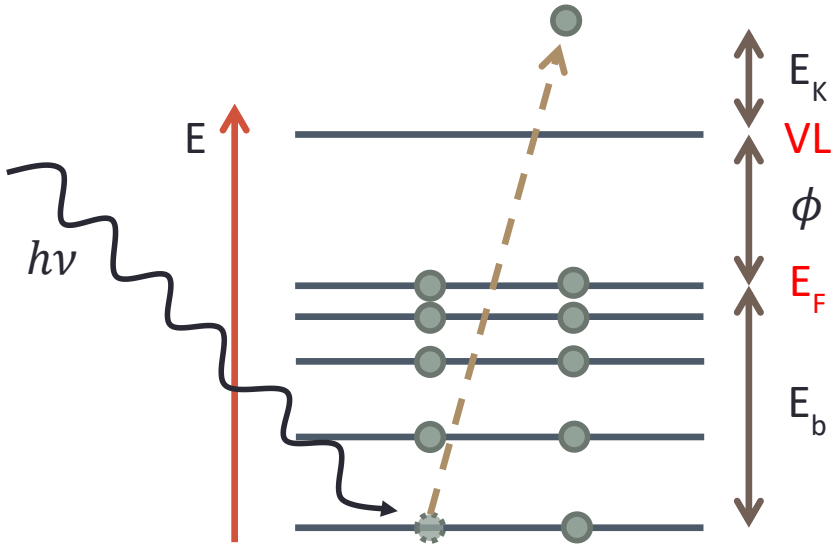

Figure 2.10. *Diagram of the photoelectric effect showing the ejection of electrons (green circles) from a core level to beyond the vacuum level, with a remaining kinetic energy that is measured by the analyser in XPS experiments.*

The kinetic energy of the photoelectron is given by the following simplified model equation:

$$E_k = h\nu - E_b - \phi$$

Eq. 2.7

Where E_k is the kinetic energy of the electron, $h\nu$ is the photon energy, E_b is the binding energy of the core electron, ϕ is the work function. Emission from core levels typically requires photons in the x-ray region of the electromagnetic spectrum, whereas valence electrons may be ejected with lower energy radiation in the ultraviolet (UV) spectrum. Valence electrons are examined using ultraviolet photoelectron spectroscopy (UPS) When using a monochromated x-ray source (i.e. photons of a single energy), the binding energy may be easily calculated using the above relation.

A more rigorous approach to the evaluation of the binding energy (E_b) of the core-electron relates to the consideration of final-state effects. The binding energy of the photoelectron is the difference between the (N-1) electron final state and the N-electron initial state of the atom that absorbs the photon. The energy gained from electronic relaxations (E_r) after the formation of a core hole must also be considered if these relaxations occur on a similar or faster time scale to the photoelectron emission:

$$E_b = E_f(N-1) - E_i(N) - E_r$$

Eq. 2.8

where E_f is the final state energy after photoemission and E_i is the initial state energy. Different chemical/bonding environments can be responsible for variation in the initial state energy. Bonds to more electronegative atoms result in a higher binding energy of the core electrons due to a decreased level of screening of the core states by valence electrons (also known as 'deshielding'). As well as the electronic relaxations, final state effects also include the occurrence of additional electronic excitations alongside the photoemission process, such as plasmon excitations in metals[181].

Peaks related to the Auger process are also detected in XP spectra. Upon the formation of a core-hole, an electron in a higher energy state may fall in energy to fill it. The energy lost by this electron can be transferred to another electron, resulting in a secondary photoemission. The kinetic energy of the second photoelectron does not depend on the photon energy used; varying it results in the movement of Auger peaks when plotting XP spectra on a binding energy scale.

An example survey XP spectrum of Cu(111) is presented in **Fig. 2.11**.

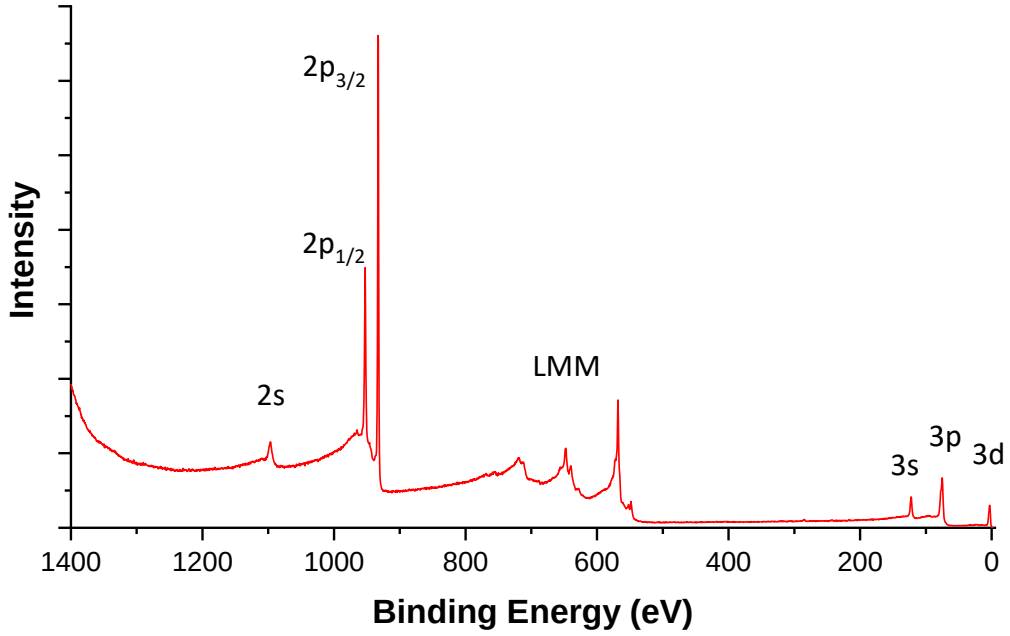

Figure 2.11. *Survey XP spectrum of a clean Cu(111) surface. The various Cu energy levels are indicated. A series of Auger emission peaks are labelled as LMM, relating to the source of the core hole, the electron filling it, and the second photoelectron. A clear split is observed for the 2p peaks due to spin-orbit splitting.*

The background of the spectrum, increasing towards higher binding energy, is related to the inelastic collisions of photoelectrons. Pronounced steps after each peak are observed; a loss in kinetic energy associated with an inelastic collision results in increased intensity at higher values on the binding energy scale.

The photoelectron kinetic energies are usually analysed with a hemispherical analyser. After being focused with electrostatic lenses and slowed down with a retarding field, the photoelectrons pass between two curved plates with a potential difference applied between them. Electrons with the correct pass energy pass through the analyser; if their kinetic energy is too high, they hit the outer plate of the analyser; if their kinetic energy is too low then they hit the inner plate. Electrons that pass through the hemisphere then pass through an exit slit and finally hit a channel electron multiplier.

2.2.2 XPS Setup

The instrument used in this project is an Omicron XPS/UPS. A photograph of the system is presented in **Fig. 2.12**. Similar sample preparation methods to the LT-STM are available, with a preparation chamber with sputtering/annealing capability and an

OMBE deposition source. Samples are mounted on Omicron sample plates, held in place via spot-welded tantalum wire.

The preparation chamber is pumped with a turbomolecular pump, with a typical pressure ranging between 2 x 10^{-11} mbar and 5 x 10^{-10} mbar. The analysis chamber is pumped by a turbomolecular pump and an ion pump, and consistently has a pressure in the low 10^{-11} mbar range.

Similar conditions to the LT-STM system are used for sputtering and annealing of metal samples, with cycles of 30 minutes of sputtering at 1 x 10^{-5} mbar and 1.5 keV followed by 10 minutes of annealing to 773 K. All samples are checked via XPS for cleanliness prior to molecular deposition. The same OMBE is used in both the LT-STM and XPS systems to ensure consistent deposition conditions. The distance between the OMBE and the sample is matched with that in the LT-STM; however, achieving the exact same position of the sample relative to the OMBE beam is difficult, as the length of the OMBE leads to angle dependent 'sag' that alters the resulting beam angle. This is because the available ports for attaching the OMBE are at different angles on the XPS and LT-STM. The XPS system has an analysis chamber with both XPS and UPS capabilities – only XPS was used in this project. The normal emission arrangement of the sample/analyser is shown in **Fig. 2.12(b)**.

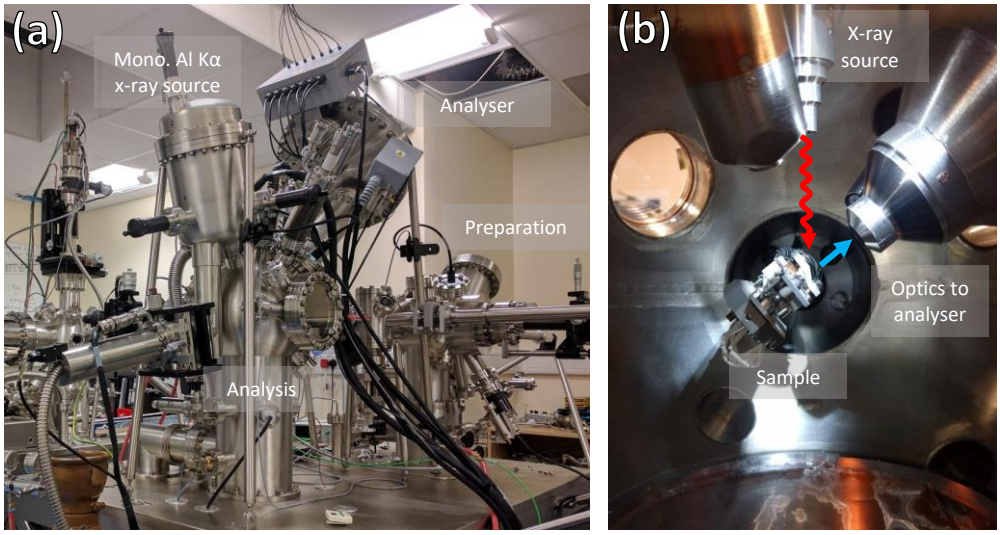

Figure 2.12. *(a) Photograph of the XPS/UPS system. (b) Photograph of the interior of the analysis chamber. The sample is held on a manipulator during the acquisition of the spectra, with the normal emission mode shown.*

The x-ray source is a monochromated Al Kα source with an energy of 1486.6 eV and the analyser work function is calibrated with silver foil with a known work function. In some cases at low molecular coverages, a large number of sweeps were averaged over due to the low signal:noise ratio. The signal was monitored to check for x-ray damage – no examples of this were found during the work carried out for this thesis.

The manipulator in the analysis chamber allows for annealing of the sample whilst in the measurement position. In the temperature-dependent work reported in this thesis, samples were post-annealed for 10 minutes and then allowed to cool down to close to room temperature before scanning. No cooling of the sample is available on the analysis chamber manipulator, so all XPS experiments are performed at room temperature. This is not expected to significantly affect comparisons with LT-STM data, as molecules in both cases are typically deposited onto the surface at room temperature.

3 Binol: Reactions at Metallic Surfaces

3.1 Introduction

Investigations into chemical reactions that occur in idealised conditions at metallic surfaces potentially lead to fundamental insights into how and why such reactions occur on larger scales with metallic catalysts. Studying molecules adsorbed on single crystal surfaces under vacuum simplifies systems to a level in which they can more precisely be characterised and understood. The use of scanning probe techniques such as STM helps lead to the characterisation and understanding of these processes at the single molecule scale, whilst complementary larger scale techniques, such as XPS, allow reliable chemical interpretation of the products of reactions at surfaces.

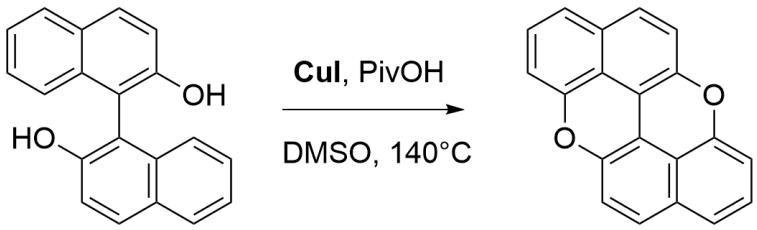

Figure 3.1. *The solution-phase reaction to form PXX from binol*[118].

One such reaction is the formation of peri-xanthenoxanthene (PXX, **Fig. 3.1**) from 1,1'-Bi-2-naphthol (binol, **Fig. 3.2**). Binol and its derivatives are commonly used in organic synthesis as a versatile chiral reagent[182]. One reaction to form PXX from binol (developed by our collaborators in the Bonifazi group, and shown in **Fig. 3.1**), takes place in solution in the presence of a Cu(I) catalyst[118], and leads to the fusing of the central hydroxyl groups with carbon atoms on each naphthalene ring to form a flat, conjugated molecule. A potential route for investigating this reaction further is to replicate it on a metallic surface in idealised conditions.

Unlike many other molecular systems commonly studied at interfaces, binol is three-dimensional in nature. This is due to the presence of only a single connecting bond between the naphthalene rings within the binol molecule, meaning that only partial

rotation of the aromatic sections with respect to each other may take place. Steric hindrance between neighbouring C-H groups prevents a full rotation around this single bond. As a result, binol is also a chiral compound, with (+) and (−) enantiomers, shown in **Fig. 3.2**.

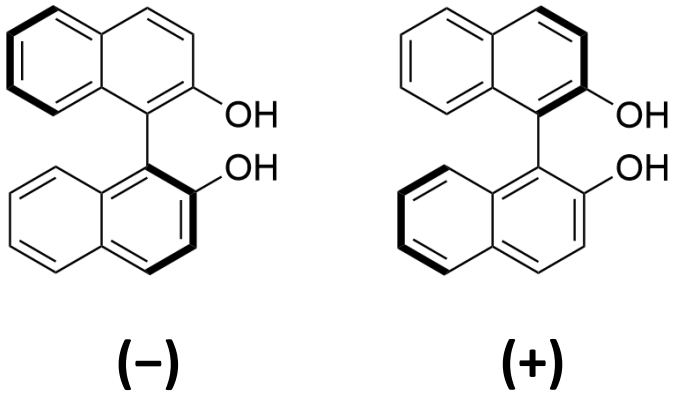

Figure 3.2. *The chemical structure of binol, with both enantiomers shown.*

In order to investigate whether the reaction shown in **Fig. 3.1** can also take place in an idealised environment, binol was deposited onto metallic single crystal surfaces in ultra-high vacuum (UHV), annealed to different temperatures, and studied via both STM and XPS. The (111) facets of both copper and gold were utilised as substrates in order to demonstrate the effects of the different reactivities (and adatom concentrations) of these metals on the resulting on-surface assemblies and reactions. In particular, Cu(111) is well-known for catalysing on-surface reactions more readily than Au(111)[122], as well as for its high adatom concentration at room temperature and above that provides a source of potential metal atom linkers for metal-organic structures[32,183,184].

Finally, the effect of co-depositing a small amount of a different reactive metal (iron) on the surface with binol was also studied – in particular, whether controlled amounts of reactive metals on more inert surfaces can significantly change the outcome of the on-surface reactions.

3.2 Results and Discussion

3.2.1 Binol on Cu(111)

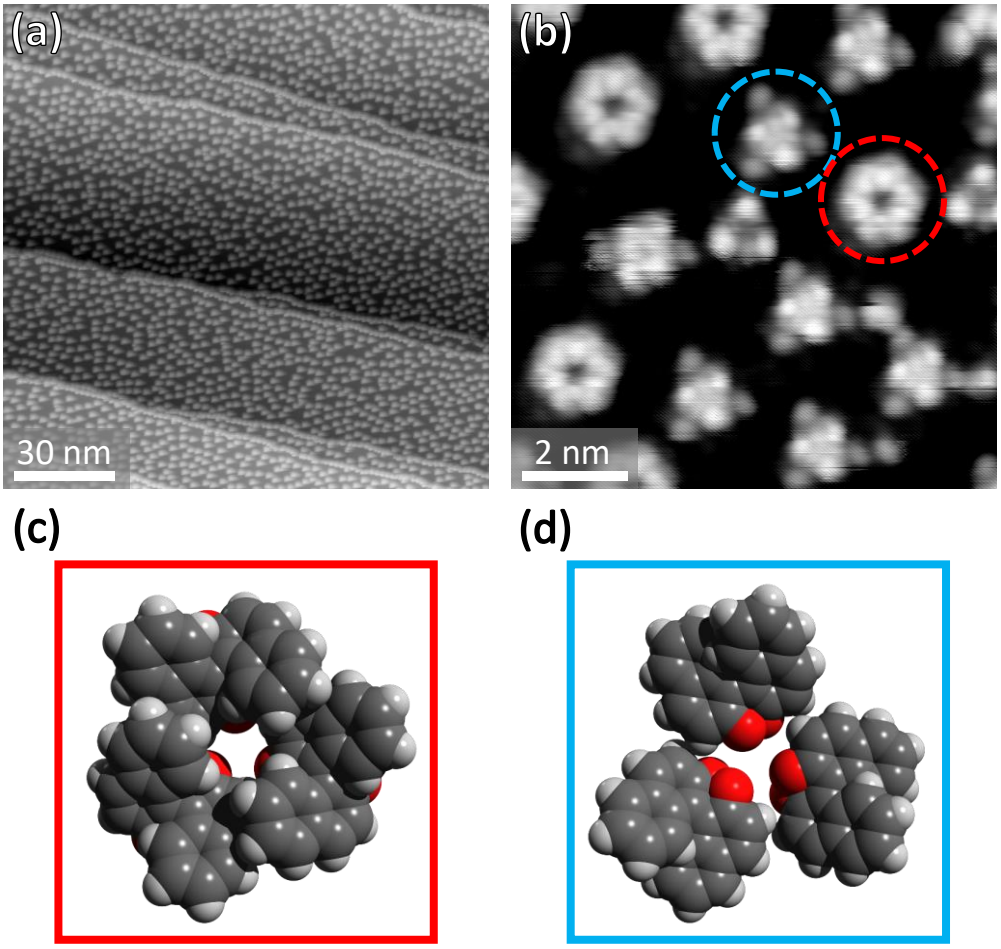

Figure 3.3. *(a) and (b) 77 K STM images (−1.2 V and 1.8 V) of binol(+) on Cu(111), with the two most common clusters highlighted with circles. (c) and (d) Potential models for the two most common clusters of binol(+).*

A sub-monolayer film of enantiomerically pure binol was deposited at room temperature onto Cu(111) via sublimation in UHV conditions. In separate experiments, both (+) and (−) enantiomers were used, in order to check for the expected differences between the two enantiomers when self-assembled on the surface (and in turn, the potential enantiomeric purity of the compounds). LT-STM measurements (77 K) reveal small clusters evenly spread out over the surface (**Fig. 3.3(a)**). Zooming into these clusters presents several regular structures, as shown in **Fig. 3.3(b)**. Fitting scaled molecular models to these clusters demonstrates that they are all approximately the size of three molecules – tentative models for the two most common clusters are also shown in **Fig. 3.3(c) and (d)**. The spread of these clusters

implies that there is a repulsive interaction that disfavours compact assemblies at low coverages. As the molecular structure of binol allows for limited rotation around the connecting single bond, different conformations on the surface are possible and thus may result in the various types of clusters observed. When 'flattening' the molecule as much as possible (i.e. bringing the two naphthalene rings to a position that is as close to planar as steric hindrance allows), two simple possibilities arise, with the oxygen groups oriented either on the same side of the molecule or towards opposite sides. There is, of course, a continuum of more three-dimensional conformations between these two extremes, as well as the potential for situations in which the molecule is upright (normal to the surface plane) rather than close to planar with the surface. More precise modelling, however, is not possible from just STM results and requires extensive theoretical input that is beyond the scope of this project.

XPS of the as-deposited binol system at a low coverage on Cu(111) is shown in **Fig. 3.4.** The position of the O 1s peak (531.0 eV) fits well with deprotonated OH group systems on Cu surfaces seen previously in the literature[102,185,186]. The C 1s spectrum also matches the expected number of carbon environments, with the ratio of 18:2 reflected in the areas of the fitted components. The O 1s peak position may help to explain the observation of clusters spread out over the surface – the deprotonation of C-OH groups leads to $C\text{-}O^{-}$ that may bind to either the substrate or Cu adatoms that are present at room temperature on the Cu(111) surface, potentially resulting in interfacial dipoles and thus dipole-dipole repulsive forces between adjacent clusters. In contrast, a similar molecule to binol in terms of functionality, bisphenol A, has previously been shown to not fully deprotonate at room temperature on Cu(111)[186], instead requiring annealing to over 400 K. This is potentially due to its adsorption conformation, with one ring upstanding away from the surface. This may suggest that for binol, both OH groups make contact with the surface. Typically, OH groups have been found to deprotonate on Cu surfaces readily at room temperature[187,188]. Similarities with bisphenol A may still be drawn due to the formation of small clusters held together by deprotonated $C\text{-}O^{-}$ groups, and computational modelling of that system also raises the possibility of intramolecular C-H --- O^{-} hydrogen bonding within binol clusters.

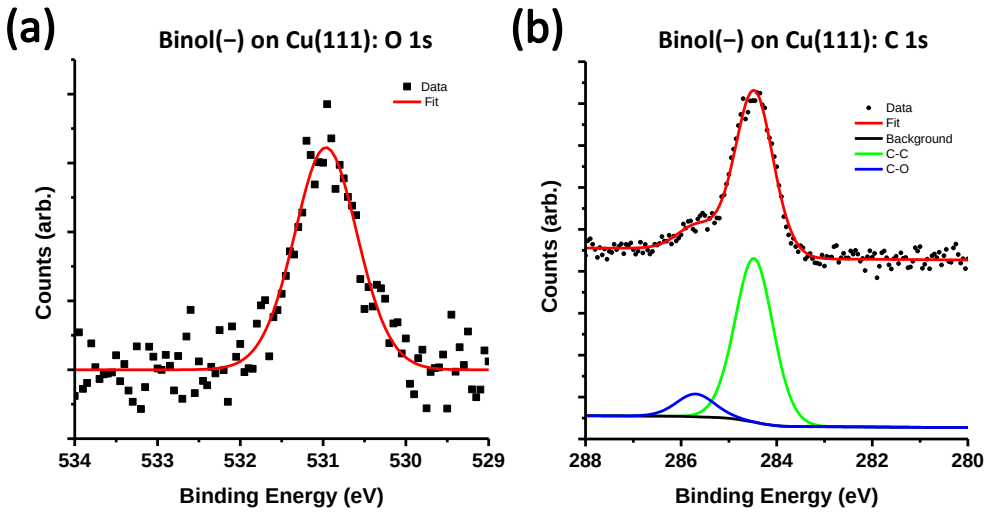

Figure 3.4. *XPS spectra of binol on Cu(111). (a) O 1s spectrum, with a subtracted linear background and a single peak fitted. A linear background is suitable in this case due to the short binding energy range and the location of the peak on the side of a large Cu substrate Auger peak. (b) C 1s spectrum, with two components fitted over a Shirley background, corresponding to the C-C and C-O environments.*

A comparison between the (+) and (−) deposition on Cu(111) is shown in **Fig. 3.5**, with the underlying Cu(111) orientations indicated. The same types of cluster shapes are observed for both depositions but with different orientations, mirrored with respect to the principal substrate directions. No indications of enantiomeric impurities in either deposition were observed. The apparent single orientation of the triangular and ring-shaped molecular clusters is due to their three-fold symmetry. Typically, several orientations (depending on the number of equivalent underlying surface directions, and the chirality of the molecule) would be expected. The chirality of the molecule/clusters, when combined with the three-fold symmetry of the Cu(111) surface, results in only three chiral cluster orientations (approximately 7° off the principle Cu(111) directions). As the cluster itself is rotationally three-fold symmetric, these orientations are indistinguishable from one another and thus simply observed as only one.

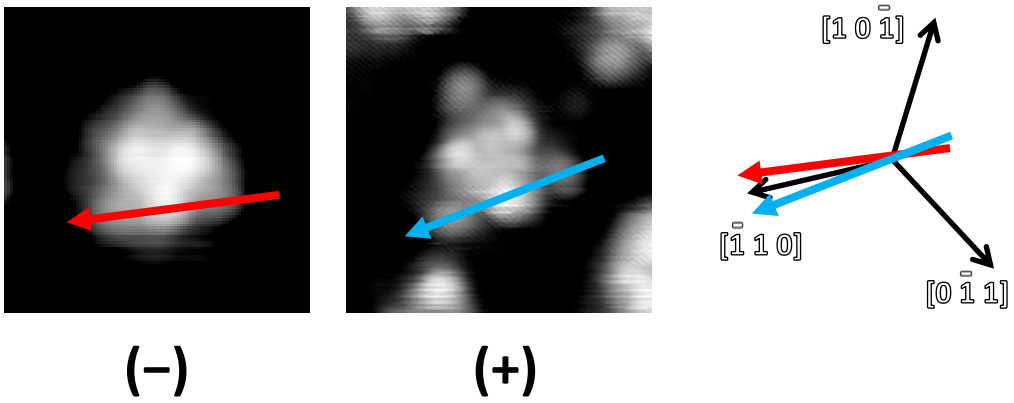

Figure 3.5. *A comparison between the chiral triangular shaped clusters formed by (−) and (+) forms of binol, with the reflection in the principle underlying Cu(111) crystallographic directions indicated. STM recorded at 77 K, with bias voltages of 1.5 V ((−) enantiomer) and 1.8 V ((+) enantiomer).*

The molecular coverage of the binol(+) sample was increased via further room temperature depositions on Cu(111). Low temperature (77 K) STM imaging of the resulting assemblies is presented in **Fig. 3.6**. Increasing the coverage initially only results in a decreasing average cluster-cluster distance, without the formation of any extended islands. Eventually, close to 1ML, the clusters are 'forced' to form hexagonally packed islands mostly consisting of just the triangular type clusters observed at lower coverage, with a unit cell with parameters **a** = **b** = 2.24 ± 0.07 nm, **θ** = 61 ± 2° (phase 1, **Fig. 3.6(d)**). Increasing the coverage further leads to the co-existence of these hexagonally packed islands with another hexagonal structure, characterised by a larger unit cell (**a** = **b** = 3.77 ± 0.07 nm, **θ** = 60 ± 2°) that contains both the triangular and the ring-shaped clusters (phase 2, **Fig. 3.6(e)**). Within the phase 2 islands, the triangular clusters are oriented in two different directions, as shown in **Fig. 3.6(e)**. One of these orientations is not the same as that which is observed in the phase 1 islands. Both chiral island assemblies also seemingly present with a single orientation for the same reason as the component clusters – their three-fold symmetry. Depositing any more molecules over this assembly results in what may be the beginning of a second molecular layer, with poorly resolved regions of mobile objects observed over areas of the underlying ordered layer (data not shown).

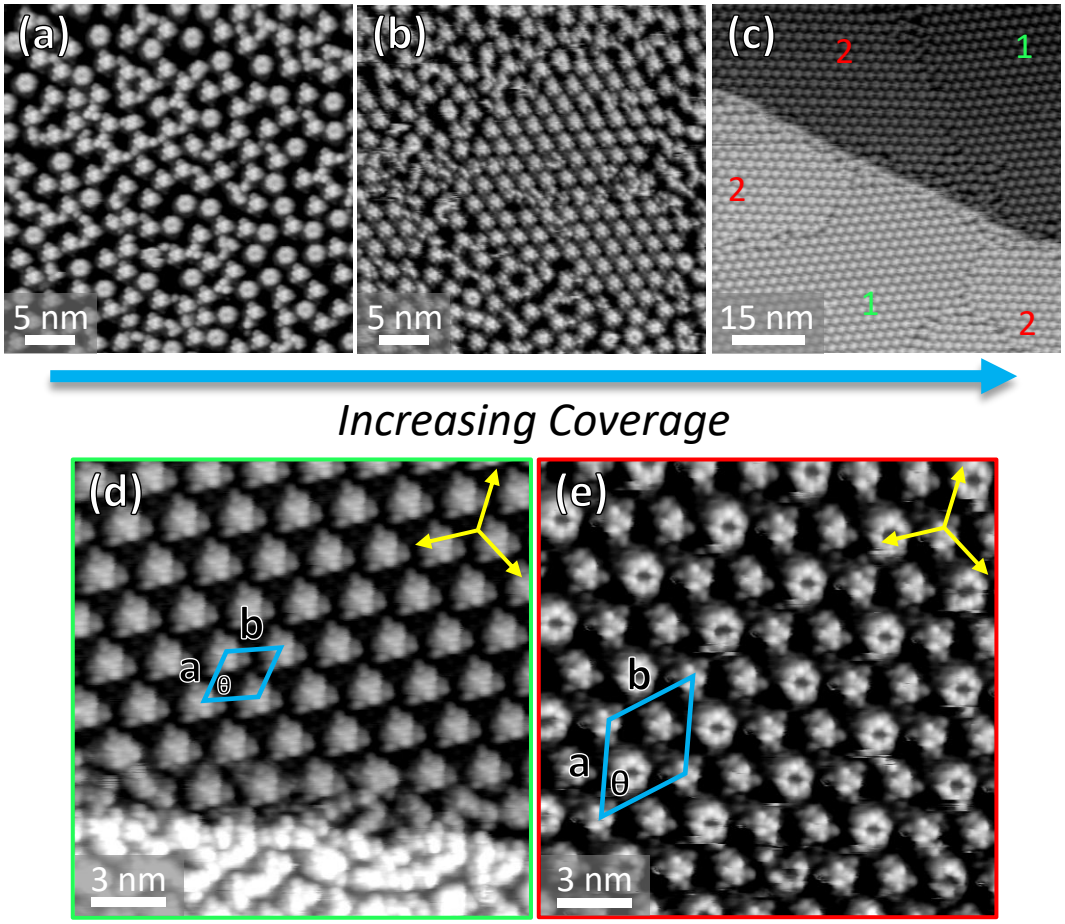

Figure 3.6. *(a) to (c) STM images of sequentially increasing coverages of room temperature binol (+) depositions on Cu(111), scanned at 77 K. Bias voltages: (a) −1.6 V (b) 1.8 V (c) 2.0 V. Domains of the two different phases at the highest coverage are explicitly indicated. (d) and (e) Zooms of hexagonal high coverage phases 1 and 2, with unit cells indicated. Bias voltages: (d) 1.2 V (e) 1.3 V.*

Annealing the highest coverage of binol(+) on Cu(111) in steps up to 423 K leads to a variety of assemblies. Simply allowing the sample presented above in **Fig. 3.6(c)** to warm up to room temperature for several hours is found to allow the adlayer to become mostly disordered (**Fig. 3.7(a)**), with a few small regions of both hexagonal phases seen previously, along with hints of a new row-type structure. Annealing further to 373 K and then 423 K in turn leads to two different row assemblies, respectively shown in **Figs. 3.7(b)** and **(c)**, with tentative molecular models. Each of these row assemblies have three different orientations with respect to the underlying substrate directions. The lower temperature assembly (**Fig. 3.7(b)** and **(e)**) has a unit cell with parameters **a** = 2.62 ± 0.08 nm, **b** = 1.57 ± 0.04 nm, and **θ** = 68 ± 3°. The higher temperature row structure (**Figs. 3.7(c)** and **(f)**) consists of both double and single rows, and there is no strict alternation between the two. As a result, there is no unit

cell to define. The periodicity along the length of both single and double rows is found to be 0.89 ± 0.05 nm. Tentative models of both of these assemblies are overlaid onto **Figs. 3.7(e)** and **7(f)**. Features in the gaps between the rows are found in both cases but they are not always consistently observed and thus are most probably not 'real' features; instead, they may be attributed to imaging artefacts that are related to the tip structure.

Assuming that no significant chemical change has taken place (see XPS data later in this chapter, **Fig. 3.9**), these results may imply that the row structure is perhaps the more thermodynamically stable. The XPS data for the higher coverage (**Fig. 3.9**) shows that desorption only starts to occur in significant amounts above 573 K, and thus a changing coverage can also be ruled out as a cause for the change in assembly.

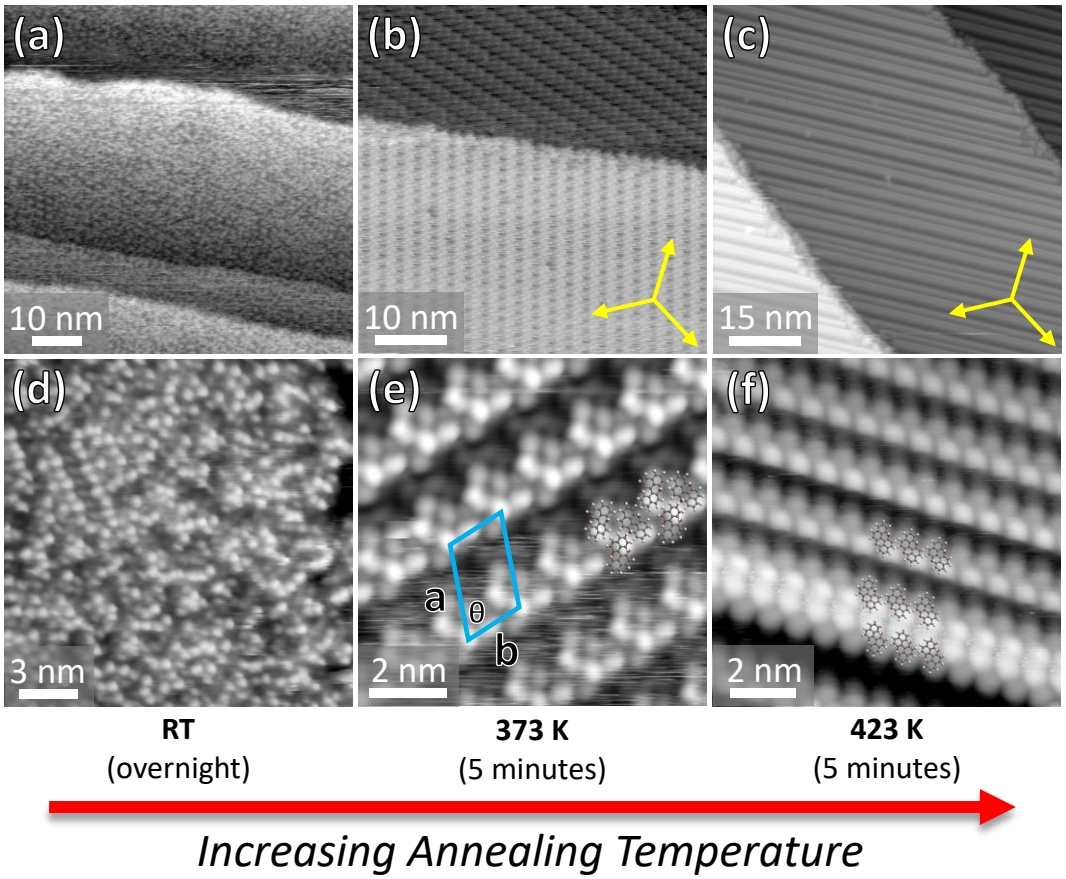

Figure 3.7. *77 K STM images of a series of annealing experiments performed on the highest coverage of binol (+), demonstrating the observed changes in structure. The lower panels are high resolution zoomed images of the structures shown in the upper panels. The unit cell for the row phase in (b) and (e) is also shown. No unit cell is shown for (c) and (f), as there is significant variation in the number of single and double rows adjacent to one another. Bias voltages: (a) 1.6 V (b) 1.8 V (c) 2.2 V (d) 1.6 V (e) 1.5 V (f) -2.0 V*

Annealing a lower coverage (sub-monolayer) of binol on Cu(111) does not show the same behaviour. Up to 423 K, the same trimer clusters (i.e. those seen in **Fig. 3.3**) are observed in low temperature (77 K) STM experiments. Annealing to higher temperatures than this, however, yields significantly different results. A series of STM images at different annealing temperatures is presented in **Fig. 3.8**. A set of XPS spectra showing the oxygen environment at different annealing temperatures is also shown in **Fig. 3.9.**

Another smaller peak in the XPS data of **Fig. 3.9** may be noted at lower annealing temperatures in the high coverage experiments at approximately 533 eV; this may be due to the formation of a multilayer. Molecules adsorbed in a second layer or above are subject to a different chemical environment, particularly for the oxygen atoms, as they may no longer be deprotonated by the metallic surface and are not bound strongly to it. This is further supported by the main peak from the underlayer being reduced in size in the as-deposited spectrum when compared to higher annealing temperatures, due to the attenuation of the photoelectron signal caused by the overlayer.

It is important to note that the STM and XPS measurements were performed on different experimental setups, and as such it cannot be guaranteed that the lower coverage of binol on Cu(111) was the same in both sets of data. As such, two sets of experiments were performed in the XPS system, with a high coverage (starting at over a monolayer, decreasing to around a monolayer with initial annealing, as noted by the loss of a multilayer peak) and a lower sub-monolayer coverage. Sub-monolayer annealing STM experiments (data not shown) were found to be fairly consistent in behaviour at a range of coverages, allowing a reasonable comparison to be formed with the lower coverage XPS data, Due to limitations in the amount of available binol(+), the (–) enantiomer was instead used in the XPS experiments – this has no impact on the measured spectra, as the chirality of the molecules only affects their orientation with respect to the surface crystallographic directions, as observed in STM experiments (**Fig. 3.5**).

The XPS and STM systems used in this study might also have slight differences in sample temperature calibration – a common problem when comparing temperature dependent results between different UHV setups. This effect is however not expected to be a significant issue in this case, as experiments with other temperature dependent

systems (e.g. the desorption of bromine after annealing Br_2PXX on Au(111), **Chapter 6** of this thesis) showed small differences (<30 K) between the measured temperatures in the STM and XPS systems.

Throughout both sets of O 1s XPS spectra (**Fig. 3.9**), two peaks are consistently observed. As previously stated, the lower binding energy peak at 531.0 eV can be assigned to the deprotonated oxygen species, bound to copper atoms. At 523 K and above, a second peak at 533.9 eV, tentatively assigned to the formation of a new C-O-C environment[102], increases in intensity with temperature, shifting slightly to 533.8 eV at 573 K and finally to 533.7 eV at 623 K. The C-O^- peak is also found to down-shift by 0.1 eV to 530.9 eV at temperatures above 473 K. Finally, there is a corresponding decrease in signal intensity at 623 K and above, most probably due to molecular desorption.

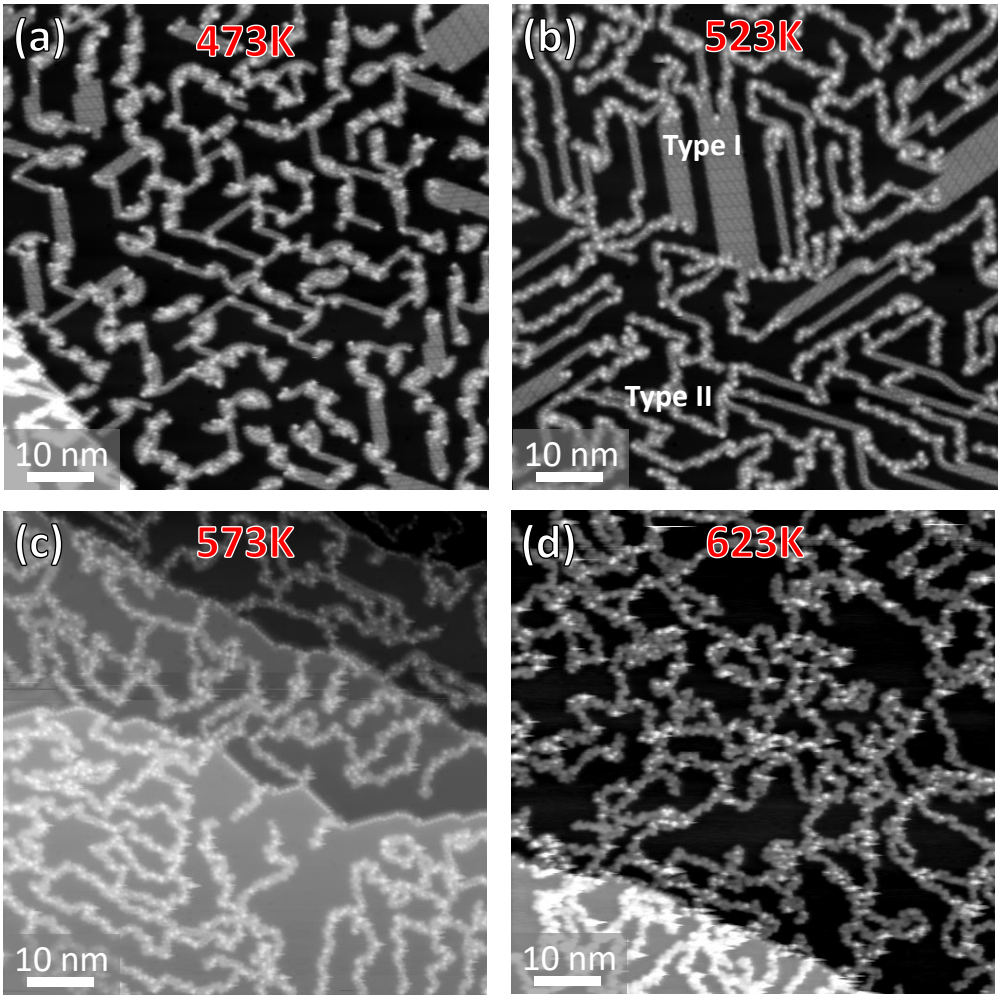

Figure 3.8. *77 K STM images of annealed binol (+) on Cu(111). Regular structures are no longer observed at and above 573 K, panels (c) and (d), most probably due to the occurrence of dehydrogenation and C-C coupling. Bias voltages: (a) 1.3 V (b) 1.1 V (c) 1.5 V (d) 1.5 V.*

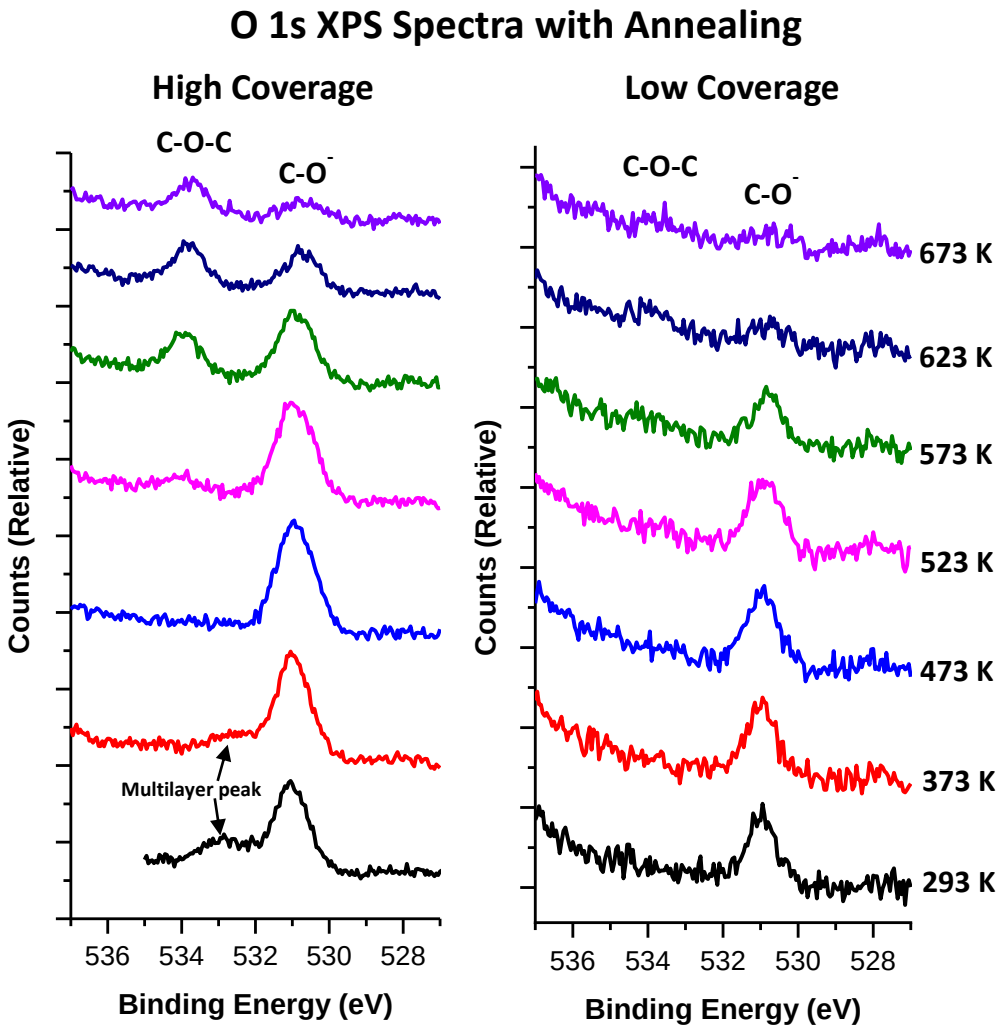

Figure 3.9. *O 1s XPS region for high and low coverage depositions of binol(–) on Cu(111) with increasing annealing temperature. Tentative assignments to the two major peaks are indicated. At lower annealing temperatures, what appears to be a multilayer peak is detected for the higher coverage experiments. This peak disappeared after the 473 K anneal, most probably due to desorption of the binol molecules that were not in direct contact with the surface.*

In the STM experiments, after reaching 473 K, straight chain-like structures (referred to in the following as type I chains) are observed. These chains are also present after annealing to 523 K, with the addition of new 'curly' chains (type II) that have a different internal structure (see later). Higher annealing temperatures result in increasingly distorted and irregular chains with no consistent internal structure, most probably due to extensive amounts of Cu(111)-catalysed dehydrogenation reactions and subsequent C-C coupling that bind molecules at various (less selective) sites. In the following, only chains of type I and type II, observed after annealing to 473 K and 523 K respectively, will be discussed in detail.

Type I Chains

After a 473 K anneal, the separated binol clusters transform into chain-like structures with both straight and curved sections. The straight parts of the chains often pack together into small islands (**Figs. 3.10 (a)** and **(b)**) characterised by a rectangular unit cell with parameters **a** = 1.15 ± 0.05 nm, **b** = 2.16 ± 0.04 nm, **θ** = 91 ± 2°. Chains are often found adjacent to clusters of binol molecules, identified by their brighter appearance (i.e. greater apparent height) in the STM images. This is perhaps indicative of a more three-dimensional conformation of the molecules within these clusters. Monoatomic step edges in the underlying Cu(111) crystal are significantly restructured after annealing, with the formation of long, straight steps decorated by regularly spaced molecules with an average molecule-molecule distance of 0.71 ± 0.03 nm. The straight, decorated sections of the reconstructed steps generally follow the three principal Cu(111) surface directions, as illustrated in **Figs. 3.10(c)** and **(d)**.

The internal structure of the type I chains can be clearly resolved, showing pairs of 'lobes' held side-to-side. The size of these lobe-pairs approximately fits the size of a semi-flattened (i.e. the rings are not exactly in the same plane due to steric hindrance, but within 45° of each other) model of a binol (+) molecule. Significant variation in the brightness (apparent height) of the lobes is observed, particularly in chains that curve. As the STM contrast is expected to relate, at least partially, to the conformation of the molecules within chains, this observation implies that the molecular conformation has to change significantly to allow the formation of curved chains. As previously stated, however, apparent heights measured in STM are often not reliable measures of molecular conformation at surfaces, as variations in the LDOS at and below the applied voltage can cause significant changes in tunnelling current. As such, although the above explanation is the most likely one, definitive conclusions cannot be made about the molecular adsorption conformation within the chains.

The type I chains are observed after both 473 K and 523 K experiments. After the 523 K anneal, however, they are found to be generally longer and straighter than those seen at the 473 K, as is evident when comparing **Figs. 3.8(a)** and **(b)**.

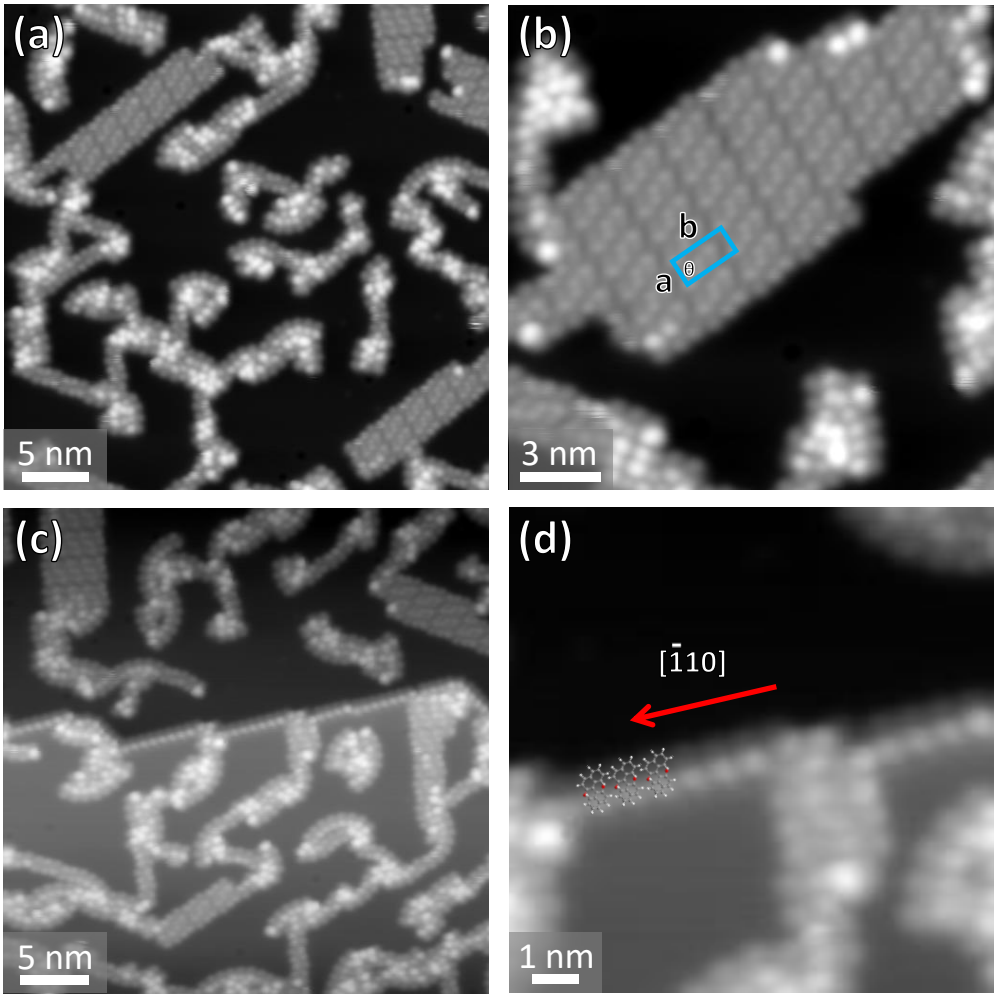

Figure 3.10. *(a) STM image of type-I chains formed by binol (+) on Cu(111) after annealing to 473 K. (b) Island of straight chains packed together. (c) and (d) Monoatomic step in the Cu(111) surface, reconstructed and decorated by binol (+) molecules. The reconstructed steps follow the three principal substrate crystallographic directions, one of which is indicated by the red arrow in (d). All images recorded at 1.3 V.*

A regular variation in the apparent height of the molecules is also recorded within straight chains, with a repeat unit containing six features that most probably corresponds to groups of three molecules in a row, with two features per molecule (**Fig. 3.11**). When comparing the repeat distance along the chain axis (2.16 ± 0.04 nm) and the angle with the Cu(111) crystallographic directions (23 ± 2° with the nearest), a regular fit with the underlying substrate is found (approximately 2.2 nm periodicity in the model system, **Fig. 3.11(c)**), suggesting that the chain structures might be commensurate with the Cu(111) surface although it is impossible to prove this with only STM measurements.

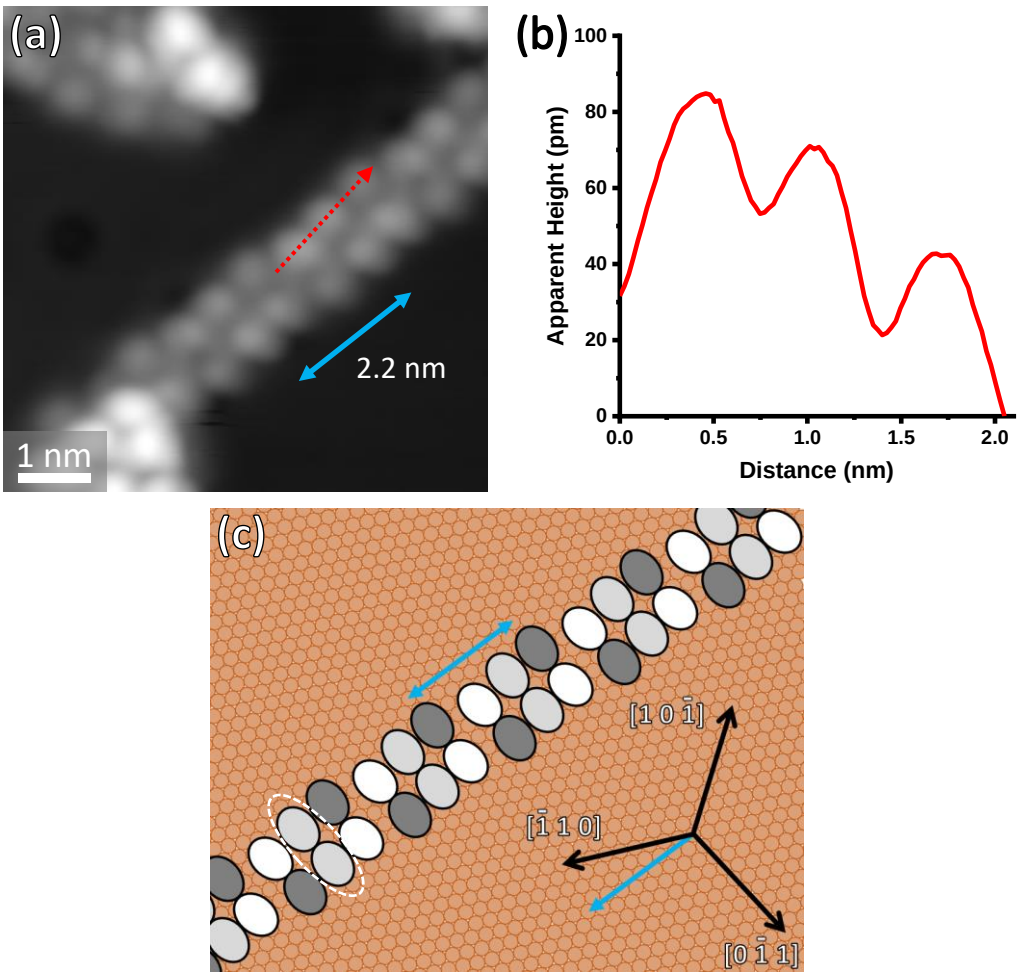

Figure 3.11. *(a) 77 K STM image (1.6 V) of a single straight chain, with a height profile taken along the red arrow, shown in (b). The direction and repeat unit distance of the chains is also shown with a blue arrow. (c) Overlay of a cartoon model of the straight chains onto the Cu(111) surface. Variations in apparent height are indicated with shades of grey. A white oval indicates the pair of features that most probably correspond to a single molecule.*

There are two general possibilities for the type of bonding within these chains: either the molecules are directly covalently bound to each other, or the molecules are instead linked by metal-organic interactions with shared Cu atoms. Covalent bonding (i.e. the formation of polymers) has several inherent constraints that would significantly restrict the possible structures of these chains. There is a limited range of allowed bonding angles, distances and bonding positions that can lead to the formation of covalently linked chains. Assuming that the pairs of lobes observed in the STM images relate to the two naphthalene rings of the binol, the molecules are limited to a certain orientation within the chains. It can thus be inferred that, if the chains are covalently bound, the oxygen atom must take part. This is because it is the only atom capable of

forming a new bond that allows the formation of covalent chains with molecules in this orientation. A potential model for a covalent polymer is shown in **Fig. 3.12(a)**. The formation of bonds to oxygen results in a high degree of buckling and twisting of the molecule when structurally optimised via molecular mechanics (MM2 force field) in the gas phase (**Fig. 3.12(b)**). Moreover, linking the binol molecules through their oxygen atoms would change their chemical environment from C-O$^-$ to C-O-C, which should be reflected in a significant shift in the position of the O 1s peak in XPS experiments, from 531.0 eV to above 533 eV. As a comparison, the C-O-C type O 1s peak of Br_2PXX, a brominated and ring-closed version of binol, is at 533.6 eV when deposited on Cu(111) (further results described in **Chapter 5**). However, this O 1s peak at higher binding energy is not visible in the XPS measurements acquired at the lower annealing temperature when the type I chains first form (around 473 K, **Figs. 3.8** and **3.9**). A peak at 533.9 eV, that can be identified with the C-O-C environment[102], starts to emerge only after annealing to 523 K, and develops significantly at 573 K.

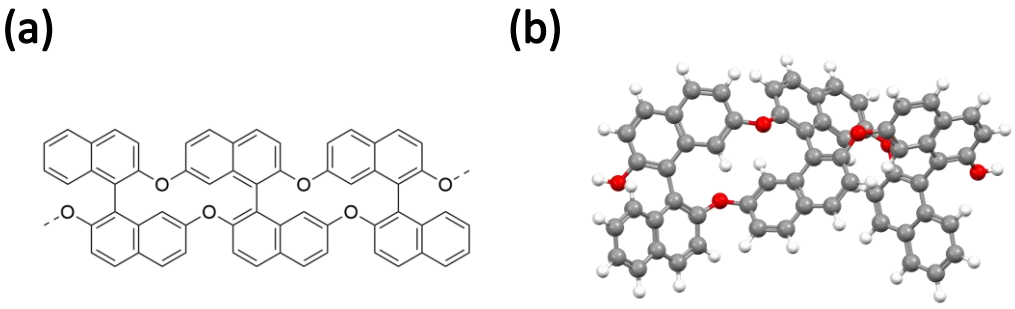

Figure 3.12. *(a) Potential structure of a covalent binol polymer. (b) 3D molecular-mechanics optimised structure of a trimer, demonstrating the high degree of buckling required by the formation of covalent bonds involving oxygen atoms.*

Metal-organic bonding (i.e. binol molecules connected by shared copper atoms, most probably via their deprotonated O$^-$ groups) is a more likely proposition for the bonding within the chains. Simply overlaying semi-flattened, scaled molecular models onto the STM images of the chains (**Fig. 3.13(a)**) demonstrates that the binol molecules would be have to be very crowded. However, if both the naphthalene rings were tilted away from the surface, there could be enough space for Cu atoms to be shared among neighbouring molecules and, potentially, for π-π stacking interactions between adjacent rings. Typically in the literature, when flat molecules are studied, metal-organic structures are easily differentiated from covalently bound chains by the

modelled bonding distance[35,189,190]. A longer bonding distance than allowed for by covalent bonding is usually seen to imply that the chains are metal-organic, even if there is no clear signal in the STM imaging for the metal atom in between the molecules. This simple analysis does not apply to this case due to the tilting of the binol rings.

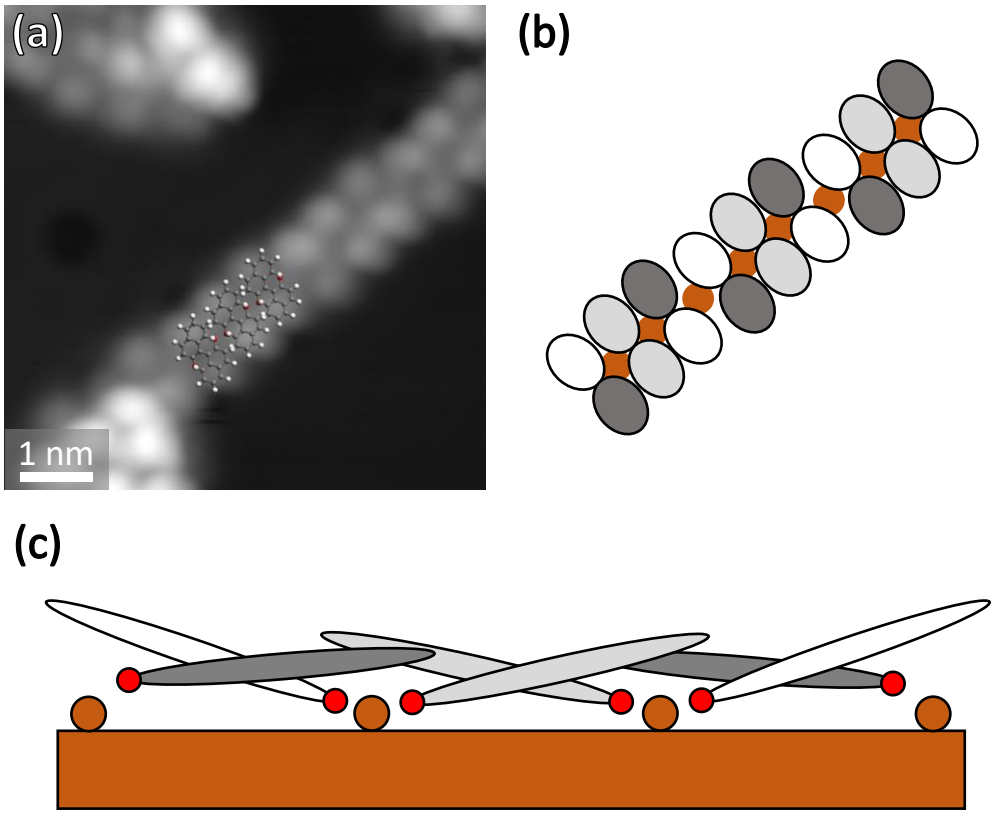

Figure 3.13. *(a) Overlay of deprotonated binol (+) molecules in a close-to planar geometry onto the chain, showing how closely packed they would have to be if forming a metal-organic structure. (b) Cartoon top view of a possible model of a metal-organic bound chain, with a greyscale indicating possible amounts of tilting of the naphthalene rings. The possible positions of Cu adatoms are indicated by brown circles. (c) Cartoon side view of the model indicated in (b), with red circles representing oxygen atoms that may bind to Cu. In this example, all bonds are with adatoms. The real system could also include bonds to pulled-up Cu atoms.*

A simplified model with tilted naphthalene rings is presented in **Figs. 3.13(b)** and **(c)**. Identification of the adatom sites cannot be achieved purely with STM experiments and requires the input of either theoretical methods or other techniques that are beyond the scope of this work. It is worth noting that the copper atoms in between the molecules do not necessarily have to be adatoms; they could instead be pulled up from the surface layer, as has been proposed in the literature for other metal-organic systems[18,62,126,131].

Metal-organic chains are also favoured by the XPS results shown in **Fig. 3.9**. The oxygen environment is characterised by only one peak at 473 K in a similar position to the as-deposited molecule, which corresponds to a deprotonated C-O$^-$ group binding to the copper surface. As previously mentioned, a small down-shift of this peak of 0.1 eV is observed at temperatures above 473 K, fitting well with the transition to the chain assembly, and possibly indicative of a slightly different chemical environment for the C-O$^-$ species – potentially binding to adatoms instead. The C-O$^-$ peak is also still the majority species at 573 K, with a reduction in size only after higher annealing temperatures. This corresponds well to STM results, in which type I chains are also found less frequently at 573 K and above.

Type II Chains

After annealing to 523 K, STM images show the coexistence of type I chains with another less regular chain structure (**Fig. 3.14(a)**), henceforth referred to as type II chains. The latter are composed of a mixture of double lobe structures with an appearance similar to that seen in the original type I chains, and 'flatter' looking objects in between (**Fig. 3.14(b)**). Adjacent to each flat object are two bright features that can be related to binol molecules with protruding naphthalene rings. The number of linking double lobe molecules between these flat objects varies (e.g. in **Fig. 3.14(b)** and **(c)**), and they often connect both types of chains. In reality, the chains are also often found to be mixed, with sections of both type I and type II packing. The size of the flat structures approximately fits with two fused binol molecules (i.e. the size of two PXX molecules) connected via a single bond, as shown in **Fig. 3.14(d)**. There are two reasonable options for the chemical structures of these flat objects, shown in **Fig. 3.14(e)** as structure **1** and **2**. Both of these dimers roughly fit the size of the flat objects, with **1** showing a slightly better match. Work by Kong et al.[102] found a similar C-C coupling reaction that took place when the brominated form of binol was deposited on Ag(111), in a step separate from the dehalogenation/intramolecular fusion (flattening) of the molecule. In their case, product **2** was found in abundance on the surface after the annealing of product **3**, which originally resulted from the fusion of a brominated binol molecule. Fusion to form a PXX molecule (in most cases still brominated) was only found on Au(111).[102] The precise nature of the dimer structures could possibly be revealed by high resolution STM measurements similar to those presented

throughout the rest of this thesis, but these measurements were not performed for binol on Cu(111).

Many examples of objects that roughly fit the size and symmetry of product **3** are found, usually at the edges of chains (e.g. in the upper right corner of **Figs. 3.14(c)** and **(d)**). The linkages (if any) between these objects and the adjoining chains, however, are unclear. For example, it cannot be excluded that these flat structures are simply incorporated into the self-assembled structures of binol(+) via attractive vdW forces and π-stacking, and do not share any strong (e.g. metal-organic, covalent) bonds with them.

At 523 K and above, a high binding energy peak starts to appear in the O 1s spectrum at values between 533.9 and 533.7 eV, as shown in **Fig 3.9**. As mentioned previously, when compared to XPS results for the brominated form of the binol molecule[102], this is consistent with the formation of a second bond between the oxygen group and a carbon atom, i.e. the formation of a C-O-C group. This fits well with the 'flat' appearance of the fused objects seen in the type II chains.

These observations, combined with the evidence from the literature, point towards the formation of objects such as **1**, **2** and **3** on the surface, albeit in a less controlled manner than the brominated form of the molecule on Ag(111). It is difficult to conclude whether it is object **1** or **2** that is present in the type II chains; the structure of **1** fits more closely with the shapes observed in the STM images, but **2** has been observed previously with a similar molecule (albeit on a different substrate) and also roughly fits with the shapes seen. The presence of **3** on the surface may also allow for the formation of **2** via surface-catalysed dehydrogenation.

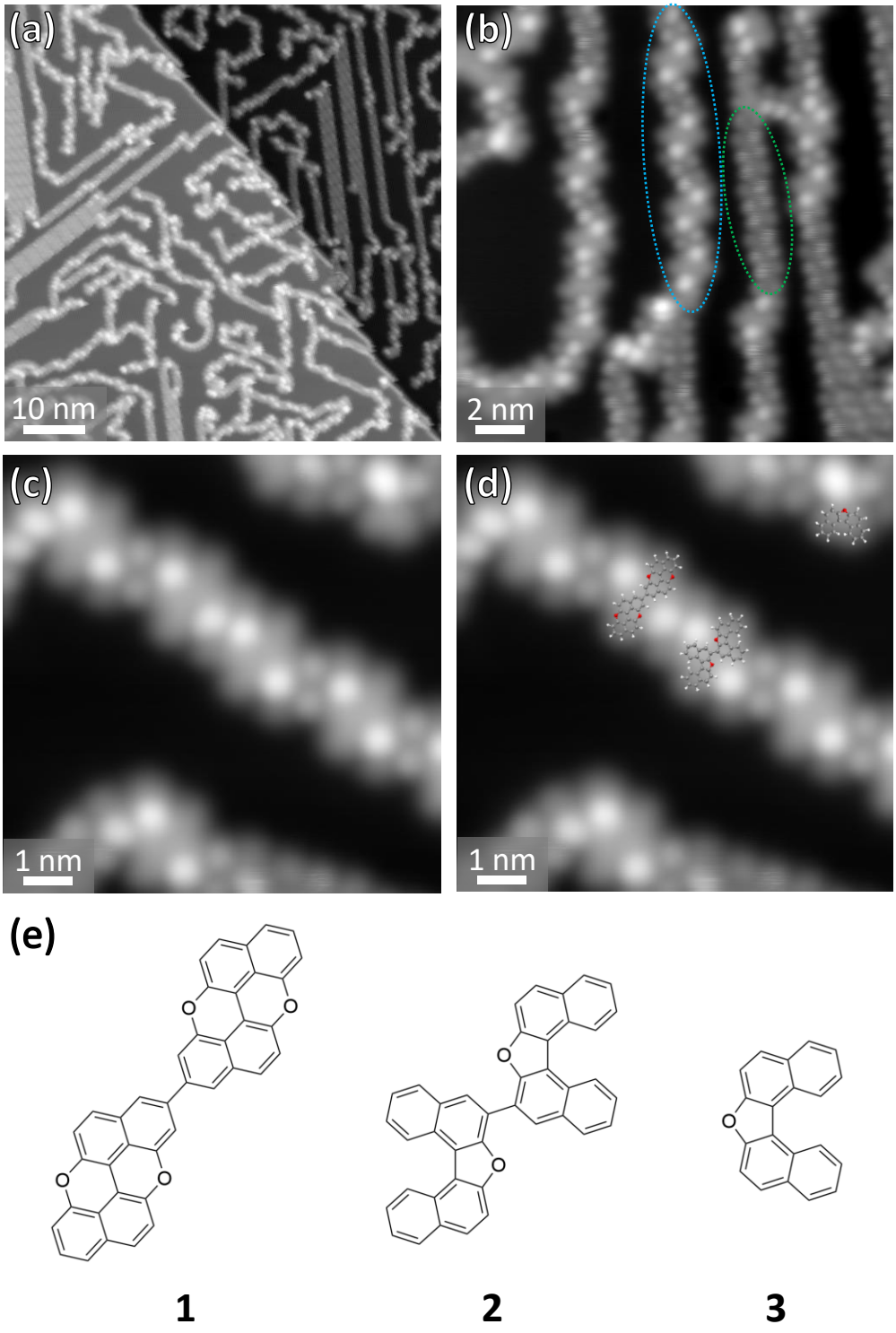

Figure 3.14. *(a) 77 K STM image showing the variety of chain structures observed in STM after annealing a low coverage of binol (+) on Cu(111) to 523 K. (b) Close-up showing the coexistence of type I (indicated by the green ellipse) and type II (blue ellipse) chains. (c), (d) Close-up of a type II chain, with possible flat model structures overlaid. (e) Three possible chemical structures of the flat features in type II chains. Bias voltages: (a) 1.6 V (b) 1.8 V (c) 1.2 V.*

Higher Annealing Temperatures

Annealing to higher temperatures (573 K and above) results in irregular, meandering structures (**Fig. 3.15**), most probably formed from covalent linkages at a variety of C-H positions on the periphery of the molecules. The general appearance of these (higher temperature) chain structures is also found to be more 'flat', suggesting a simultaneous increase in ring fusing reactions that produce more planar molecules. The fact that these reactions are observed at higher temperatures also adds further proof that the type I chains originally observed at lower annealing temperatures are more likely to be metal-organic in nature.

Occasionally more regular structures are found within the chains (**Fig. 3.15(c)**, blue ellipse) after the 573 K anneal. These typically resemble a more extended version of the dimers seen within the type II chains. A possible model for one of these polymers is shown in **Fig. 3.15(e)**. Similar results were not reported by Kong et al. with the brominated form of the molecule on Ag(111), but this may be due to the low annealing temperatures used in that study, as well as the less reactive metallic substrate.

The XPS measurements performed for annealing temperatures above 573 K, show a decrease in the size of both peaks in the O 1s spectra (**Fig. 3.9**), a phenomenon that is attributed to molecular desorption. The formation of the proposed fused furan-ring products also causes a reduction of the oxygen signal, as H_2O is lost in the reaction, and water easily desorbs from Cu(111) at these temperatures[191]. It should be noted that the C-O-C peak does not diminish in size with increasing temperature as quickly as the C-O^- peak; this is most probably due to the reactions forming C-O-C at those temperatures, combined with an increased level of thermal stability once the planar sections of the chains have formed.

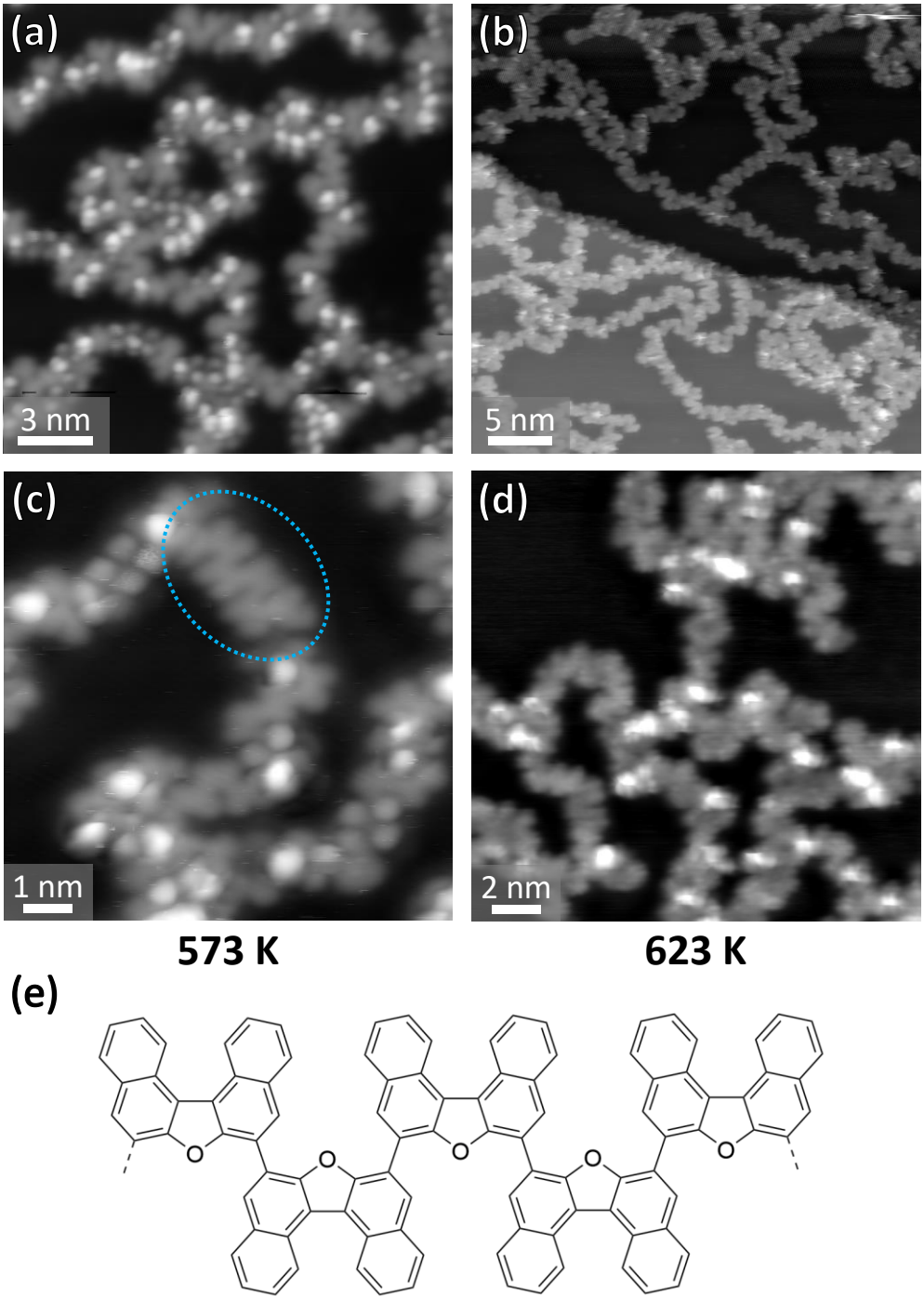

Figure 3.15. *(a) and (c) 77 K STM images of the 573 K anneal of binol (+) on Cu(111). (b) and (d) 623 K anneal. (e) Possible structure of the polymeric chain fragment highlighted in (c). Bias voltages (a) 1.2 V (b) 0.8 V (c) 1.3 V (d) 1.2 V.*

3.2.2 Binol and Fe on Cu(111)

An indirect method for further proving that the type I chains found at lower annealing temperatures are metal-organic in nature is to verify whether the co-deposition of another metal species on the surface with binol *after* it has formed type I chains leads

to a change in the molecular organisation. It has previously been shown that iron can displace copper adatoms in metal organic structures on Cu(111)[32] and Au(111)[192]. If the type I binol chains are significantly disrupted or changed after the deposition of iron, this provides further evidence that they consist of metal-organic linkages and are not covalently bound polymers, as it is unlikely that thermally co-deposited Fe atoms would catalyse the breaking of C-C or C-O covalent bonds at room temperature. To test this, iron was evaporated (via an e-beam metal source mounted on the preparation chamber of the LT-STM) onto a Cu(111) surface that already had binol(–) type I chains formed on it.

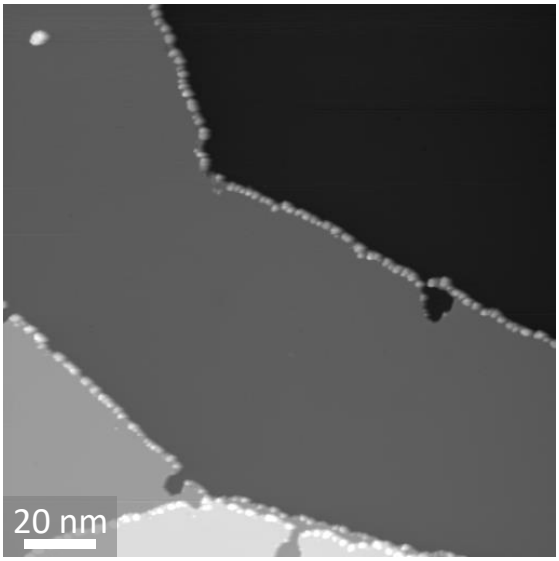

Figure 3.16. *77 K STM image (1.1 V) of approximately 0.05 ML of Fe deposited on Cu(111) at room temperature.*

Prior to this, the rate of the Fe deposition was calibrated by depositing onto a clean Cu(111) surface at room temperature and scanning the resulting assembly in STM. In **Fig. 3.16**, the low coverage (approximately 0.05 ML) Fe/Cu(111) assembly is shown. Adsorption of a low coverage of iron results in the formation of small clusters at the upper part of step edges. **Fig. 3.16** also shows occasional undecorated 'caves' in the substrate steps that have been previously observed in the literature for the Fe/Cu(111) system[193,194] and were attributed to the effects of Cu diffusion from steps as a mechanism of strain relief[195].

77 K STM images of the binol(–) chain assembly before and after two subsequent Fe depositions (0.05 ML each) are shown in **Fig. 3.17**. The chain structures clearly

disappear after the first deposition of Fe, leaving behind smaller irregular clusters – presumably binol molecules bound to clusters of iron – of which the internal structure could not be clearly resolved. This result, combined with previous STM and XPS experiments, adds further evidence to the assertion that the type I chains are stabilised by metal-organic and not covalent bonds.

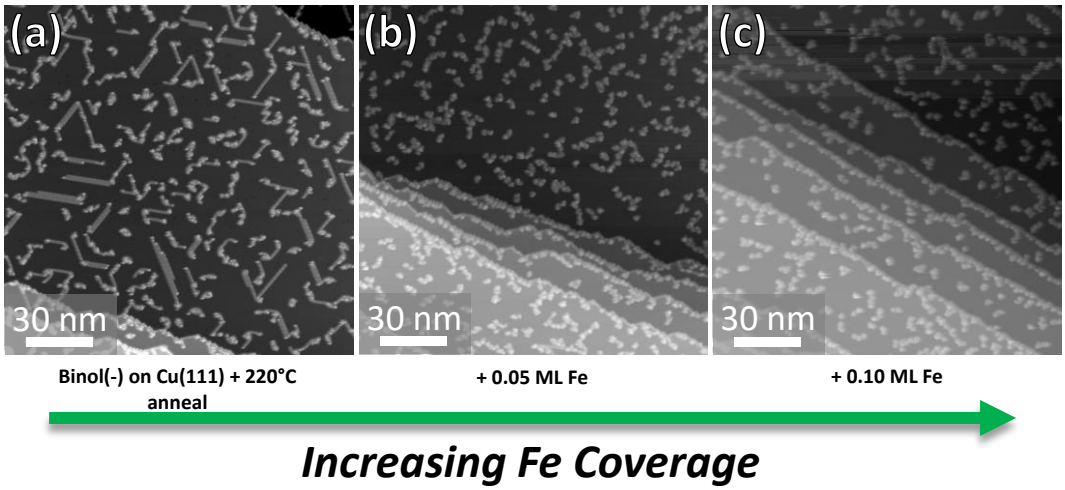

Figure 3.17. *(a) – (c) Increasing coverage of Fe deposited over a pre-prepared sample of binol(–) type I chains on Cu(111). After even a small amount of Fe, the type I chains are disrupted. Bias voltages: (a) 1.2 V (b) 1.5 V (c) 0.9 V.*

Further experiments involving iron deposition and annealing were performed in order to ascertain whether it was possible to induce different reactions or to determine if precisely controlled amounts of a different metal could lead to the formation of other types of self-assembled structures.

Annealing the deposition shown in **Fig. 3.17(c)** (binol(–) chains + 0.10 ML Fe) up to 373 K did not significantly change the appearance of the clusters. Higher annealing temperatures lead to a more 'chain-like' organisation with some of the clusters displaying a 'hollow' geometry (**Fig. 3.18(b)**), possibly due to the formation of small, flatter Fe islands that binol molecules can co-ordinate to at the edges. In any case, the original chain structure was never recovered whilst iron was present on the surface, indicating that the type I chains are specific to copper and further demonstrating the preference of binol binding to Fe instead of Cu.

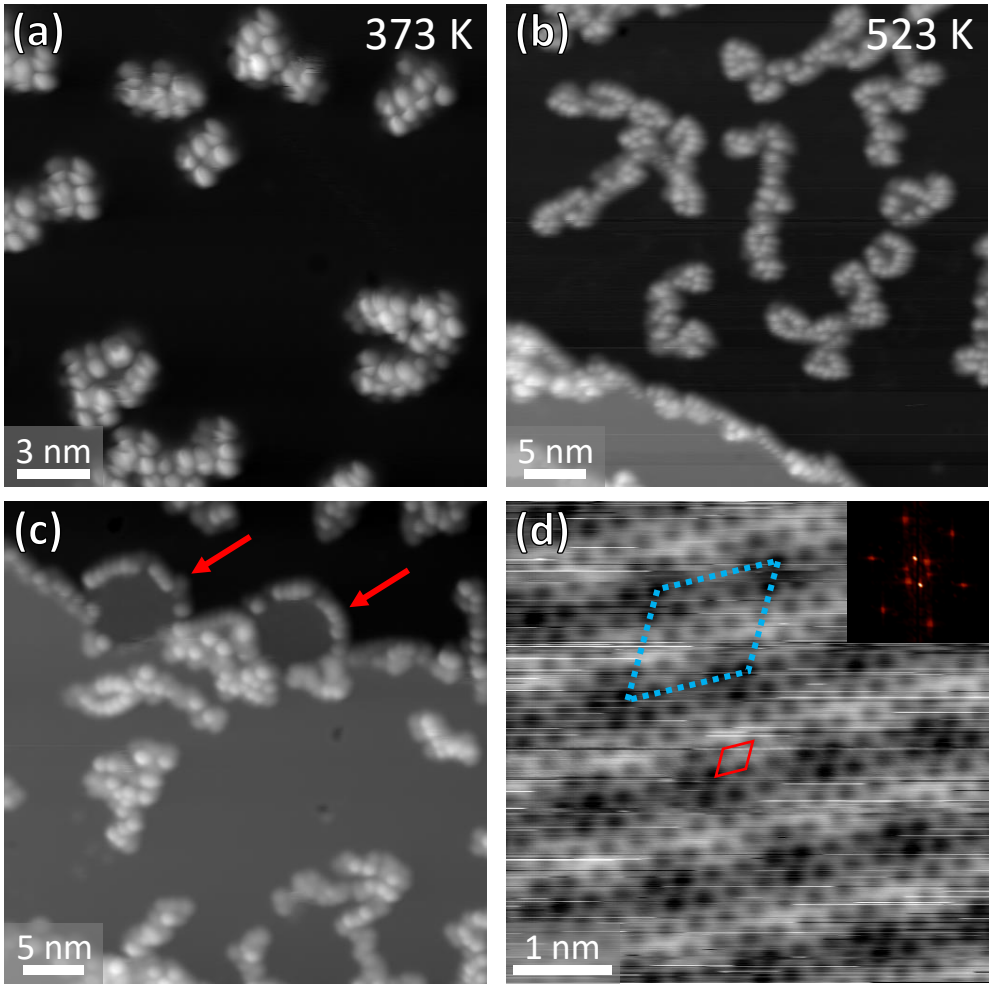

Figure 3.18. *(a) and (b) 77 K STM images of irregular binol(-) cluster structures after 373 K and 523 K annealing. (c) STM image after 573 K annealing. The red arrows indicate FeO islands growing from the lower step edges. (d) Higher resolution image of an FeO island. The large blue dotted unit cell indicates the moiré pattern, whilst the small red unit cell relates to the FeO periodicity. Inset: FFT of the STM image in (d). Bias voltages: (a) 0.9 V (b) 0.8 V (c) 1.0 V (d) 0.2 V.*

Interestingly, above 493 K, small, flat islands with an apparent height lower than that of a copper monoatomic step (**Fig. 3.18(c)**) are also observed in STM images at the bottom of steps in the Cu(111) surface. These islands slightly increase in size with higher annealing temperatures, whilst the binol structures become increasingly irregular and display more 'flat' sections, hinting at the occurrence of semi-random ring fusing reactions (similar to what was observed at higher annealing temperatures in the absence of iron, see **section 3.2.1**). Zooming in on these step-edge islands (**Fig. 3.18(d)**) reveals a hexagonal structure (lattice parameter **a** = **b** = 3.18 ± 0.07 Å, θ = 60 ± 1°) with a larger hexagonal moiré pattern of periodicity 1.26 ± 0.05 nm. As the islands are only observed when annealing the molecule in the presence of iron atoms,

it is reasonable to assume that they either contain iron or are a result of a reaction that is catalysed by iron. The measured lattice parameters and directionality (matching the underlying surface) fit well with values taken from the literature for FeO/Cu(111)[196]. The moiré pattern occurs as a result of four FeO spacings fitting into every five Cu(111) spacings (equivalent to 1.279 nm) along the three principal surface directions; this approximately matches the observed moiré periodicity of 1.26 ± 0.05 nm. Similar FeO islands with moiré patterns have also been observed on Pt(111)[197] and Au(111)[198]. We therefore tentatively assign the structures in Figs. 18(c) and 18(d) to FeO, noting that, based only on STM data, it is impossible to be completely certain of this assignment due to the chemical insensitivity of STM. Assuming that there is no other source of oxygen present, this result implies that FeO islands have formed from oxygen that has been removed from the binol molecules, possibly during ring fusion reactions. Examples of such could be those leading to the formation of furan-containing products that, as seen previously, involve a loss of H_2O (see **section 5.2.1**). A control experiment in which the same coverage of Fe on Cu(111) (without binol) was annealed to the same temperatures did not yield these islands, further indicating that binol acts as a source of oxygen.

A study involving the co-deposition of binol(-) and iron *without* annealing was also performed in order to investigate whether regular chain structures similar to those formed by binol with Cu adatoms could also be formed with Fe without the extra thermal energy (and Cu adatoms) provided by annealing. To this end, an increasing amount of Fe was deposited onto a Cu(111) surface with a constant binol coverage. Small amounts of iron (approx. 0.05 - 0.1 ML, 60s deposition time) resulted in the formation of a new type of network hitherto unseen with binol on Cu(111), as presented in **Fig. 3.19(a)**. Porous, triangular islands with a hexagonal internal structure and a rhombic unit cell (parameters $\mathbf{a} = \mathbf{b} = 2.37 \pm 0.06$ nm, $\theta = 60 \pm 1°$) were observed, alongside less frequent fragments of a second assembly with a higher porosity (hexagonal unit cell $\mathbf{a} = \mathbf{b} \approx 5$ nm, $\theta \approx 60°$). A small scale STM image of the main assembly is shown in **Fig. 3.19(d)** and demonstrates that the hexagonal unit cell is oriented 5.4 ± 0.5° clockwise from the nearest underlying Cu(111) principal directions. As with the original binol/Cu(111) experiments (**section 3.2.1**), only 'one' orientation of the chiral assembly is observed for binol(–)/Fe. There are several possibilities for the orientation of the molecules within the hexagonal packing and for

the position of Fe atoms, with potential sites of the latter indicated with green circles in **Fig. 3.19(e)**. Interestingly, the structures that best fit with the double lobe shape of binol (**2** and **3** in **Fig. 3.19(e)**) do not involve the C-O$^-$ groups sharing metal atoms between nodes of the packing, while in the structure that does have the groups oriented in such a fashion (**1**), the C-O$^-$ groups are too far away from each other to be sharing a single atom. Iron atoms within the assembly are not resolved, as is often the case in STM measurements of metal-organic networks[34,199,200]. As a consequence, it is not possible to precisely determine the actual structure of this assembly; for example, it might even be that the hexagonal lattice simply results from the aggregation of molecules binding to Fe atoms that are not shared between them.

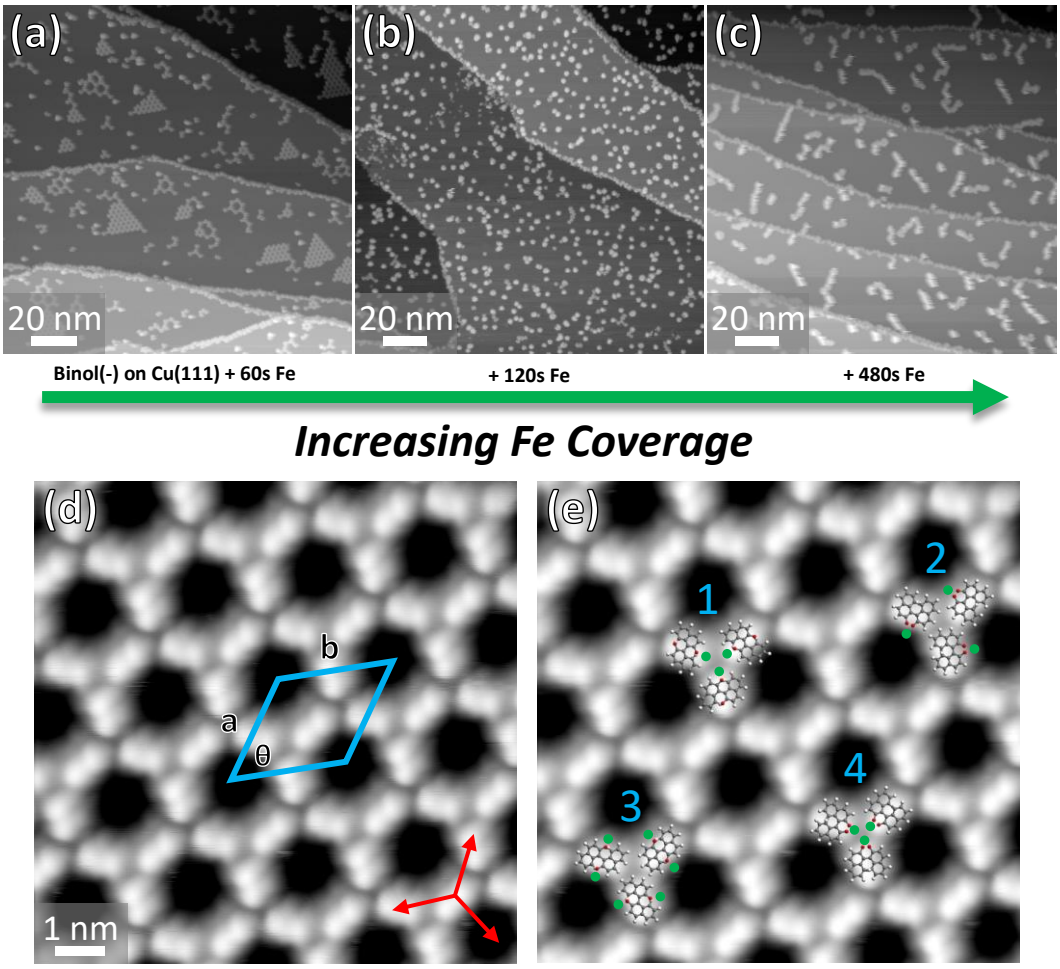

Figure 3.19. *(a)-(c) 77 K STM images of an increasing coverage of Fe (measured in deposition time) over binol(–) on Cu(111). The formation of ordered structures is only observed at the lower coverage. (d) Close-up STM image of one of the triangular islands in (a). (e) Potential different models showing the position/conformation of binol(–) with Fe shown as green circles. Bias voltages: (a) 0.9 V (b) 1.4 V (c) –1.6 V (d) 1.0 V.*

Depositing a larger amount of iron results in the formation of irregular clusters (**Fig. 3.19(b)**) that become longer and more aligned with an increasing the Fe coverage (**Fig. 3.19(d)**). Similarly to what was observed during annealing, it was not possible to clearly resolve the structure within these clusters, which may consist of rows of binol molecules surrounding increasingly large iron clusters. However, without annealing, no regular step reconstruction and no significant formation of flatter objects was observed, irrespective of the Fe coverage. Again, this observation (in combination with the previous) points towards a temperature-induced loss of oxygen from the binol molecules, most probably resulting from ring fusion reactions.

3.2.3 Binol on Au(111)

Binol molecules were also deposited on the Au(111) surface and the results were directly compared with the behaviour seen on Cu(111). Examining a more inert surface helps to further rationalise the effect the substrate has on the self-assembly and reactivity (e.g. deprotonation leading to metal-organic or covalently bound new structures) of the binol molecules.

Attempts to image a sub-monolayer coverage of binol(–) (room temperature deposition) on Au(111) by STM at 77 K were unsuccessful. The molecule is found to be too mobile to self-assemble at that temperature, most probably due to very weak molecule-molecule and molecule-substrate interactions. This assumption is supported by XPS measurements of a room temperature deposition: the O 1s peak appears at 533.0 eV (**Fig. 3.20**), approximately 2 eV higher than on Cu(111), which fits with a molecule that has *not* been deprotonated upon adsorption on Au(111)[102,186]. As the most probable interaction between binol molecules and the Cu(111) surface is binding via the deprotonated hydroxy group (as seen with other molecules on Cu surfaces in the literature[186,188]), the protonated form of the molecule is expected to only weakly physisorb onto the Au(111) surface. Annealing the surface after deposition results in no change other than an eventual desorption of the molecule at around 423-473 K. Thus, in stark contrast to what is observed with Cu(111), the inherently more inert Au(111) surface does not catalyse the deprotonation of binol molecules.

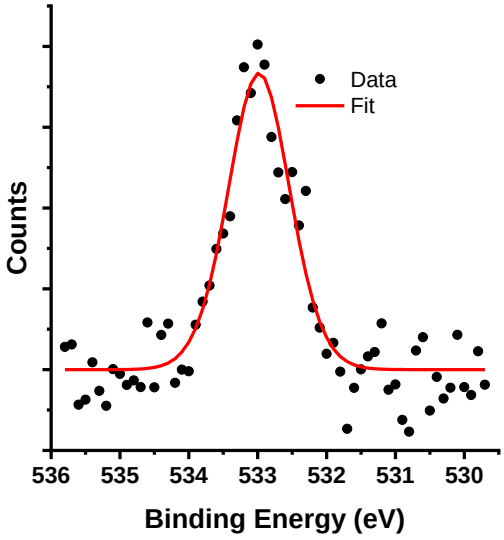

Figure 3.20. *O 1s XPS spectrum of binol(–) deposited at room temperature on Au(111).*

Cooling the sample to 7 K reduces the mobility of the binol molecules, allowing them to organise into two different self-assembled structures, as illustrated in **Fig. 3.21**. Potential models for these structures are shown in **Figs. 3.21(c)** and **(d)**. The intermolecular interactions are most probably mainly van der Waals, although hydrogen bonding between adjacent OH groups may also be possible. As no deprotonation has occurred, there are no options for strong metal-organic binding. The absence in general of strong intermolecular interactions is supported by the fact that these assemblies are not observed at 77 K.

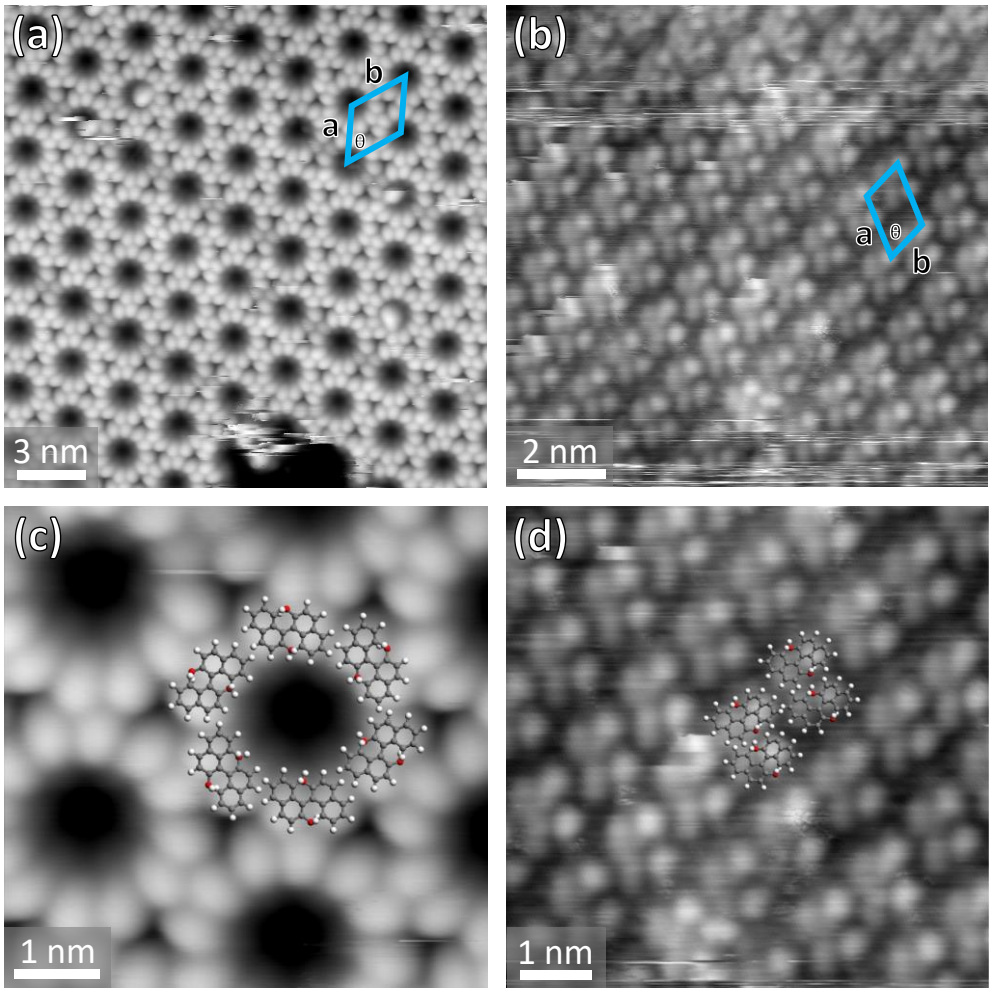

Figure 3.21. *(a) and (b) The two assemblies of binol(–) on Au(111) observed in STM at 7 K. (c) and (d) Proposed models for these structures. Bias voltages: all 1.3 V.*

3.2.4 Binol and Fe on Au(111)

Co-deposition experiments of Fe atoms and binol molecules were performed to investigate whether the intrinsic inertness of Au(111) could be enhanced by the addition of a limited amount of a more reactive metal and to examine whether this could induce or catalyse on-surface reactions.

Depositing iron alone on Au(111) leads to the formation of iron clusters, particularly located at the elbow sites of the herringbone reconstruction (**Fig. 3.22**). A rough estimate of the rate of deposition was made by making a comparison to reports on the Fe/Au(111) system from the literature[201,202]. The internal structure of these small clusters was not clearly resolved, possibly due to their disordered three-dimensional nature.

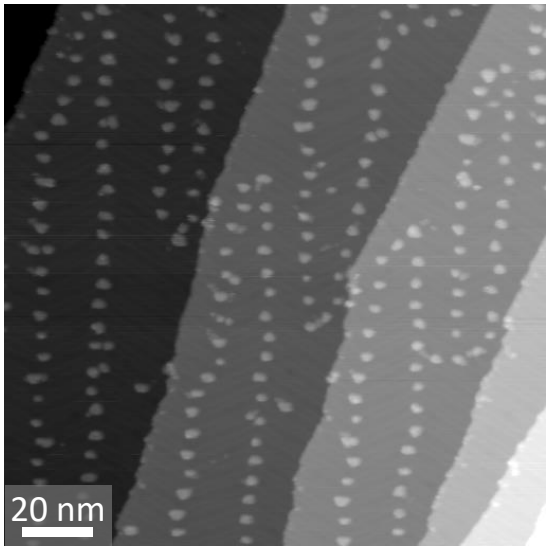

Figure 3.22. *77 K STM image (1.1 V) of a low coverage (<0.1 ML) of Fe on Au(111). Fe clusters form at the elbow sites of the herringbone reconstruction and thus show a regularity in their dispersion.*

Binol(–) was deposited over the Fe/Au(111) surface at room temperature. STM images acquired at 77 K demonstrate that that the surface is covered by small, irregular chain-like clusters (**Fig. 3.23(a)** and **(c)**). Importantly, it is clearly possible to identify binol molecules within these clusters, as they are stabilised by the presence of iron. Annealing this assembly to 373 K and 423 K leads to the formation of longer and more regular chain structures (**Fig. 3.23 (b)** and **(d)**), presumably consisting of binol molecules in metal-organic structures with iron, similar to what was observed on Cu(111) without co-adsorbed iron (**Fig. 3.10**). In this case, however, the chains form a double row instead of a single row structure. Moreover, the maximum apparent height of the chains is approximately 5 Å, significantly larger than that measured for the straight type I chains on Cu(111) (around 1.5-2 Å). Attempting to overlay molecules on the sides of these chains leaves a central region (consisting of pairs of lobes, highlighted with a red ellipse in **Fig. 3.23(d)**) that may consist of a lower row of binol molecules, possibly bound to Fe, underneath. As such, there may actually be three binol molecules across each unit of the chain. Another possibility is the formation of a regular central Fe structure that the binols on each side are adsorbed onto, in a similar fashion to molecules sitting over an atomic step on a surface. In either case, the two central features cannot be easily identified due to the proximity/overlap of the neighbouring molecules.

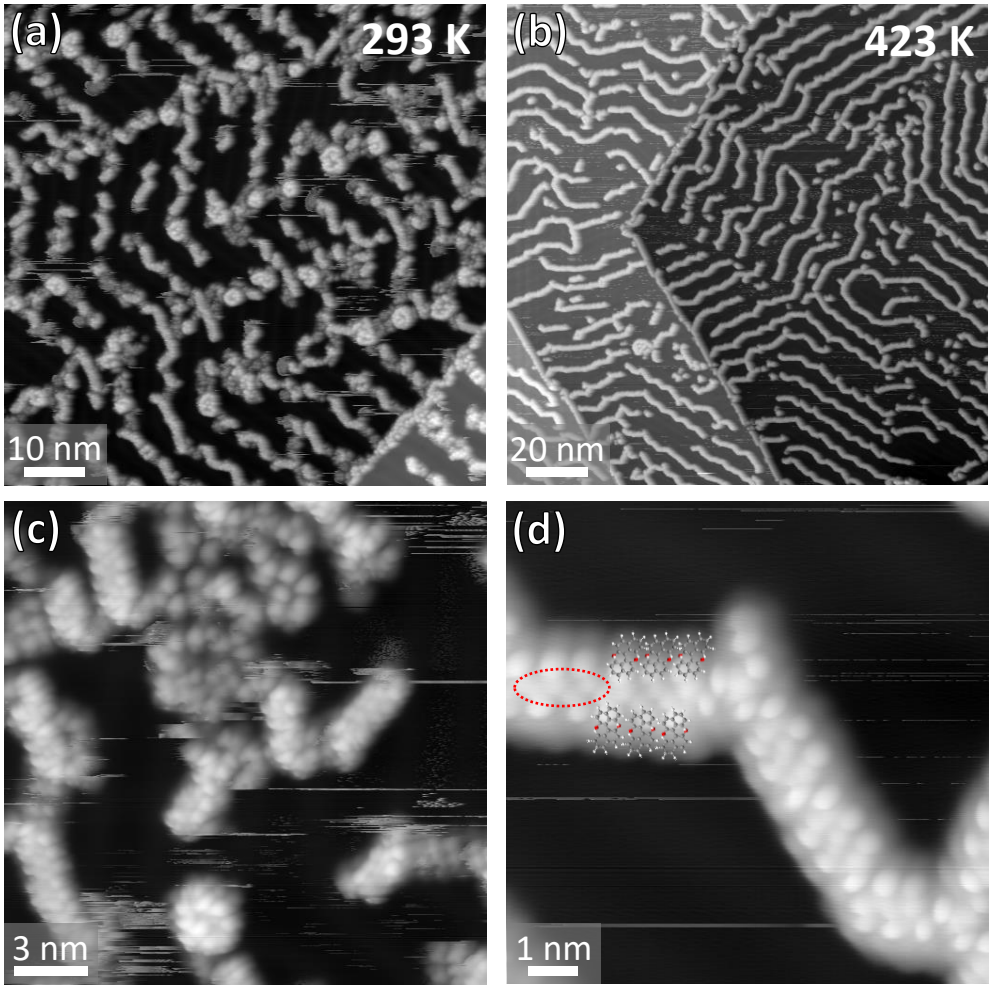

Figure 3.23. *(a) and (c) STM images (77 K) of binol(–) deposited on Fe/Au(111). (b) and (d) STM images of the same surface after annealing to 423 K. Molecules are overlaid onto the sides of the chains in (d), and the central region of the chain – which may have a lower layer of binol or a Fe structure – is indicated with a red oval. Bias voltages: all 1.5 V.*

The chains as a whole typically follow the direction of the herringbone, but individual straight sub-sections do not, with shifts in position and changes in direction to accommodate the directionality of the herringbone. Steps, decorated with chains of molecules (and possibly iron) are also reconstructed in straight lines along the principal substrate directions – again, in a similar fashion to Cu(111). It is unclear whether Fe is always involved in these suspected metal-organic structures; in fact, there is also the possibility that it is only responsible for deprotonating the molecules, after which they could also bind to atoms from the Au(111) substrate. The demonstration of regular chain formation with Fe on Au(111) and *not* Cu(111) could also be related to the different inter-atomic spacing on these surfaces, with a better fit to the larger lattice of Au(111).

STM images (77 K) acquired after annealing to 473 K and 523 K show hints of new mobile objects in between the binol-Fe chains and at the edges of (binol-decorated) Au(111) monoatomic steps (**Fig. 3.24(a)** and upper panel of **(b)**). As these new molecules are too mobile to be imaged on the timescale of the STM (approx. 1-2 minutes per image), they are simply imaged as an average of their position. The dark lines seen over the herringbone may be indicative of a preference for these objects to occupy the regions in between the herringbone lines (i.e. they spend less time on top of the lines and thus the average height over these positions is lower than in the surrounding areas). In a similar fashion to some of the electron donor molecular systems shown later in this thesis (PXX and Br_2PXX, **Chapters 4** and **5**) any sign of the mobile objects disappears upon scanning at a negative sample bias voltage, which is most probably the result of a repulsive interaction between the molecules and the positively charged STM tip. This is clearly shown in the lower panel of **Fig. 3.24(b),** in which the faint objects clustered around the metal-organic structures that are seen in the upper panel disappear, and the typical bright lines of the Au(111) herringbone become apparent.

In an attempt to properly identify these objects by immobilising them, STM experiments at 7 K were performed on the same systems. The resulting images (**Fig. 3.24(c)**) reveal individual molecules located preferentially close to step edges but also scattered across the surface terraces. Their uniform appearance and their lower height with respect to the metal-organic chains, suggest that they are the result of an intramolecular ring-closure reaction of binol (–), leading to a fully planar product. The symmetry, shape, and size of these objects seems to indicate that, instead of forming PXX, the binol molecules have instead fused to form a furan ring on one side. Overlaying the structural model of this molecule onto the STM images indeed shows a good fit (**Fig. 3.24(d)**). A dI/dV spectrum **(Fig. 3.24(e)**) of the furan product was also recorded at 7 K, revealing an occupied state at approximately −1550 mV. If this corresponds to the HOMO of the molecule, then it fits well with a lower expected HOMO energy when compared to that observed with PXX on Au(111) (see **Chapter 4** of this thesis), as predicted by cyclic voltammetry measurements in the literature[6].

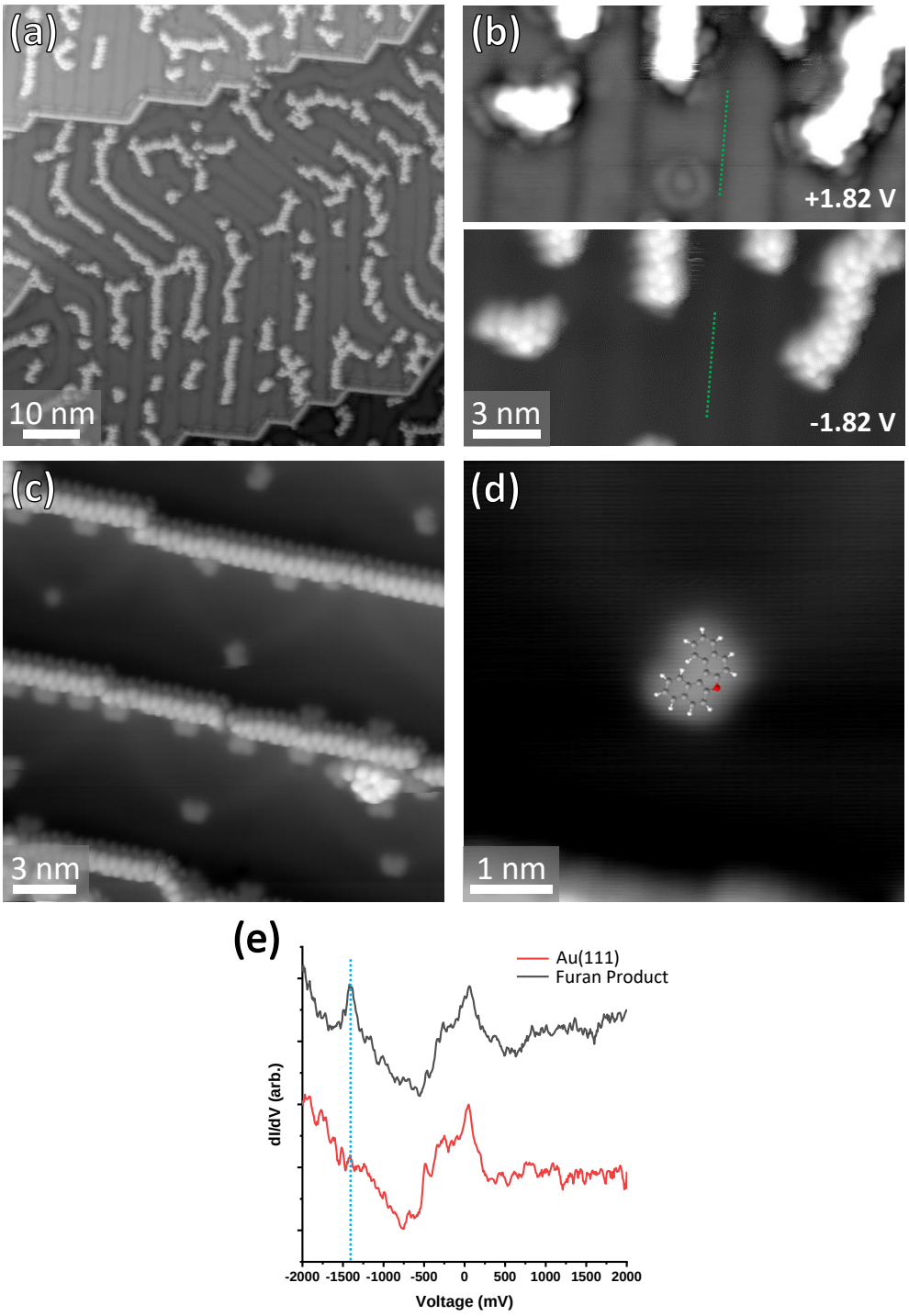

Figure 3.24. *(a) 77 K STM image (1.5 V) of binol(–)/Fe/Au(111) after annealing to 573 K. (b) Voltage dependent STM, demonstrating the change in the appearance of both the herringbone lines and the mobile objects stabilised by the metal-organic structures. The height scale of the upper panel is adjusted for higher contrast over the mobile objects. The green dashed line is the same position on the herringbone reconstruction in both panels. (c) and (d) STM images (1.1 V) of the same system at 7 K, showing the previously mobile objects scattered over the terrace, with a good fit to the furan-containing structure in (d). (e) dI/dV spectrum of one of the products, showing its occupied peak at approx. −1550 mV (blue dashed line).*

Previous results reported in the literature for a brominated form of binol on Au(111)[102] provide an interesting comparison with the unfunctionalised binol molecule. In the case of brominated binol, a stable island assembly formed and could easily be imaged at 77 K, unlike the unfunctionalized molecule. Furthermore, annealing the brominated molecule on Au(111) (without any additional co-deposited metal) led to ring fusing reactions and eventually polymers formed via C-C bonds at the positions of the former C-Br groups. The ring-fused products (prior to polymerisation) in that case were both the furan molecule and PXX. In the case of unfunctionalised binol presented above, a more selective reaction has taken place, with seemingly only furan products formed. It should be noted that the increased adsorption stability of the brominated molecule on Au(111) may reduce the activation energy of the fusing reactions; they were found to occur at only 380 K, whereas even with iron on the surface, the reaction of the unfunctionalized molecule does not take place until above 473 K.

3.3 Conclusions

In this chapter, the self-assembly and on-surface reactions of binol molecules on Cu(111) and Au(111) substrates have been examined in depth. Whilst the original aim of reacting binol to form PXX was not achieved, a variety of other reactions were investigated. In particular, the direct comparison between Cu and Au surfaces showed the significant effects of their different surface reactivities.

Binol was found to readily form clusters upon adsorption on Cu(111), most probably involving metal-organic bonds via deprotonated O-H groups to Cu atoms. A variety of structures was observed at higher coverages before and after annealing, with a tendency towards a striped phase after annealing. Annealing the system to higher temperatures initially led to the formation of metal-organic chains and eventually reactions that formed covalent bonds, albeit not in a controllable manner. No temperature was found at which the majority of the molecules were converted to a single product. Experiments with Fe adsorption further proved the metal-organic nature of the chains.

In the case of Au(111), due to its lower reactivity, XPS results demonstrated that the O-H bond of binol remained intact upon adsorption. Self-assembled structures could only be observed at 7 K, most probably due to weak intermolecular and molecule-surface interactions. Adding Fe resulted in the formation of chain structures, and

higher annealing temperatures eventually led to the formation of a fused molecule containing a furan ring, demonstrating an on-surface Fe-catalysed reaction.

4 PXX at Metallic Surfaces

4.1 Introduction

PXX (*peri*-xanthenoxanthene) has shown its potential as an electron donor in previous studies[6], as well as its role as an active organic semiconductor in flexible OLED displays[113,203]. In particular, modification of the chemical structure of PXX allows the tailoring of the energy of its molecular states, potentially allowing the formation of stronger donor molecules with a lower-lying highest occupied molecular orbital HOMO[6]. It has been shown that short O-doped zig-zag molecular ribbons containing PXX-type structures can be formed in solution, with a corresponding upshift in the energy of the HOMO with increasing length[116]. Conversely, the opposite effect has been achieved via the addition of alkyl-imide groups, with an overall slight compression of the HOMO-LUMO gap and an overall shift downwards in the energy of both frontier energy levels[7]. When moving to on-surface studies, it is important to study PXX in its unmodified state before structurally altering the molecule, in order to more precisely determine the effects of structural alteration. When adsorbed on metallic surfaces, the behaviour of PXX may be examined by STM at the single molecule level. Using surfaces with different work functions may also demonstrate the effect of the energy level alignment on interfacial charge transfer processes[82], as the HOMO of PXX must be close to or above the Fermi level of the metal in order for charge transfer to occur.

With these aims in mind, PXX was deposited onto both Au(111) and Cu(111) surfaces and studied via STM, STS and XPS. PXX was thermally sublimed (with the evaporator held at 438 K) onto room temperature metal single crystals in UHV conditions and studied at low temperature (77 K and 7 K) with STM/STS. XPS measurements were performed on room temperature samples.

4.2 Results and Discussion

4.2.1 PXX on Au(111)

Upon sublimation and adsorption on a Au(111) single crystal, PXX is seen to be extremely mobile when studied via STM at 77 K. At lower coverages, molecules

cannot be imaged at all (data not shown), due to the speed of their diffusion being greatly in excess of the scanning rate of the STM, despite the low temperature utilised. Increasing the coverage to close to a monolayer (i.e. when the surface is completely covered by molecules) results in the appearance of rows on the surface that often follow the underlying herringbone of the substrate, as depicted in **Fig. 4.1**. Within the majority of the rows, individual molecules cannot be observed but, in a few cases, they can be more clearly visualised. This may be due to the stabilising effects of contaminants co-adsorbed with the molecules or to changes in the underlying surface adsorption potential due to the presence of defects in the Au(111) crystal. Another possible explanation for this is a locally higher molecular density in these regions/rows. The more mobile rows are simply imaged as an average of the molecular positions; the dark regions in between the mobile rows may indicate a preference (on average) for regions in between the herringbone reconstruction lines at this coverage. However, as the reconstruction lines cannot be clearly seen through the adlayer, this cannot be confirmed by STM imaging at this temperature. Molecules have been shown in the literature to preferentially adsorb upon different parts of the herringbone reconstruction due to variations in adsorption potential, often with a particular preference for the elbow and the fcc sites[76,204,205]. In this case, however, a preference for fcc sites is not shown, potentially due to the high coverage. There is also no tendency for the more stable rows to be located on the fcc regions of the herringbone. An interference pattern is also occasionally observed in regions where the direction of the molecular rows do not follow the herringbone and both the molecular rows and the herringbone reconstruction lines are simultaneously imaged (**Fig. 4.1(b)**).

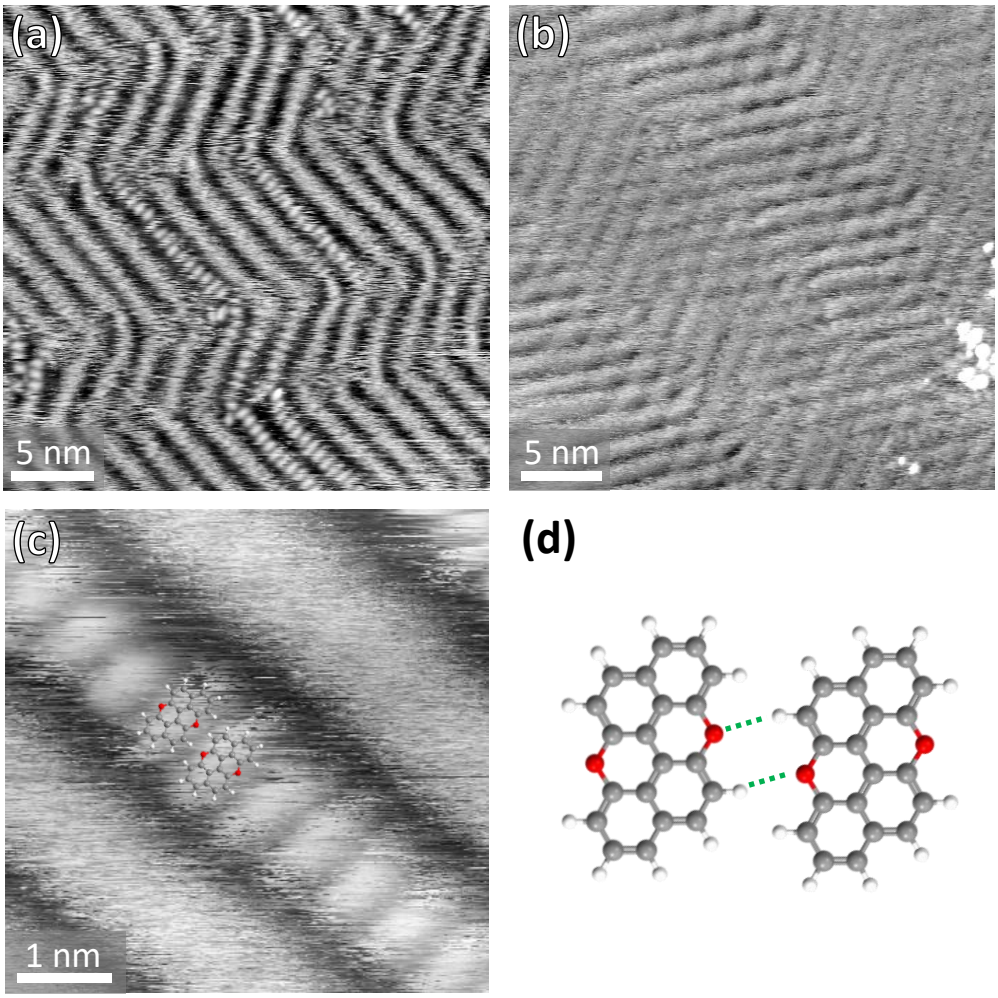

Figure 4.1. *(a) STM image (77 K, 2 V) showing a mixture of mobile and more stable rows. (b) Interference patterns of molecular rows that do not completely follow the Au(111) herringbone reconstruction (2 V). (c) Zoom into one of the more stable rows (2 V) with overlaid molecular structure. (d) H-bonded model of the row structure, with an O---H distance of approximately 2.5 Å.*

The periodicity of the molecular features within these rows is found to be relatively consistent (7.8 ± 0.5 Å), with some variation that can be attributed to differing degrees of mobility of the PXX molecules found in some rows. A possible model for the interaction between adjacent molecules is shown in **Fig. 4.1(d)**. Weak, non-classical hydrogen bonds between peripheral oxygen atoms and hydrogen atoms on the aromatic rings of adjacent molecules may be responsible for the row formation. More variation (approximately 10%) can be found in the inter-row distance, with a periodicity of 21.2 ± 2.1 Å. This may be due to weaker attractive inter-molecular interactions along this axis (such as van der Waals forces) and local variations in the surface coverage of PXX.

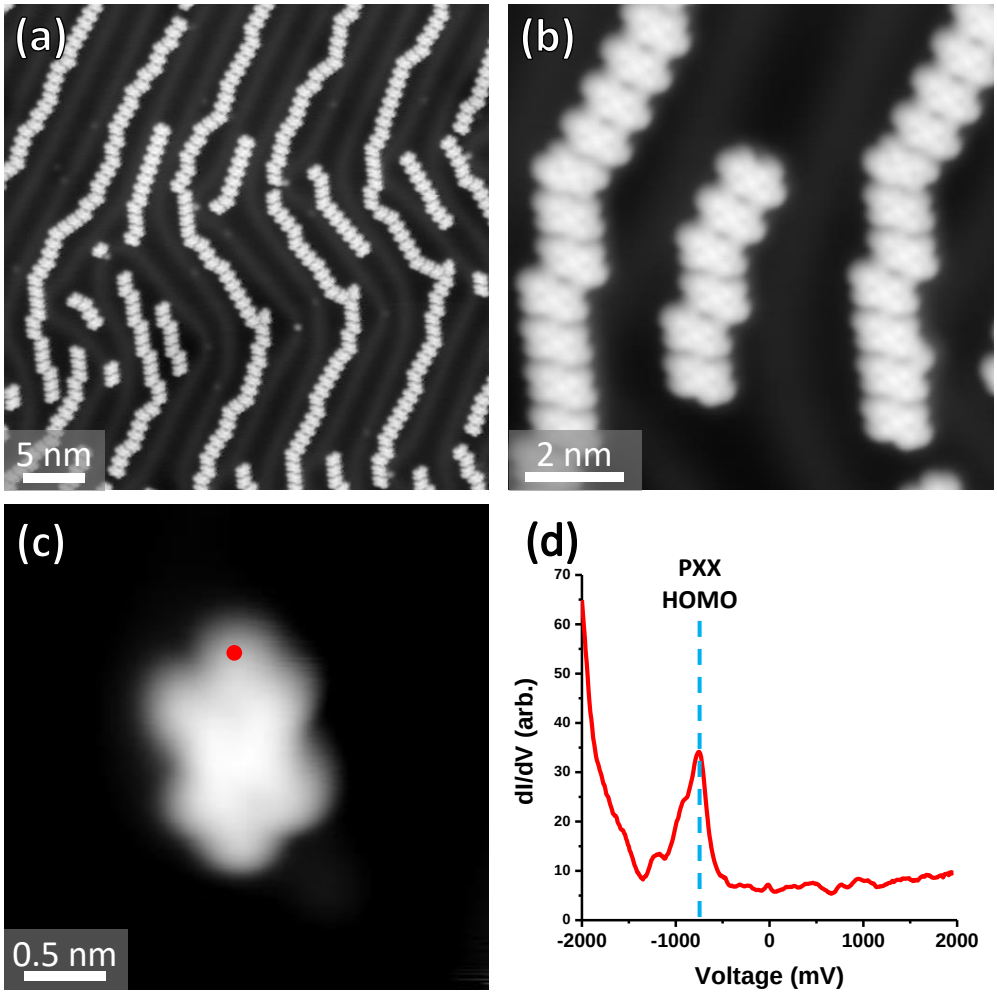

Figure 4.2. *(a) 7 K STM of a sub-monolayer coverage of PXX on Au(111) (−1.26 V). (b) Zoomed in STM image (−2.00 V) showing the chains. (c) A single PXX molecule (−1.06 V). The red dot indicates where the point spectrum shown in (d) was recorded. (d) dI/dV point spectrum of a PXX molecule on Au(111). An occupied state attributed to the HOMO of the molecule can be seen at approximately −800 mV.*

Reducing the temperature of the STM to 7 K with liquid helium cooling allows the imaging of a sub-monolayer coverage of PXX on Au(111), as shown in **Fig. 4.2(a)**. The reduction in temperature of the metal sample in turn reduces the thermal energy of the molecules and thus the extent of their diffusion. Single, immobilised molecules are clearly observed, along with molecular rows (length dependent on coverage) with a periodicity of 8.5 ± 0.2 Å , again held together by weak hydrogen bonds with a O---H distance of 2.2 ± 0.2 Å, as modelled in **Fig. 4.1(d)**. The significant lack of 2D island formation, even at low temperatures, is perhaps indicative of an intermolecular repulsive interaction that competes with the hydrogen bonding interaction. This may also be responsible for the high molecular mobility observed at higher temperatures.

The origin of this repulsive force could be PXX's tendency to act as an electron donor – a surface dipole may have formed between the molecule and the surface due to some amount of charge transfer from PXX to Au(111). However, it might instead just be a manifestation of repulsion between dipoles formed by the 'pillow effect'[26,206], combined with a lack of strong attractive intermolecular forces. A similar repulsive molecular arrangement has been observed for the electron donor molecule tetrathiafulvalene (TTF) adsorbed on Au(111)[76]. In that case, this was attributed to charge transfer at the interface, as shown by DFT calculations, although no dI/dV measurements were shown that could help to demonstrate this. Charge-transfer dependent assemblies have also previously been observed with the tetra[1,3-di(tert-butyl)phenyl]pyrene (TBP) molecule[82], showing significantly different supramolecular organisations on different metallic surfaces, depending on the level of charge transfer between the molecule and metal.

Measurements of the dI/dV signal over a single molecule (**Fig. 4.2(d)**) reveal an occupied state at −830 ± 30 mV, which can be identified as a state relating to the HOMO of PXX. Imaging the molecule at this (or at a more negative) voltage results in an appearance that matches well the shape of the PXX gas phase HOMO, as shown in **Figs. 4.3(a) and (b)**. As this state is well into the occupied region of the dI/dV spectrum, this may indicate that no/little charge transfer with the surface has yet taken place.

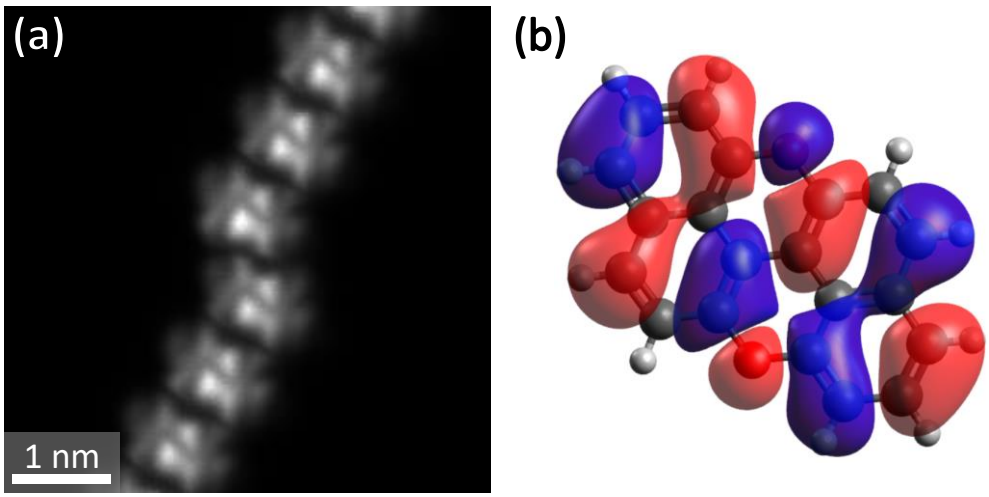

Figure 4.3. *(a) Constant height image of a PXX row recorded at a slightly more negative voltage than the HOMO resonance with a bias voltage of −1.00 V. (b) DFT-calculated (B3LYP) HOMO of PXX, oriented in a similar fashion to the molecules in (a). Calculations performed by Harry Pinfold, University of Warwick.*

High resolution constant height measurements (HR-STM) with a CO functionalised tip performed on a short row of PXX molecules reveal their internal structure (**Fig. 4.4**). Each of the internal rings displays clear features, with the central rings that contain oxygen appearing much darker than the naphthalene end-sections of the molecule. This may be due to differences in the local density of states over these rings at the scanning voltage (30 mV), or to a difference in the level of repulsion felt by the CO tip as it passes over them. The features seen in HR-STM imaging can indeed be the result of a complex mixture of probe-substrate interactions and of the effects of the density of states[167]. It is important to note that the image in **Fig. 4.4(b)** also shows both possible H-bonded positions between adjacent molecules within the molecular rows.

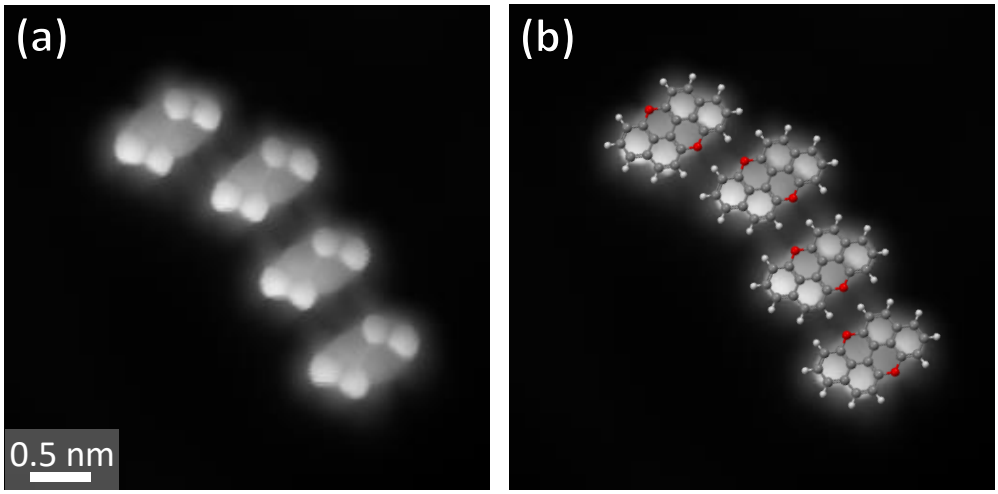

Figure 4.4. *(a) Constant height HR-STM image (CO tip, 30 mV) of a row of PXX molecules on Au(111). (b) Overlay of scaled models of PXX demonstrating the fit of the observed features with the molecular structure.*

XPS spectra of a sub-monolayer coverage of PXX on Au(111) (recorded at room temperature) are shown in **Fig. 4.5**. The C 1s spectrum (**Fig. 4.5(a)**) shows two clear signals, corresponding to C-C and C-O carbon environments. The spectrum fits well with two peaks within the C-C environment, corresponding to carbons bound to either two or three neighbours. The expected ratio of the carbon environments (10:6:4) also fits well with the data. As expected, the O 1s spectrum (**Fig. 4.5(b)**) only shows one peak at 533.2 eV, corresponding to an oxygen bound to two carbons, in agreement with values found in the literature[102].

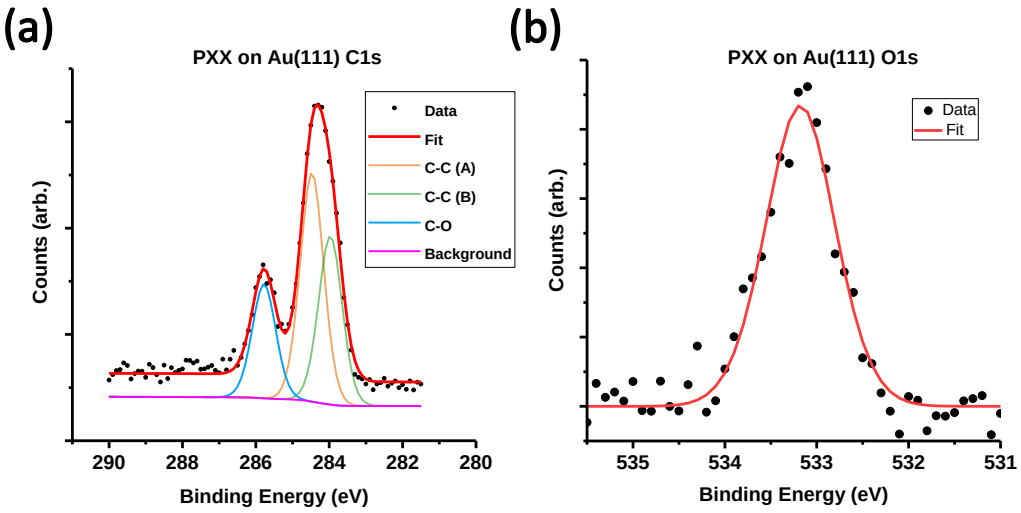

Figure 4.5. *(a) C 1s XPS spectrum of sub-monolayer PXX on Au(111). C-O peak: 285.8 eV, C-C(A) peak: 284.5 eV, C-C(B) peak: 284.0 eV. Fitted with Shirley background. (b) O 1s spectrum, peak at 533.2 eV. Fitted with a (subtracted) linear background.*

4.2.2 PXX on Cu(111)

In terms of its molecular self-assembly, some similarities with Au(111) are found when PXX is adsorbed onto Cu(111). At 77 K, the molecules are too mobile to image at coverages well below a monolayer. In contrast to the low coverage results on Au(111) (data not shown), however, some indications of the absorbed molecules are observed at lower coverages. Namely, 'ripples' emanating from the steps in the Cu(111) surface and from co-adsorbed contaminants can be seen in STM images. Periodic features (attributed to single molecules) within these 'ripples' can sometimes also be observed. The positions on the substrate at which these features are observed (steps and contaminants) most likely correspond to regions with a deeper absorption potential, leading to a greater stability of the PXX molecules and a lower rate of diffusion. As a result, these are potentially regions where PXX is more likely to be stabilised and thus observed in STM imaging. The ripples observed on Cu(111) are not imaged as protrusions from the surface when compared to the rest of the terraces; instead, there are simply regions (dark lines in **Fig. 4.6(a)**) in between rows and molecular positions within the rows, where molecules are less likely to be found. The apparent 'depth' of these ripples (**Fig. 4.6(b)**) decays away from these stabilising surface features. The molecule-molecule distance within each ripple is found to be approximately 8.2 ± 1.0 Å, corresponding to a similar weakly hydrogen bonded

arrangement to that seen on Au(111). When taking all of these observations into account, it can thus be concluded that the molecules are less mobile on Cu(111) than Au(111) in the sub-monolayer regime at similar coverages.

This interpretation is further supported by STM imaging of the high coverage (close to 1 ML) regime at 77 K; semi-ordered rows of molecules that display limited mobility are observed in STM imaging (**Figs. 4.6(c)** and **(d)**). Unlike Au(111), individual molecules are much more commonly observed within these rows. Variations in the appearance of the molecules can also be attributed to different levels of mobility that most probably relate to differences in stability due to their local surroundings. Some rows (**Fig. 4.6(d)**) are found to be particularly stable, and a distinct molecular shape is observed. Within these more stable rows, a molecule-molecule distance of 8.3 ± 0.3 Å was measured, similar to that found at lower coverages and on Au(111). The rows can again be modelled as H-bonded, and measurements of overlaid molecular models on stable rows yield an O---H distance of 2.2 ± 0.1 Å, again similar to that seen on Au(111). Discrepancies between these measurements (similar H-bond lengths but slightly different intermolecular distances) can be associated with the uncertainty that is related to the position and rotation of the molecules within the more mobile assemblies; the Au(111) H-bond length was estimated from 7 K measurements.

As PXX is a pro-chiral molecule, the two conformations of the molecule that occur upon adsorption are clearly observed in STM imaging upon deposition due to their distinctive shapes. Only one orientation is shown in **Fig. 4.6** in the stable section of the row, but for comparison, both are shown later in **Fig. 4.7**. Switching between these conformations requires flipping the molecule at the surface; presumably a process with an excessively high potential barrier when the molecules are already adsorbed. Annealing the PXX/Cu(111) system has no effect; the molecules simply desorb after reaching approximately 570 K.

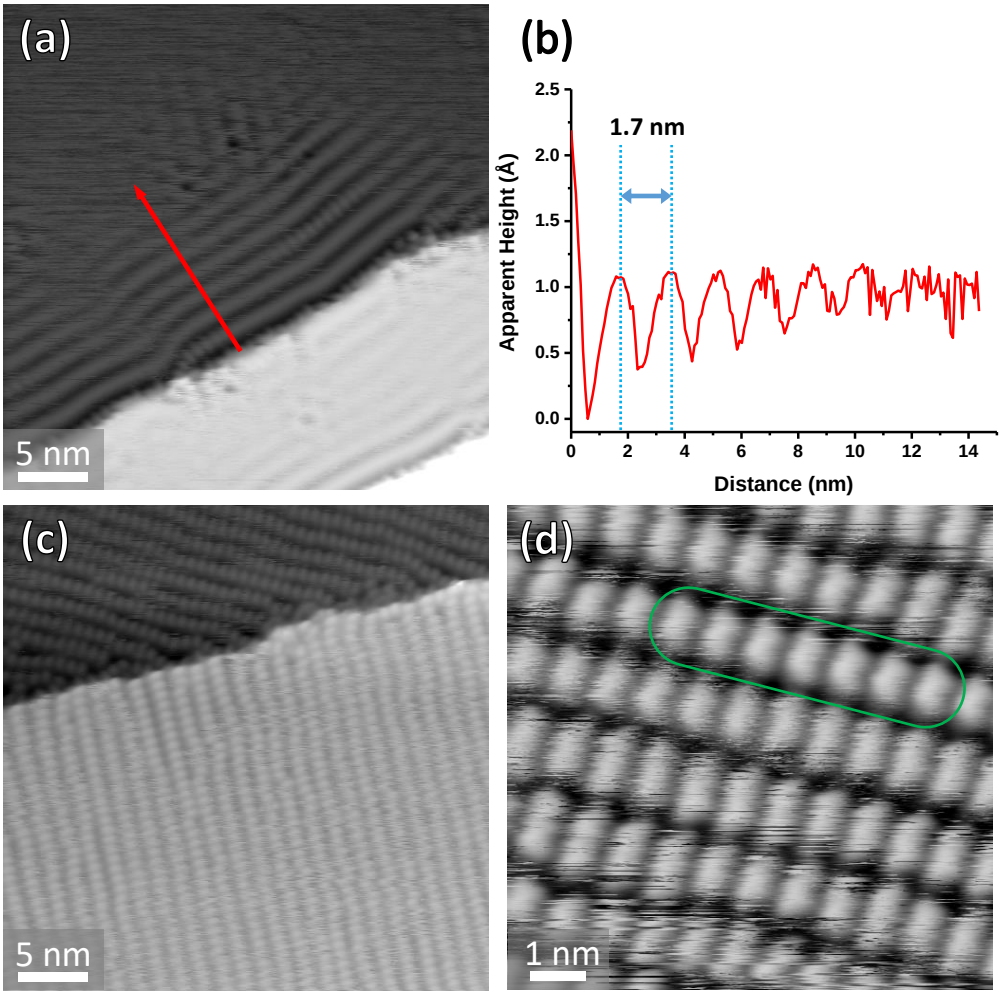

Figure 4.6. *(a) 77 K STM (2 V) of a low coverage of PXX on Cu(111). Ripples at steps and contaminants are observed. (b) Line profile of a set of ripples from (a), marked with a red arrow on the image. (c) STM image (2 V) of a higher coverage (close to 1ML) of PXX/Cu(111). (d) Zoom of the higher coverage, with a more stable row highlighted (2 V).*

Increasing the coverage via longer deposition times results in more stable ordered structures, as shown in **Fig. 4.7**. Initially a parallel row structure, similar to that shown in **Fig. 4.6**, is observed – with stability now both along the molecular rows and across them, and a unit cell with parameters **a** = 1.21 ± 0.05 nm, **b** = 0.84 ± 0.01 nm, θ = 87 ± 2°. Large ordered domains are formed, generally segregated by chirality. Increasing the coverage (**Figs. 4.7(c)** and **(d)**) even further causes the formation of a new type of packing with a larger unit cell (**a** = 1.26 ± 0.03 nm, **b** = 1.72 ± 0.02 nm, θ = 70 ± 2°) that consists of groups of four molecules arranged in an 'X' shape. Within these groups, a 50:50 racemic mixture of 'enantiomers' is generally observed, although with a large number of defects, as can be seen in larger scale images such as **Fig. 4.7(c)**.

The PXX molecules in this packing are held together by similar weak hydrogen bonds to those seen in the other assemblies.

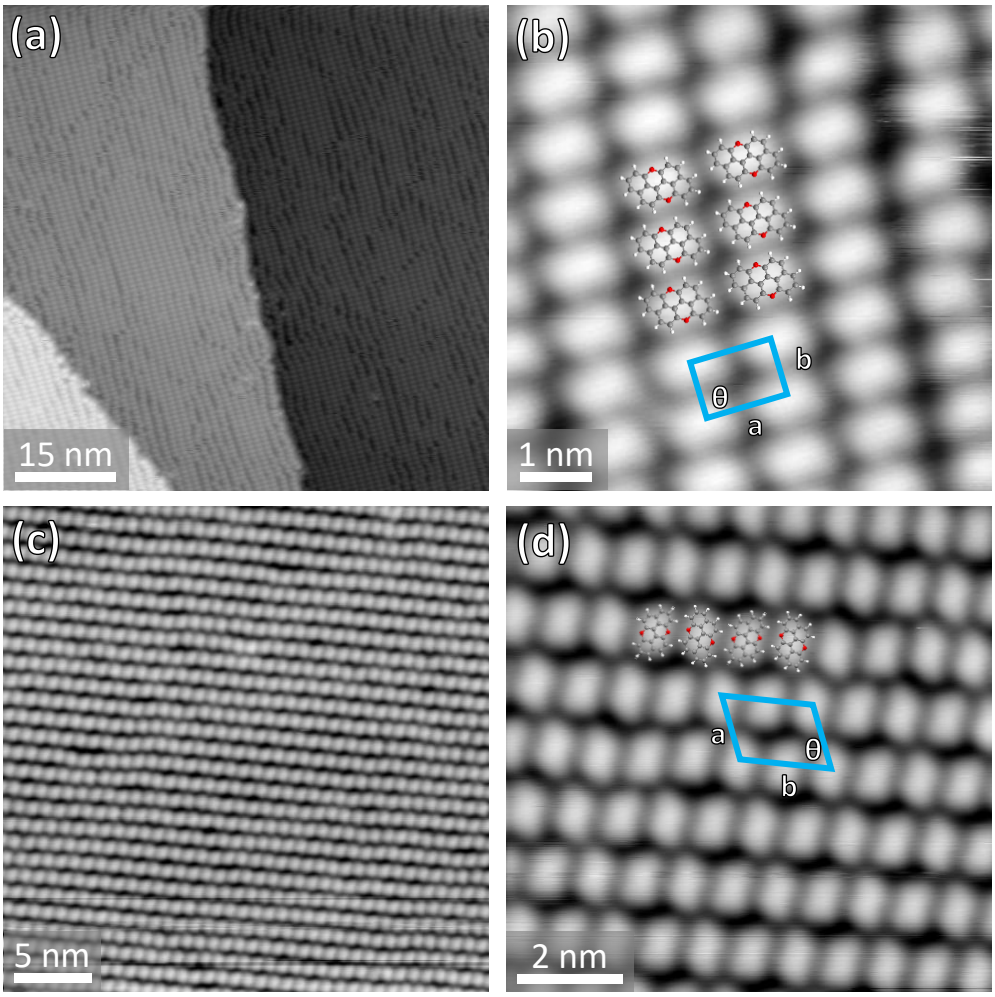

Figure 4.7. *(a) 77 K STM image (1.3 V) of an increased coverage of PXX on Cu(111). Ordered, stable islands are visible, with a zoom in (b) showing their internal structure (0.6 V). (c) and (d) Higher coverage phase of PXX on Cu(111), containing both on-surface 'enantiomers' of PXX. Bias voltages both 1.3 V.*

Cooling a sub-monolayer coverage on Cu(111) to 7 K again resulted in a high level of dispersion of the PXX molecules over the surface, as shown in **Fig. 4.8**. Interestingly, fewer hydrogen-bonded chains of molecules were observed when compared to the same coverage on Au(111), shown previously in **Fig. 4.2(a)**. This is perhaps indicative of an increased level of repulsive interactions present between PXX molecules on Cu(111). As the work function of Cu(111) is lower than Au(111), it is unlikely that this increased repulsive behaviour is a simple result of an increased level of simplistic (i.e. not involving significant levels of rehybridization) charge transfer between the

molecule and metal. It may, however, be that the molecule is more strongly bound to Cu(111) – as shown by its lower mobility at higher temperatures – and that this stronger binding is linked to some level of hybridisation between PXX and the underlying surface, resulting in a higher effective charge transfer than what would be expected from simply comparing work functions. The resulting dipole at the molecule-metal interface could in turn lead to greater levels of dipole-dipole repulsion between molecules on Cu(111), resulting in the more dispersed assembly. However, there appears to be somewhat of a contradiction in behaviour when comparing the assembly of PXX on Au(111) and Cu(111) at both temperatures. Despite the increased level of dispersion observed at low temperatures on Cu(111), there are more hints of self-assembled structures at 77 K than on Au(111) due to the lower mobility of the molecules. A notable depletion in molecular coverage was also observed on Cu(111) close to the upper part of steps in the surface, which could be a result of the changes in adsorption potential close to Cu(111) steps, with spatial oscillations in the LDOS of Cu(111) having previously been found to have greater modulations on the upper terraces of steps[134], along with effects on the adsorption of molecules[207]. This was not observed at 77 K, most probably due to the increased mobility of the molecules.

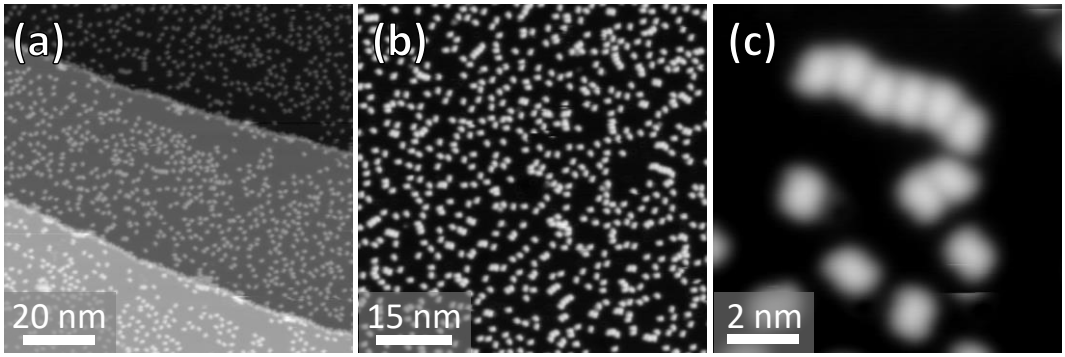

Figure 4.8. *(a) Large scale 7 K STM image (1.5 V) of PXX on Cu(111). Areas near the tops of steps are clearly less populated. (b) STM image (2.0 V) of a terrace showing the dispersion of PXX into single molecules and short rows. (c) Zoom (2.0 V) of an area containing a short row and separated PXX molecules.*

4.3 Conclusions

In this chapter, the deposition of unfunctionalized PXX on Au(111) and Cu(111) has been investigated. STM measurements at 77 K and 7 K revealed the assembly of PXX at sub-monolayer coverages on both substrates, showing the tendency of the molecule towards repulsive behaviour in both cases, with an increased level of dispersion

observed on Cu(111). Weak hydrogen bonding was found to hold together chains of molecules when stabilised at lower temperatures, with this extended to larger structures at monolayer coverages, as shown on Cu(111). Measurements with a CO tip of short H-bonded chains on Au(111) unambiguously revealed the structure of both the molecule and of the weakly H-bonded arrangement.

PXX was also characterised on Au(111) via dI/dV STS measurements. A strong resonance in the occupied states was observed, which could be assigned to the HOMO with a high level of confidence, due to the distinct shape that was observed in STM measurements when scanning at or below its voltage. With the HOMO well below the Fermi level, it is unlikely that there is any significant level of charge transfer between PXX and Au(111). Potential future work may lie in STS measurements and theoretical calculations of PXX adsorbed on Cu(111) to examine how this compares to Au(111) and to help explain the differences observed in STM imaging.

5 The Self-Assembly of Br_2PXX at Metallic Surfaces

5.1 Introduction

The modification of PXX via the addition of a halogen atom at each end of the molecule potentially allows for the formation of PXX polymers via the on-surface Ullmann reaction[74], combined with a dehydrogenation, as in the typical on-surface synthesis of graphene nanoribbons[97,208,209]. This reaction usually requires a post-deposition annealing of the surface in order to induce homolysis of the C-X bond, catalysed by the metallic surface. However, the halogen end-groups of the modified molecule also potentially allow the molecule to self-assemble in significantly different ways to the standard PXX molecule. The presence of peripheral oxygen atoms, hydrogen atoms, and Br atom end groups may result in the formation of self-assembled structures based on other interactions (not possible with PXX) such as halogen bonding, as well as allowing for hydrogen bonding between the end groups of one molecule (i.e. Br, H) and the side groups of another (O, H).

Halogen bonded assemblies are considerably less common but are increasingly being studied and seen as an important addition to the 'toolbox' of supramolecular assembly. Typically, iodine[55,210–212] and bromine[213–217] atoms are used in halogen bonding due to their larger size and polarisability, but there are also examples of chlorine[218] and fluorine[164,219] based assemblies that have some aspects of halogen bonding. Halogen bonds often involve halogen atoms acting simultaneously as both donor and acceptor[35,211,214,215,220], with the positive electrostatic potential of the sigma hole oriented towards the central 'belt' of negative electrostatic potential found on an adjacent halogen atom. Alternatively, nitrogen[55,210,212,217] and oxygen[215,221–223] groups may also act as acceptors.

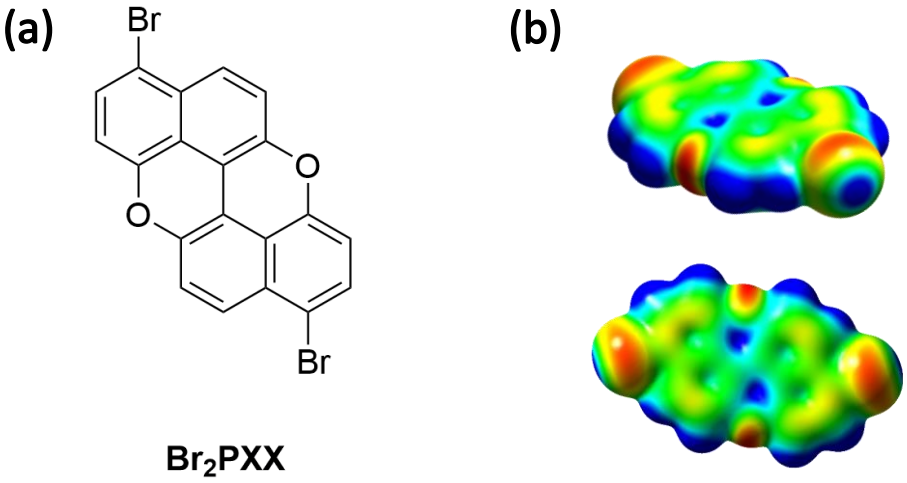

Figure 5.1. *(a) The chemical structure of Br_2PXX. (b) Electrostatic potential surface maps of Br_2PXX depicted in two different orientations. Blue: more positive, red: more negative. The sigma hole on the end of the Br (blue region) is clearly visible. Calculations performed by Harry Pinfold, University of Warwick.*

Our collaborators in the Bonifazi lab (Cardiff University) have synthesised a di-brominated form of PXX, named Br_2PXX (**Fig. 5.1(a)**). This molecule can be readily sublimed and adsorbed onto metal single crystal surfaces. DFT-calculated electrostatic potential maps (**Fig. 5.1(b)**) demonstrate its potential ability to form halogen bonded supramolecular self-assembled networks. A clear 'sigma hole' of positive electrostatic potential is located on the bromine atoms, which may interact with regions of negative electrostatic potential on other molecules, such as the oxygen or bromine atoms.

It is important to note that, despite extensive attempts by our collaborators to purify the Br_2PXX product, a high purity sample could not be obtained. In particular, PXX molecules with different numbers/positions of bromine atoms are formed as by-products of the synthesis, potentially leading to different assemblies when adsorbed on metal surfaces. The effects of these contaminants are shown throughout the results within this chapter.

In this chapter, the self-assembly of Br_2PXX after deposition at room temperature (and *prior* to annealing) is studied via STM. Both Au(111) and Cu(111) surfaces have been utilised, in order to examine the effects of substrate reactivity and adatom concentration on the self-assembly of the molecule. Au(111) is known to be more inert than Cu(111), and Cu adatoms are often found to play an important role in the assemblies of molecules on Cu(111)[32,122,224], especially when halogenated precursors are deposited on the substrate at room temperature or higher. Typically, these systems are found to form metal-organic structures on Cu(111) at room temperature after the substrate catalyses the homolysis of the C-Br bond(s) and the resulting radicals form bonds to Cu adatoms[35,98,122,124,190]. On the other hand, the same halogenated molecules are often found to remain intact on Au(111) after room temperature deposition[98,122].

Br_2PXX was sublimed at 483 K and deposited onto room temperature Au(111) and Cu(111), then scanned at low temperatures (77 K and 7 K) in the STM. Both standard STM and HR-STM have been used to determine the precise structure of the supramolecular assemblies observed. The electronic properties of the molecule were also measured via STS, including dI/dV spectroscopy and imaging, in order to form a comparison with PXX and examine the effects of halogenation on the electron donor strength of the molecule.

5.2 Results and Discussion

5.2.1 The Self-Assembly of Br_2PXX on Au(111)

At sub-monolayer coverages, three main types of self-assembled structure are observed after adsorption on Au(111) surface, as shown in **Fig. 5.2**. At lower coverages, a spiral-type assembly (**1**) and a more dense, semi-ordered assembly (**2**) dominate, both confined to the fcc regions of the herringbone. A similar behaviour has been documented with other molecular systems on Au(111) in the literature[76,128], and this preference can be attributed to a deeper adsorption potential in these sites than the hcp areas of the herringbone. At 77 K, significant molecular mobility is observed, with the peripheries of islands varying between scans. Combined with the lack of herringbone distortion observed, we attribute this mobility to the molecule being weakly bound to the surface. Increasing the coverage (but still in the sub-monolayer regime) leads to the formation of island structures that are no longer confined to just

the fcc regions of the surface (**3**). The structure of each of these assemblies is described in the following section.

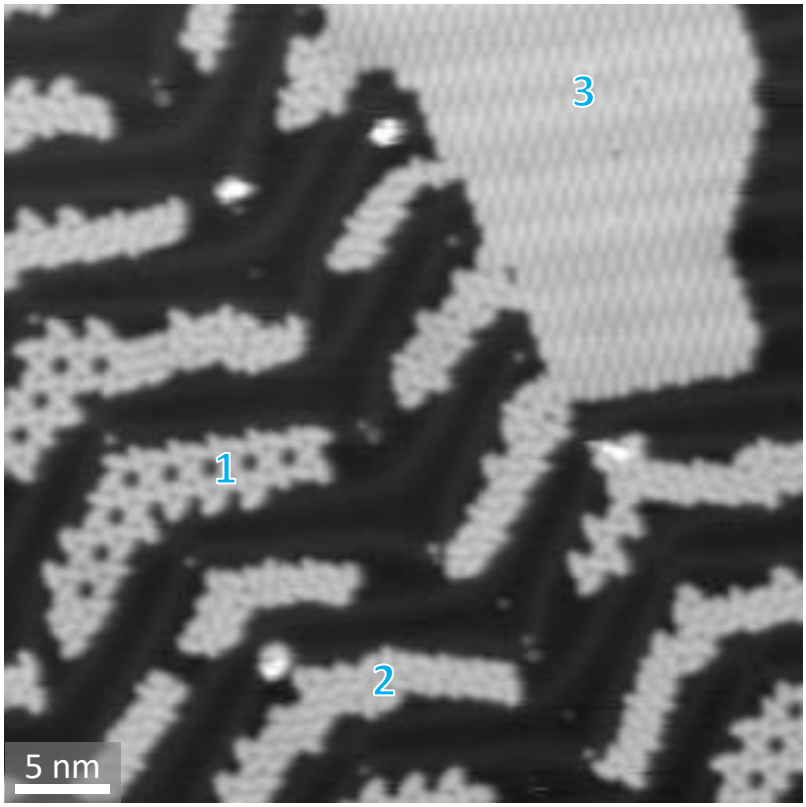

Figure 5.2. *7 K STM image (1.1 V) of the three main varieties of assembly observed with sub-monolayer coverages of Br_2PXX. Island packing 3 is only observed when increasing the coverage beyond approximately 0.5 ML.*

Structure 1: Spirals

Two different orientations of the spiral structures can be found when it is adsorbed on the surface; as the molecule is pro-chiral, with two orientations after adsorption, these are expected to be segregated chiral domains (**Fig. 5.3**). The spiral structures themselves are made up of triangular sub-units consisting of three molecules, each appearing to be bound via the end of one molecule pointing to the side groups of the other. This indicates that the molecular end groups are bound in some way to the oxygen side groups, though the nature of this interaction is not immediately clear, as is seen below in **Fig. 5.4**. The spirals can be classified as a chiral kagome lattice, similar to other systems seen in the literature[225,226]. The triangular sub-units are packed into a hexagonal unit cell with a lattice vector of **a** = **b** = 2.2 ± 0.1 nm, and an angle of 60 ± 2°. Full unit cells are rarely found due to the confinement of the assembly in the fcc regions of the herringbone reconstruction. When scanning low coverages of the

molecule at 77 K, the spiral structures cannot be easily imaged with a negative bias voltage, as they often disappear, leaving an apparently bare surface (data not shown). This may be related to some repulsion felt between the tip and the molecules that is only manifested at negative voltages. The same effect is not seen at 7 K when the molecules are more immobilised, as they presumably do not have enough energy to 'escape' the effect of the tip.

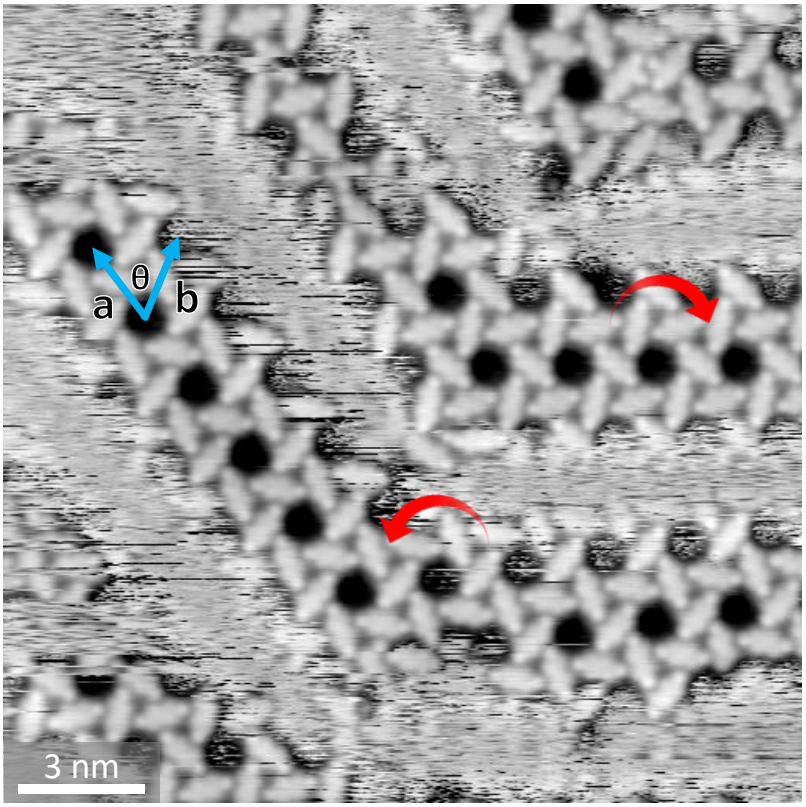

Figure 5.3. *STM image of the Br_2PXX spiral packing recorded at 77 K (1.3 V). The rhombic unit cell is indicated with vectors a and b, acute angle θ. Spirals of both orientations are indicated with curled arrows.*

Initial modelling of the spirals by overlaying molecular models onto the STM images results in two distinct possibilities for the type of intermolecular interaction that governs the assembly. The unit cell dimensions and possible orientations of the molecule allow for either halogen bonding between the Br end groups and the O side groups of adjacent molecules, or two non-classical hydrogen bonds (Br---H and O---H) (**Fig. 5.4**). The relatively featureless appearance of the molecules in typical STM tunnelling conditions does not present an obvious solution to this, even when varying the bias voltage. In this case, the position of the molecular groups (and thus the type of assembly) cannot be directly inferred from standard STM techniques. As may be

seen later, some intra-molecular features can be observed when at a negative voltage, but the majority of the time they cannot be easily correlated to the appearance of the occupied states of the molecule (and thus its orientation) due to either a lack of resolution or the character of the tip (e.g. with CO, see **Chapter 6**). Theoretical calculations provide a potential way of resolving this issue.

Our collaborator at the University of Warwick (Dr. Gabriele Sosso) performed density functional theory (DFT) calculations on free standing monolayers of both types of assemblies. DFT calculations were performed using the mixed Gaussian and Plane-Waves (GPW) method implemented in the CP2K package[227]. Two different fully self-consistent non-local exchange-correlation functionals (vdW-DF[228] and optB88-vdW[229]) were used to assess the reliability of the results. A single unit cell (in-plane dimensions of ~20 Å and containing three Br2PXX molecules, thus totalling 96 atoms), together with a vacuum region of ~20 Å inserted between the periodic replica of the 2D self-assemblies was found to be sufficient to ensure a high level of accuracy.

As the molecules appeared to be weakly adsorbed on the relatively inert Au(111) surface, and since the commensurability of the molecular adlayer could not be determined purely from STM measurements, the calculations were performed on free-standing monolayers, taken as reasonable theoretical approximations of the experimental structure. The molecular unit cells were optimised from initial conditions taken from the experimentally determined values, but for both assemblies remained within the experimental error after optimisation (see **table 5.1** summarising the differences calculated). The difference in energy between the halogen bonded and hydrogen bonded assemblies was also found to be rather small, with the halogen bonded assembly slightly favoured (0.82 meV/atom lower than the hydrogen bonded assembly). Calculations were also performed on dimers of halogen and hydrogen-bonded molecules as a function of the Br---O and O---H distances, respectively (**Fig. 5.5**). The halogen bonded dimer is characterised by a slightly larger (0.1 Å) equilibrium distance and is found to be more stable by 25 meV. Whilst these results point towards the halogen bonded assembly being marginally more likely to form, it would also be expected that, due to the small energy differences relative to the thermal energy available to the molecules at room temperature (the temperature at which these

molecules are deposited on Au(111)), there would still be a coexistence of both types of assembly present on the surface, with a ratio determined by the corresponding Boltzmann factor. However, STM experiments did not resolve two different types of the kagome spirals and thus, even in conjunction with DFT calculations, were unable to unambiguously identify the intermolecular bonding mode.

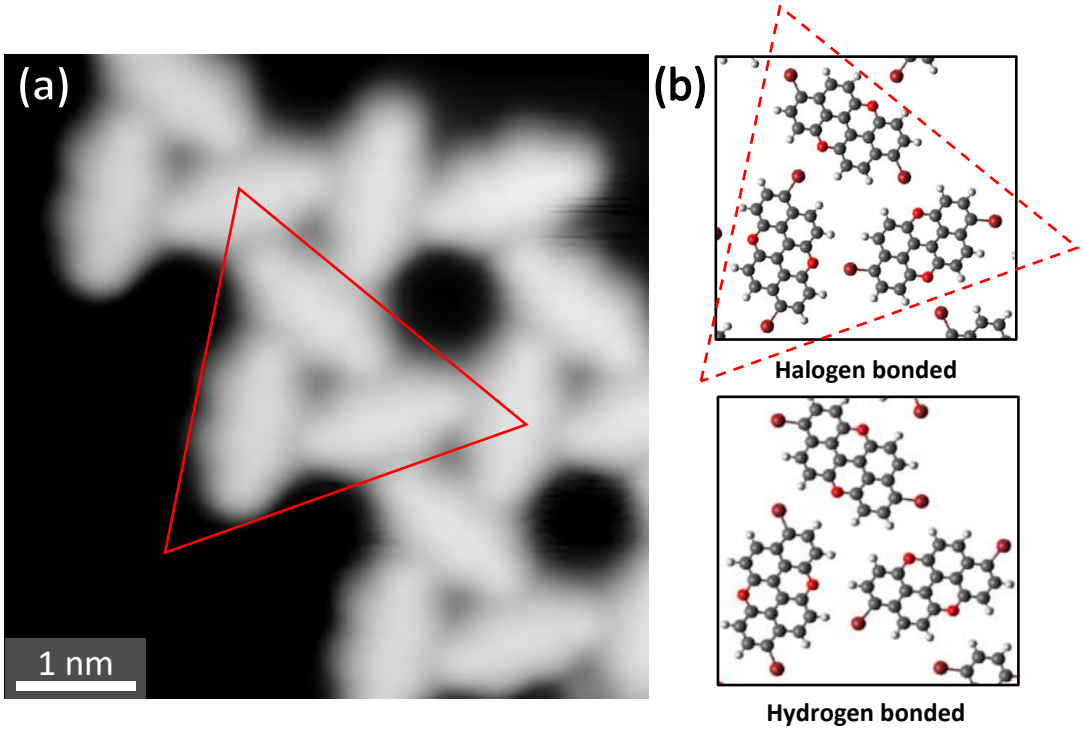

Figure 5.4. *(a) STM image (7 K, 0.5 V) of the spiral packing. Red triangle overlay around a group of three molecules, as indicated in (b). (b) Two proposed models for the spiral assembly, based around either halogen or hydrogen bonding. It is not clear from standard STM imaging which of these is the thermodynamically more stable assembly.*

ΔE (Halo.-Hyd.) (exp.) /meV/atom	ΔE (Halo.-Hyd.) (opt) /meV/atom	Halo. Unit cell dimensions /Å	Hyd. Unit cell dimensions /Å	Halo.B (O---Br distance) /Å	Hyd.B (O---H) distance /Å
−3.83	−0.82	22.67, 22.61	22.12, 22.27	3.235	3.205

Table 5.1. *Comparison between the energies and bonding dimensions of the geometry optimised DFT calculated assemblies for both halogen and hydrogen bonding. Similar energies and dimensions were found for the optimised structures of both halogen and hydrogen bonded assemblies. The underlying surface was not accounted for in these calculations as the commensurability of the molecular adlayer could not be ascertained purely from STM measurements. Calculations performed by Dr. Gabriele Sosso, University of Warwick.*

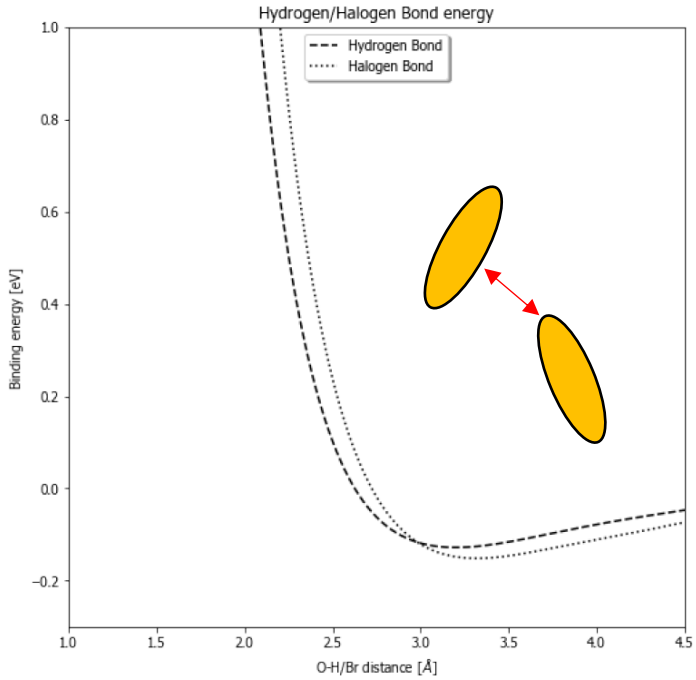

Figure 5.5. *Calculated bond energies for dimers bound via halogen or hydrogen bonding, plotted against the distance between the end and side groups. A slightly lower energy is calculated for the halogen bonded dimer. Calculations performed by Dr. Gabriele Sosso, University of Warwick.*

In order to settle this question, high resolution scanning tunnelling microscopy (HR-STM) measurements were undertaken at 7 K with a CO tip. After deposition and pick-up of CO on the Au(111) surface at low temperature (for more information, see the experimental section of this thesis, **Chapter 2**), constant height measurements at a low bias voltage (typically in the range ± 40 mV) were performed. As was reported in previous HR-STM experiments and theoretical studies[167], intramolecular features are clearly resolved when approaching the CO tip close to adsorbed molecules (**Fig. 5.6**). These features are not observed with a 'stiff' metallic tip. The rings of the molecule (in particular, the naphthalene aromatic sections) are resolved, as are the positions of the C-Br end groups. All examples of the kagome spiral packing studied via HR-STM were unambiguously determined to be governed by halogen bonding. No examples of hydrogen bonded assemblies could be found, further demonstrating that the Br_2PXX spirals on Au(111) consist of only one type of intermolecular bond. We attribute differences between this result and those of the DFT calculations to the effects of the underlying surface on the self-assembled structures that free-standing monolayer DFT calculations cannot consider. Overlaying molecular models onto HR-STM images for more precise measurements gives an estimated Br---O halogen bonding distance of

3.1 ± 0.1 Å. This value is slightly lower than that predicted by the DFT calculations (3.24 Å), possibly also due to the effects of the substrate. It is worth noting that the sharp dark features observed between the bromine and oxygen atoms cannot be simply assigned to 'imaging' the halogen bond, as it has been demonstrated that such intermolecular features can be attributed to the relaxation of the flexible CO probe[166,167]. A contrast in tunnelling current between the central rings and the naphthalene sections is also evident – this may be related to some combination of the LDOS at this voltage and interactions between the CO tip and the underlying molecules. As shown in **Fig. 5.7**, acquiring HR-STM images at slightly different heights also leads to differences in the observed distortion of the molecular structure due to the changes in forces felt by the CO tip.

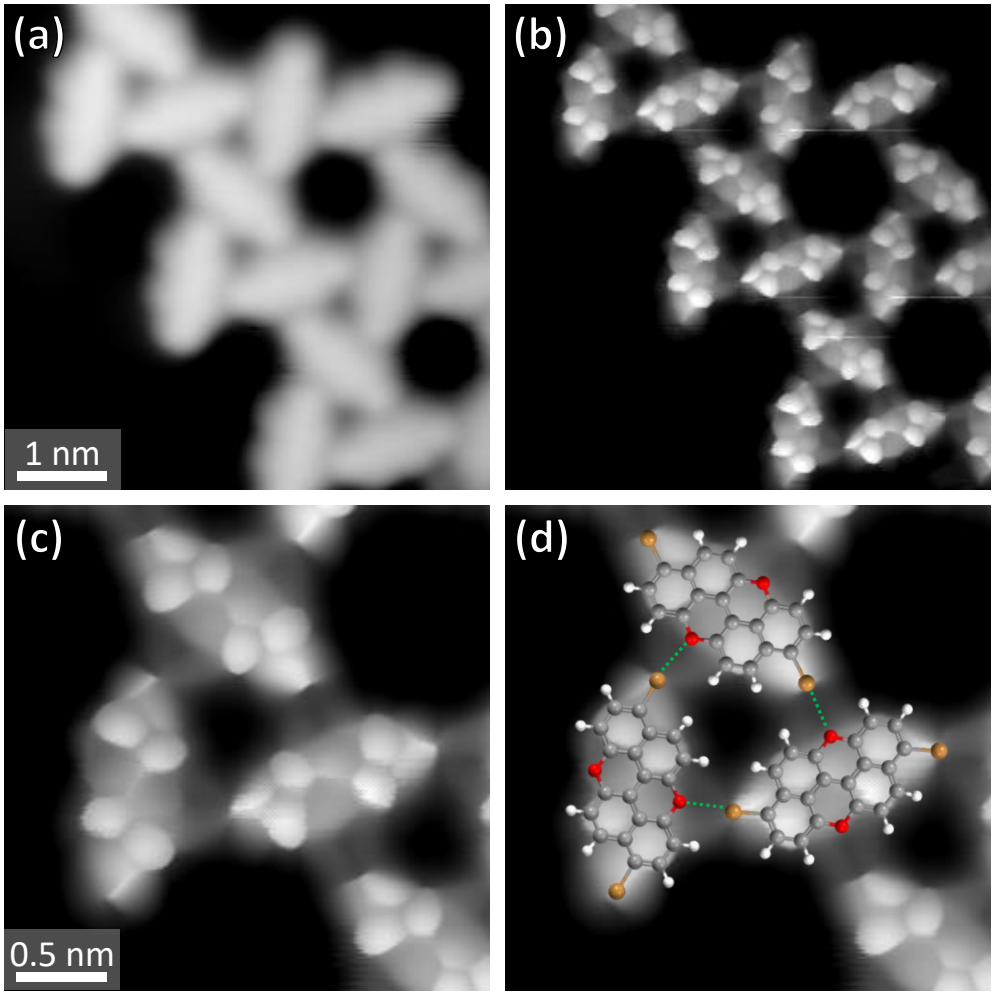

Figure 5.6. *(a) Constant current STM of the spiral packing, as shown in Fig. 5.4 (CO tip, 7 K, 0.5 V). (b) The same area in constant height mode with the CO tip close to the molecules (7 K, 30 mV). (c) Zoom of the area shown in (b), also constant height (30 mV), CO tip. (d) Br_2PXX molecular overlay of (c), clearly showing the halogen bonded assembly. All spirals studied by this method were halogen bonded.*

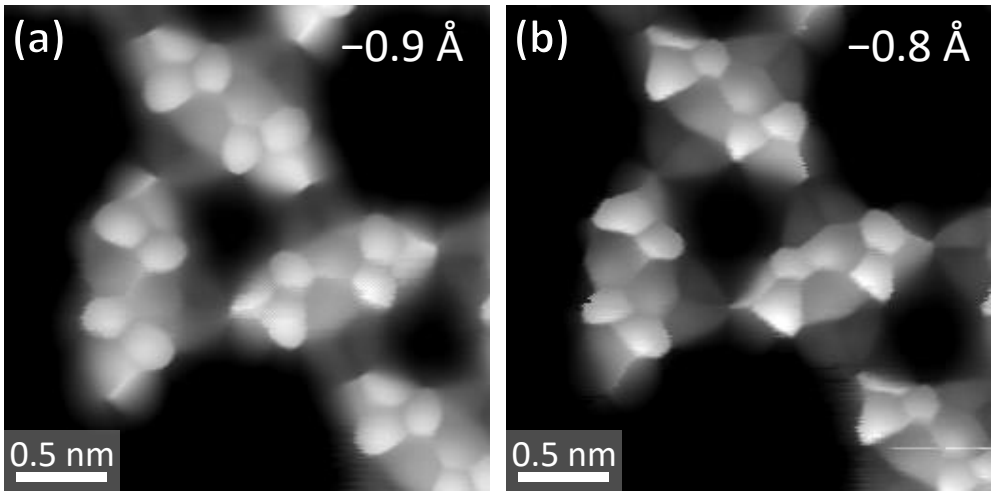

Figure 5.7. *Comparison showing the differences in the levels of distortion and sharpness observed with different stabilisation heights for CO tip HR-STM imaging of Br_2PXX (30 mV). In (b) the tip is less retracted from the initial position that is determined by the stabilisation parameters and is thus closer to the molecules, leading to greater levels of distortion due to stronger interactions between the CO and underlying molecules.*

Structure 2: Dense/disordered packing

Packing **2**, also only present in the fcc regions of the herringbone (**Fig. 5.8**), was initially thought to be a self-assembled mixture of intact molecules, Br atoms (that had dissociated upon adsorption from molecules), and fragmented molecules. However, as stated above, it is not usually the case that halogenated molecules dissociate upon adsorption on Au(111) at room temperature.

When studying these regions with HR-STM (CO tip), the nature of these structures, not clear from standard STM imaging, becomes apparent. Packing **2** consists of a mixture of molecules with either a bromine end group shifted over by one position onto an adjacent carbon or an extra bromine atom bound onto a side position. Interestingly, no examples of molecules (in a sample of several hundred) with both of these changes could be found. Fitting a scaled model of these molecules, as shown in **Fig. 5.8(d)**, demonstrates that a Br bound directly to the molecule, with a bond length of approximately 1.9 Å, provides a better fit than with a 'free' Br atom bound to the metal. The presence of a distinct line feature corresponding to the C-Br bond in HR-STM imaging and the required proximity of the Br atom also adds weight to this interpretation; when molecules are assembled with 'free' Br atoms on a surface, the Br atoms are commonly imaged in HR-STM as a distinct separate signal, considerably further away from the molecules (see **Chapters 6, 7** and **8** for several examples of

this). As mentioned previously, the presence of these molecules relates to issues with the purity of the synthesised product that could not be overcome.

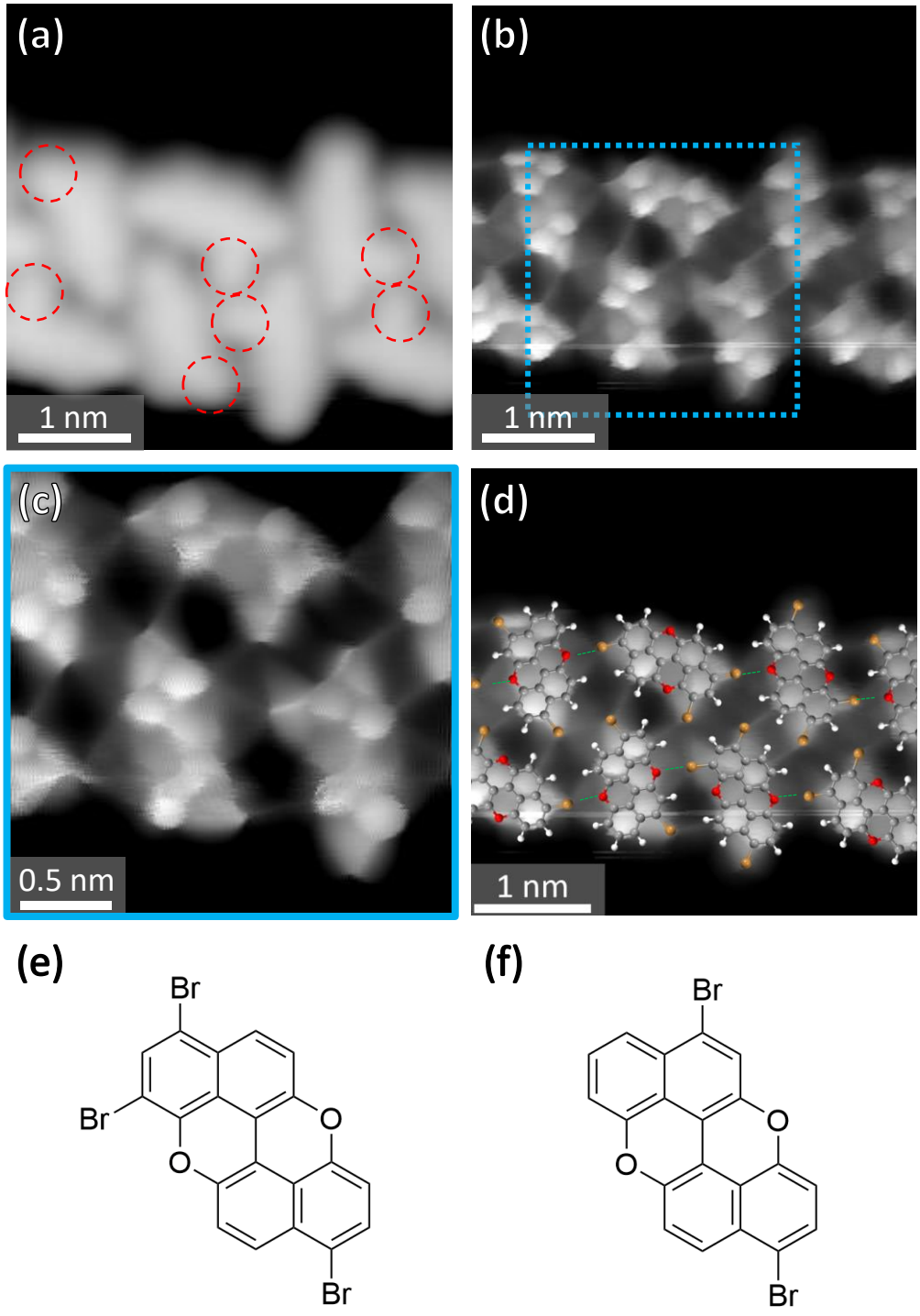

Figure 5.8. *(a) Constant current STM (CO tip) of an area of packing 2. Objects on the sides of molecules are indicated with red circles (7 K, 1.1 V). (b) Constant height (CO tip) HR-STM of the same region as (a) in the repulsive regime (−30 mV). (c) Zoom of highlighted area (30 mV) in (b) showing distinct features on the sides and ends of molecules corresponding to Br bound to the wrong carbon atoms – image has been low-pass FFT filtered to remove electronic noise. (d) Overlay of (b) showing the fit of contaminant molecules with the structure, with Br---O halogen bonds indicated. (e) and (f) Structures of the contaminant molecules.*

As with packing **1**, halogen bonding is again possibly one of the main driving forces behind the assembly in packing **2**. The extra Br atom found on the side of some defect molecules can be seen forming halogen bonds with adjacent molecules (**Fig. 5.8(d)**). Weaker hydrogen bonds may also play a role in the assembly.

Unlike packing **1**, packing **2** is notably found to rarely show signs of forming a fully ordered structure; in most 'islands', few examples of regular repetition of molecular features were observed. The reason for this may lie in the size of the unit cell of the fully ordered structure; the confines of the fcc region of the herringbone rarely allow for a full unit cell to be observed due to its size. As such, fragments of the ordered structure are found packed together within the fcc regions of the surface. At higher coverages, small hexagonally-packed islands of just the tri-brominated molecules are rarely found in elbow sites of the herringbone (**Fig. 5.9**), with a hexagonal unit cell of approximately **a** = **b** ≈ 3.1 nm, θ ≈ 60°. Few examples of this packing were found, and as such, reliable statistics for the unit cell dimensions could not be ascertained.

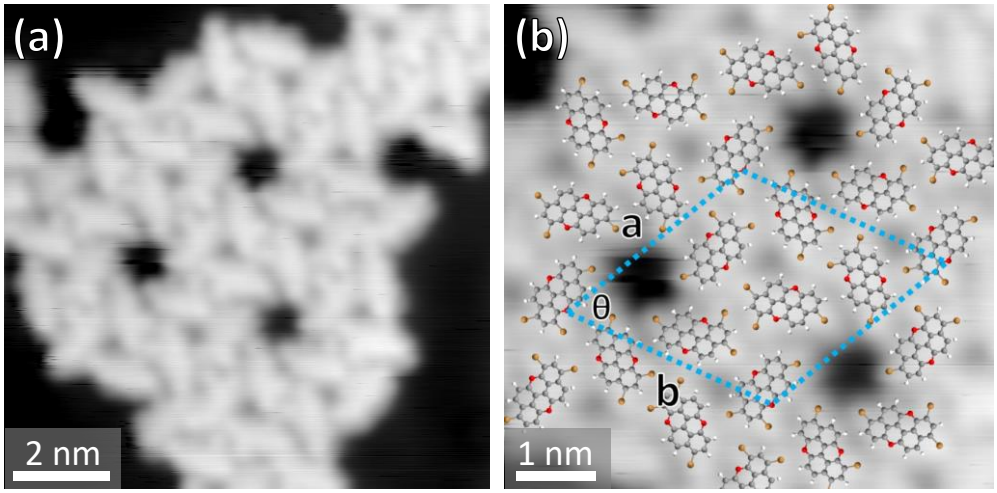

Figure 5.9. *(a) STM image (7 K, 0.6 V) of an elbow site in the herringbone construction with an assembly consisting of tri-brominated molecules, with other molecules as peripheral defects. (b) Zoom of (a), showing the unit cell of the assembly and a molecular overlay.*

Structure 3: Island packing

Increasing the coverage of Br_2PXX to around 0.5 ML and above results in the formation of extended island structures (**Fig. 5.10**). Molecules within these islands are packed into parallel rows with a unit cell of **a** = 0.83 ± 0.02 nm, **b** = 1.31 ± 0.06 nm, **θ** = 75 ± 3°. As the orientation of the molecules is again not clear from standard STM imaging, HR-STM was used to elucidate the structure of the islands. As is shown in

Fig. 5.10(b), molecules are found arranged with weak hydrogen bonds between the O and H atoms of adjacent molecules (similar to that seen with unfunctionalised PXX in **Chapter 4**), along with the 'type I' form of halogen bonding[40] between the C-Br bonds of molecules with their end groups directed towards each other. The modelled O---H distance was found to be similar to that measured with PXX in **Chapter 4** (2.2 ± 0.1 Å), and the Br---Br distance was also modelled as 3.6 ± 0.2 Å. This distance is comparable to that found in other examples of this type of Br---Br halogen bond in the literature[230].

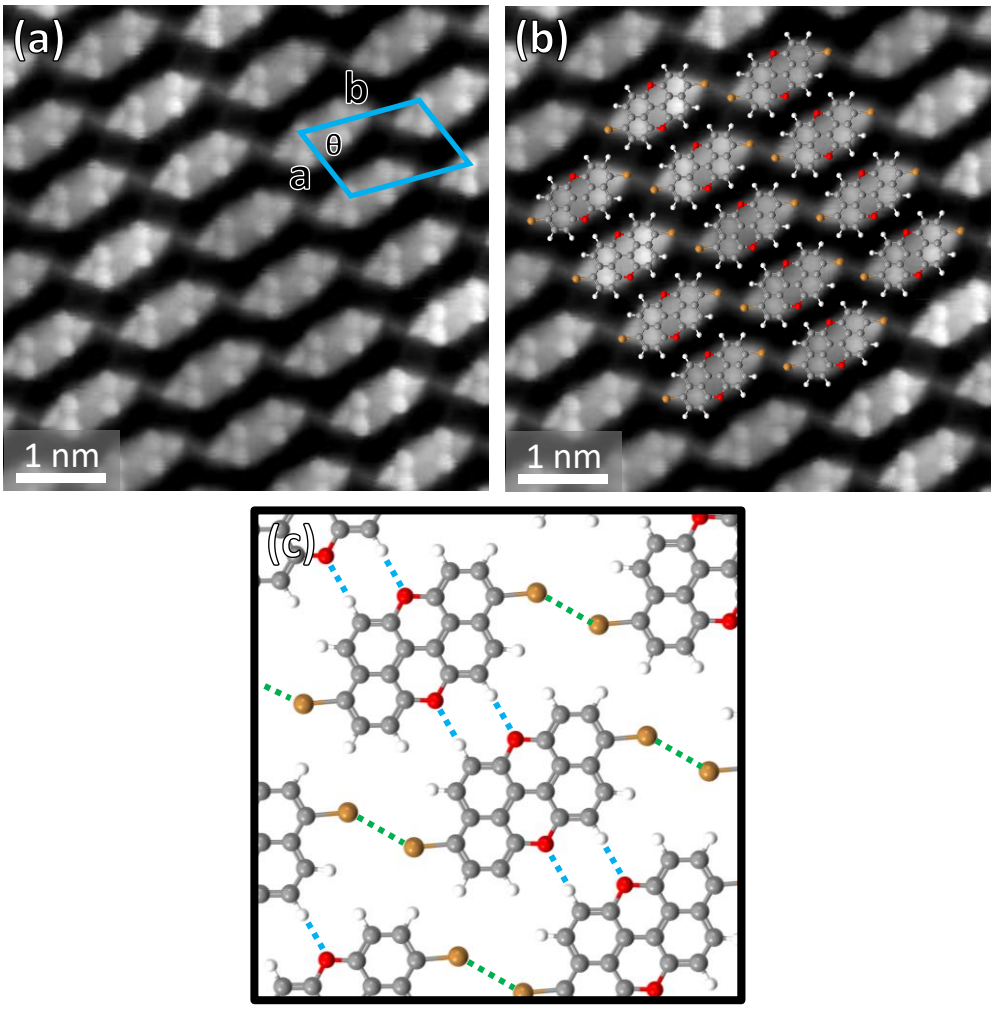

Figure 5.10. *CO-tip constant height STM image (30 mV) of the high coverage island packing, with molecular overlay in (b). (c) Model of the packing. Molecules interact via hydrogen bonding (blue dashed line, O---H distance of 2.2 ± 0.1 Å) and type I halogen bonding (green dashed line, Br---Br distance 3.6 ± 0.2 Å)*

HR-STM experiments also reveal the presence of defects within these islands. Both types of defective molecules found in packing **2** are observed within the islands **(Fig.**

5.11), as are molecules that have been singly de-brominated, often found at the peripheries. It is unclear as to whether these molecules are de-brominated upon adsorption, or if they are unwanted synthesis products. XPS results for the as-deposited molecule, (shown later, in **Chapter 6**) do not reveal any significant amounts of de-bromination upon adsorption at room temperature, and few objects that can be identified as 'free' Br atoms are ever observed.

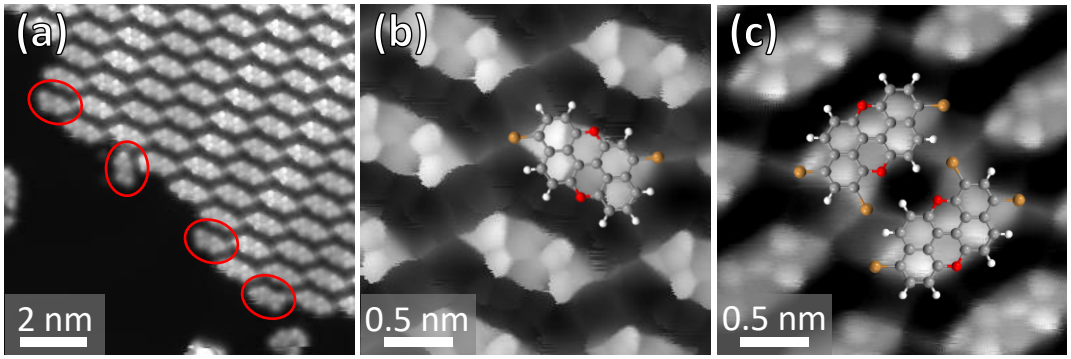

Figure 5.11. *Constant height CO tip images (all 30 mV) of defect molecules found in and around the island packing. (a) Singly de-brominated molecules at the edge of an island. (b) A defect molecule found within an island with a Br on the wrong position. (c) Two adjacent tri-brominated molecules found within an island.*

5.2.2 Electronic Properties of Br_2PXX on Au(111)

STS measurements were also performed on Br_2PXX molecules in order to determine the effect bromination has on its donor strength. As this strength can be related to the position of the molecule's HOMO in energy (i.e., a stronger donor has a HOMO that is higher lying in energy), this can be revealed using dI/dV spectroscopic measurements by examining energetic shifts in the highest occupied state that occur with bromination. Recording the current or dI/dV signal at a certain voltage whilst scanning at a constant height also allows the direct visualisation of states localised on molecules (the current signal is sufficient for this if there are no other states between the voltage used and the Fermi level). If molecules are relatively uncoupled from surfaces, the appearance of these states can fit well (assuming sufficient resolution) with molecular orbitals seen in gas phase DFT calculations[172,231,232].

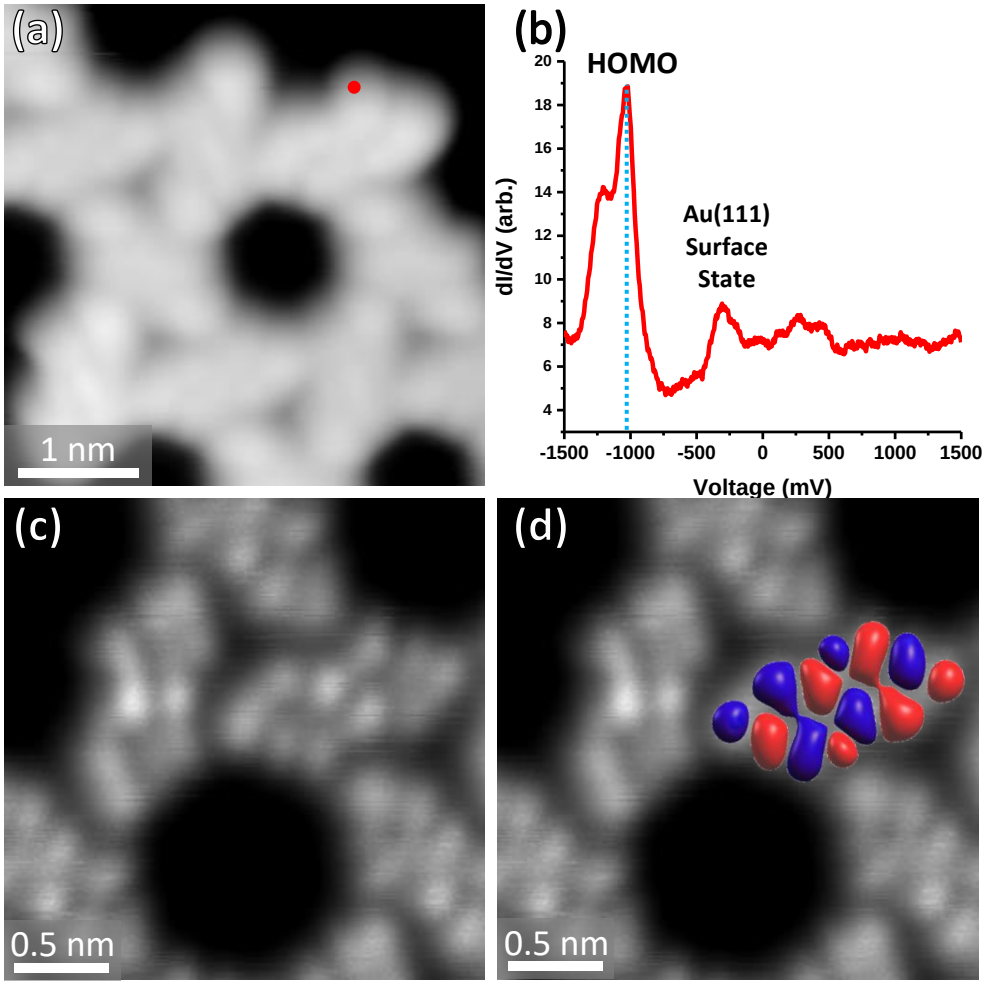

Figure 5.12. *(a) and (b) STM image (−1.1 V) and corresponding dI/dV spectrum (recorded in the position of the red dot) of Br_2PXX, showing an occupied state at approximately −1060 mV that corresponds to the HOMO of the molecule. (c) and (d) Constant height STM image (−1.1 V) of Br_2PXX, with a scaled overlay of the DFT-calculated gas-phase HOMO (DFT performed by Harry Pinfold, University of Warwick).*

A peak in the occupied states between −1.0 and −1.1 V is observed over intact Br_2PXX molecules (**Fig. 5.12**), most probably corresponding to the HOMO state of the molecule. This demonstrates a shift of approximately −0.2 V when compared to PXX. This is consistent with the shift seen in DFT calculations of the energies of the frontier molecular orbitals for PXX and Br_2PXX: a downshift of approximately −0.3 eV of the HOMO upon addition of Br, with a corresponding rigid downshift of the LUMO. Whilst the absolute values of the STS results and DFT cannot be compared, the presence of a shift in both is still notable.

Small variations of the position of HOMO peak (within a range of 100 mV) can be found within molecules packed in the same island. Although the spiral islands are

confined within the fcc region of the herringbone, there may be small shifts in surface potential across this region that are responsible for the observed range in peak position. Constant height images recorded at −1060 mV (**Fig. 5.12(c)**) show a distinct shape resembling the gas phase DFT-calculated HOMO of the molecule. The tip termination at the time of these measurements was unknown. Performing these measurements instead with a CO tip may allow for a high spatial resolution of the localisation of the state. However, this can also result in differences observed when comparing to DFT calculated molecular orbitals, due to the p-wave nature of CO tips. This means that bright features may be detected where nodes are expected[174]. These differences in contrast are discussed further in **Chapter 6**.

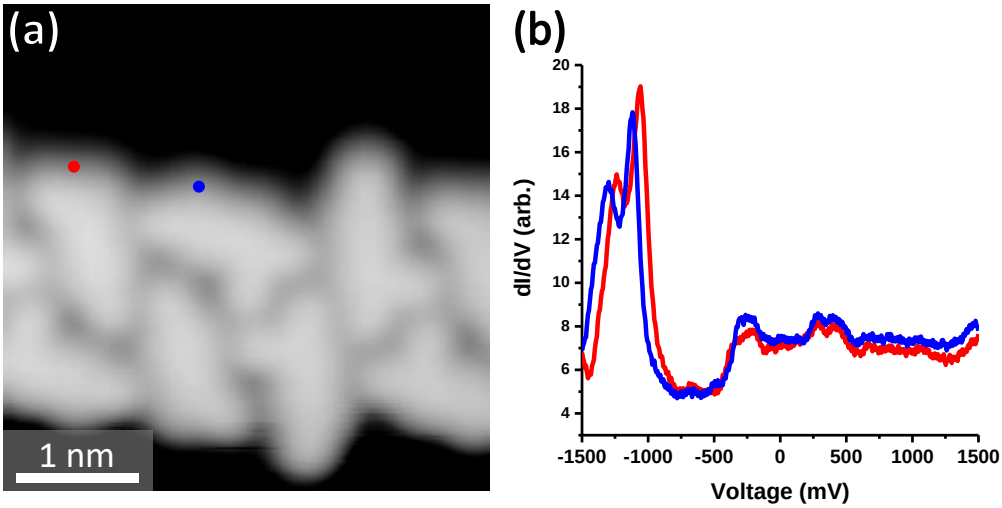

Figure 5.13. *7 K STM image (1.1 V) and dI/dV spectra recorded over a molecule with the Br shifted to the wrong position (red) and a tri-brominated molecule (blue). A shift of approximately −60 mV was observed with the addition of the third bromine. Spectra have been smoothed to remove electronic noise.*

Shifting of the HOMO peak is also observed when recording dI/dV spectra of contaminant molecules with an extra bromine atom. The peak is shifted by approximately a further −60 mV on molecules with a third bromine atom attached (**Fig. 5.13**). No significant difference in dI/dV peak position between normal Br_2PXX molecules and those with the Br shifted over by one position (e.g. the red spectrum in **Fig. 5.13(b)**) is observed. De-brominated molecules also exhibit a shift in the highest occupied peak to higher (more positive) energies. Spectra taken before and after debromination via the STM tip (occurred during dI/dV acquisition, +2 V to −2.5 V

sweep, **Fig. 5.14**), clearly show a significant shift of approximately +200 mV of the HOMO state upon removal of one bromine atom. As locally adsorbed bromine can result in rigid shifts of molecular peaks in dI/dV spectra, this value may not be a precise indication of the actual HOMO shift of the molecule upon de-bromination. The radical nature of the de-brominated end group may also affect the observed dI/dV peak position. Similar shifts have been seen previously with the tip-induced dehalogenation of a porphyrin on Ag(111), but were not assigned to a pure shift in the HOMO, but rather different orbitals becoming visible in the dI/dV spectra[233]. However, not all experimental results in that study (in particular, the position of the HOMO of the intact molecule) were fully compatible with theoretical calculations.

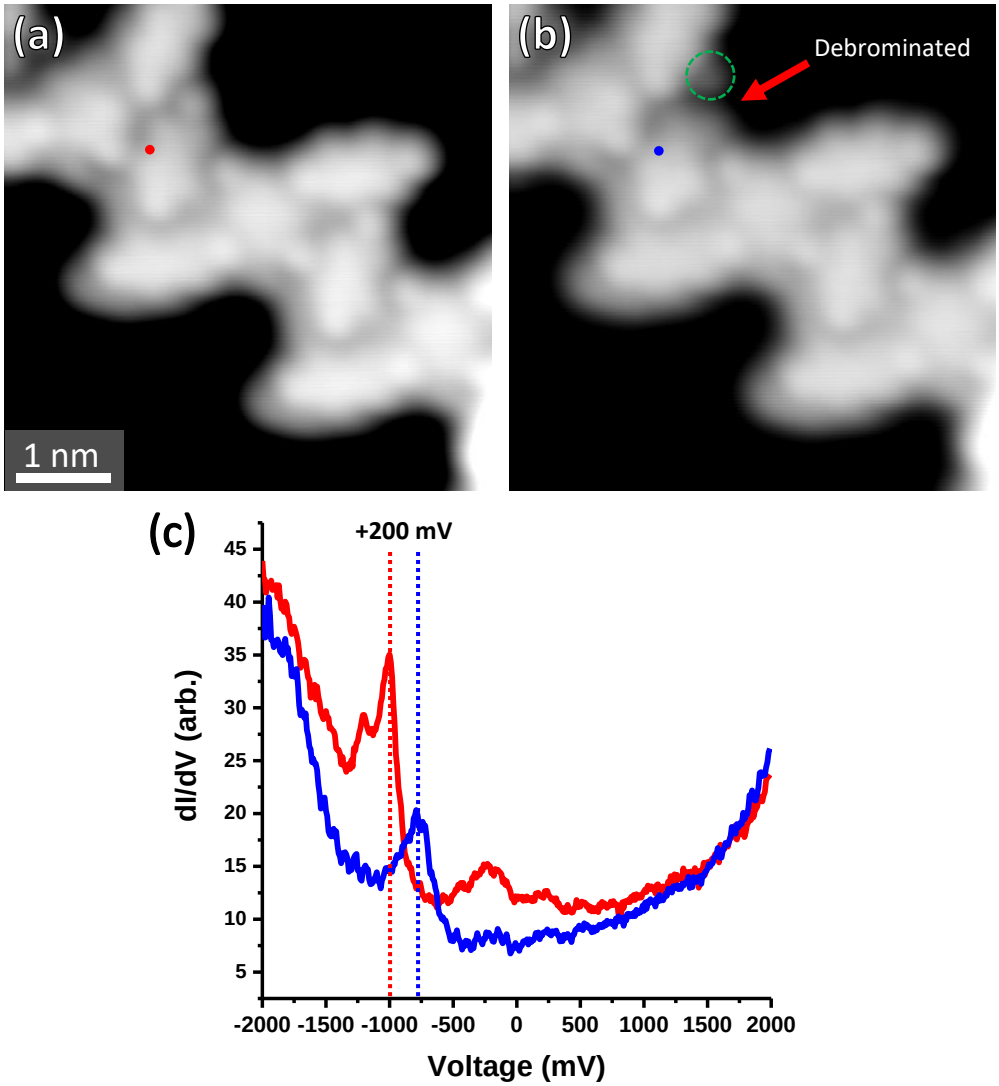

Figure 5.14. *(a) 7 K STM image (1.0 V) of Br_2PXX spirals prior to debromination of a single molecule. (b) Image (0.8 V) acquired after a series of spectra were recorded close to the C-Br bond, showing the clear separation of Br (green) from the molecule. (c) Spectra recorded before and after debromination on the same part of the molecule, with a clear +200 mV shift in the HOMO peak after debromination.*

5.2.3 The Self-Assembly of Br_2PXX on Cu(111)

Deposition of a sub-monolayer coverage of Br_2PXX on the more reactive Cu(111) surface at room temperature yields a significantly different (although not unexpected) result. Chains following the underlying three main crystallographic orientations of the substrate are observed (**Fig. 5.15(a)**). Clusters of small objects are found adjacent to the chains, along with dark regions (imaged as depressions in the surface) that are generally seen in-between groups of chains at higher coverages. These observations lead to the conclusion that the molecules most probably de-brominate upon adsorption on Cu(111) at room temperature and form metal-organic chains with Cu(111) adatoms, with bromine atoms clustered nearby. Similar dark islands observed after a metal-organic chain formation that resulted from the debromination of molecules have previously been attributed to holes (measured approximately 2 Å deep) in the Cu(111) surface, resulting from the extraction of Cu atoms from the upper layer of the terrace for the formation of metal-organic chains[234]. The measured apparent depth of the dark features is found to vary in the Br_2PXX system (from 0.5 – 1.7 Å), possibly due to their small size and the effects of the lateral width of the tip (i.e. the tip does not 'fit' into the hole and cannot measure its true depth). As a result, a simple comparison to the step height of Cu(111) (2.08 Å) cannot be easily made in this case. No clear internal structure of these dark objects could be resolved, and thus no solid conclusion about their identity can be made. Experiments at a higher coverage that may result in larger dark patches could resolve this issue.

Imaging the chains in standard STM conditions (**Fig. 5.15(b)**) generally does not reveal any distinct molecular features that can help with assigning the position/rotation of the molecule more precisely. Furthermore, within the chains there are clearly changes in orientation of the molecule that lead to small kinks/bends, most probably due to both possible conformations of the molecule (as Br_2PXX is pro-chiral) participating in the same chains, rather than segregating into separate chains. This may suggest that there is some flexibility in the allowed positions of the Cu adatoms between molecules, but that these defects cannot be extended significantly due to a loss of registry with the surface (i.e. it no longer becomes favourable in terms of bond-length and surface registry). Generally, bends in chains simply redirect them by 120° towards another high-symmetry substrate direction.

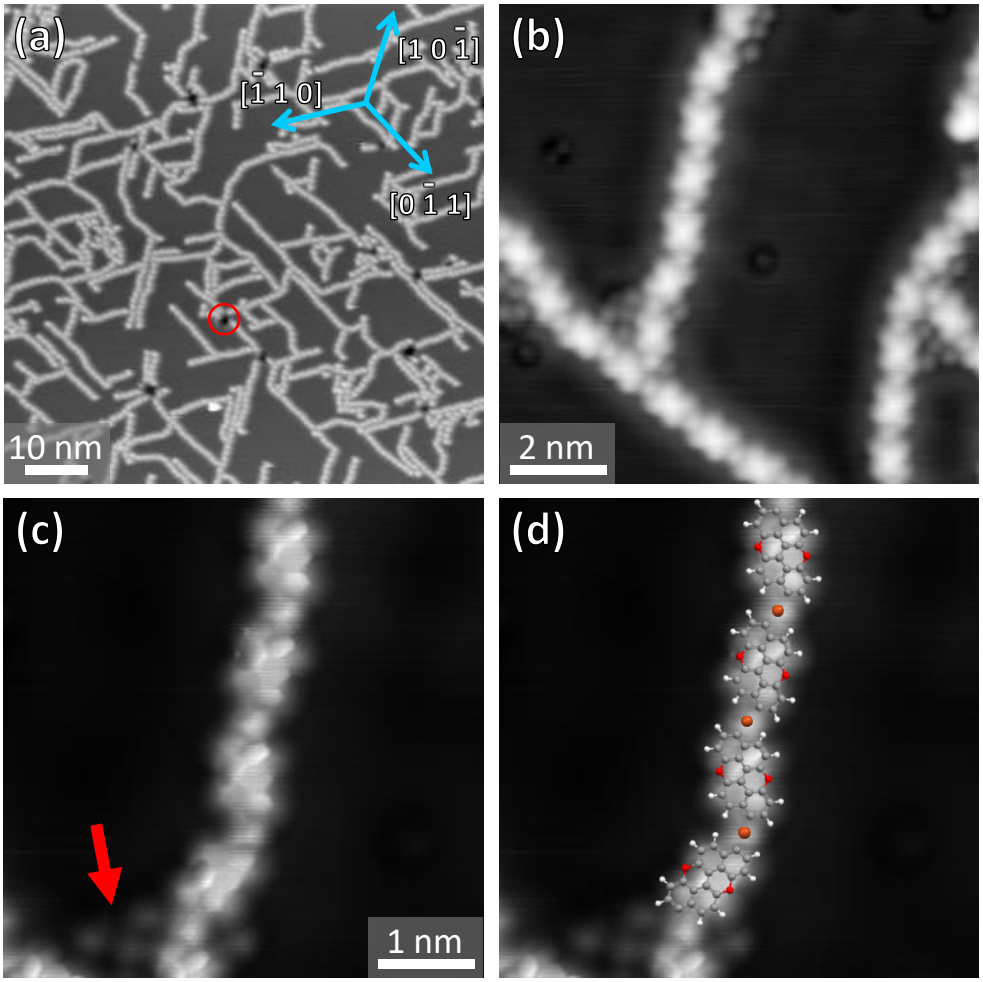

Figure 5.15. *(a) Large-scale STM image (1.1 V) of Br_2PXX on Cu(111) after a room temperature deposition. The underlying crystallographic directions are shown, and a dark patch is highlighted with a red circle. (b) Zoom of an area (CO tip, 0.4 V) showing the chain structure, including various kinks and bends. Clusters of Br atoms (red arrow) can also be seen. (c) and (d) Constant height CO tip HR-STM (30 mV) of a chain, with overlaid structure consisting of debrominated molecules and Cu adatoms*

HR-STM imaging with a CO tip (**Fig. 5.15(c)** and **(d)**) clearly elucidates the structure and confirms the metal-organic nature of the chains – the modelled distance between carbons of adjacent molecules (approximately 3.5 – 4.0 Å) is too great for covalent bonding. The existence of bright signals in-between the carbon radical positions also hints towards a metal-organic chain structure. Overlaying the structure of the molecules, and placing a Cu adatom in an equidistant position between adjacent carbon radicals reveals an estimated C---Cu bond distance of approximately 2 Å. The nature and origin of the Cu atoms, whether they are adatoms or Cu atoms pulled up from the upper layer of the underlying Cu(111) terrace, cannot be determined from STM imaging.

Many examples of junctions between chains can also be found; two are shown in **Fig. 5.15(b)**. Many of these can be associated with the tri-brominated contaminant molecules that were also observed (intact) in experiments on Au(111). As the bromine on the side of these molecules is probably also dissociated upon landing on Cu(111) at room temperature, this allows for another position with which a metal-organic bond to a Cu atom may be formed. An example of one of these junctions is shown in the HR-STM image presented in **Fig. 5.16**.

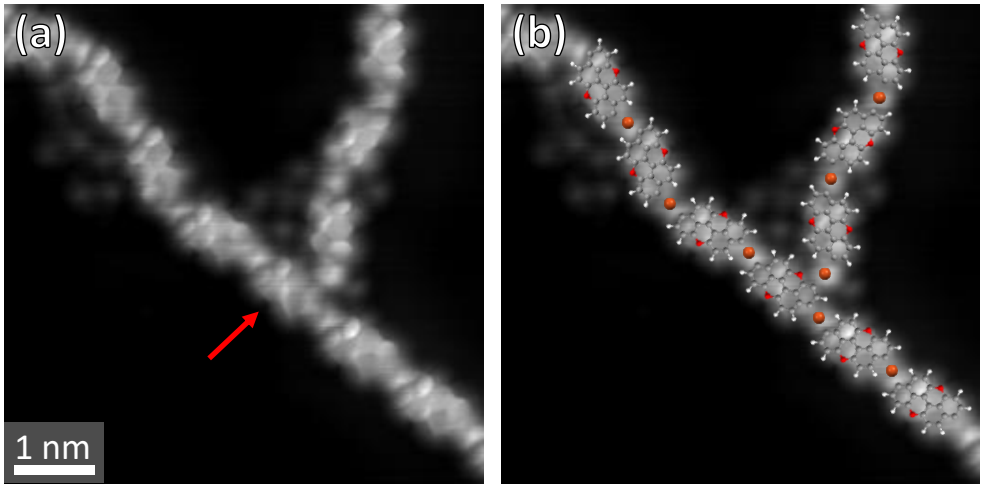

Figure 5.16. *(a) Constant height CO tip HR-STM image (30 mV) of a chain junction. The molecule indicated with a red arrow has three metal-organic connections, most probably due to it being formerly a tri-brominated contaminant. (b) Molecular overlay.*

Attempts at performing voltage-dependent STM imaging of Br_2PXX on Cu(111) were inconclusive. Few intramolecular features were observed in the typical voltage ranges employed (± 2 V). Similarly, dI/dV spectra were mostly found to be relatively featureless. This may be a reflection of increased levels of hybridisation between the molecules and the substrate when compared to the more inert Au(111) surface.

5.3 Conclusions

In this chapter, the bromination of PXX has been shown to significantly affect the structure of its molecular self-assembly at surfaces. In particular, the presence of a C-Br group allows the formation of stronger self-assembled networks through halogen bonds on Au(111).

High resolution STM performed with a CO-functionalised tip was found to be the only way to conclusively identify the type of intermolecular bonding in the on-surface self-

assembled molecular network. Whilst standard metallic-tip STM was unable to differentiate between halogen and hydrogen assembly motifs, DFT calculations predicted a coexistence of these two bonding types that is not experimentally observed. HR-STM, on the contrary, unambiguously identified Br---O halogen bonding as the only source of the observed kagome spiral assemblies of Br_2PXX on Au(111). Following on from cases in which HR-SPM has been shown to be an invaluable tool for the identification of the chemical structure of unknown molecules[152–154] or for the determination of the intermediates and products of on-surface reactions,[155–157] these results show the unique analytical insight that HR-SPM can give in establishing the nature of intermolecular interactions.

Significant amounts of contamination of undesired products from the organic synthesis were also found on the surface – these were revealed by HR-STM to be either molecules with Br on the wrong position, or tri-brominated molecules.

The position of the HOMO of all of the species (when adsorbed on Au(111)) was clearly observed in STS measurements, with small shifts corresponding to changes in the amount of Br bonded to the molecules. The state was clearly imaged in STM and corresponded well to the expected shape of the gas phase orbital.

Deposition of the molecule on the more reactive Cu(111) surface yielded a metal-organic type chain assembly composed of de-brominated molecules bound to Cu adatoms via their radical positions. Some deviations in the chain structures can be assigned to the presence of contaminant molecules allowing different binding positions, as well as the mixture of orientations of the molecules that are incorporated into the chains.

6 The Formation and Properties of PXX Nanoribbons

6.1 Introduction

A potential way to tweak the optoelectronic properties of PXX is to react Br_2PXX to form nanoribbons. The formation of these nanoribbons would result in fused perylene sections separated by oxygen-containing rings, as shown in **Fig. 6.1**. As demonstrated by the recent work of the Bonifazi group[6,118], the addition of these aromatic sections to PXX and related molecules may result in frontier orbital energetic shifts and the narrowing of the HOMO-LUMO gap, with a corresponding increase in the strength of the molecules as electron donors (due to the their energetically higher-lying HOMOs). The same group has also demonstrated via cyclic voltammetry and photophysical data that similar short PXX polymers have an increasingly higher HOMO level than the PXX monomer[116]. However, initial attempts to form long polymers of PXX in solution were hampered by problems with precipitation of ribbons after a certain length was achieved, due to strong π-stacking interactions[118].

On-surface synthetic methods, although on a smaller scale in terms of quantity, potentially allow an alternate pathway to the formation of longer PXX nanoribbons (NRs), as the precipitation problem is avoided. Many examples of the formation of 'long' (>10 units in length) nanoribbons at surfaces exist in the literature[97,235–240], although this is very much dependent on the monomer/surface combination used. Simply annealing Br_2PXX on metallic surfaces may yield polymers via the on-surface Ullmann reaction combined with a dehydrogenation reaction. In the typical on-surface synthesis of nanoribbons on Au(111), these reactions take place in two steps[97,241]. After an initial deposition of the halogenated precursor on the surface, annealing yields dehalogenation, followed by diffusion and combination of the resulting molecular radicals to form polymers. Heating these polymers to a higher temperature then allows a metal-catalysed dehydrogenation reaction to occur[208], resulting in flat nanoribbons. In the case of Br_2PXX, as the precursor molecule is flat, forming polymers prior to nanoribbons may not be favourable, as it would require significant twisting and lift-

off (from the surface) of the chains. It may thus take place in one heating step rather than two. Different surfaces, such as Cu(111), have been shown to allow the formation of different NRs (with the same precursor) via other pathways[240,242]. Similar monomers, such as di-bromo perylene, have been shown to form graphene nanoribbons (GNRs) on both Au(111)[238] and Cu(111)[190]. In the case of Cu(111), no polymeric intermediate was observed, with a dehydrogenation and metal-organic structure instead preceding GNR formation. On Au(111), it was reported that a polymer structure formed at lower temperatures preceded the formation of the GNR, but no evidence of this was provided[238].

In this chapter, the formation of PXX nanoribbons at metallic surfaces is studied via STM/STS and XPS. The progress of the reaction can be followed by XPS; any shifts in carbon and bromine environment with annealing may indicate the temperature dependence of the de-bromination and fusion processes[243]. Likewise, studying the resulting species via STM after annealing can also yield similar information, as well as demonstrate how the polymers self-assemble after their formation. Using dI/dV spectroscopy and imaging to examine nanoribbons of different lengths allows the investigation of their local electronic properties, with a specific focus on demonstrating a trend in the changing position of their frontier energy levels due to finite length effects. If the PXX nanoribbons do not interact strongly with the surface (i.e. if there is no significant hybridisation between molecule and underlying metal), the molecular states should also give clear peaks that are limited to the molecule and not related to hybrid states between the molecule and the underlying metal[159].

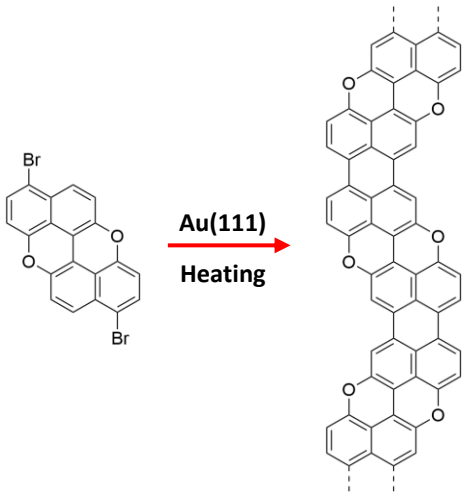

Figure 6.1. *Possible reaction scheme for the formation of PXX nanoribbons. The end sections of PXX, formerly naphthalene rings, are fused to form perylene moieties.*

6.2 Results and Discussion

6.2.1 PXX Nanoribbon Formation on Au(111)

After sublimation and deposition of Br_2PXX on room temperature Au(111) (described in the previous chapter), the sample was post-annealed from room temperature up to 673 K in 50 K steps. After every step, the sample was cooled to 77 K or 7 K and studied via STM and STS. In XPS experiments, after each annealing step the sample was left to cool down to less than 370 K before spectra were recorded.

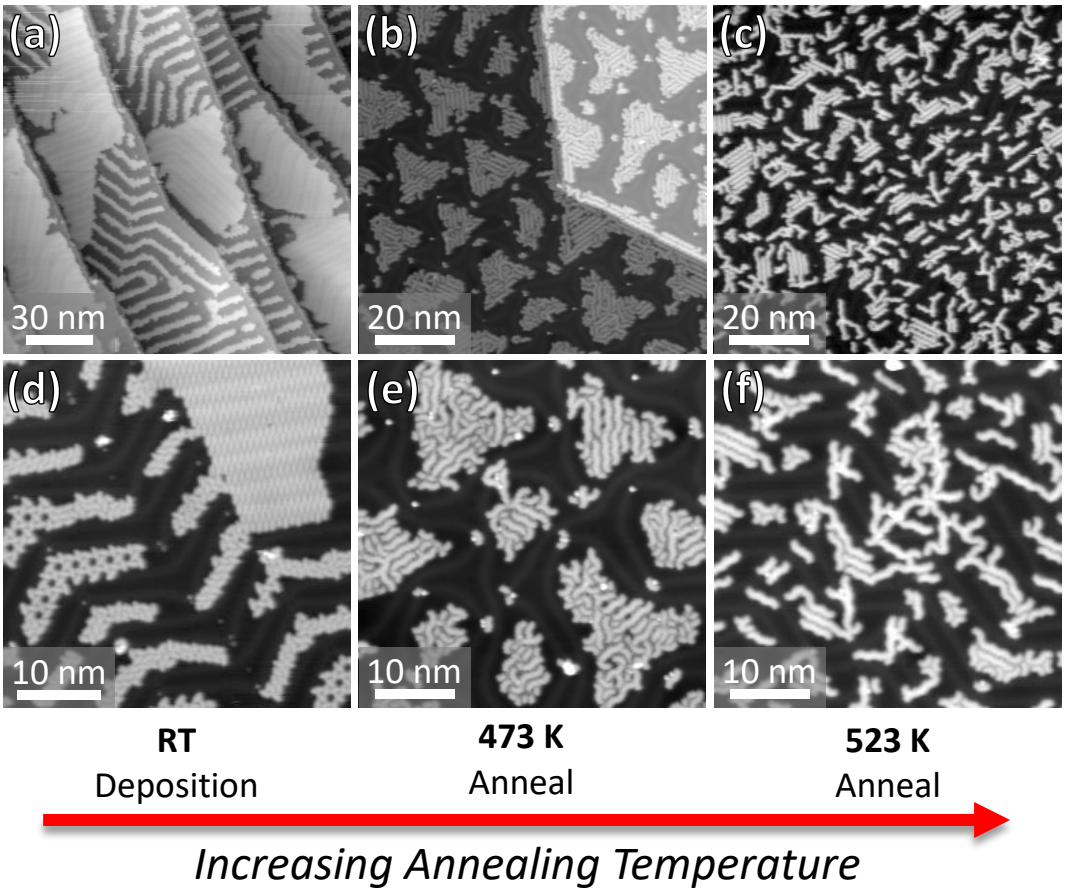

Figure 6.2. *STM images of Br_2PXX (recorded at 7 K) with increasing annealing temperature. After the 473 K anneal ((b) and (e)), ribbons of various lengths have formed, and are packed together with 'free' Br atoms into islands, with the herringbone reconstruction distorted around them. Annealing to 523 K results in the desorption of most of the remaining bromine. Bias voltages: (a) −0.7 V, all others 1.1 V.*

The first formation of nanoribbon structures on Au(111) can be observed in STM experiments after annealing to 473 K. Mostly triangular islands composed of ribbons of varying lengths, mixed in with small objects, are observed (**Figs. 6.2(b)** and **(e)**). The herringbone reconstruction can clearly be seen distorting around these islands, implying a strong interaction with the surface[129–131,244]. This, combined with the

presence of small objects between the nanoribbons, suggests the presence of 'free' bromine atoms on the surface that form self-assembled structures with nanoribbons, as previously reported in the literature for other Ullmann coupling systems[98,102]. These bromine atoms presumably dissociated from the Br_2PXX molecules but did not have enough energy to desorb from the surface. Annealing the surface to 523 K results in the desorption of the majority of the bromine and a greater level of dispersion of the nanoribbon islands (**Fig. 6.2(c)** and **(f)**). This result implies that the islands of nanoribbons observed in **Figs. 6.2(b)** and **(e)** were only held together by the presence of bromine atoms. After bromine desorption, the nanoribbons generally exhibit similar repulsive behaviour to that of the PXX monomers, with some still held together by the few remaining bromine atoms. This repulsive behaviour can be attributed to similar phenomena, such as dipole-dipole interactions resulting from a charge transfer between the ribbons and the underlying surface[76,82]. As shown in **Fig. 6.3(a)**, modelling the nanoribbon structure yields a good fit with the scheme proposed in **Fig. 6.1**; the Br_2PXX molecules have clearly fused their naphthalene-type aromatic end sections to form perylene structures, bordered on each side by anti-aromatic oxygen-containing rings. Due to nature of their synthesis (via the Ullmann coupling of Br_2PXX), the ends of the ribbons are naphthalene sections from one end of a precursor molecule, with the exception of a minority of defective ribbons that have undergone additional unwanted reactions, such as further dehydrogenation of other carbon positions, or reactions due to the presence of tri-brominated molecules (described in **Chapter 5**). The majority of the observed nanoribbons contain connections of the *alternating* type; however, some ribbons also contain '*straight*' sections as well, and very rarely a completely straight ribbon is observed (**Fig. 6.3(b) and (c)**). This general preference for the alternating type may relate to the surface-catalysed mechanism of the nanoribbon formation, and perhaps how it correlates to the position of the bromine atom on the majority of the precursor molecules. If monomers that react to form nanoribbons only do so when the C-Br positions (and resulting radicals) are aligned with each other, then for the majority of the molecules, the alternating type is favoured due to the position of the radical that results from the C-Br homolysis (**Fig. 6.3(d)**). Straight sections of the nanoribbons may be explained by considering the contaminant molecules that are brominated in different positions (**Fig. 6.3(e)**), as presented in the previous chapter. It is not expected that any significant difference may be found in

terms of the HOMO/LUMO energies of the two different ribbon types; however, this could not be proven, as very few isolated examples of short, straight nanoribbons were observed.

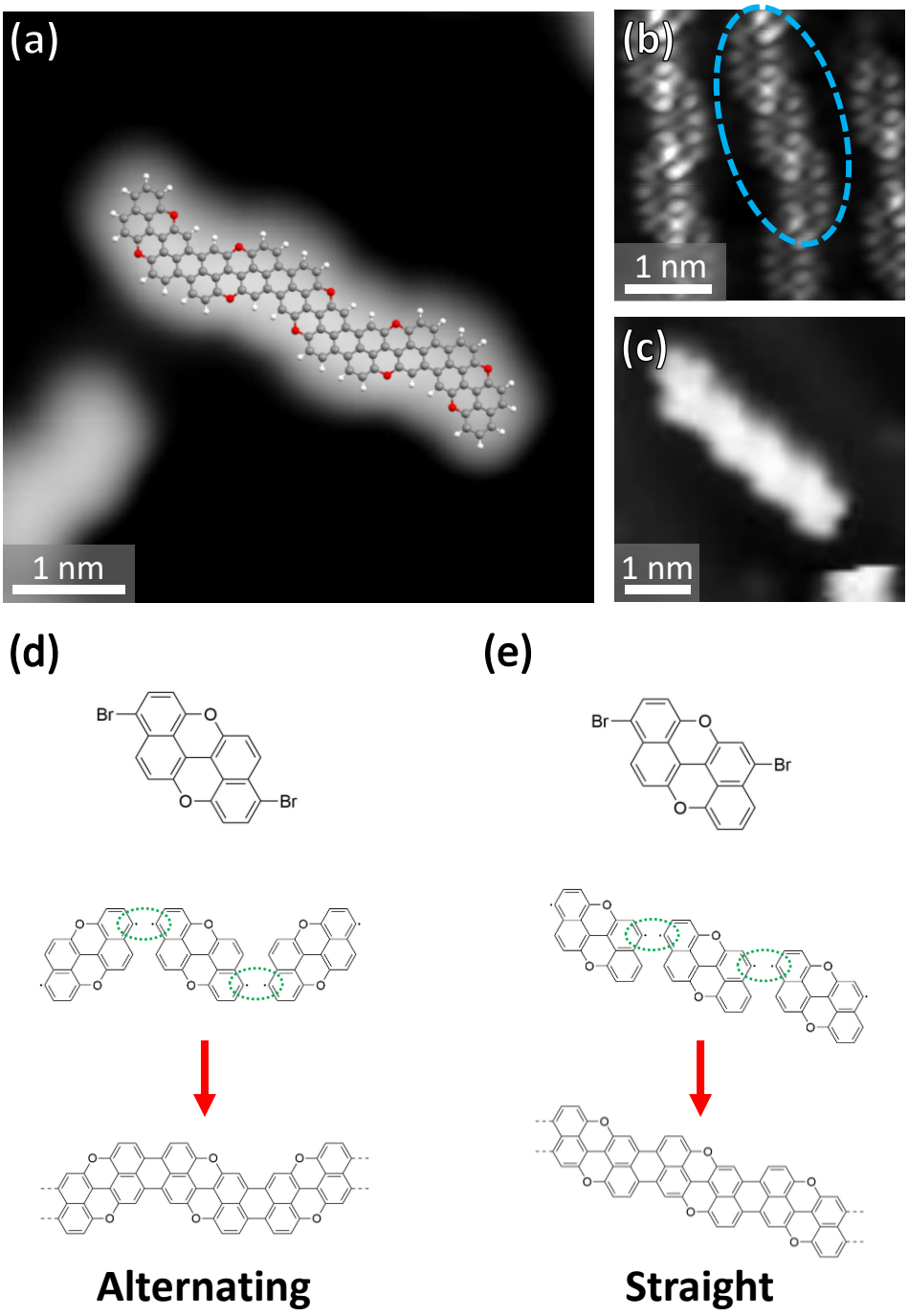

Figure 6.3. *(a) STM image (7 K, 1.1 V) of an alternating type pentamer nanoribbon with a scaled molecular model overlay. (b) and (c): 7 K STM images (30 mV and −0.9 V) of examples of straight sections of nanoribbons. A straight section found in the middle of a nanoribbon is indicated with a blue oval, and an entirely straight tetramer nanoribbon is shown in (c). The different contrast in (b) is due to constant height imaging with a CO tip. (d) Connecting the Br_2PXX monomer to make an alternating nanoribbon. (e) Connecting the Br_2PXX contaminant (different Br position) to make a straight nanoribbon.*

The interpretation of the STM imaging of annealing experiments is further supported by XPS experiments that follow the Br 3d and C 1s signals with increasing annealing temperature steps, as illustrated in **Fig. 6.4**. Each Br 3d signal (ideally) appears as a doublet in XPS measurements, with a $3d_{5/2}$ and a $3d_{3/2}$ peak in a 3:2 ratio due to spin-orbit splitting. Up to 413 K, the bromine environment is unchanged, with binding energies of approximately 69.8 and 70.8 eV for the Br $3d_{5/2}$ and $3d_{3/2}$ peaks, respectively, matching those of an intact C-Br bond. Between 410 K and 493 K, an increasing amount of the Br signal shifts to a lower binding energy (67.7 and 68.8 eV for the Br $3d_{5/2}$ and $3d_{3/2}$ peaks, respectively), corresponding to 'free' bromine atoms bound to the Au surface[102,239,245]. By 553 K, the Br 3d signal disappears due to desorption from the surface, in agreement with the STM experimental evidence.

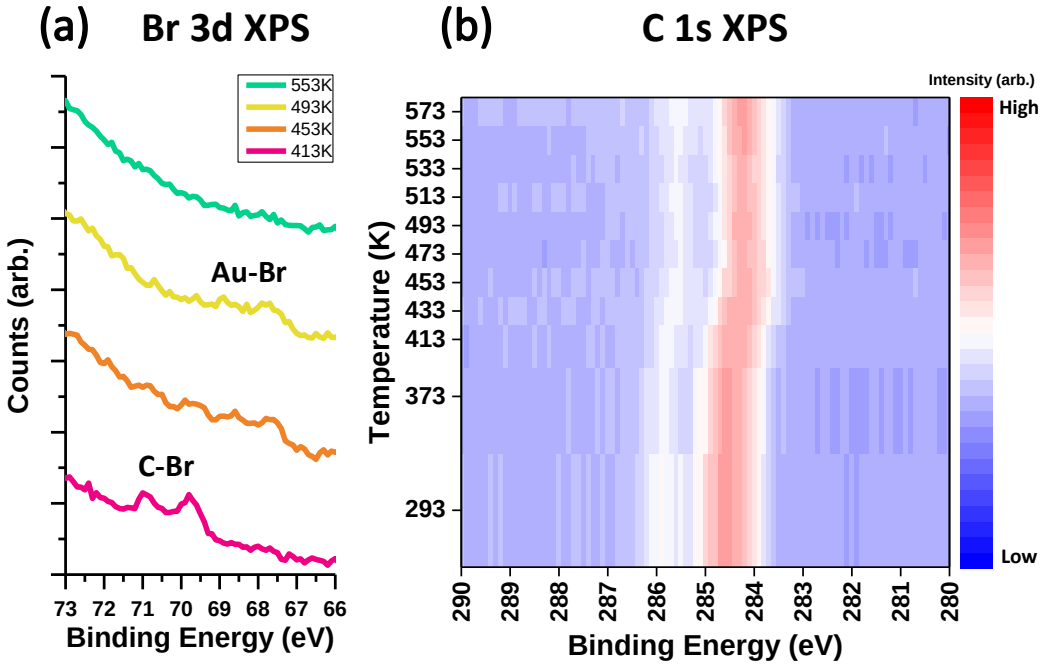

Figure 6.4. *(a) Selected Br 3d XPS spectra showing the change in the bromine environment with annealing temperature. The signal first shifts to lower binding energies as the Br atoms detach from the molecule to form Au-Br complexes, then disappears when Br atoms desorb at higher temperatures. (b) Change in the C 1s XPS binding energies with annealing temperature. Ribbon formation starts to occur above 413 K, as evidenced by the shift in binding energy. Certain spectra (293 K, 453 K and 513 K) had lower overall intensities due to some variability in the x-ray source output – as such, the spectra were normalised using the background intensity.*

Examining the C 1s signal with annealing temperature (**Fig. 6.4(b)**) also shows a small binding energy shift upon ribbon formation, with the reaction starting to occur above 413 K. Few changes are detected above 453 K, potentially indicating that the ribbons

are no longer increasing in length above this point (i.e. most of the chains have been terminated/passivated).

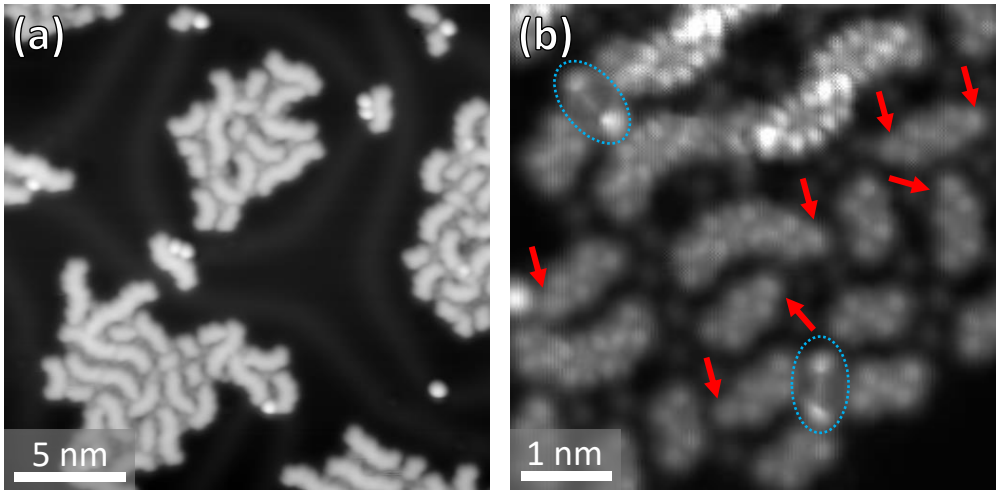

Figure 6.5. *(a) 7 K STM image (1.1 V) of islands of ribbons (of varying length) mixed with bromine atoms. The herringbone reconstruction is distorted around the islands. (b) Constant height CO tip HR-STM (30 mV) image of a mixed island, showing the various different sizes of ribbons mixed with bromine atoms. Some molecules still have intact C-Br bonds (red arrows). A small number of features appearing in pairs near the end of some ribbons, circled in blue, are also observed.*

STM images of the mixed nanoribbon-Br islands (after annealing to 473 K, i.e. prior to bromine desorption) are shown in **Fig. 6.5**. Small objects of the size of monomers can also be seen within these mixed islands; these are presumably unreacted/partially reacted monomers and PXX molecules, the latter formed from di-radicals that have been terminated by hydrogen before being able to react to form longer ribbons. With the exception of Br-terminated objects, the termination of the monomers and ribbons is not necessarily easy to correlate with their appearance in standard constant current mode STM imaging. In the literature, however, it has been shown that such images may be used, when combined with theoretical calculations, to identify terminations[246]. HR-STM experiments with a CO tip (**Fig. 6.5(b)**) clearly reveal the structure of mixed ribbon-bromine islands, demonstrating the variation in nanoribbon structure length and the location of intermixed bromine atoms. Molecules terminated by C-Br groups (indicated with red arrows) can be easily recognised, as they typically resemble the features observed in HR-STM imaging of the intact precursor molecule (**Chapter 5**) and are always found in the expected positions on the molecules. Other terminations (such as doubly hydrogenated carbon atoms or metal-organic structures) could not be clearly identified using this technique, although some unknown bright pairs of objects

were occasionally detected near the ends of nanoribbons, as in **Fig. 6.5(b)**, circled in blue. Their location near to the termination of the objects may imply that they are bonded in some way to the radical carbon positions, although few conclusions may be drawn from the imaging.

Interestingly, attempting to image longer ribbons with constant height HR-STM at low bias voltages is found to be increasingly difficult with length. As will be described later in this chapter, longer ribbons have a higher local density of states (LDOS) around the Fermi level (0 V), and thus there is increasingly a convolution of the repulsive contrast (due to the CO probe) and the signal that is due to electronic states on the nanoribbon. No voltage was found that allowed a compromise in terms of HR-STM imaging. As demonstrated in **Fig. 6.6**, imaging a long nanoribbon (4 units or more) at a constant height (CO tip, 30 mV bias) with a larger tip-sample distance reveals the shape of an electronic state (**Fig. 6.6(a)**) that eventually combines with the repulsive contrast when the tip is close enough to the underlying ribbon (**Fig. 6.6(b)**). This is similar to experimental and theoretical studies of other molecules that have been imaged with HR-STM in which features from both the molecular structure and electronic states were observed and predicted by theory[167]. This is an inherent issue with HR-STM that is not found with NC-AFM.

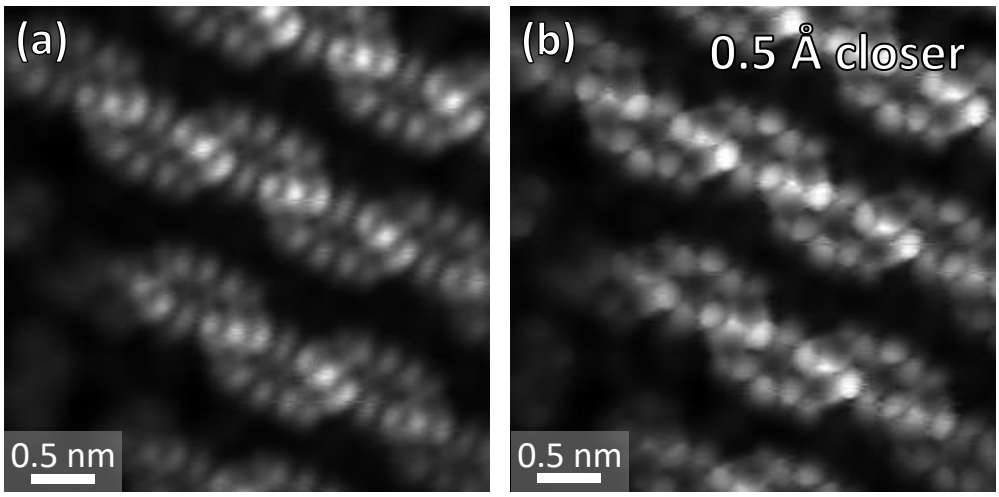

Figure 6.6. *Constant height CO tip STM images (30 mV) of longer PXX nanoribbons, with differences in tip height offset. Image in (b) has the tip 0.5 Å closer to the surface. An electronic state at this voltage with a distinct shape clearly interferes with attempts to image the structure of the nanoribbons.*

At higher annealing temperatures, a few isolated ribbons (**Fig. 6.7**) are observed due to the partial desorption of bromine from the surface. The annealing temperature

required for this depends significantly on the coverage, i.e. at higher precursor coverages, a higher temperature is required to desorb enough bromine to isolate most of the nanoribbons on the surface. As mentioned above, the nanoribbons are not found to aggregate without bromine atoms, with the exception of occasional short H-bonded rows of PXX monomers, as described previously in 7 K STM experimental results for PXX on Au(111) (**Chapter 4**). The isolation of the nanoribbons, along with a wide variation in their length, is useful for studies of their electronic structure via STS; locally adsorbed molecules/atoms (such as bromine) can lead to shifting in the observed position of peaks in dI/dV spectra. This can be attributed to the effect of Br adatoms on the local work function of metal surfaces, as described previously in the literature[101,247–249].

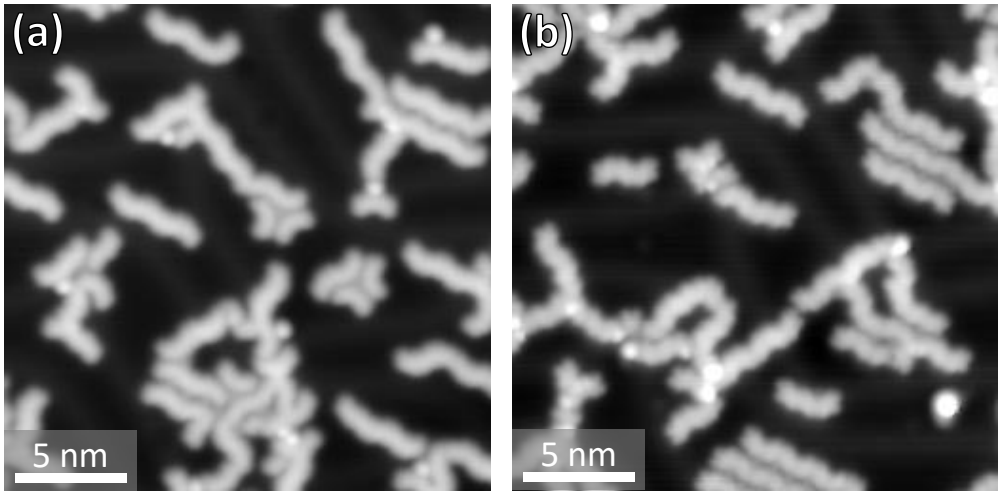

Figure 6.7. *(a) and (b): 7 K STM images (1.0 V and −1.5 V) of PXX nanoribbons after a 523 K anneal. Most of the bromine has desorbed, with some still remaining to pack nanoribbons together into small islands. Short, isolated ribbons can now be individually studied via STS.*

6.2.2 Electronic Properties of PXX Nanoribbons

Short, isolated ribbons (from monomer to tetramer) were studied via STS to investigate the dependence of the energy of various molecular states on the nanoribbon length. In particular, changes in the position of the HOMO were compared between ribbons of different lengths in order to judge changes in their strength as electron donors. Spectra for the occupied and unoccupied states were typically recorded separately because the peaks in the occupied states (for the dimers and above) were significantly weaker than those in the unoccupied states. As a result, it is preferable to choose two different tip stabilisation conditions (that essentially govern the height of

the tip during the acquisition of dI/dV spectra and thus the resulting strength of the tunnelling current signal), one for the occupied and the other for the empty state spectra. Attempts to scan across the whole voltage range typically resulted in either the occupied state peaks being barely detectable or over-saturation of the signal from the unoccupied states (when the tip was close enough to get a reasonable signal for the occupied states). For the occupied states, the tip was typically stabilised at a higher current/lower voltage over the ribbons, resulting in it being closer to the sample and leading to a larger dI/dV signal that more clearly showed the position of peaks in the negative bias range.

Fig. 6.8(a) illustrates the observed changes in the occupied states when increasing in ribbon length from monomer to trimer. The monomer (PXX, described in **Chapter 4**) shows a single clear peak in the occupied states at approximately −830 mV. The highest occupied peak in the dimer spectrum is significantly shifted upwards in energy to −200 mV and is in turn shifted to −70 mV for the trimer. It is important to note that in the case of the trimer, even when adsorbed alone with no neighbouring species, there was some variation in the appearance and position of the HOMO peak. In some cases, no peak could be seen at all, with a general rise in DOS towards 0 V, as seen with longer ribbons. This could be indicative of variations in the underlying surface potential due to the herringbone reconstruction that lead to different relative alignments of the molecular and metal states, or could even be the impact that other adsorbates have at longer ranges than expected (i.e. in the order of nanometres).

Due to the proximity of the Fermi level (i.e. 0 V in the STS spectra), ribbons longer than the trimer no longer have a HOMO state that can be reliably identified in this region. This is most probably because upon reaching a certain length, a significant charge transfer from ribbon to metal may take place due to the relative alignment of the HOMO and the Fermi level. Similar effects have been seen previously with other donor type molecules adsorbed at metallic surfaces[238]. However, in the case of PXX nanoribbons, there is no clear unoccupied state feature close to 0 V after the ribbons reach a certain length. The reason for this is unclear; it may be that the state is weak and broad, and as such was not detected in STS measurements. Occupied states that are lower in energy (e.g. HOMO−1, −2…) can still be detected for longer ribbons, as shown in **Fig. 6.8** in the occupied states of the tetramer.

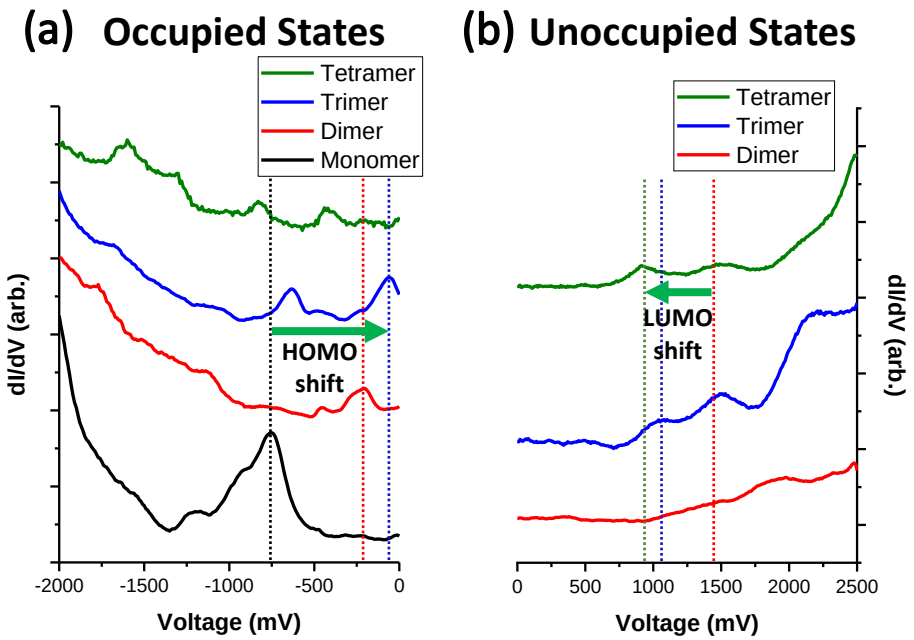

Figure 6.8. *Occupied and unoccupied states dI/dV spectra for short ribbons of varying lengths, with the shift in HOMO/LUMO indicated. No peak was observed for the monomer in the unoccupied states. The LUMO peak for the dimer in (b) was unclear, so the exact assignment of its position is somewhat arbitrary, and the shift may be smaller than indicated. The tetramer occupied states spectrum has been scaled up to make the features more obvious when compared to other ribbon lengths; the spectrum was recorded in different conditions to the other occupied states spectra and thus has a lower signal:noise ratio.*

Fig. 6.8(b) shows a similar (opposite) trend for the unoccupied states of the ribbons. A general shift of the LUMO downwards in energy is predicted by simple gas phase DFT calculations and reflected in the dI/dV spectra of nanoribbons of various lengths. Only the trend from dimer to tetramer is shown – this is because no clear peak in the unoccupied states for the PXX monomer was ever observed in the ±2.5 V range. This may be because higher voltages (which can often lead to damage of molecules when performing STS experiments) are required to access it. Whilst the general trend in the shift of the unoccupied states with ribbon length is clear, the placement of the LUMO peak for the dimer is somewhat arbitrary due to there being a general rise (‘lump’) in the dI/dV signal, rather than a strong peak. As such, the absolute value for this shift is not reliable, and may be smaller than indicated.

The relative changes in energy with increasing length approximately fit with the expected trend as predicted by DFT calculations of gas phase nanoribbons, shown in **Fig 6.9**. Whilst the absolute values that come out of these calculations might not be fully reliable, it should be possible to correlate relative changes in the calculated

energies to similar changes observed in the dI/dV spectra. It should however be noted that the shifts observed in the dI/dV spectra of the adsorbed molecules are not expected to correspond exactly to those calculated for molecules in the gas phase (or even to those potentially measured by other experimental methods in solution). This is due to the general reduction of molecular HOMO-LUMO gaps upon molecular adsorption on metallic surfaces, which can be related to the image charge effect (as described earlier in this thesis)[21,250].

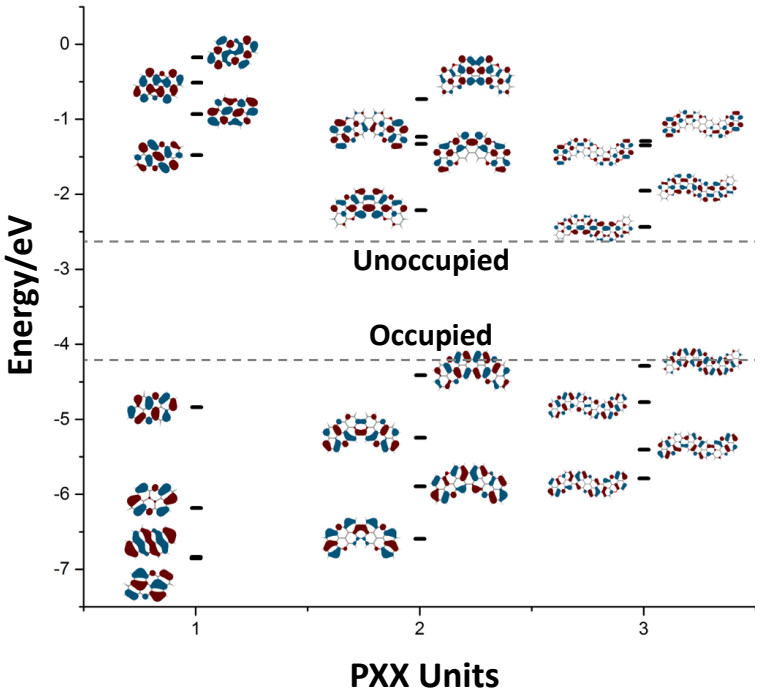

Figure 6.9. *DFT calculated frontier occupied and unoccupied states of PXX ribbons, up to a trimer. The dashed line indicates the energies the HOMO and LUMO tend towards with increasing length, as estimated by examining the decreasing calculated energy shifts of longer ribbons. DFT calculations performed by Dr. Luka Đorđević, University of Trieste.*

After observing this trend in the overall shift upwards in energy of the HOMO of the ribbons, an explanation of the issues with constant height imaging of longer nanoribbons (as mentioned earlier in this chapter) becomes apparent. As the ribbons become longer, they exhibit a higher LDOS near to the Fermi level. In order to acquire simple HR-STM images, voltages close to 0 V (i.e. the Fermi level) are usually used; there is often a low LDOS in this region for molecular systems, allowing the imaging contrast in HR-STM to mainly derive from the repulsive mechanism described previously in this thesis and in the literature[167]. When the tip is very close to the sample

molecule, having a weaker electric field (i.e. lower voltage) is also desirable, as some molecules may be 'delicate' and undergo tip-induced reactions and/or fragmentation. Due to the higher density of states of longer ribbons near E_F, there is increasingly an issue of molecular states interfering with attempts at HR-STM imaging. This is illustrated in **Fig. 6.10**: a mixture of long and short ribbons (at lower annealing temperatures, packed together with bromine atoms) is imaged in HR-STM conditions (Constant height, 30 mV, CO tip close to molecules). A much brighter signal can be observed over the longer ribbons (mainly present in the upper right portion of the image), and the shape of an electronic state (presumably the HOMO) is much more apparent. Some influence of the HR-STM mechanism can also be seen, with the bright rings of the perylene sections interfering with similarly located lobes of the HOMO. There may potentially be other ways of imaging the structure of long PXX nanoribbons with STM methods, such as via CO tip IETS[170] imaging, but this was not attempted.

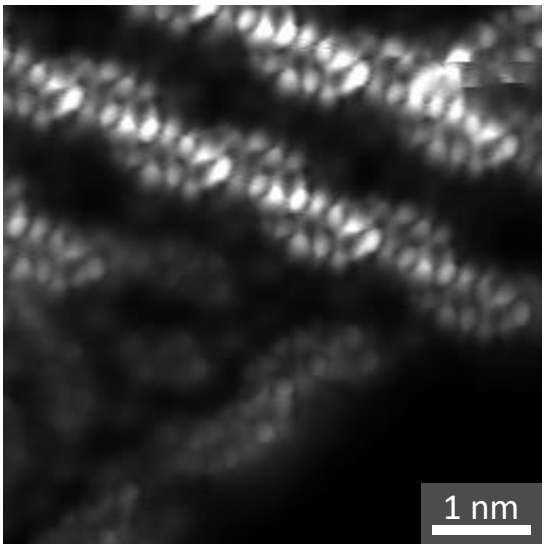

Figure 6.10. *Constant height STM image (CO tip, 30 mV) of a mixture of ribbons/bromine. Longer ribbons (top right) appear with much more signal than shorter ribbons (bottom left).*

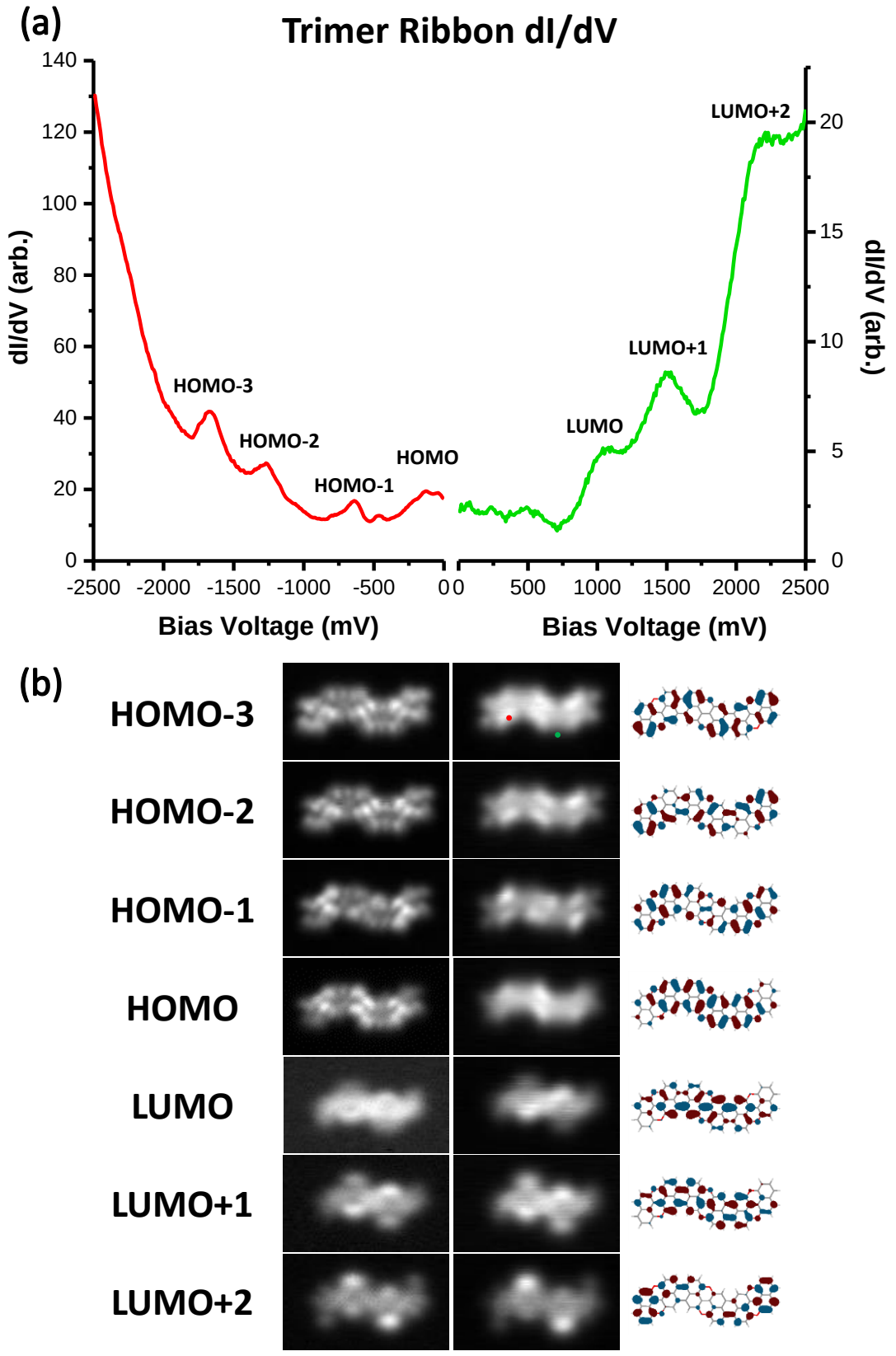

Figure 6.11. *(a) Combined occupied and unoccupied states dI/dV spectra of a trimer ribbon, with tentative peak assignments. Spectra recorded with a metallic tip at the locations indicated with red and green dots in an image shown in (b). (b) Constant height dI/dV images of two different trimers with (left) and without (right) a CO tip, compared to the DFT calculated gas phase orbitals. DFT calculations performed by Dr. Luka Đorđević, University of Trieste.*

Constant height dI/dV images were recorded for each observed state (both occupied and unoccupied) of the monomer, dimer, trimer and tetramer ribbons. These were in turn compared to gas phase DFT calculations for the nanoribbon orbitals, potentially allowing the identification of each peak in the dI/dV spectrum if there is not a significant hybridisation between the ribbons and the underlying surface. **Fig. 6.11(a)** shows the whole dI/dV spectrum (recorded in two parts for the reasons mentioned above) of a trimer nanoribbon. In **Fig. 6.11(b)**, dI/dV constant height images (with and without a CO tip) are shown, with each image recorded at voltages corresponding to the states shown in **(a)**. A different trimer was used for each set of experiments (i.e. for each tip); both had states at similar voltages. The occupied states all appear to be relatively similar in terms of shape, albeit with changes in intensity over different parts of the ribbon for different energies. These general changes in intensity are present both with and without a CO tip. Differences between the unoccupied states were also observed, with regions of varying intensity found mainly at the edges of the perylene sections of the ribbon. In **Fig. 6.11(b)**, a comparison is also made between the DFT calculations and the observed dI/dV images, with an assignment of the molecular states to each peak in the spectrum.

Comparing the images produced by both metallic and CO tips shows the same general trends in intensity variation between the different states, allowing an assignment to be made according to the similar general trends seen in the DFT results. As expected, this comparison identifies the peak at approximately −100 mV as the HOMO. However, the distinction between the HOMO−2 and HOMO−3 images is not clear – and as such, these assignments are only tentative. This is also the case for the LUMO and LUMO+1 resonances. Noticeably broader/more diffuse features were observed in the dI/dV maps of the unoccupied states when compared to the occupied states, along with broader resonances in the spectra. A similar effect on the unoccupied states has been previously seen with an armchair ultra-narrow GNR formed from dibromo-perylene precursors, and was attributed to a shorter lifetime of tunnelling electrons resulting in increased lifetime broadening[238].

A significantly higher level of resolution is also observed with the CO tip. However, as is often found with CO tip imaging of electronic states in STM, there is not a clear match between the features observed and the expected number of lobes/nodes in each orbital. This can be attributed to the p-wave nature of the CO tip; imaging molecular

states with CO tips has previously been shown to give significantly different results to metallic (s-wave) or other s-wave type tips, due to it having a mixture of both p-wave and s-wave character[174]. This is because tunnelling via the π-orbitals of the CO takes place, leading to a greater intensity over the nodes in the orbitals of the underlying sample molecule due to higher amounts of overlap. More generally, it can be considered that CO tip images resemble the lateral gradient of the underlying molecule's orbital, rather than just its intensity. When comparing the shapes expected over these perylene sections with the number of lobes observed with a CO tip, it becomes clear that the bright features observed correspond to the location of the nodes in the molecular orbital, as is expected with a p-wave tip[174] (**Fig. 6.12(b)** and **(c)**).

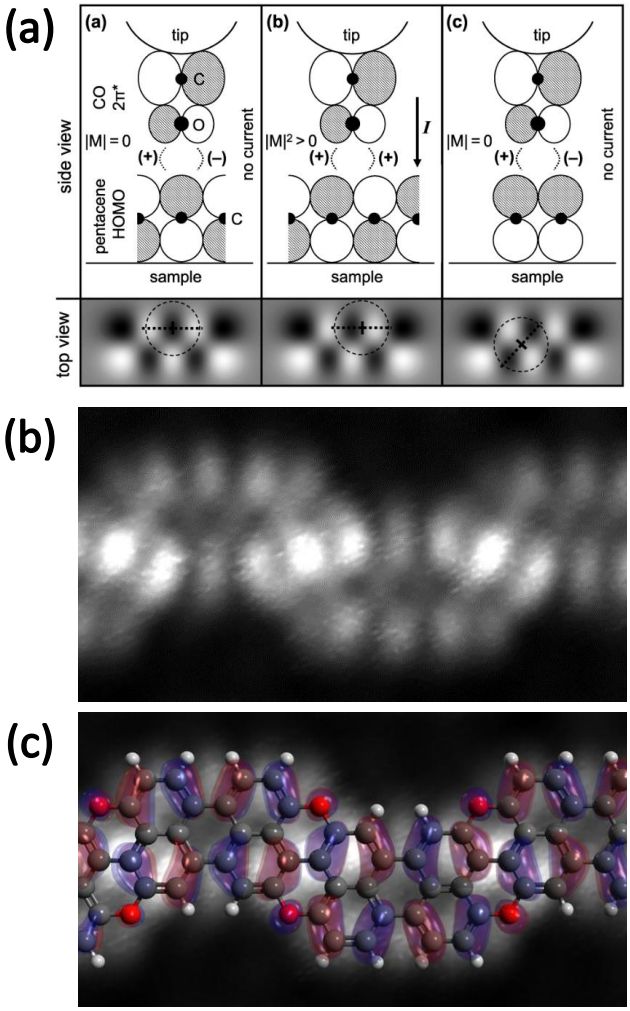

Figure 6.12. *(a) Figure reproduced from Gross et al.*[174]*, with a cartoon illustrating the contrast mechanism when imaging molecular states with a CO tip. (b) Constant height STM image (30 mV, CO tip) of a long ribbon (7 units), with an overlay of the HOMO of a tetramer ribbon in (c). There are clearly signals that are mostly found in the nodes of the HOMO, as expected with a CO p-wave tip. It is important to note that when the nanoribbons reach above 3 units in length, the shape of their HOMO becomes visible in the low positive bias range (despite the lack of a clear peak in the dI/dV spectra), hence the shape still being visible at a +30 mV bias voltage in (b) and (c).*

Typically, the general shape of the features in both the occupied and unoccupied states did not change with the length of the ribbons. This is also illustrated in **Fig. 6.12** with a CO-tip constant height image (30 mV) of a long ribbon (7 units), which bears a great similarity to the dimer/trimer occupied states also shown in **Figs. 6.11** and **6.13**. This is also clear when examining the DFT-calculated gas phase orbitals (e.g. **Fig. 6.9**).

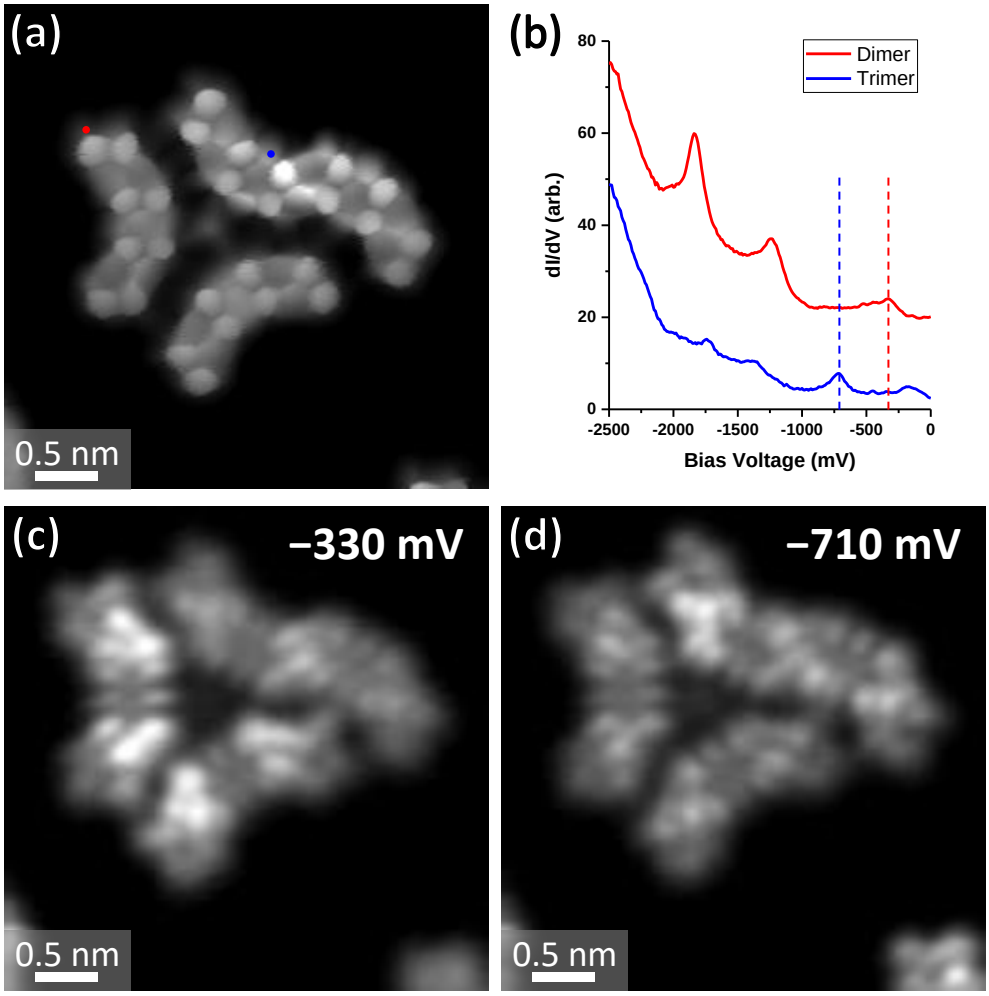

Figure 6.13. *(a) HR-STM image (CO tip, −30 mV) of a cluster of two dimers and a trimer, held together by a central bromine atom. (b) dI/dV spectra recorded at the points highlighted in (a). (c) and (d): Constant height dI/dV images (CO tip) of the cluster recorded at voltages corresponding to peaks in the dI/dV spectra. Greater intensity at each voltage can be observed on the ribbon with the corresponding peak in its dI/dV spectrum.*

dI/dV spectra and images of ribbons of different lengths (dimers and trimers) are shown in **Fig. 6.13**. It should be noted that the more negative voltages of the occupied state resonances than those previously reported are due to the presence of locally adsorbed bromine that downshifts the HOMO in energy. **Fig. 6.13(c)** and **(d)** demonstrate the localisation of the states seen in dI/dV spectra on each type of ribbon.

In **(c)**, the HOMO resonance of the dimer at −330 mV is imaged, with a clearly stronger signal found over the dimers than the trimers. Imaging the HOMO−1 resonance of the trimer at −710 mV in **(d)** also shows the reverse of this, with more intensity found over the trimer.

Making a direct comparison between PXX ribbons and other nanoribbons from the literature, in particular graphene nanoribbons, is difficult. The anti-aromatic nature of the central (oxygen-containing) rings of the PXX unit may indicate that it cannot be technically labelled as a 'graphene' nanoribbon, unlike other examples of heteroatom-containing nanoribbons (such as those containing boron[251,252], nitrogen[237] and sulfur[11]), which all have an aromatic 'core' with edge dopants[159] or aromatic heterocycles[237] in their structure, also often at the edges. Non-aromatic edge doping via the conjugation of lone pairs[253] or double bonds[159] into the π-system has also been used to both rigidly shift the GNR band gap as well as tweak it. In these studies, groups involving oxygen have been used, with furan-type rings[253] or ketone groups[159] at GNR edges.

The width of the PXX nanoribbons is on a par with other ultra-narrow GNRs[238], but the edge types vary between armchair on the perylene sections and zig-zag on the PXX sections, albeit with the caveat of edge oxygen atoms and anti-aromaticity. The measured band gap of longer PXX NRs tends towards a value of approximately 1 eV, thus demonstrating that the PXX NRs retain their semi-conducting character. This is quite different from armchair rylene-type GNRs of a similar width, which have been shown to possibly be close to metallic with a small band gap of 100 mV due to their $N = 3p + 2$ characteristic (where p is an integer and N is the number of carbon atoms across the width of the GNR)[238,239]. There is no report in the literature of an equivalent all-carbon GNR of the same width with a fully zig-zag character. Only one example of an all carbon, somewhat similar mixture of zig-zag and armchair GNR has been demonstrated[254] (albeit with a shorter zig-zag section), but was not characterised with any STS band gap measurements. Further electronic structure calculations, along with conductance measurements of the PXX NRs, were not within the scope of this study but may provide promising future avenues of research, in particular to determine how similar the PXX nanoribbons are to other GNRs. Potential for comparisons may also lie in examining anthanthrene derivatives for the synthesis of an all-carbon equivalent

GNR, but correctly functionalising the molecule with end groups whilst preserving the reactive side carbon positions may prove difficult.

6.3 Conclusions

In this chapter, it has been demonstrated that donor-type PXX nanoribbons can be formed from Br_2PXX on Au(111) when annealing the surface to temperatures above approximately 400 K. In contrast with attempts to synthesise these nanoribbons in solution, polymers of much greater length have been made possible via the utilisation of on-surface synthesis. The energies of the HOMO levels of the resulting ribbons have been measured via dI/dV spectroscopy and have been found to indicate increasingly strong donor molecules with increasing length. This is evidenced by a clear shift of the HOMO level to less negative voltages. Various electronic states of the nanoribbons, visible as peaks in the dI/dV spectra, have been imaged and assigned to molecular states via a comparison with gas phase DFT-calculated orbitals. The high surface diffusivity of the ribbons and the lack of distortion of the herringbone reconstruction of the substrate suggest the absence of a strong interaction between the ribbons and the Au(111) surface – which in turn adds validity to any comparison with gas-phase calculated orbitals. Experiments with a CO tip show the structure of ribbons and add a further demonstration of the effects of a p-wave tip when imaging molecular states at surfaces.

More studies are required to determine the properties of PXX NRs, in particular their relation to graphene NRs and the effect of the anti-aromatic central O-containing rings on their electronic characteristics. However, the possibility demonstrated here of tweaking the PXXs donor strength via polymer formation is an important first step in this direction. Promise also lies in selectively forming polymers of a certain length to aim for specific HOMO energy levels via careful synthesis of precursor monomers (e.g. reacting singly brominated molecules to form purely dimers).

7 Vat Orange 3: An Acceptor Analogue

7.1 Introduction

The demonstration of PXX nanoribbons increasing in donor strength as they simultaneously increase in length naturally leads to a related molecule that may demonstrate the opposite effect: an electron acceptor molecule that may also be strengthened by the formation of conjugated nanoribbon polymers.

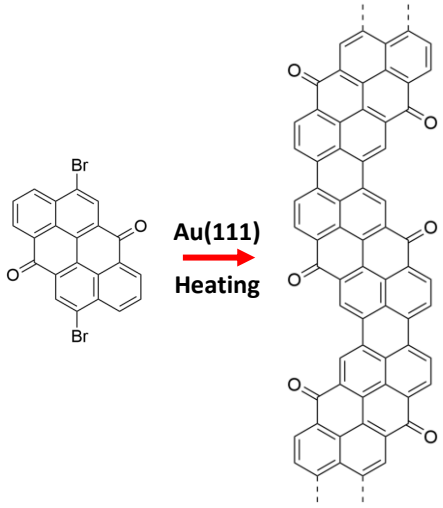

Figure 7.1. *Structure of Vat Orange 3 (left), with the proposed reaction scheme for the formation of acceptor-type nanoribbons (right) on Au(111).*

Vat Orange 3 (VO3, 4,10-dibromoanthanthrone, also known as indanthrene brilliant orange RK, structure shown in **Fig. 7.1**), so-called due to its use as a vat dye compound for its distinctive red-orange colour[255,256], is a natural acceptor analogue of Br_2PXX. It shares the same naphthalene end aromatic groups, with C-Br end groups that may allow for the formation of nanoribbons at surfaces in a similar fashion to Br_2PXX (albeit on the adjacent carbon position). The main differences lie in the central rings of the molecule: where before there were simply oxygen atoms linking the naphthalene sections, there are now electron-withdrawing ketone groups, which are a common moiety in electron acceptor molecules[32,257–259]. As such, the DFT-calculated LUMO of the molecule is significantly lowered relative to Br_2PXX, and the on-surface

formation of polymers may further lower it, allowing it to become a stronger electron acceptor (**Fig. 7.2**).

Apart from its use as a pigment, it has also been demonstrated that VO3 and other related compounds can be used as organic semiconductors in organic field-effect transistor (OFET) devices with good charge mobility, in particular for their low toxicity and biodegradability that is suited to more 'green' devices[260–262].

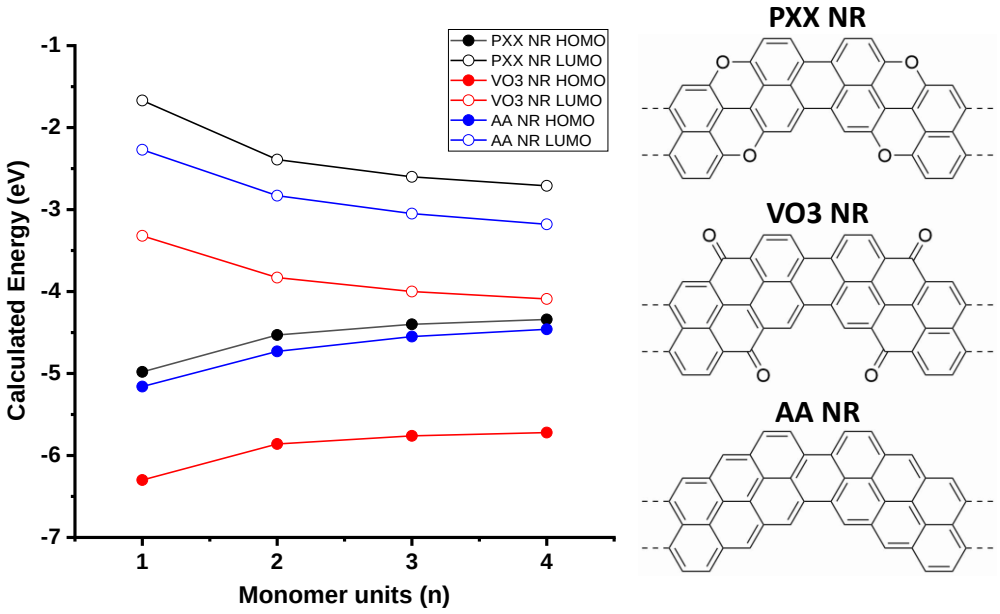

Figure 7.2. *Comparison between the calculated frontier energy levels of PXX nanoribbons, VO3 nanoribbons and an all carbon equivalent (from the anthanthrene monomer, AA), with a structural model of each NR type. The ketone groups of the VO3 ribbons significantly lower the HOMO and LUMO levels in energy when compared to PXX, demonstrating that VO3 ribbons may act as the strongest acceptor. This acceptor strength also clearly increases with length, as shown by the decreasing LUMO energy. Calculations performed by Dr. Luka Đorđević, University of Trieste.*

The C-Br groups on each end of the molecule allow for the formation of halogen bonds when the molecule is self-assembled on a surface, and the ketone groups on the periphery of the molecule may be able to participate as a halogen bond acceptor. Indeed, in the crystal structure, determined by Schmidt et al.[256], C-Br groups point towards the ketone groups, albeit off (21.4°) the ideal axis with the sigma hole location, with a Br---O distance of 3.291 Å, within the expected range for halogen bonding[40].

A study of the self-assembly and on-surface reactions of VO3 on Au(111) via STM is described in this chapter. As with Br_2PXX, STS is used to measure changes in acceptor strength with increasing length by following the trend in the LUMO energy.

7.2 Results and Discussion

7.2.1 Self-Assembly of Vat Orange 3 on Au(111)

VO3 was found to readily sublime in UHV conditions at approximately 540 K. Deposition of VO3 on room temperature Au(111) at sub-monolayer coverages results in large islands of only one type of self-assembled structure when examined via STM, as shown in **Fig 7.3**. Experiments close to 1 ML also only result in the same type of packing. Small, mobile molecular clusters at the elbow sites of the herringbone reconstruction are also observed at lower coverages when scanning at 77 K (data not shown).

The island is found to consist of molecules packed into an approximately square unit cell (unit cell parameters **a** = **b** = 1.53 ± 0.04 nm, θ = 89 ± 1°). As with Br_2PXX, the molecule is pro-chiral and thus has two possible orientations when adsorbed on the surface which segregate into separate islands. The herringbone reconstruction lines of the underlying Au(111) can still be observed through the island assembly, so it may be assumed that there is not a significantly strong interaction between VO3 and the Au(111) surface as the reconstruction has not been altered or lifted[98,130,244]. Individual VO3 molecules are found to be mobile outside of the islands at 77 K, which is a further indication of a weak interaction with the surface. HR-STM experiments at 7 K (**Fig. 7.3(c)**) with a CO tip reveal the structure to be held together by type II halogen bonding[40] with the sigma hole on Br end groups pointing to the region of negative electrostatic potential on the side of adjacent Br atoms. The modelled Br---Br distance of 3.9 ± 0.1 Å implies that the halogen bond is relatively similar in length to others of the same type (type II, four-way Br---Br) seen on surfaces in the literature[125,215,263,264]. The ketone side groups of the molecule are clearly visualised in the HR-STM imaging as a sharp pointed region. Notable similarities between the network presented here and one of the phases found by Yoon et al. in their study of dibromoanthraquinones on Au(111)[215] can be found – in particular due to the structural similarities between the two molecules (both being poly-aromatic molecules with two bromine and two ketone

substituents). Multiple orientations of the molecular packing were found, but the large number of possibilities (due to chiral segregation and the three-fold symmetry of the underlying substrate), combined with the large island sizes, meant that not all possible orientations of the packing were observed and thus a full analysis could not be performed.

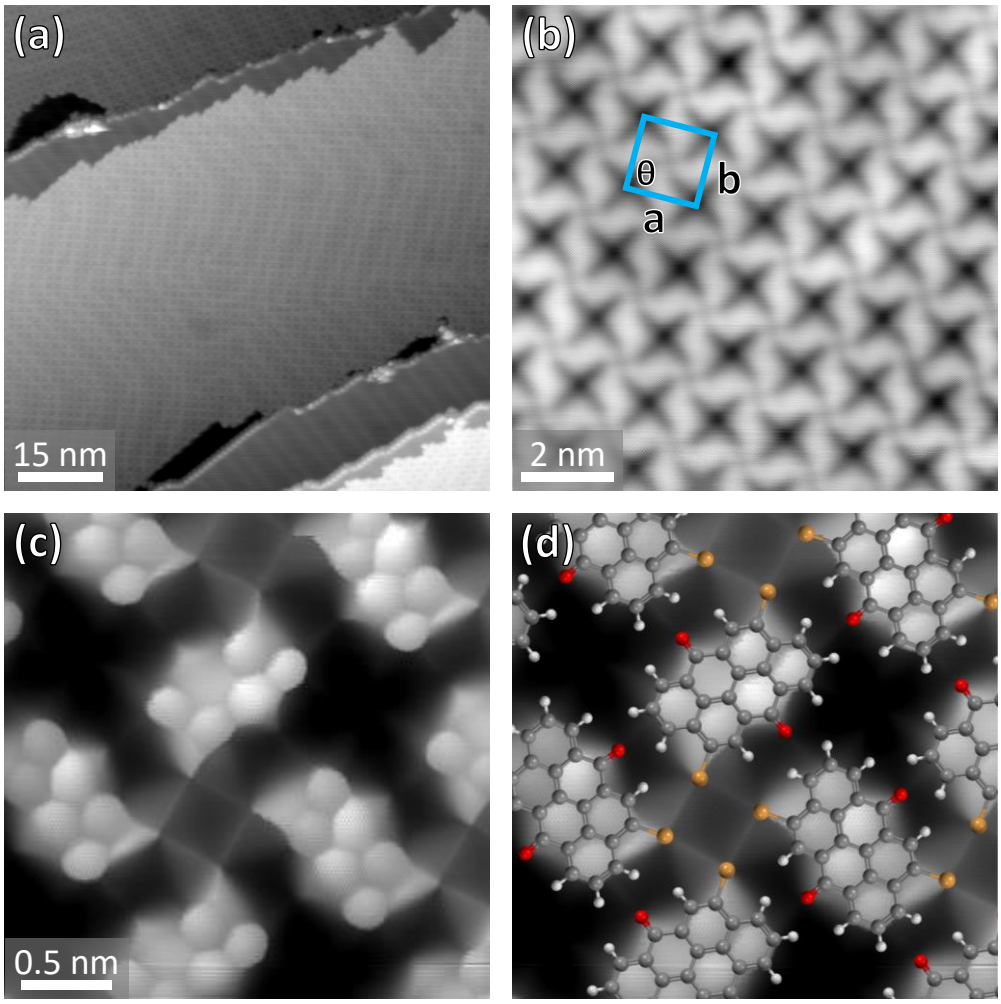

Figure 7.3. *(a) Large scale 7 K STM image (1.1 V) showing the VO3 islands on Au(111), with the herringbone reconstruction still visible underneath. (b) Zoom of an island (0.9 V), with the unit cell indicated. (c) HR-STM constant height CO tip image (30 mV) of VO3, with a scaled molecular model overlaid in (d). The sigma hole of each bromine atom approximately points towards the side of an adjacent bromine.*

dI/dV spectroscopy of VO3 on Au(111) at 7 K reveals a strong peak over the molecules in the unoccupied region of the spectrum at approximately +1000 ± 50 mV (**Fig. 7.4(b)**) – this is assumed to be the LUMO of the molecule. Variations in the energetic position of the LUMO could be seen in different parts of the islands and may

relate to the adsorption site of the molecule relative to the underlying substrate's herringbone reconstruction.

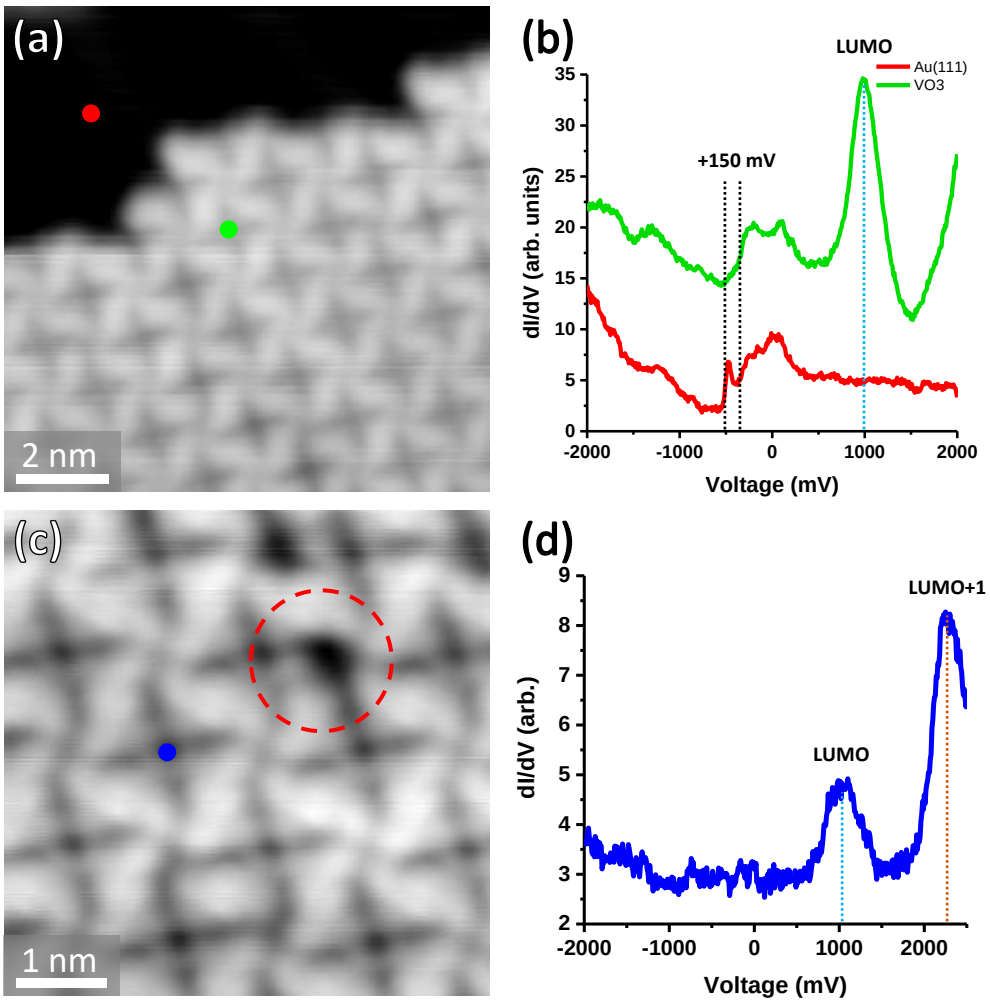

Figure 7.4. *(a) and (b) 7 K STM image (0.9 V) and dI/dV spectra of VO3 and the bare Au(111) surface, showing the LUMO peak and the shift of the Au(111) surface state under the molecules. Features at approximately 0 and −1300 mV may be related to the tip as they are present in both cases. (c) and (d) 7 K STM image (1.2 V) and a wide range spectrum showing a peak that is potentially related to the LUMO+1 of the molecule, and the damage (red circle) that can be caused by taking spectra at higher voltages. Attempts to mitigate this with the tip further away from the surface (hence the lower signal:noise ratio in (d)) did not make a significant difference.*

Constant height CO tip imaging at this voltage (**Fig. 7.5**) shows some similarity to the DFT calculated LUMO shape, although some asymmetry is also noticeable, possibly due to an asymmetric structure of the metal tip 'above' the CO molecule. Unlike the PXX NR occupied states, the 'p-wave' tip effects were not found to be as significant in this case – this could be related to a number of factors, including the positive bias

voltage (unoccupied states), the tip material (most probably Au), and the molecule itself.

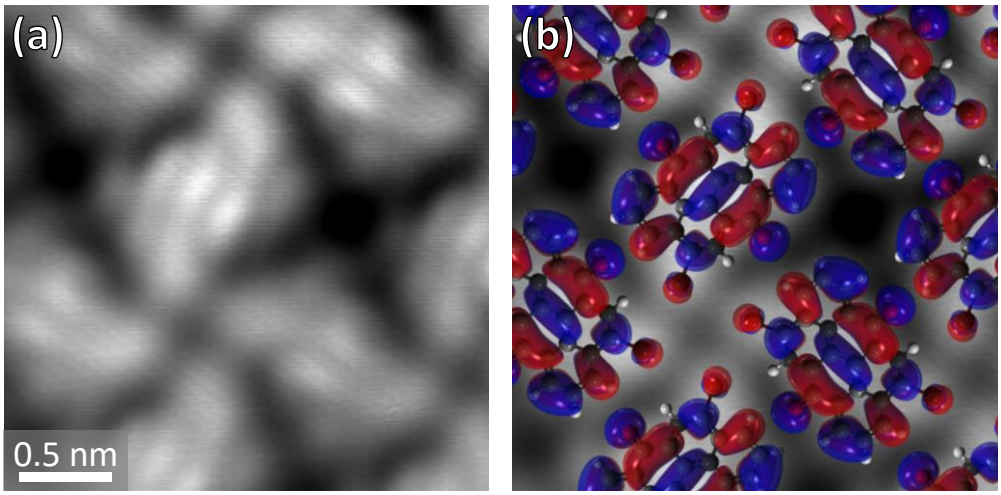

Figure 7.5. *Constant height CO tip STM (1.0 V) at the LUMO resonance of VO3, with a scaled overlay of the gas phase DFT-calculated LUMO.*

Taking spectra with a wide range (±2500 mV) also consistently reveals a further unoccupied state at approximately +2250 mV (**Fig. 7.4(d)**). However, recording spectra at higher voltages is usually found to result in damage to the molecules (such as debromination) and, as such, this peak cannot be assigned to the LUMO+1 with a high level of confidence. A shift is also observed in the onset of the Au(111) surface state underneath the molecule of approximately +150 mV, and is most probably due to the 'pillow effect' of the adsorbed molecule[84,206,231]. A weak feature at around −2000 mV and below is occasionally detected (data not shown), possibly indicating the position of HOMO of the molecule, leading to an estimated HOMO-LUMO gap of approximately 3.0 eV. In a similar fashion to the LUMO+1, recording spectra with a wider range that could include this resonance often resulted in damage to the molecules.

7.2.2 Nanoribbon Formation from VO3 on Au(111) with Annealing

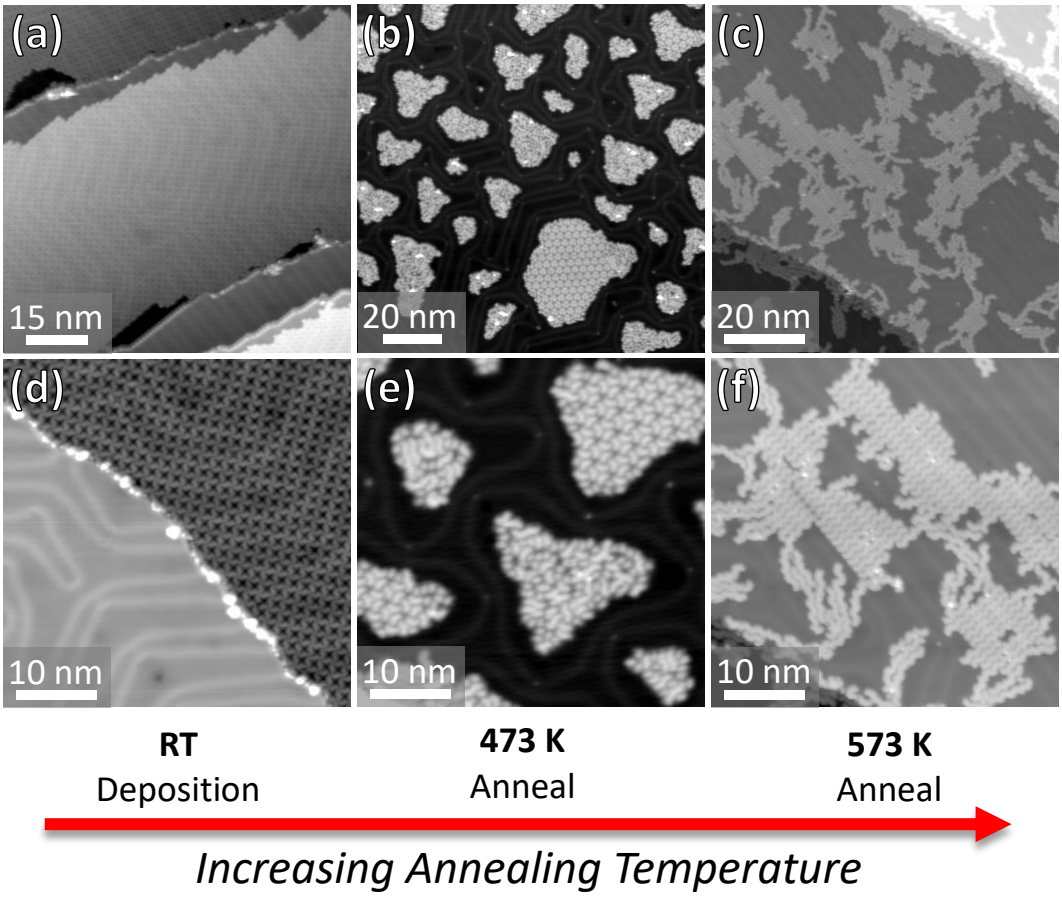

Figure 7.6. *7 K STM images of annealing experiments with VO3. (a) and (d): As deposited; self-assembled islands of VO3. (b) and (e): 473 K anneal; islands of short ribbons mixed with bromine atoms. (c) and (f): 573 K anneal; longer ribbon formation, desorption of bromine. Bias voltages: (a) 1.1 V (b) 0.9 V (c) 1.1 V (d) 0.9 V (e) 0.7 V (f) 1.1 V.*

The sample shown in **Fig. 7.3** was annealed in steps to 473 K and 573 K (**Fig. 7.6**). Annealing to 473 K resulted in the formation of similar structures to those seen with Br_2PXX: mixed islands (**Fig. 7.7(a)-(d)**) of bromine and short nanoribbon sections, with the herringbone reconstruction of the underlying Au(111) substrate significantly distorted around them. As suggested in the case of Br_2PXX, this is most likely the effect of the bromine contained within these islands that strongly binds to Au(111), altering the reconstruction, as has been reported for other strongly bound systems[129,130,244]. Similar islands that distort the herringbone have been observed in other Ullmann coupling reactions at surfaces when bromine atoms were still present[98,102].

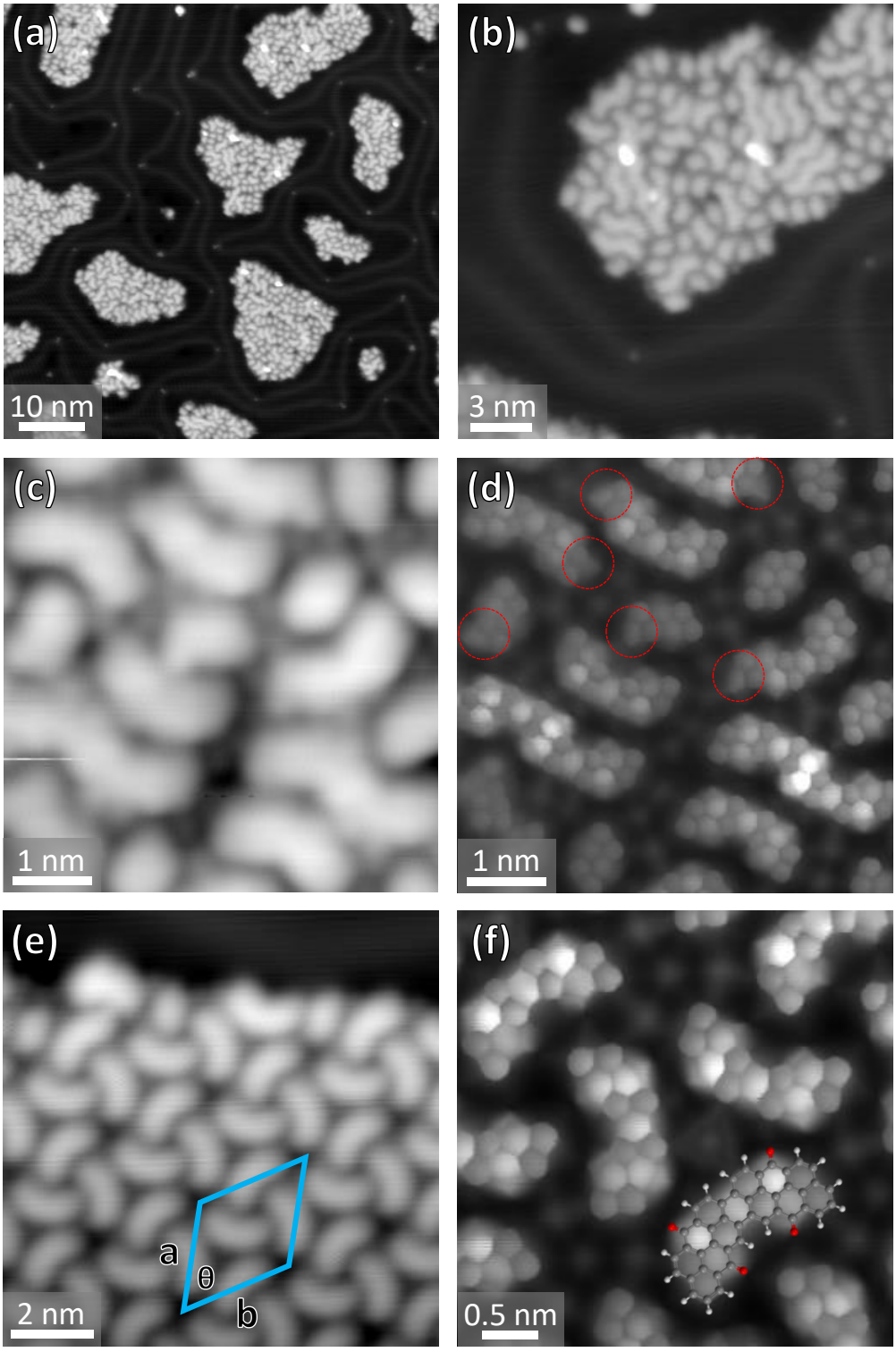

Figure 7.7. *(a) and (b) 7 K STM images (0.9 V and 0.8 V) of mixed islands of short ribbons and bromine atoms (formed after a 473 K anneal) imaged at different magnifications. (c) Zoom (0.5 V, CO tip) of a mixed island in constant current mode. (d) Constant height CO tip HR-STM image (30 mV) of the same area. Intact C-Br bonds are indicated with red circles. (e) Edge of an island of dimers/bromine (−0.4 V). (f) CO tip constant height STM (30 mV) zoom of a dimer/Br island, with the overlaid structure of a dimer. The faint objects in-between the molecules are assumed to be Br atoms.*

An example of an island containing various different-sized fragments after a 473 K annealing is shown in **Figs. 7.7(c)** and **(d)**, with and without HR-STM imaging. Unlike Br_2PXX, one regular type of island is also formed: a hexagonal arrangement of nanoribbon dimers and bromine atoms, with a unit cell of **a** = **b** = 2.72 ± 0.03 nm, θ = 60 ± 1°, shown in **Fig. 7.7(e)**. HR-STM imaging (**Fig. 7.7(f)**) clearly resolves the internal structure of these islands.

Several examples of molecules with intact C-Br bonds are indicated with red circles in **Fig 7.7(d)**. Interestingly, there is also evidence of other fusion reactions having taken place that do not follow the expected reaction scheme shown previously in **Fig. 7.1**. HR-STM imaging allows the identification of such cases; for example, **Fig. 7.8** shows two different cases of nanoribbon fragments that have fused to form a 5-membered ring. Within these fragments, the expected radical positions (from the homolysis of the C-Br bonds) have reacted, but with the molecules in the 'wrong' orientation for nanoribbon formation. A different dehydrogenation reaction has thus taken place, with the ribbons fusing to form a 5-membered ring instead of the desired 6-membered ring. These structures are also observed when annealing to higher temperatures. As it is in principle possible to arrange also the Br_2PXX molecules in a similar way that may form a 5-membered ring, it is not clear why such alternative ring closure reactions are not observed for Br_2PXX – it may relate to the position of the C-Br bond within the molecule.

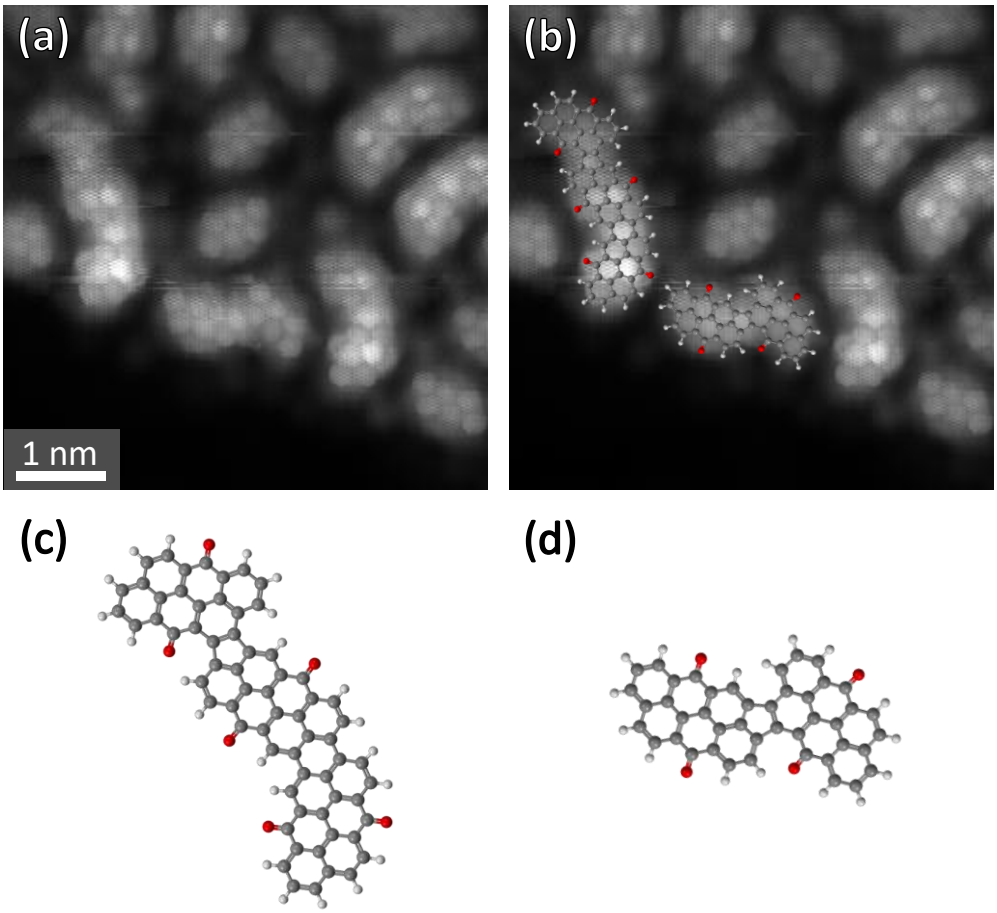

Figure 7.8. *(a) and (b) HR-STM with a CO tip (30 mV) of an area of mixed nanoribbons and bromine atoms, with two different possible examples of molecules that have fused to form a 5-membered ring. (c) and (d) Molecular models of the two fused molecules.*

Longer ribbons are also observed at the lower annealing temperature. In particular, islands of long nanoribbons packed together with their long axis perpendicular to the direction of the herringbone reconstruction lines can be seen (**Fig. 7.9(a)**). Within these chains, bright features at positions that approximately match the location of the herringbone lines are detected in STM images. At a first glance, it might simply be assumed that these bright areas are due to imaging the bright lines of the herringbone through the molecular adlayer, as has been seen previously in the literature[98,231,265,266] and within this thesis, for the island packing of both Br_2PXX and VO3 (**Fig. 7.3(a)**). However, zooming in on these regions reveals more interesting features.

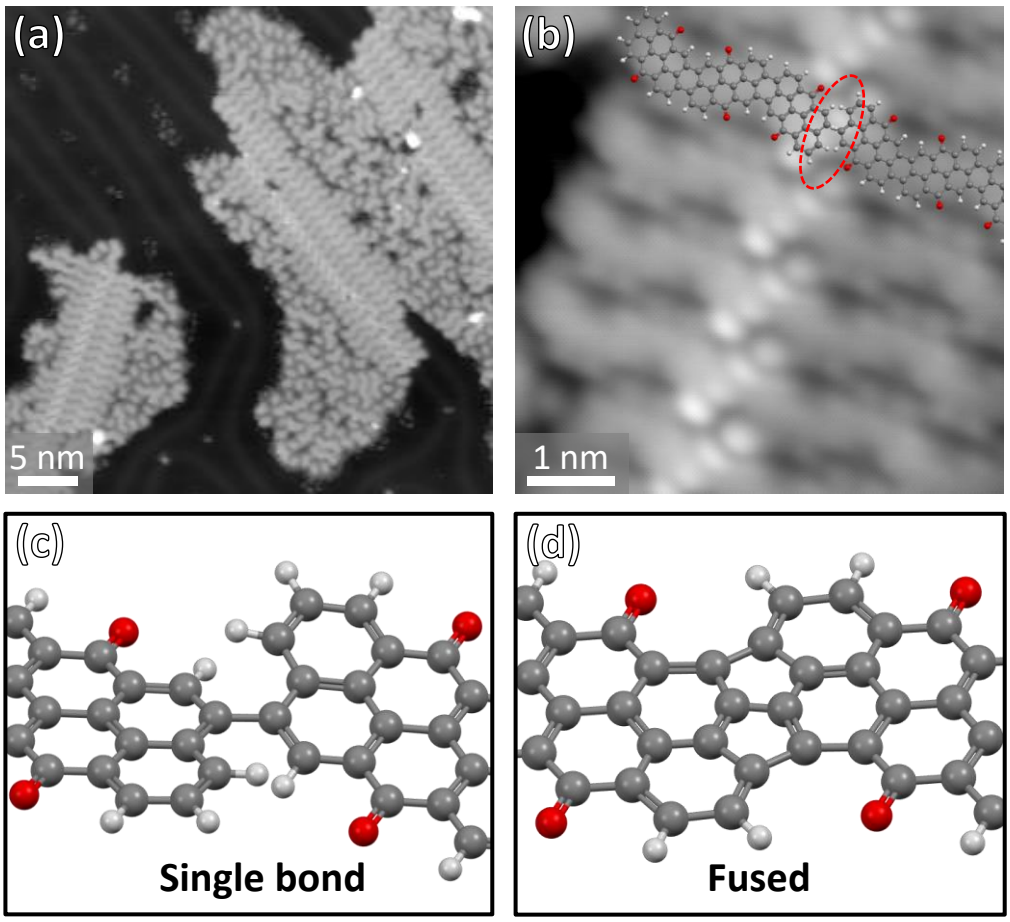

Figure 7.9. *(a) 7 K STM image (1.1 V) of longer ribbons packed together, with adjacent islands of mixed smaller fragments and bromine. Co-adsorbed CO clusters are also visible. Bright lines within ribbon islands can be seen, perpendicular to the long axis of the ribbons, and approximately following the underlying herringbone lines. (b) Zoom of the area in (a), showing the distinct bright features observed at positive voltage (1.1 V in this image). Two ribbons are overlaid onto the image, with the region of steric clashing highlighted. (c) and (d): Side views of two potential linkages in the end-to-end VO3 nanoribbon junctions. In (c) the ribbons are twisted to avoid steric clashing between C-H groups.*

Imaging at a positive bias (unoccupied states) reveals a distinct structure to these regions, with a line of bright signals at each nanoribbon row. Furthermore, the structure of these rows does not fit with a single continuous alternating nanoribbon passing over the herringbone lines. Overlaying two scaled molecular models of nanoribbons across these junctions (**Fig. 7.9(b)**) results in ends of the ribbons being too close to simply be interacting via intermolecular forces (e.g. van der Waals) due to steric hindrance. The measured distance instead fits better with the formation of at least one C-C bond between the end sections of the ribbons, potentially at the radical position that is expected after C-Br homolysis. This leads to two distinct possibilities for the structure of these junctions. The first is that a single C-C bond has formed at

this position, with the local sections of ribbon either side of this bond twisted (via a slight lift off from the surface) to avoid unfavourable steric clashes between C-H groups, shown in **Fig. 7.9(c)**. The second possibility (shown in **Fig. 7.9(d)**) is that, along with the formation of this C-C bond, there is also the fusing of C-H groups on both sides of this bond, leading to two new 5-membered rings (the possibility of such single ring-fusion reactions was already demonstrated above, see **Fig. 7.8**). The formation of these rings may lead to distinct electronic states located at these ribbon junctions, with a strong resonance in the unoccupied states.

There are two potential ways of clarifying this with STM experiments: through HR-STM (to reveal the structure of the junction and the location of the possible new rings) and dI/dV spectroscopy (to find any peak in the positive bias region/unoccupied states that is localised at these junctions). The latter is not necessarily a good demonstration of the hypothesis by itself, as there could also potentially be different states located at the singly bonded junction.

Attempts to image the junctions via HR-STM were only partially successful (shown in **Fig. 7.10**). The structure of the ribbons away from the junctions is relatively clear, but in the area around the junctions little can be made out. This may indicate that there is only a single bond and that no fusing reaction has taken place, as molecular rings that are pointing out of the surface plane are notoriously difficult to image (and interpret) with HR-STM and NC-AFM[267]. In particular, as the signal in HR-STM depends on the tunnelling current, which in turn is not purely affected by the height of molecules at the surface, but also the local density of states, few solid conclusions about conformation may be made from the imaging of three-dimensional molecules at surfaces.

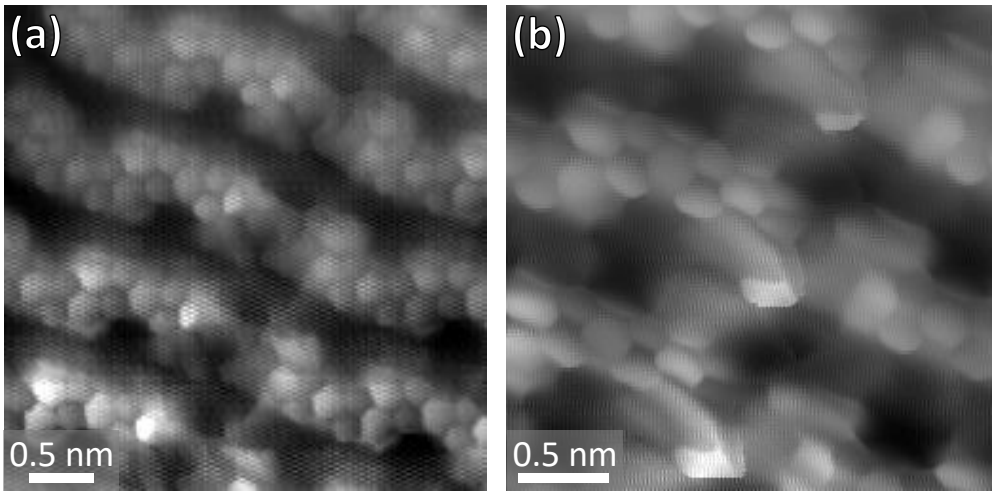

Figure 7.10. *(a) HR-STM (CO tip, 30 mV) of junctions between nanoribbons. (b) Zoom (30 mV) of the same region, showing that, close to the junction, ring features are no longer resolved.*

Imaging the molecules at a low negative bias in constant current mode, in which they appear to be relatively featureless (and thus imaging is likely not strongly affected by changes in the LDOS), does show some slight differences in brightness around these junctions (**Fig. 7.11(a)** and **(b),** shown with a line profile) when compared to an equivalent position at the other end of the molecule, which could in turn indicate differences in apparent height.

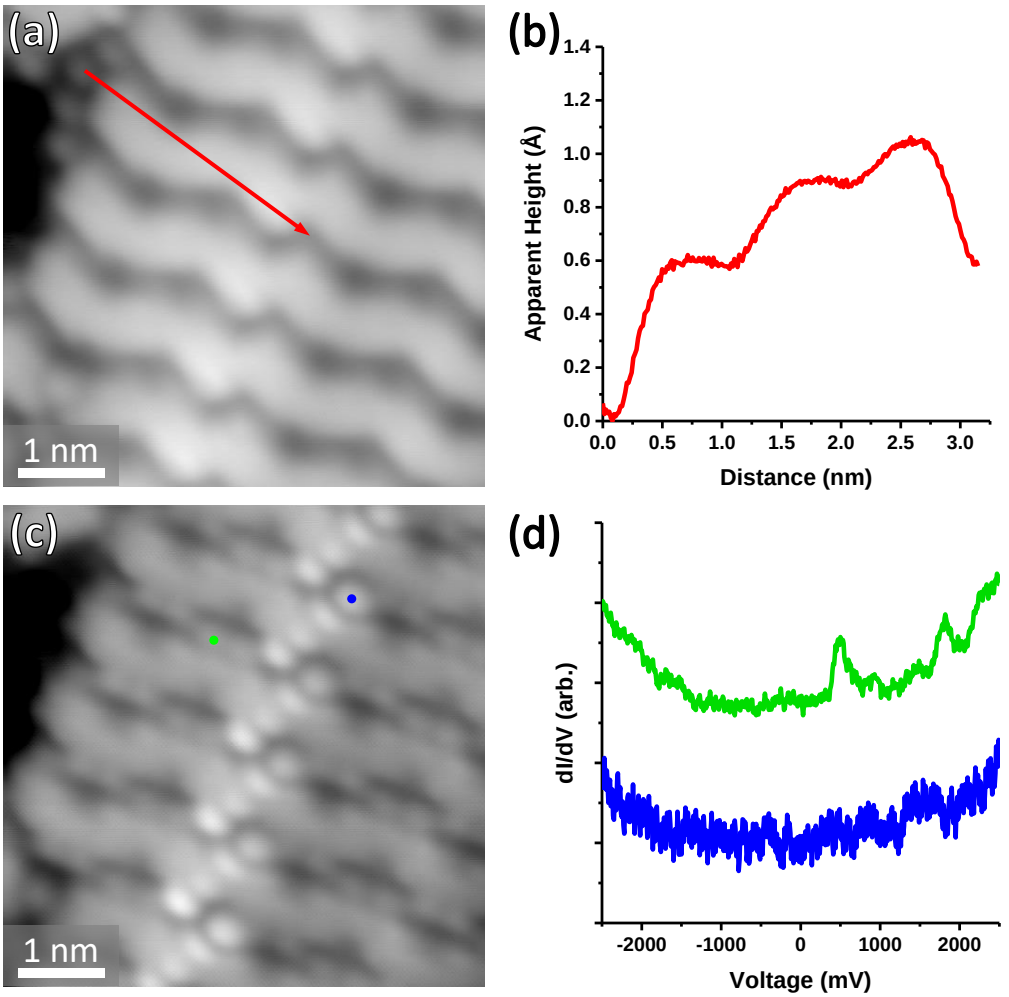

Figure 7.11. *(a) Occupied states 7 K STM image (−0.8 V) of the same region as (c), with an apparent height profile (b) along the red arrow demonstrating the difference in apparent height at the junction region over equivalent positions along the ribbon. (c) and (d): STM image (1.1 V) and corresponding dI/dV spectra of the junction and another part of a ribbon, demonstrating that unoccupied states features are not observed over the junction. The state at around 0.5 V on the 'normal' section of the ribbon is attributed to the LUMO, as discussed later in this chapter.*

On the other hand, it is still possible that there is simply a state interfering with HR-STM imaging (**Fig. 7.10**) that obscures the structure of the junction.

dI/dV spectroscopy (**Fig. 7.11(d)**) does not reveal any particular features localised at these junctions, despite their clear features in the positive bias range constant current imaging. This may be further proof that the bright features may relate to the twisting of the ribbon ends rather than the formation of new rings and thus new states. The features seen at positive voltages may instead merely correspond to the distinctly shaped state seen over the rest of the nanoribbons, with an increased level of brightness related to an apparent height increase.

The DFT-optimised geometry of a fused VO3 dimer is presented as a simplified model for the fused junction in **Fig. 7.12.** As is clear from the side-view shown in **Fig. 7.12(b)**, a significant buckling of the ribbon takes place in order to accommodate the shorter bond (between the five-membered rings) in the centre of the fusing position. This buckling, combined with the shorter bond, results in a poor fit when overlaid onto any images of the junctions.

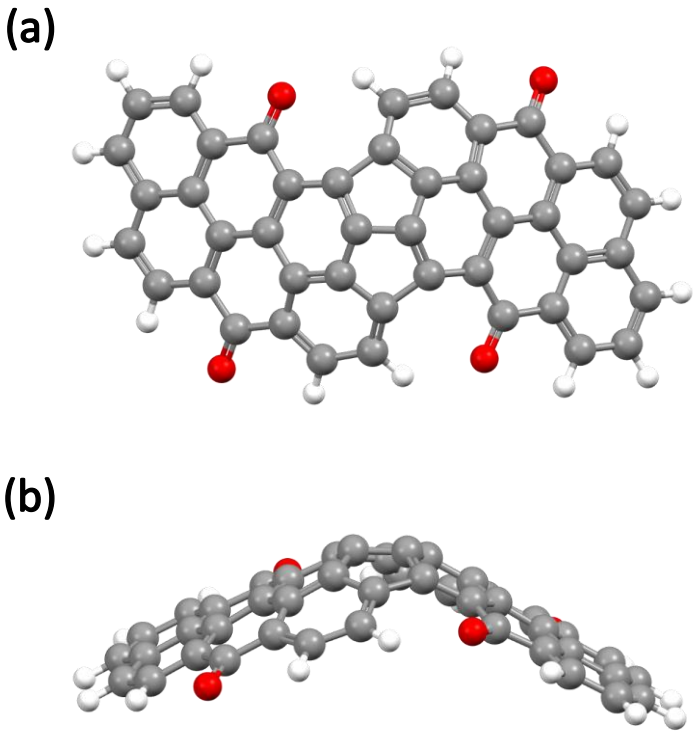

Figure 7.12. *(a) top view and (b) side view of the DFT-optimised structure of a doubly-fused dimer. The structure buckles and contracts in order to accommodate the shorter bonds required by the 5-membered rings. DFT calculations performed by Harry Pinfold, University of Warwick.*

Whilst it is not possible to be certain about the structure of these junctions, the above evidence points more towards the formation of only a single C-C bond and the twisting of the ribbons at their connection points. The location of these binding points over the herringbone lines may be related to an increased level of stability at these positions for adopting the twisted conformation. Future experiments with NC-AFM imaging could potentially clarify the structure of these junctions, as the Δf signal in NC-AFM is not subject to the effects of changes in the LDOS with bias voltage[166,168].

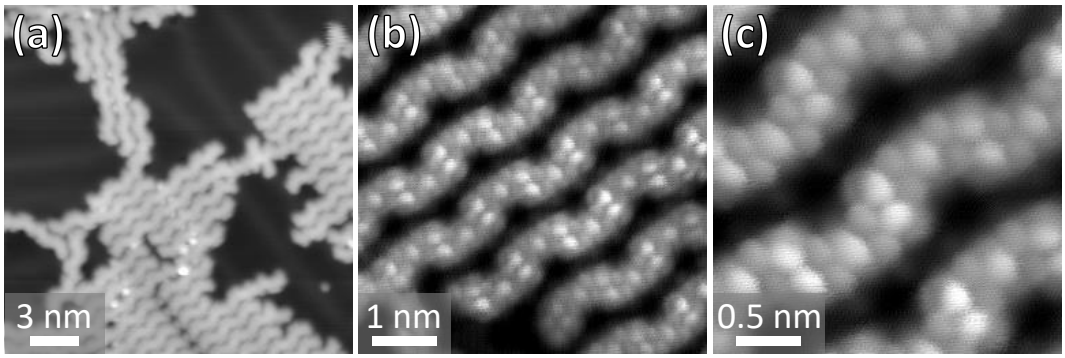

Figure 7.13. *(a) 7 K STM image (1.1 V) of VO3 after annealing to 573 K on Au(111). No herringbone distortion around the nanoribbon islands is observed, most probably due to the desorption of bromine. (b) and (c) HR-STM (CO tip, −10mV) of long VO3 ribbons.*

Increasing the annealing temperature to 573 K results in the formation of much longer ribbons (**Fig. 7.13**) some of which appear to be bonded in unusual locations/orientations. This is most probably due to more unwanted side-reactions, such as dehydrogenation reactions at other positions on the molecules. Few signs of bromine remain (most probably due to its desorption, in a similar fashion to Br_2PXX at a similar annealing temperature), with the herringbone no longer distorting around nanoribbon islands.

Reliable dI/dV experiments on VO3 ribbons of increasing length were found to be significantly more difficult to perform than those on the PXX nanoribbons. Shorter ribbons and monomers are mostly only found at lower annealing temperatures (such as 473 K) in the presence of co-adsorbed bromine (e.g. **Fig. 7.7**), which may shift the energetic position of dI/dV peaks[101,247–249] As VO3 does not demonstrate similar repulsive characteristics to PXX (and PXX NRs), short isolated ribbons that could be studied without considering the effects of locally adsorbed species were rarely, if ever, found. Because of these issues, it was decided to focus on short ribbons surrounded by bromine atoms, which still seem to have relatively consistent peak positions in their dI/dV spectra. As such, the dI/dV spectra for ribbons of different lengths are tentatively presented in **Fig. 7.14** as being indicative of the general trend of increasing ribbon acceptor strength with increasing length. As stated above, the exact values for peak shifts, however, have some considerable uncertainty, which is particularly true for monomers and dimers that were mainly found packed into islands with bromine

atoms. It should be noted (for example, when comparing **Fig. 7.4** to **Fig. 7.14**) that there is a considerable difference in the peak position for the monomer LUMO. This shift can be attributed to the effect of both no longer having either of its C-Br groups (as shown previously with Br_2PXX in **Chapter 5**), as well as the effect of the surrounding adsorbed bromine atoms.

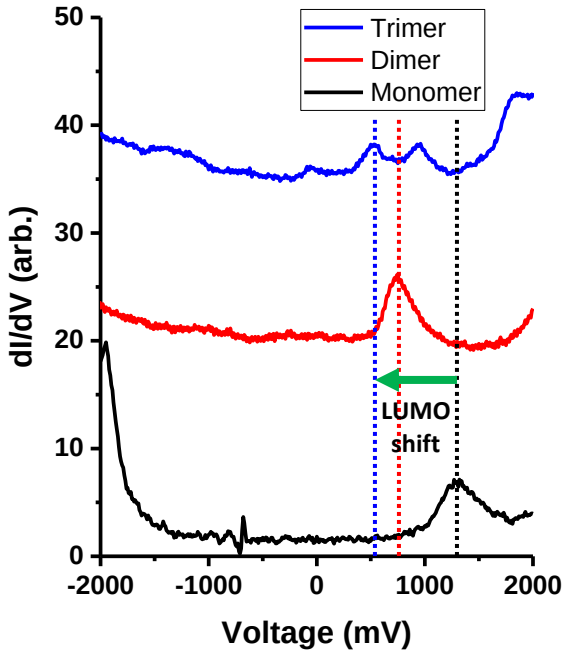

Figure 7.14. *dI/dV spectra of VO3 nanoribbons of varying lengths, with a down-shift in the LUMO indicated.*

Despite these issues, the increased acceptor strength upon nanoribbon formation is clear from the spectra from the downshift in energy of the LUMO state. The shift quickly levels off at around +0.5 V with increasing length, as verified by measurements on longer ribbons (data not shown here). This result potentially paves the way towards using VO3 nanoribbons in donor-acceptor complexes. For example, the LUMO value of longer VO3 ribbons is lower than that of the classic electron acceptor molecule tetracyanoquinodimethane (TCNQ), which has its LUMO (as measured by STS) at approximately +0.7 V when adsorbed on Au(111)[231].

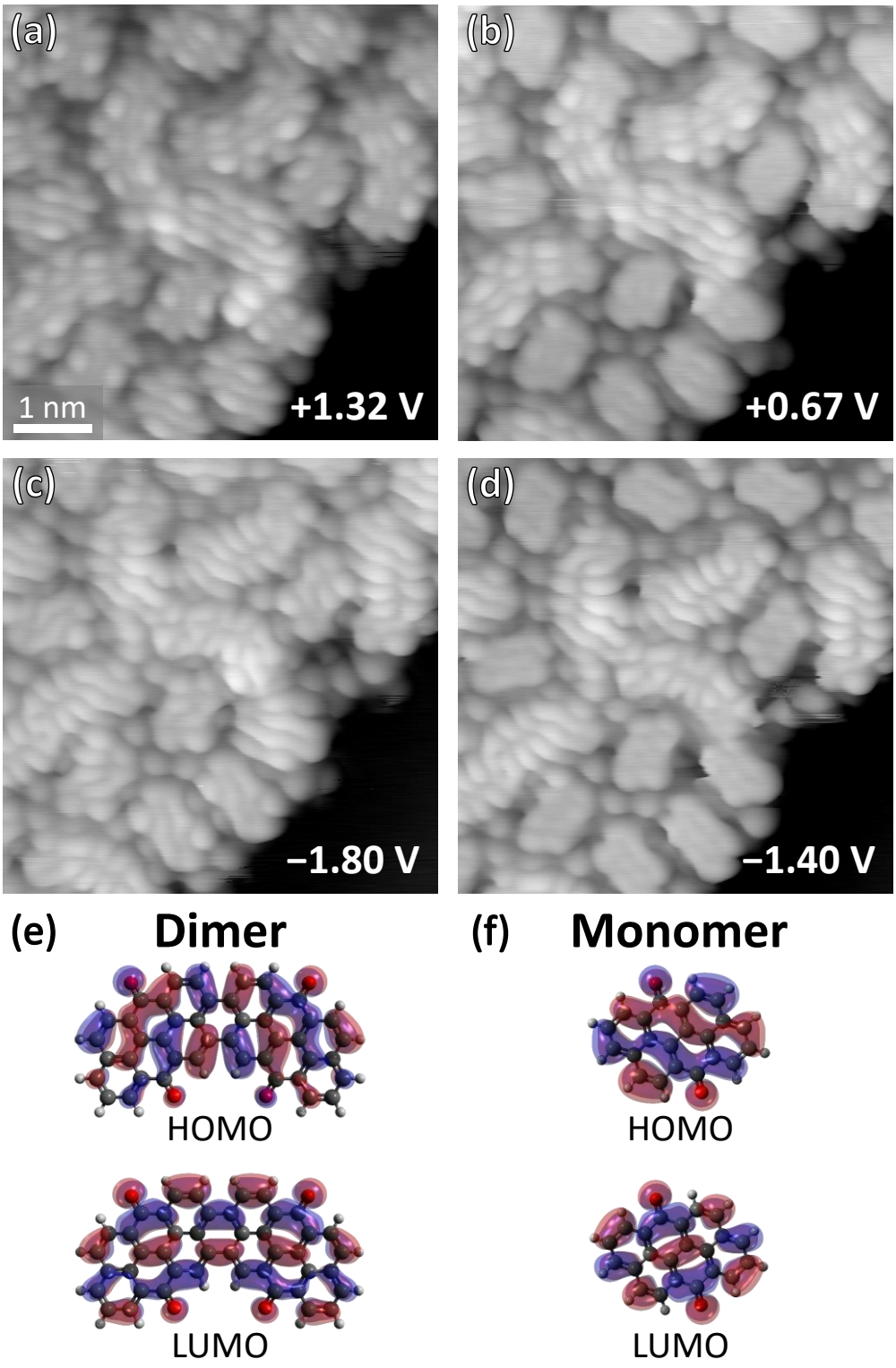

Figure 7.15. *(a)-(d) Voltage dependent constant current STM imaging of a mixed VO3 nanoribbon/bromine island with an unknown tip state. (a) and (b) Unoccupied states, (c) and (d) Occupied states. More positive/more negative voltages were required to clearly image the LUMO/HOMO of the monomers than the dimers, implying a narrowing in the HOMO-LUMO gap with increased ribbon length. (e) and (f) DFT-calculated frontier MOs for the monomer and dimer (without bromine). A clear resemblance to the STM images can be seen: HOMO in occupied states (negative voltages), LUMO in unoccupied states (positive voltages). Calculations performed by Harry Pinfold, University of Warwick.*

Voltage dependent STM imaging was performed on VO3 nanoribbons of various lengths. Some hints of the shapes of both occupied and unoccupied states were seen with a tip of unknown character (**Fig. 7.15**; the tip may have picked up a bromine atom or molecule from the surface, leading to a drastic increase in resolution when compared to typical metallic tip states), despite the lack of clear peaks in the occupied states of the spectra of the ribbons. This lack of peaks could be related to using the same stabilisation conditions for the entirety of each dI/dV spectrum, and the disparity in signal intensity when comparing occupied to unoccupied states. A clear demonstration of the increased acceptor strength of ribbons with increased length is shown in **Fig. 7.15** – at lower positive voltages in constant current imaging (**Fig. 7.15(b)**), the distinctive LUMO shape is mainly visible on the dimer nanoribbons and not the monomers, because its energy is lower in the nanoribbons with increased length. At higher positive voltages (**Fig. 7.15(a)**), it becomes clear in both. When imaging at a negative voltage (in this case, −1.4V and −1.8V), another shape becomes clear, with a resemblance to the HOMO of the molecules, with the same apparent trend (more negative voltages are required to clearly image the monomer HOMO). This dependence in both voltage ranges is consistent with the narrowing of the HOMO-LUMO gap with increased ribbon length. The DFT-calculated gas phase HOMO and LUMO shapes are presented in **Figs. 7.15(e)** and **7.15(f)**, showing a good fit with the shapes of both HOMO and LUMO.

7.3 Conclusions

Vat Orange 3 has proven to be a useful analogue to Br_2PXX for forming electron acceptor-type nanoribbon structures, with the *acceptor* strength clearly increasing with nanoribbon length via a lowering of the LUMO energy.

The deposition of the VO3 molecule on room temperature Au(111) (prior to nanoribbon formation) was studied via STM and found to result in islands consisting of a self-assembled structure held together by halogen bonding, with a noticeably increased stability (characterised by a much lower mobility, as well as more extended island structures) over Br_2PXX at 77 K. Annealing this assembly resulted in nanoribbons of various lengths, connected by the formation of two C-C covalent bonds. Other interesting connections between ribbons were also observed, which most

probably are due to the formation of a single bond between ribbons, with some twisting of the end groups in the junction region to avoid steric clashes. dI/dV experiments give indication of the increased acceptor strength upon formation of nanoribbons, with an overall downward shift of the LUMO energy. This is further supported by voltage dependent imaging of the ribbons, which show a distinct LUMO shape for longer ribbons at lower voltages than the monomers.

The formation of VO3 acceptor nanoribbons further extends the possibility for a variety of tuneable extended nanoribbon structures, also allowing for the potential formation of mixed donor-acceptor type ribbons via an on-surface reaction with Br_2PXX.

8 2D Donor-Acceptor Systems: Non-covalent and Covalent Mixtures

8.1 Introduction

Monolayer donor-acceptor (D-A) systems at surfaces are commonly studied as 2D analogues to typical 3D D-A systems. These assemblies share similarities with their 3D counterparts, but the mechanism of charge transfer is substantially different. Often, the required orbital overlap between adjacent donor/acceptor unit frontier orbitals is not possible when adsorbed at an interface in a mixed monolayer, due to their orientation normal to the surface (in typical flat adsorption of planar organic molecular systems on metallic substrates). The main drivers of charge transfer in bulk structures are the ionisation potential and electron affinity of donor and acceptor molecules, respectively. The situation is more complex at metallic interfaces, with charge transfer to and from the metal itself, along with the effects of electrostatic screening of the highly polarisable metal, and the potential electronic hybridisation between the organic overlayer and the substrate[88].

There are many examples of monolayer donor-acceptor systems at metallic surfaces in the literature. A commonly used acceptor unit is the TCNQ molecule (**Fig. 8.1(a)**) and its derivatives. 2D analogues of the famous 3D donor-acceptor system TTF/TCNQ (the first 'organic metal'[268]) have been examined via STM[85,86], and various studies involving tweaking either the donor or acceptor structure have been undertaken to examine the effect on the resulting charge transfer. These include TMTTF/TCNQ[269], TTF/TNAP[88], TTT/TNAP[270] and 6T/F_4TCNQ[271]. Other D-A systems involving TCNQ also include co-depositions with alkali metals[89,272].

In the first half of this chapter, PXX is co-deposited with TCNQ onto metallic substrates to study its behaviour at surfaces as an electron donor. This behaviour will be contrasted with the 3D crystal of PXX-TCNQ (**Fig. 8.1(b)**), first studied in the 1990s[273], which did not display similar properties to TTF-TCNQ; in particular, rather than a columnar arrangement that allows for metallic type conduction down a line of

TTF or TCNQ molecules, the PXX-TCNQ crystal was instead found to have columns of alternating molecules. The estimated level of charge transfer (from the geometry of the TCNQ molecule, which distorts upon accepting charge) was thought to be low in the crystal, with an ensuing low estimated conductivity. D-A crystals in which PXX has been combined with halogenated TCNQ derivatives such as F_2 and F_4-TCNQ have also been studied in terms of their charge transfer and suitability for organic field-effect transistor devices[274], with higher levels of charge transfer found. Other 3D complexes in which PXX acts as an electron donor have also been found[275], including salts with I_3 and also $[Ni(mnt)_2]$.

Particular emphasis will be placed on a comparison with the TTF-TCNQ (and related) complexes that have been studied at surfaces, as they offer an interesting reference when relating bulk to 2D properties. A comparison to a similar co-deposition that instead involves PXX nanoribbons (of a stronger donor character, as shown in **Chapter 6**) will also be made.

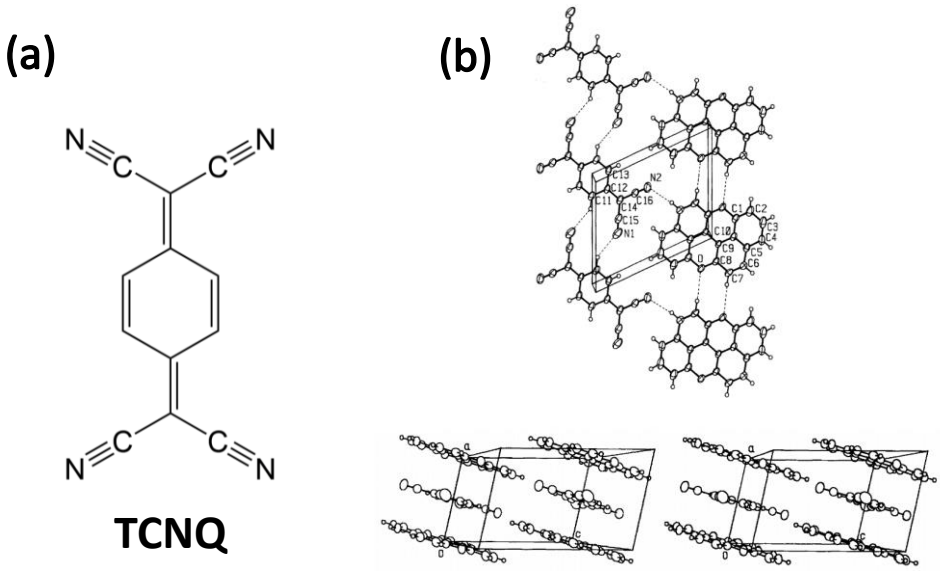

Figure 8.1. *(a) Structure of TCNQ, a prototypical electron acceptor molecule. (b) Crystal structure of PXX-TCNQ, adapted from Hjorth et al.*[273] *The alternating stacks of PXX and TCNQ can be seen in the lower half of (b).*

In the second half of this chapter, preliminary investigations into mixed PXX/VO3 nanoribbons will be presented. Both Br_2PXX and VO3 have been shown in this thesis to form nanoribbons on Au(111) with annealing, potentially opening the door to the formation of nanoribbons consisting of both units in sequence, to form a type of donor-

acceptor polymer. The sequencing of the resulting polymers will be studied, as will the electronic properties of simple examples (dimers, trimers) of the mixed nanoribbons, including how the sequencing of these trimers affects the observed peaks in the STS spectra.

Recently, donor-acceptor polymers have been widely studied in the context of their use in photovoltaic devices. Forming regular arrays of donor-acceptor units allows the narrowing of the band gap, and precise control of these units in turn allows the tweaking of optoelectronic behaviour and other physical properties such as their packing and microstructure[276]. The characteristics of PXX-VO3 polymers may be different to typical D-A polymers due to their rigid conjugated ribbon backbone – parallels may instead be drawn to graphene nanoribbon heterojunction type structures. Examples of these from the literature include precise control of monomer structure to form ribbons with junctions that involve changes of width and thus band gap (for armchair GNRs)[208,277], as well as regular heteroatom doping for similar results, along with rigid shifts in the gap[11,159,237,253,278]. As previously mentioned, however, the anti-aromatic nature of rings in both component molecules make drawing precise parallels with these structures difficult.

8.2 Results and Discussion

8.2.1 TCNQ on Au(111)

To act as a reference, the behaviour of TCNQ adsorbed alone onto Au(111) is shown in **Fig. 8.2**. The results shown reproduce previous measurements of this system well, as first reported by Torrente et al.[231] The molecule packs into large islands of a brickwork network via CN---H-C hydrogen bonding, with a unit cell of parameters **a** = **b** = 9.00 ± 0.07 Å, **θ** = 97 ± 2°. dI/dV measurements of TCNQ on Au(111) have also been described previously in the literature[84,231], showing a peak in the unoccupied states at approximately + 0.7 V that was attributed to the LUMO state of the molecule due to its distinct shape in STM imaging at positive biases[231]. The molecule has a featureless appearance when scanned at typical negative bias voltages (occupied states, **Fig. 8.2(a)**). HR-STM (CO tip) measurements on TCNQ islands are shown in **Fig. 8.2(b)**, with the distinct shapes of the cyano groups and central ring resolved well, with similarities in appearance to NC-AFM images of F_4TCNQ in the literature[279,280].

The herringbone reconstruction is seemingly unaffected by the adsorption of TCNQ; it is clearly detected through the islands in STM imaging, indicating a weak binding with the surface.

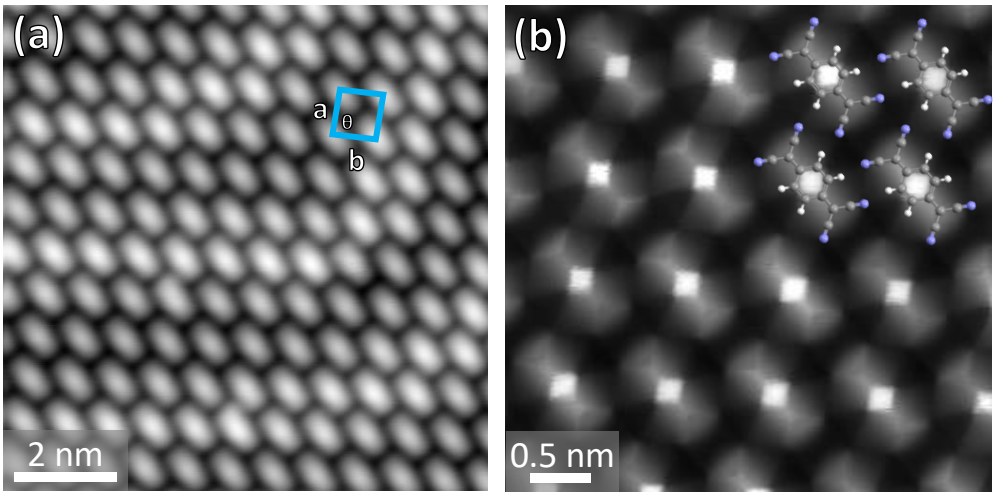

Figure 8.2. *(a) STM image of a TCNQ island on Au(111) at 7 K, −1.0 V. (b) CO tip constant height HR-STM image (−30 mV) of the same island, with overlaid TCNQ models.*

8.2.2 PXX and TCNQ on Au(111): Structure

After a room temperature sub-monolayer deposition of both PXX and TCNQ on Au(111) (in sequence, with an initial deposition of PXX followed by TCNQ), large islands of a mixed phase are observed in low temperature STM imaging (**Fig. 8.3(a)**). At 77 K, PXX molecules outside of the islands are mobile; as reported earlier in this thesis, PXX is extremely mobile at sub-monolayer coverages on Au(111). At 7 K, these PXX molecules are immobilised and dispersed in a similar manner to the deposition presented in **Chapter 4**, with short H-bonded chains and isolated molecules mostly confined to the fcc regions of the herringbone. Islands of pure TCNQ are also occasionally found.

Two types of mixed PXX-TCNQ islands are observed. The majority phase (**Figs. 8.3(b)** and **(c)**) consists of large islands of alternating rows of PXX and TCNQ molecules with a unit cell of **a** = 2.02 ± 0.02 nm, **b** = 0.83 ± 0.01 nm, **θ** = 92 ±2°. However, from examining any STM image of the assembly at lower bias voltages it is obvious that within the TCNQ rows, there are several ‘types’ of TCNQ, as described later in this chapter. As a consequence, whilst this unit cell describes the geometrical

arrangement of both molecules, it does not describe the repeat unit of the molecules in terms of their electronic state, as will be discussed later in this chapter.

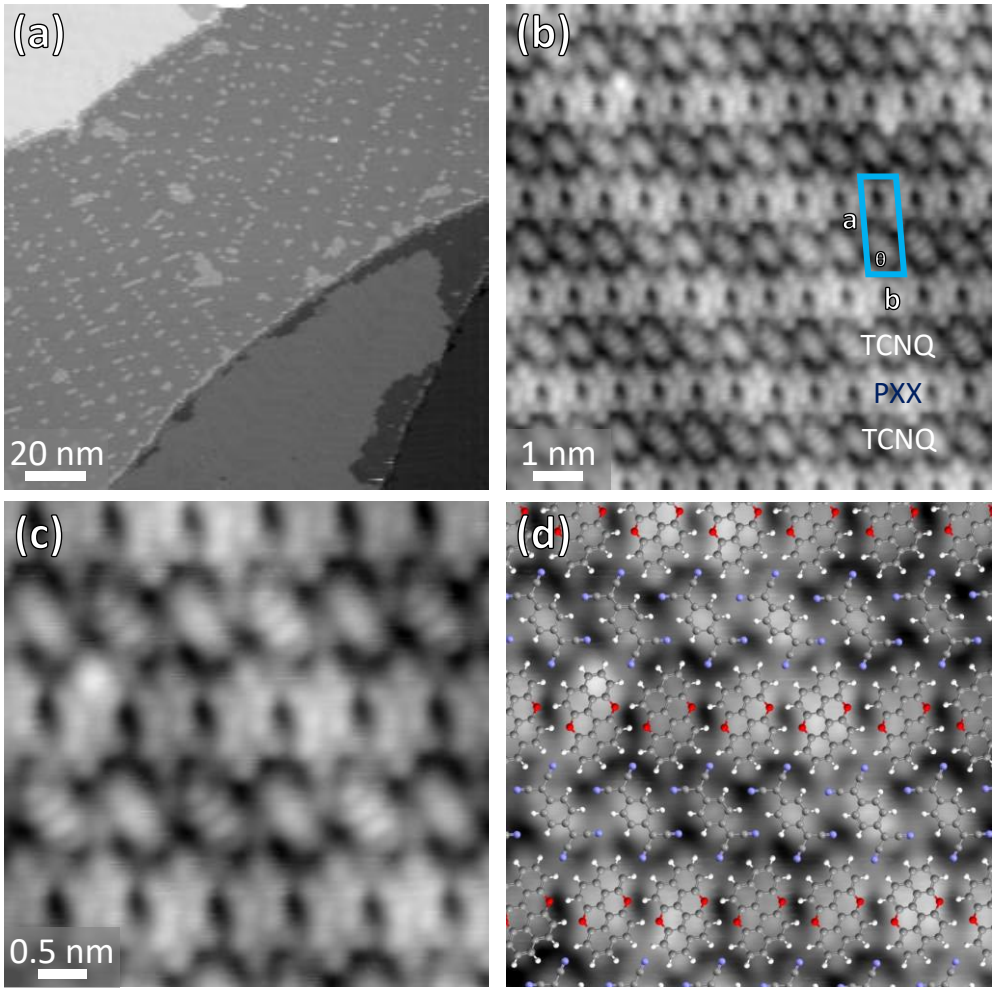

Figure 8.3. *(a) Overview 7 K STM image (1.3 V) of the PXX/TCNQ on Au(111) co-deposition. Large islands of the mixed row phase can be seen, with PXX molecules spread out over the terraces in between, along with small islands of the minority core-shell mixed phase. (b) A mixed PXX/TCNQ row island, with the unit cell indicated (Bias voltage −1.1 V). (c) and (d) Zoom (−0.8 V) of the same island, with a molecular overlay in (d).*

Within the rows, the molecules are in positions that favour hydrogen bonding (**Fig. 8.3(d)**). Similar O---H bonds to those seen in between adjacent PXX molecules in **Chapter 4** can be observed within the PXX rows in the mixed phase; however, the H-bonds are slightly shorter (by 0.2 Å) in this case, as they are 2.0 ± 0.1 Å. Similarly, the TCNQ molecules are also oriented in a position that is slightly offset from the rows observed in the pure TCNQ packing on Au(111), but still may allow for hydrogen bonding between CN and CH groups. H-bonding between TCNQ and PXX molecules may also occur, with the structure being reminiscent of the alternating plane in the 3D

crystal shown above in **Fig. 8.1(b)**. The row-type mixed phase also bears a strong resemblance to the assembly reported in the literature for some of the other donor-acceptor pairs on surfaces in which TCNQ and related molecules participate; in particular, TTF/TCNQ[85,86], TMTTF/TCNQ[269], and TTF/TNAP[88].

A minority mixed phase is also found on the surface. Small core-shell type islands are observed in STM (**Fig. 8.4(a)** and **(b)**), with a central region consisting of TCNQ, surrounded by a monomolecular rim of PXX molecules at the borders of the islands. As will be discussed later in this chapter, the appearance of the TCNQ molecules in the core of these islands in STM is found to be substantially different to those found in the row-type mixed phase, and very much depends on the bias voltage polarity. Similarly structured core-shell islands have been observed with TCNQ and another donor molecule, TBP[84]. The islands are generally too small to exhibit a repeat unit in their core, and the shell structure (i.e. the arrangement of the PXX molecules) is highly irregular.

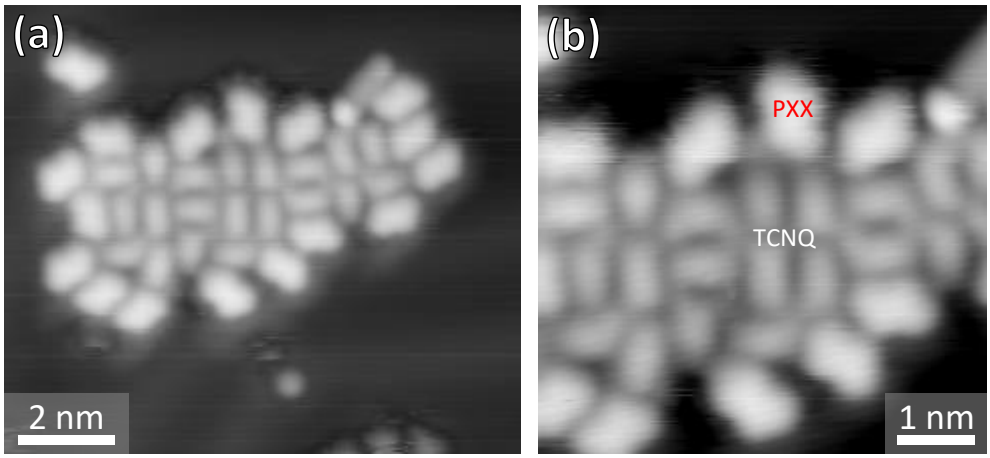

Figure 8.4. *(a) 7 K STM image (1.1 V) of a core-shell island. (b) Zoom (0.5 V) of the island in (a), with identifying labels for each molecule.*

Elsewhere on the surface, large islands of pure TCNQ may also be observed. The dependence of the relative amounts of these assemblies on the overall coverage of each molecule was not examined, and may provide interesting future avenues of research (in particular, whether the core-shell islands can be increased in number/size by altering the PXX:TCNQ ratio).

8.2.3 PXX and TCNQ on Au(111): Electronic Properties

Voltage dependent imaging and dI/dV spectra of the mixed row PXX/TCNQ assembly show many similarities to results on the TMTTF/TCNQ on Au(111) system presented in the literature by Torrente et al.[269]. In particular, the results suggest that TCNQ can accept a single charge when co-assembled with PXX in a mixed row phase, and that STM measurements can also affect the molecular charge state.

In the TMTTF/TCNQ study, it was found that in the mixed assembly with TMTTF, TCNQ adopts one of two possible charge states: neutral or singly charged. These differences in charge state were attributed to variations in the underlying adsorption potential that influence the alignment of the TCNQ LUMO with the Fermi level when assembled in the mixed phase. Changes in charge state from being neutral in the 'pure' TCNQ packing can also be attributed to the local presence of a 'donor' molecule, as will be discussed below. Furthermore, distinct, sharp peaks and 'dips' in dI/dV spectra of the TCNQ molecules were observed. These features were explained via a double barrier tunnelling junction (DBTJ) model, in which the TCNQ is decoupled enough from the underlying Au(111) surface that when an electric field is present (i.e. when the STM tip is in close proximity and a bias voltage is applied), there is a voltage drop between the TCNQ molecule and the metal sample. This model is presented in **Fig. 8.5**. As a result of this voltage drop, the alignment of the states on the TCNQ relative to the Au(111) surface chemical potential may change with the bias voltage. By contrast, if the coupling of the TCNQ molecule with Au(111) was stronger, the relative energy alignment would not change with the applied bias voltage, i.e. the electronic structure of molecule and surface would move "rigidly" with the bias. For a singly charged molecule, if the singly occupied LUMO (i.e. the SOMO) is raised above the surface chemical potential when a voltage is applied, then a discharging from the molecule to the metal may take place, resulting in a spike observed in the dI/dV spectrum at positive voltage. This spike is due to changes in the tunnelling characteristics of a neutral molecule relative to a charged one; these changes are associated with the 'coulomb blockade' effect of tunnelling into a charged molecule[269]. Likewise, a neutral molecule's LUMO may be pushed down relative to the surface potential by applying a negative bias, and thus a charge transfer (with a corresponding charging 'dip' in the dI/dV spectrum at the required voltage) may take place from the surface to the SUMO. In some cases, a second dip at a more negative

voltage may also be observed – this may be related to a second charging event, i.e. the formation of $TCNQ^{2-}$.

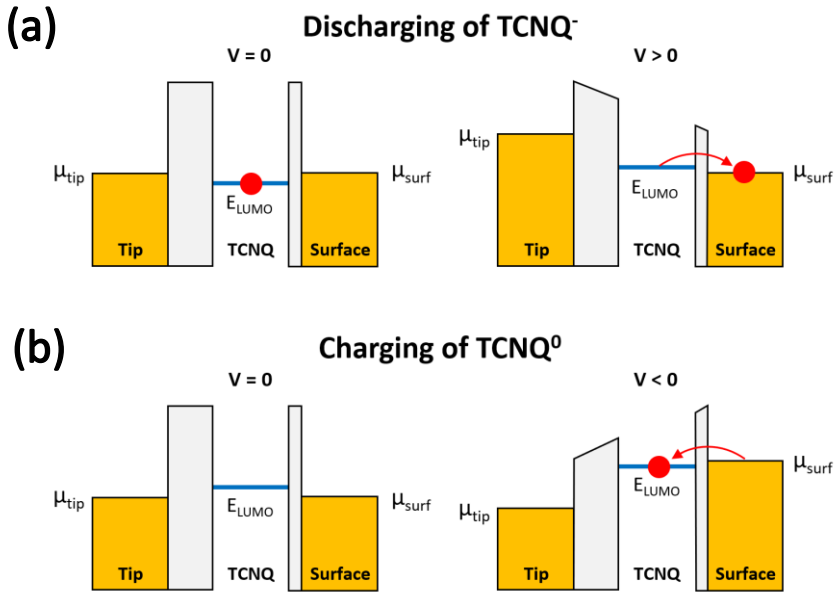

Figure 8.5. *Simplified version of an energy diagram adapted from the study of TMTTF/TCNQ*[269]*. Electrons are represented by red circles. (a) Model for the discharging of a $TCNQ^-$ in the mixed PXX-/TCNQ assembly via the application of a positive bias voltage to the surface. (b) Model for the charging of a neutral TCNQ molecule when applying a negative bias voltage to the surface. In both cases, a small bias drop between TCNQ and Au(111) is responsible for the shifting of the TCNQ LUMO relative to the Au(111) surface potential when applying a voltage.*

These features are also clearly observed in the case of PXX/TCNQ, with some of the TCNQ molecules in the mixed assembly displaying a behaviour fitting with the transfer of one electron to their LUMO. Images showing both 'types' of TCNQ molecules (at a voltage that does not perturb their ground state), along with examples of the tip-induced charging and discharging phenomena, are shown in **Fig. 8.6**. As with TMTTF/TCNQ, an important aspect to note is that whilst the TCNQ molecules are either in a charged or neutral ground state when an electric field is not being applied, the relative energetic alignment of the molecular states with the Au(111) surface chemical potential does vary across the mixed islands. As a result, for molecules that are in a charged ground state, different voltages may be required in order to discharge them – this manifests as a different position of the discharging peaks (in voltage) when recording the dI/dV spectra with all conditions (position relative to the molecule, initial stabilising current/voltage) kept constant. The same is also true for the charging of neutral molecules, with the 'dips' observed at different voltages for

different molecules that are in the same neutral ground charge state. Small changes in the energetic position of these peaks on the same molecule are also observed when altering the initial conditions of the dI/dV spectra. For example, moving the tip closer to the molecule results in a slight downshift of the discharging peak (i.e. less voltage is required to discharge the molecule), as shown in **Fig. 8.6(d)**. This fits well with the DBTJ model, as a smaller tip-molecule distance results in a stronger electric field when the same voltage is applied, and a greater proportion of the voltage is dropped between the molecule and surface.

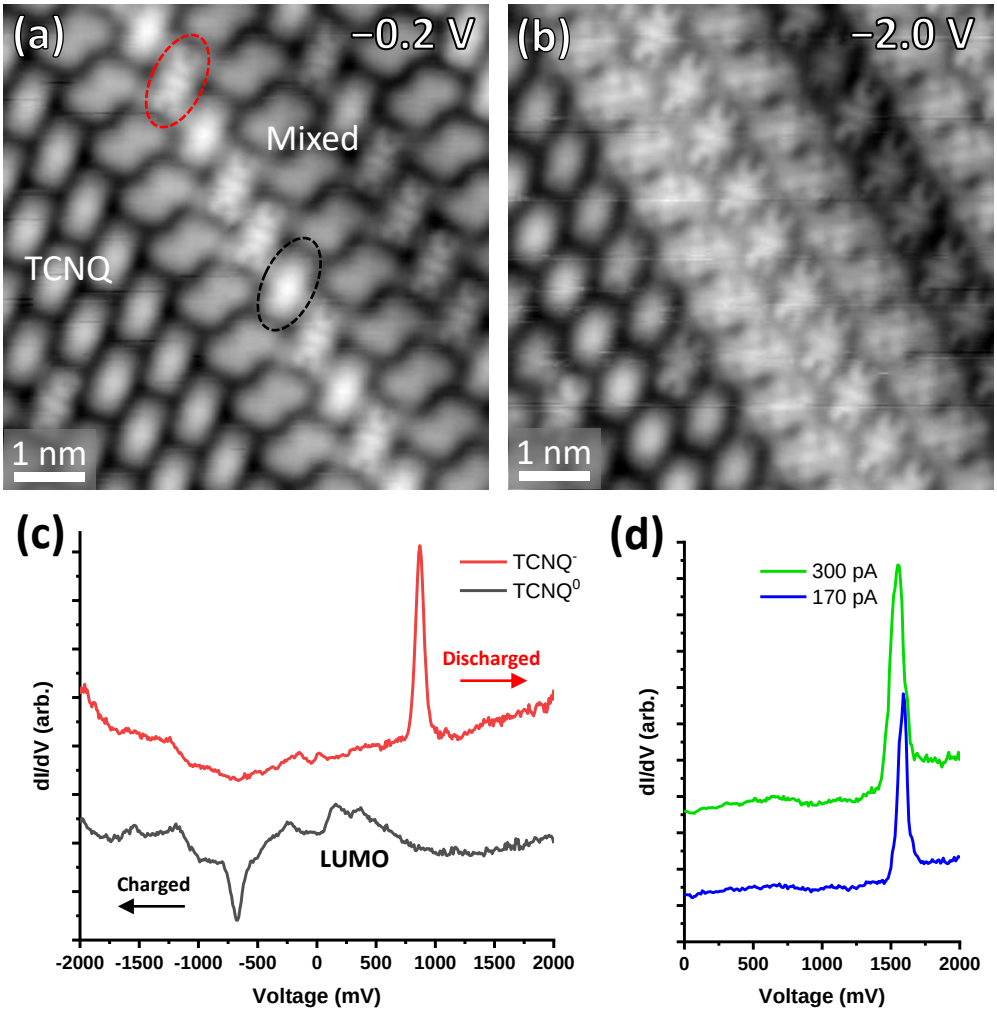

Figure 8.6. *(a) 7 K STM image of an area of mixed PXX-TCNQ packing (labelled as "Mixed") adjacent to a small strip of pure TCNQ (labelled as "TCNQ"), with another mixed island starting in the lower left corner. The image was recorded at −0.2 V, a voltage that does not cause the charging of neutral molecules. Charged ground state molecules appear as the (CO tip convoluted) LUMO shape (red circled molecule), while neutral molecules appear featureless (black circled molecule). (b) The same region, imaged at −2.0 V. All of the neutral molecules in the mixed phase have become charged due to the bias voltage. (c) Examples of charged and neutral dI/dV spectra. A discharging peak (red line) is visible on the charged molecule, a charging dip is present on the neutral molecule. (d) Discharging peaks measured on a $TCNQ^-$ molecule, with a corresponding shift that depends on the vertical proximity of the tip (i.e. the stabilising current prior to recording a spectrum).*

Sometimes features that correspond to the neighbouring molecule are also detected, leading to situations in which two discharging peaks are observed over a single molecule.

Unlike the TMTTF/TCNQ system, the peak that in that work was assigned to an interface state localised at the TCNQ molecule[86,269] in the low positive bias region of the spectra is not consistently observed for charged TCNQ molecules in the PXX/TCNQ assembly (e.g. **Fig. 8.6(c)**). However, features in this region are present for the neutral molecule, and may be assigned to its downshifted LUMO.

As most of these experiments were performed with a CO molecule adsorbed on the tip, it is important to note the appearance of the LUMO; as with several other experiments presented in this thesis, imaging with a p-wave CO tip results in intensity over the nodes of the orbital. This is very apparent when comparing the DFT-calculated gas phase LUMO to the shapes seen with and without a CO tip. A clear signal in the position of the central node of the molecule, along with a signal corresponding to the node surrounding the 'head-like' feature on each end can be observed. A comparison with a metallic tip is shown below in **Fig. 8.7**.

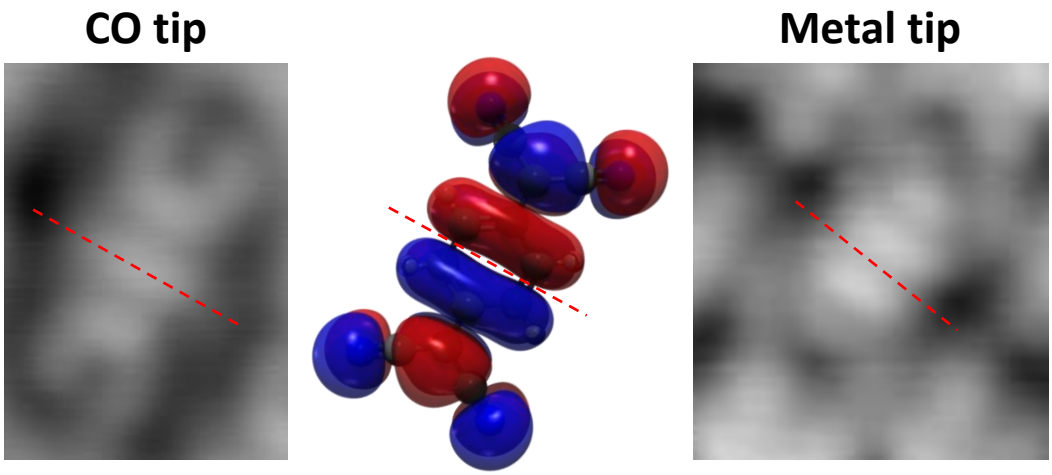

Figure 8.7. *Comparisons of STM imaging of charged TCNQ molecules in the mixed phase (imaged at negative voltage; CO tip image −1.0 V, metallic tip image −0.8 V) with and without a CO tip. The central feature in the CO tip image is in fact located at a node in the LUMO shape, as shown via the indicated nodal planes in the DFT calculated LUMO (centre) and the metallic tip image (right).*

The singly charged ground state of some of the TCNQ molecules is clearly shown by the presence of a zero bias Kondo peak, which is indicative of a magnetic/singly charged species at a metallic surface[85,232]. The feature is attributed to a spin-flip

tunnelling process that may take place at zero bias at low temperatures. The same peak was also observed in the case of TTF/TCNQ[85] and TMTTF/TCNQ[269], as well as the Na/TCNQ system on Au(111)[89]. Molecules that are in a neutral ground state when no electric field is applied do not have this feature, nor do adjacent PXX molecules. Examples of spectra in this region for both general types of molecules are shown in **Fig. 8.8**.

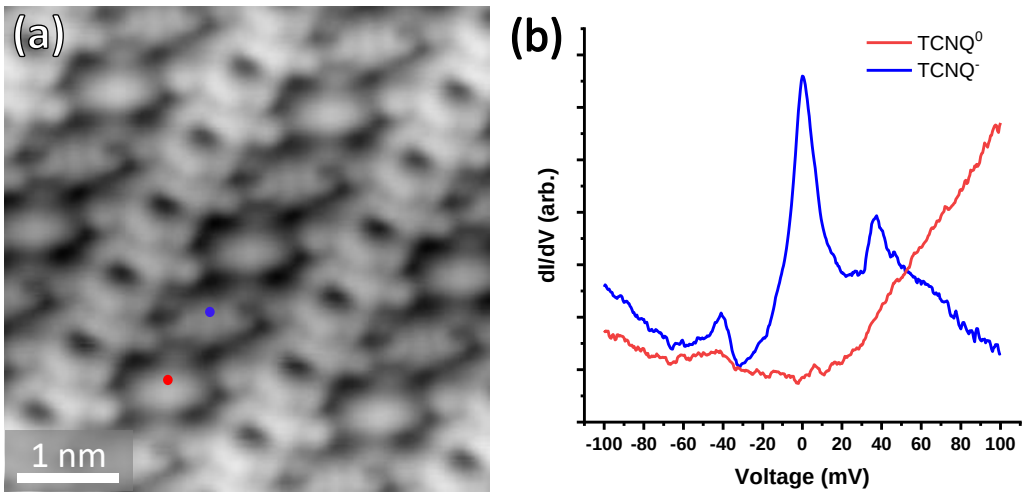

Figure 8.8. *(a) STM image (−1.0 V) of the mixed row PXX/TCNQ assembly. (b) Point dI/dV spectra at low bias voltages recorded on the TCNQ molecule positions indicated in (a). The TCNQ molecule with a charged ground state has a zero bias Kondo peak, whereas the neutral molecule is fairly featureless in this region, with a rising signal towards more positive voltages that may relate to the onset of its LUMO.*

Small peaks either side of the Kondo peak at approximately ± 40 mV have been previously attributed to coupling with in-plane vibrational modes of the molecule[85,269], and show the same dependence on position within the TCNQ molecule as the TTF/TCNQ on Au(111) system, with more intensity on the vibrational peaks at the centre of the molecule. There are, however, no apparent peaks close to 0 V that may correspond to the SOMO/SUMO resonances, as seen in the TTF/TCNQ system[85] at ±67 mV. It may simply be that these resonances are still present, but too weak to detect. Another clear indication of charging is the presence of the LUMO shape at both low positive and low negative biases (data not shown). The charging of neutral molecules in the mixed phase when applying a more negative bias is also apparent in voltage dependent imaging, as the LUMO shape only appears at *more* negative biases (as well as at the expected positive biases when the molecule is still neutral and the LUMO is unoccupied). Examples of these effects are shown in **Figs. 8.6(a)** and **(b)**.

Unlike the TMTTF/TCNQ system, in which a pattern could be discerned in the ground state of the TCNQ molecules (e.g. alternation of charged rows and neutral rows of TCNQ, or a gradual transition along a row of molecules), in the PXX/TCNQ system no such simple overall pattern is observed. Often molecules with very different relative alignments are found adjacent to one another. In some areas, alternation between charged and neutral TCNQ molecules is observed. It should be noted, however, that generally more charged TCNQ molecules are found in the fcc regions of the Au(111) herringbone reconstruction. This is evident in some STM images of the mixed row-type islands, such as that presented in **Fig. 8.9**, in which more TCNQ molecules with a 'dark' appearance (i.e. charged) are found in those regions.

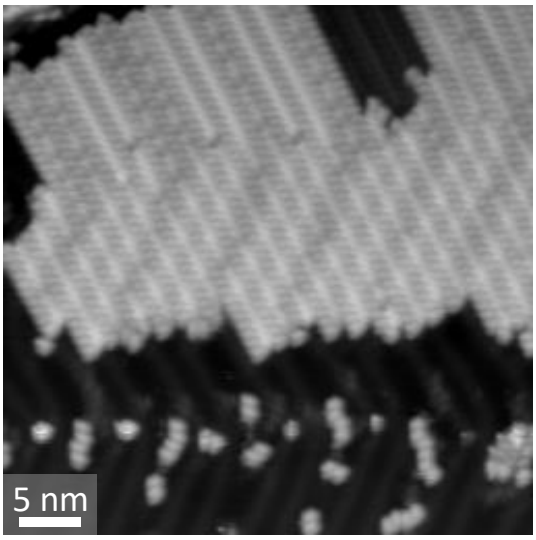

Figure 8.9. *7 K STM image (0.8 V) of a mixed row island of PXX/TCNQ. More variation in the appearance of TCNQ rows is observed in the fcc regions of the herringbone reconstruction.*

The surface potential of the Au(111) surface does vary with the reconstruction, so the above results may be rationalised. More detailed explanations of the large amount of variance often found in the same part of the reconstruction may be much more complex, involving factors such as the local positions of the PXX molecules and how they relate to the herringbone/underlying surface. The commensurability of the islands with the Au(111) substrate could not be determined via just STM results. Another aspect in which the PXX/TCNQ system differs from those reported so far in the literature is the switching of molecules between ground states when in close proximity

to the STM tip. Scanning the same area of a mixed row island repeatedly under the same conditions (bias voltage, tunnelling current, STM feedback and scanning speed) is occasionally found to induce switching between states in TCNQ molecules. An example of the same area, scanned three times at +1.85 V, is shown in **Fig. 8.10**. TCNQ molecules in the 'dark' state can be seen changing in subsequent scans. Whilst this voltage may be enough to discharge some molecules from their charged state, it would be expected that the *ground* state of the molecules would be unchanged, and thus their state during scanning should also be constant when the same voltage is applied between all three images. Instead, it seems that the molecules have been switched. The mechanism of this is unclear and warrants further investigation. One possibility is a tip-induced change in the adsorption position/conformation of the TCNQ molecules within the assembly that may in turn affect the alignment of their LUMO relative to the surface potential. The amount of switching in different islands of the mixed row assembly was also not always the same, and may relate to the local concentration of defects in the underlying Au(111) substrate.

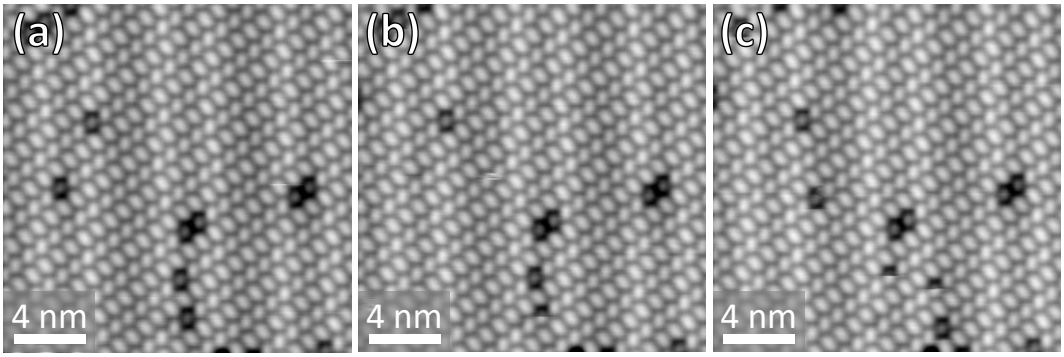

Figure 8.10. *(a)-(c) Subsequent 7 K STM images (all in the same conditions, +1.85 V) of an island of the mixed row assembly of PXX/TCNQ. TCNQ molecules with a dark appearance are observed switching during scanning.*

In the minority phase core-shell islands, the state of the TCNQ molecules is quite different. Imaging at positive and negative bias voltages gives very different results, as shown in **Fig. 8.11**. At a positive voltage, the TCNQ molecules appear as featureless objects with a close-to rectangular shape. At a negative voltage, bright signals are present in between the cyano groups of the molecules, and the LUMO shape (again, seen with a CO tip here) appears. dI/dV spectra over the bright regions (**Fig. 8.11(c)**) reveal a peak in the negative voltage range that does not move as a function of the

stabilising conditions (i.e. it does not show the same characteristics of the charging/discharging peaks observed in the row assembly as it does not depend on the electric field). As the LUMO shape appears only at negative bias voltages, this implies that the LUMO has been completely filled by charge transfer, i.e. the TCNQ molecule is doubly negatively charged, $TCNQ^{2-}$. There is some variation in the position (in energy) of the occupied state when examining different areas – this may relate to the position of the molecules within the island relative to the 'shell' of PXX. However, the islands studied were not extensive or regular enough to make any firm conclusions on this matter.

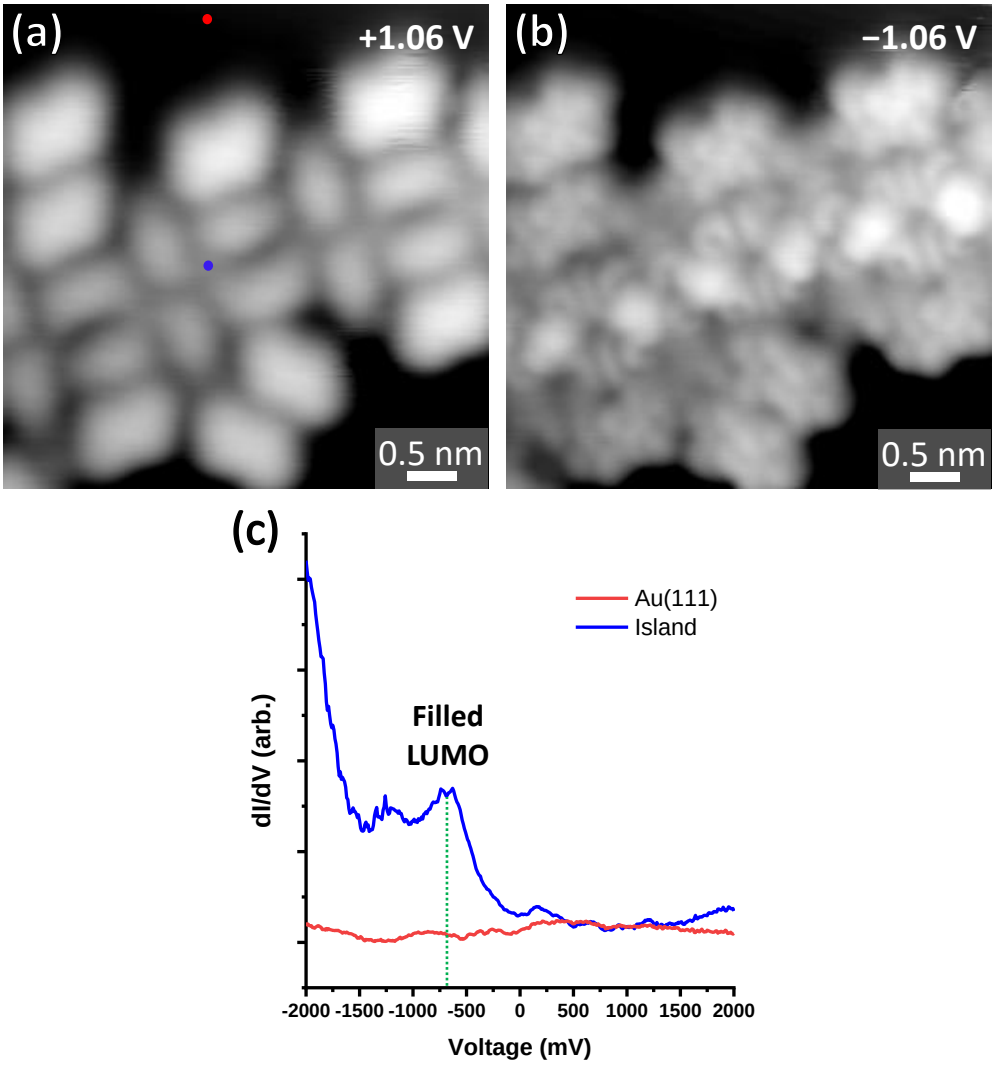

Figure 8.11. *(a) and (b) 7 K STM images of a core-shell island at positive and negative voltages. The (CO tip convoluted) TCNQ LUMO shape is visible at negative voltage, as are bright protrusions between the cyano groups of the molecules. (c) dI/dV spectra recorded at the positions indicated in (a). An occupied state is found in the vicinity of the bright regions, corresponding to a filled TCNQ LUMO.*

A similar assembly and voltage dependences have been previously reported by our group for TCNQ mixed with another donor molecule, 1,3,6,8-tetrakis(3,5-di-*tert*-butylphenyl)pyrene (TBP)[84]. The parallel packed assembly was ascribed to a mixture of charged TCNQ molecules and Au adatoms. This was supported by DFT calculations, and further rationalised by the position of the TCNQ molecules relative to one-another. When TCNQ becomes doubly charged, the charge is mostly localised at the cyano end groups as the central ring becomes aromatic[33]. It is therefore unfavourable to have these end groups oriented towards each other in a parallel packed assembly. As such, having a positively charged metal atom that 'screens' the charge in between the end groups helps to stabilise such an assembly. A similar parallel arrangement was seen with the stronger acceptor F_4TCNQ and Au adatoms, and also in Mn/TCNQ networks on Au(111)[281]. A model for this assembly will be presented in the next section (PXX NRs/TCNQ).

When considering the results presented above, the question remains: why do both of these assemblies occur, and why does one result in more charge transfer than the other? The answer may relate to the relative stabilities of each assembly, along with the stoichiometry of the deposition. In the TBP/TCNQ core-shell islands[84], the charging of TCNQ was considered to be a result of the stabilising effect of the surrounding ring of 'donor' molecules on the charged state of TCNQ. Charge transfer from the surface was favourable because $TCNQ^{2-}$ was rendered more stable by the presence of interactions between the interfacial dipoles located at the position of the donor molecules and those of an opposite orientation on the charged TCNQ molecules. This was further supported by Monto Carlo simulations. As stated above, the assembly was also stabilised by metal-organic interactions with Au atoms.

dI/dV measurements (**Fig. 8.12**) on PXX molecules in both types of assemblies still show the presence of a HOMO peak (at a similar position to that seen with the molecule alone on Au(111)) in the occupied states – as such, the PXX may not be actively 'donating' integer charges to the substrate or TCNQ within the co-assembly. Rather, its presence, along with any interfacial dipole that may be present due to its interaction with the surface, may be the stabilising factor that allows the charge transfer from Au(111) to TCNQ to occur.

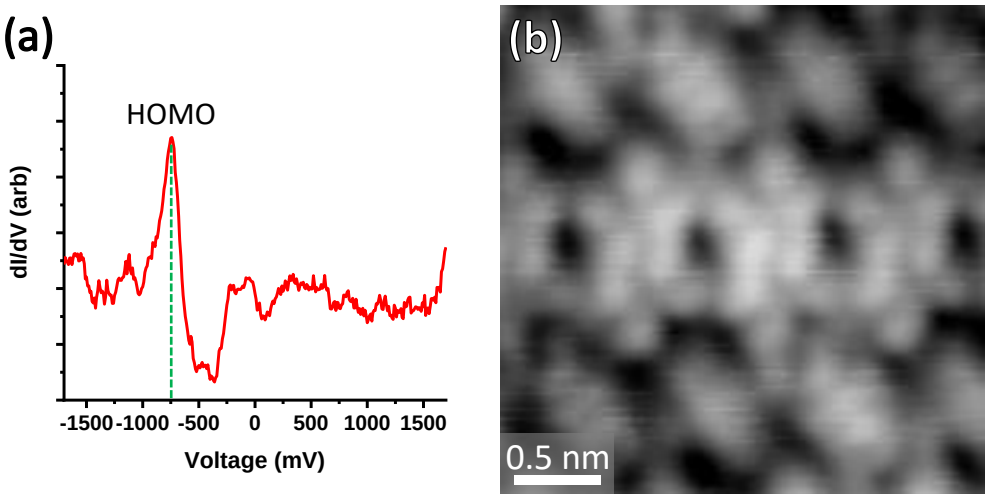

Figure 8.12. *(a) Example dI/dV spectrum of a PXX molecule in a mixed row island, with a clear signal relating to its HOMO resonance labelled. (b) Example of an STM image of PXX molecules in the mixed row phase, imaged at −1.25 V, with the distinct shape of the HOMO as observed in* ***Chapter 4****.*

Whilst more charge is transferred in the case of the core-shell islands, other considerations for the overall stability of each system must be accounted for when rationalising why one assembly is more abundant. In particular, inter-molecular interactions between PXX/PXX, PXX/TCNQ and TCNQ/TCNQ have a further stabilising effect, but the resulting assembly may not favour the formation of *doubly* charged TCNQ. Factors such as the energy cost for adatom formation must also be taken into account. In the case of TBP/TCNQ, it may be that there was no stable mixed row type assembly (unlike TTF and TMTTF), possibly due to a more limited potential for intermolecular interactions between both molecules. PXX, on the other hand, allows for hydrogen bonding with TCNQ and, as a consequence, mixtures of TCNQ and PXX co-crystallise in 3D, while this is not the case when TCNQ is mixed with TBP[84].

8.2.4 PXX Nanoribbons and TCNQ

Depositing TCNQ with pre-formed (via on surface coupling) PXX nanoribbons allows an interesting comparison to be made with the PXX/TCNQ system. Whilst the ribbons may be stronger electron donors, their structure also changes the possibilities for intermolecular interactions in any potentially resulting assemblies due to the fixed orientation of PXX sub-units within the ribbons.

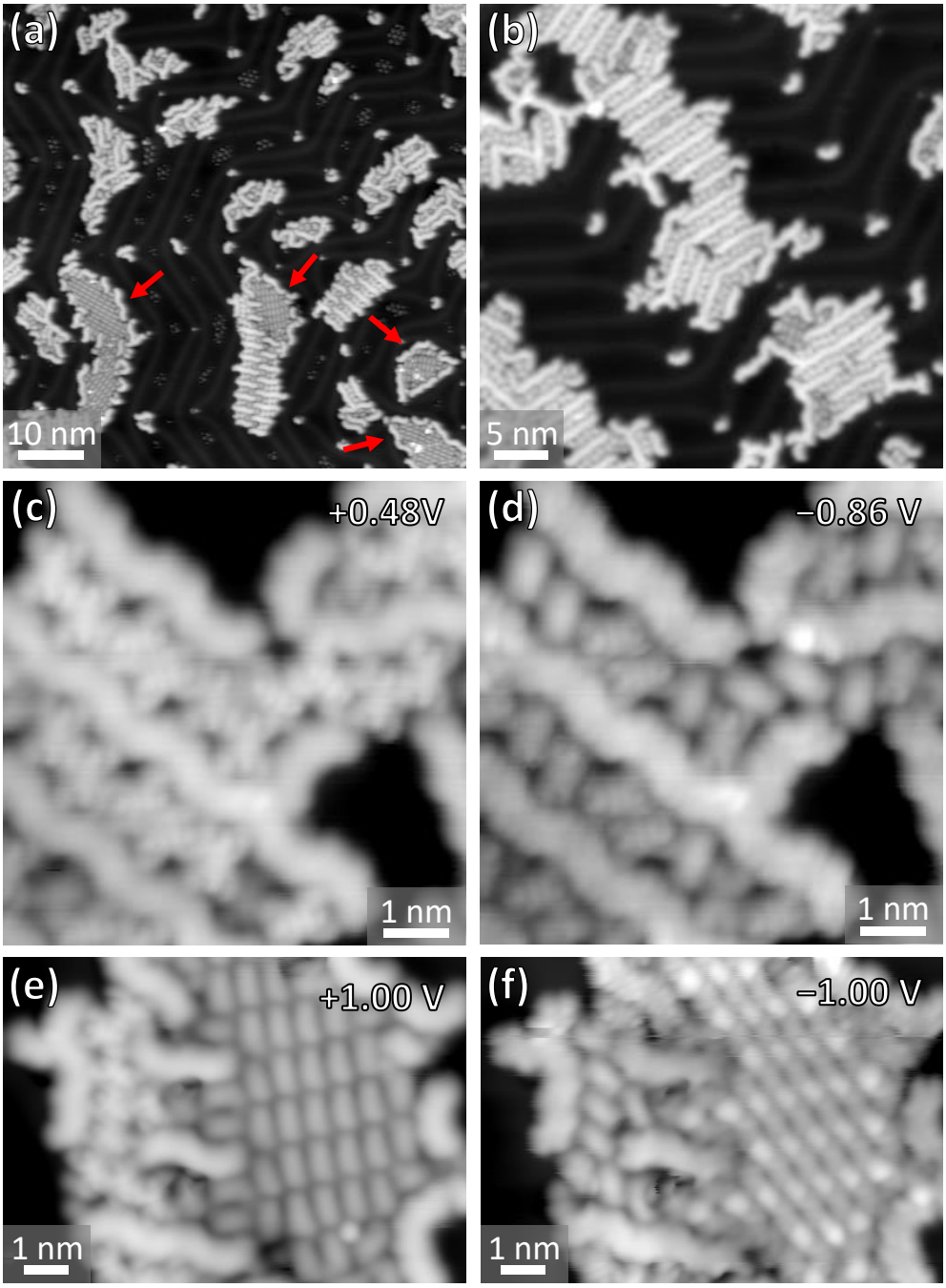

Figure 8.13. *(a) and (b) Overview 7 K STM images (1.1 V and 1.0 V) of the PXX NR/TCNQ co-assembly. Large core-shell islands are indicated with red arrows. Clusters of CO molecules can also be seen as faint features in (a). (c) and (d) Zoom of a mixed row assembly at two different voltages, showing the same variance in ground state and charging/discharging effects as seen with PXX/TCNQ. (e) and (f) A core-shell island adjacent to a small row island, at positive and negative bias. The bright signals between the TCNQ molecules become clear when imaged at negative voltages.*

STM images of nanoribbons (formed via annealing Br_2PXX to 573 K on Au(111)) intermixed with TCNQ molecules are shown in **Fig. 8.13**. As with PXX, two types of assembly are observed: the 'row'-type, with nanoribbons alternating with rows of

TCNQ, as well as the core-shell type island. However, the most significant difference is the relative amount of each: there are far more core-shell type islands than seen with PXX/TCNQ when at a similar coverage. Furthermore, their size is significantly larger.

STM images of both types of assembly are shown in **Fig. 8.13**. One noticeable difference when comparing the row assemblies is that often TCNQ molecules are oriented in several directions within a row adjacent to nanoribbons, most likely to accommodate for their structure and to maximise the number of intermolecular bonds. CO-tip HR-STM of the core-shell islands is shown in **Fig. 8.14**. In these images, the structure of the TCNQ molecules is clearly resolved, but no signals from metal atoms in between the cyano groups of the molecules are detected. As mentioned earlier in this thesis (**Chapter 3**), adatoms in metal-organic structures are not always detected via STM or AFM. However, in 'normal' constant current imaging at negative biases, the position of the bright signals in between the cyano groups fits well with the expected adatom position. When placing an Au atom at the centre of each gap between the molecules, it becomes clear that two of the TCNQ cyano groups (of the surrounding four) are closer to/form a stronger bond with the metal atom. This is in agreement with the model proposed by Della Pia et al[84]. The unit cell of the TCNQ cores is found to be **a** = 0.69 ± 0.02 nm, **b** = 1.10 ± 0.02 nm, **θ** = 83 ± 2°, which is also in good agreement with the experimentally measured unit cell for the core-shell assembly of TBP/TCNQ[84].

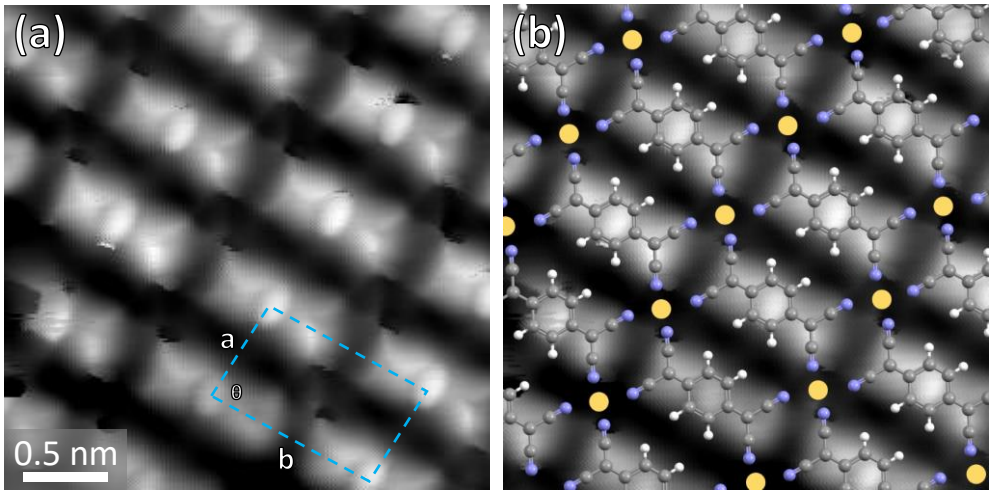

Figure 8.14. *(a) 7 K HR-STM (CO tip, 30 mV) of the TCNQ inner part of a core-shell island. (b) Scaled overlaid model of the metal-organic assembly, with Au atoms represented by yellow circles.*

Both assemblies exhibit similar electronic properties to those found in the PXX/TCNQ system. TCNQ molecules within the mixed 'row' type assembly often have discharging/charging peaks/dips, as well as a clear Kondo peak for molecules in a charged ground state (data not shown). In general, more molecules with charging features (i.e. a neutral ground state) were observed with the ribbons. However, clear conclusions about any general change that may be correlated with the length of the NRs in these islands (when compared to PXX) cannot be made, due to the irregularity of the islands; the row assembly is often found to consist of long nanoribbons of various lengths with many deviations. Further experiments with lower coverages and lower annealing temperatures could yield more regular islands consisting of shorter NRs mixed with TCNQ, and in turn reveal differences in their effect on neighbouring TCNQ molecules.

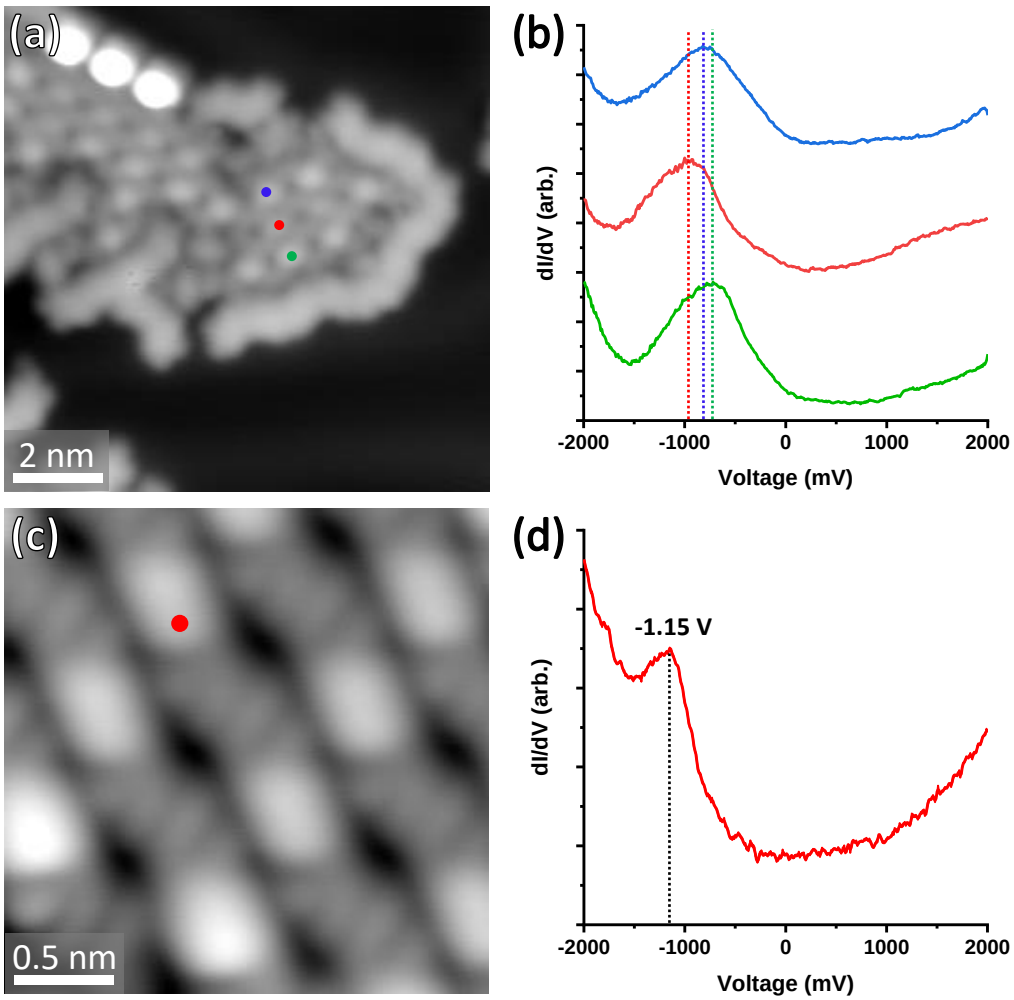

Figure 8.15. *7 K STM Images and dI/dV spectra of the bright TCNQ-metal features in core-shell islands. (a) and (b) Examples of the shift (between −720 and −1000 mV) in the filled LUMO as a function of the position of a TCNQ molecule within the island. (c) and (d) STS of a bright TCNQ-metal area deep within a core-shell island, with a filled LUMO at an even lower energy.*

dI/dV measurements on the NR core-shell islands also yield an occupied state at negative bias voltage, with a resemblance to the TCNQ LUMO in STM imaging, along with bright signals where metal atoms are expected. Variance in the position of this peak is observed and may be related to the position within the island, as shown in **Fig. 8.15**. In some cases, when in the centre of a regular core-shell island, the filled LUMO peak may be found as low as −1.1 V. Few features are observed in dI/dV spectra of the centre of the TCNQ molecules; instead, the occupied spectral features are generally more limited to the cyano groups/metal atom.

The higher abundance of core-shell islands relative to the PXX/TCNQ system may be related to a number of factors. Formation of the mixed row assembly with nanoribbons may be slightly disfavoured (relative to PXX) by the change in possible inter-molecular interactions within these islands when compared with PXX/TCNQ. For the same length of row (i.e. for a row of *n* TCNQ molecules), there may be fewer/weaker hydrogen bonds possible. The effect of the increased donor character of the nanoribbons could also favour the core-shell assembly; stronger dipoles located at the nanoribbons (related to a possible increased level of charge transfer with the surface) can in turn stabilise the opposing dipoles of doubly charged TCNQ molecules in the core-shell assembly, and potentially also increase the core-shell domain size.

8.2.5 Mixed PXX/VO3 Nanoribbon Formation and Properties

The formation of mixed nanoribbons of VO3 and PXX on Au(111) is straightforward. Due to the presence of C-Br groups on VO3 and Br_2PXX, both molecules can simply be deposited together on the Au(111) surface at room temperature, and then annealed to temperatures between 473 K and 573 K. Both molecules were observed forming NRs when alone on the surface at these temperatures – as such, mixed NRs may well result from the same treatment due to the similar end group functionality of both molecules.

The co-assembly of Br_2PXX and VO3 after RT deposition was not studied extensively via STM and may provide interesting results in future work. However, no mixed assembly was observed when briefly scanned in the STM at 77 K (data not shown). A co-deposition of a high coverage of both molecules was annealed to 573 K, resulting

in the observation of islands consisting of NR objects mixed with bromine atoms (**Fig. 8.16**).

Higher annealing temperatures that could desorb the Br were not used; this is because shorter mixed ribbons were the desired product, and VO3 in particular generally forms much longer ribbons when annealing high enough to desorb Br atoms. As such, the majority of the dI/dV spectra presented in this section are recorded over ribbons that are co-adsorbed with bromine atoms, and as such may exhibit small shifts in the position of spectral features relative to the 'ideal' case of NRs adsorbed alone on Au(111). In order to easily identify the components of mixed ribbons, CO was deposited onto the surface after NR formation so HR-STM measurements on the islands could be performed.

STM and HR-STM images of the mixed NR/Br islands on Au(111) are presented in **Fig. 8.16**. As seen with both Br_2PXX and VO3 in previous chapters of this thesis, these islands distort the herringbone reconstruction due to the presence of adsorbed bromine. Examining the islands via HR-STM reveals a diverse collection of objects, ranging from monomers of each molecule to longer mixed ribbons.

The amount of each molecule present after the annealing was estimated by counting the total observed numbers of PXX or VO3 units (including units within polymers and lone monomers) in HR-STM images of the assembly. Despite an estimated 50:50 coverage deposition, the observed ratio was 43% PXX, 57% VO3 in a count of 798 total units after the 473 K anneal. Examining the connections within the polymers revealed that 62% involved VO3-PXX coupling, 13% VO3-VO3 and 25% PXX-PXX. Furthermore, 36% of the VO3 units observed were present as lone monomers, whereas 7% of PXX units were alone. Despite the slightly increased amount of VO3 relative to PXX, there were disproportionately more examples of cross-coupled connections, indicating a general preference of VO3 for the formation of the PXX-VO3 junction.

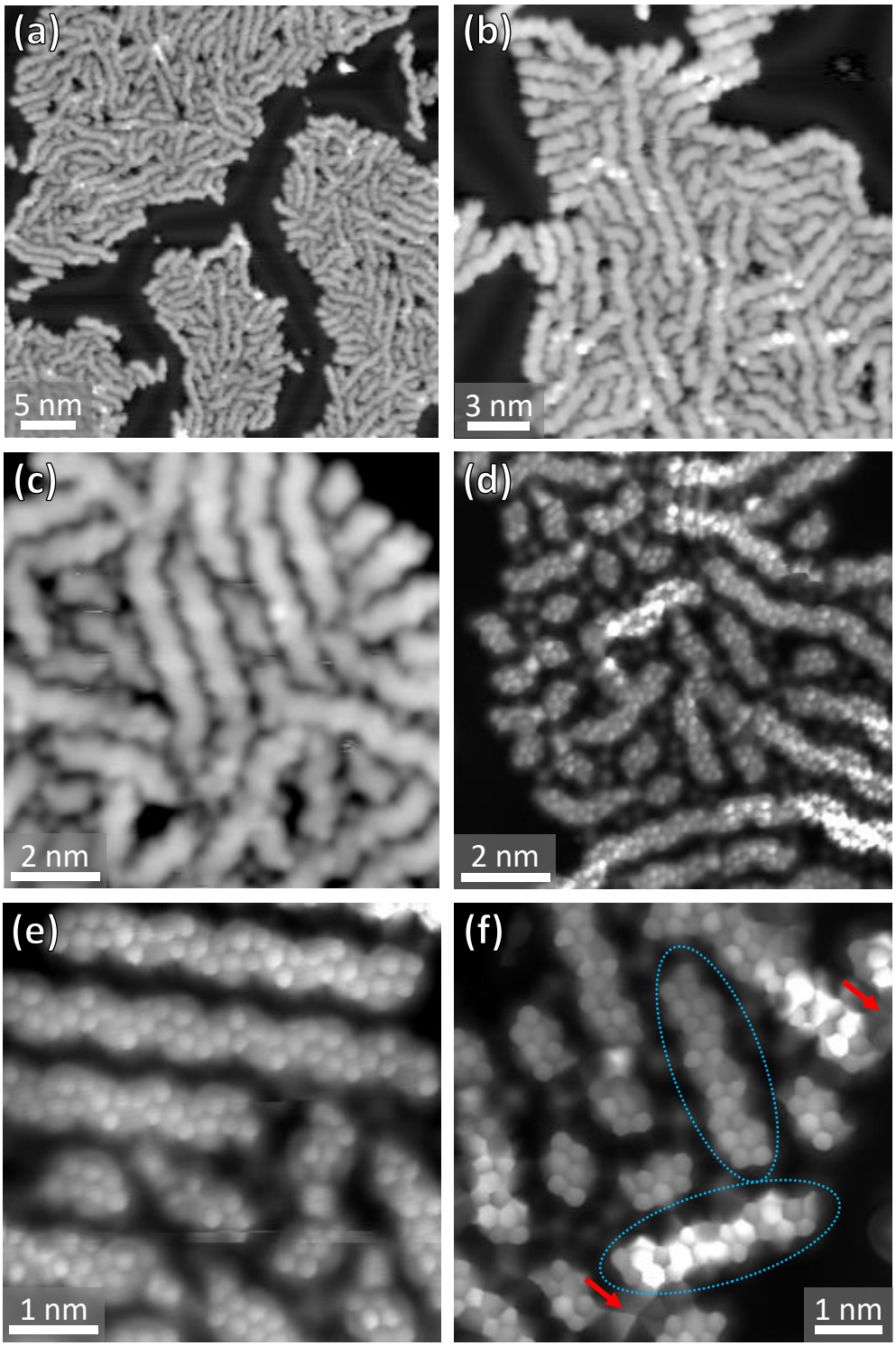

Figure 8.16. *(a)–(c) 7 K STM images of mixed-NR/bromine islands on Au(111). (d)-(f) HR-STM (CO tip) images of the islands, demonstrating that the internal structure (in terms of VO3 and PXX units) can be easily discerned. In (f), the highlighted nanoribbons (blue circles) have the same structure, but substantially more tunnelling current is detected over one of them in constant height mode. This may be due to the unknown adjacent objects, two of which are indicated with a red arrow. Bias voltages: (a) −0.9 V (b) −0.9 V (c) −1.5 V (d)-(f) 30 mV.*

HR-STM of the structure of these junctions also reveals that, for all examples of PXX-VO3 coupling found, every junction is of the 'straight' type rather than one that forms a bend. This preference is not exhibited when forming nanoribbons of PXX or VO3 alone – both tend to have alternating bends formed from precursors with alternating chiral orientations. The simplest explanation for this, as shown in **Chapter 6**, relates to the position of the C-Br group on the precursors and may also offer an insight into the mechanism of the nanoribbon formation. The only orientation that connects the positions of the C-Br bonds on adjacent VO3 and PXX molecules and allows NR formation (i.e. the formation of a perylene unit) results in a straight nanoribbon. By contrast, for both PXX and VO3, the only orientation that allows this results in a 'bendy'/alternating nanoribbon. The small amount of straight connections observed previously in PXX nanoribbons may be explained by the presence of contaminant molecules, as described in **Chapter 5**, that have a C-Br group on an adjacent position on the molecule. This observation also gives further weight to the conclusion that the molecules must primarily connect at the radical positions before dehydrogenation, as with other NR formation seen in the literature, and also that both steps must happen at the same temperature. These conclusions are summarised in **Fig. 8.17**.

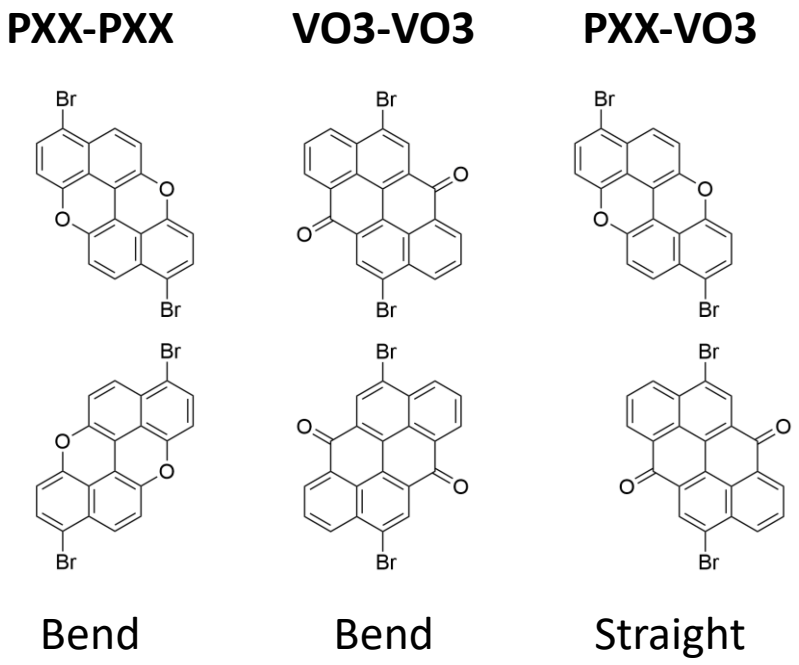

Figure 8.17. *Diagram showing the preference for bends in NRs exhibited by PXX and VO3 homopolymers due to the C-Br bond locations, and the preference for straight NRs in PXX-VO3 connections due to the different locations of the C-Br groups.*

The electronic properties of shorter mixed ribbons were examined via dI/dV point spectra and constant height imaging; in particular, VO3-PXX dimers, along with all possible mixed trimers: PXX-VO3-PXX, PXX-PXX-VO3, VO3-VO3-PXX, and VO3-PXX-VO3. The termination of these objects (as some are still brominated) was disregarded for the comparison – difficulty was had finding examples of all of these objects with the same termination (i.e. no C-Br groups or fully brominated). These bromine terminations result in small shifts of the dI/dV peaks, as shown in previous chapters. Combining this effect with that of the locally adsorbed bromine leads to considerable uncertainty in the positions of the states for all of these objects, and thus precise comparisons of the energy of states are not possible; rather, general trends in energetic position and spatial localisation of the states are presented here. The electronic properties of longer mixed ribbons were not extensively characterised and thus are not shown.

As shown in **Fig. 8.16(f)**, there are cases in which objects with the same structure have large differences in brightness when performing HR-STM measurements at constant height. In general, these brighter nanoribbons were adjacent to another unknown object (presumably a contaminant) that appears as a sharp apex in HR-STM imaging, and a bright feature in normal constant current imaging. When taking dI/dV spectra of nanoribbons, any ribbons in the vicinity of one of these objects were disregarded, as there is clearly a substantial effect on the LDOS of the NRs when in close proximity to the contaminant. This may relate to charge transfer between the surface and the ribbon that only occurs when this object is nearby, in a similar fashion to that seen with PXX/TCNQ.

dI/dV spectra and constant height images of a VO3-PXX dimer are shown in **Fig. 8.18**. The HOMO state of the dimer is found at approximately −800 to −1000 mV, in a similar position to that of PXX. The LUMO state, however, is found in the 300-450 mV region, significantly lower than that of a PXX-PXX dimer as presented in **Chapter 6** (with a LUMO at approximately 1200-1500 mV and a HOMO at −200 mV**)**. As such, the band gap is ~1300 mV, compared to the ~1550 mV of a PXX dimer. A distinct peak for the HOMO level of VO3 dimers was not measured, so an accurate comparison cannot be made. These measurements demonstrate that combining the two monomers allows tweaking of the energies of the frontier orbitals, with both a shift of the HOMO and LUMO levels along with a narrowing of the gap. Also of note is that

constant height imaging at the HOMO and LUMO resonances of the mixed dimer demonstrates that they are not both localised onto the donor (PXX) and acceptor (VO3) units respectively. Whilst the HOMO state has slightly more intensity over the PXX unit, the LUMO state is more delocalised around the junction. This is not entirely unexpected, due to the connecting perylene section and the small size of the molecule.

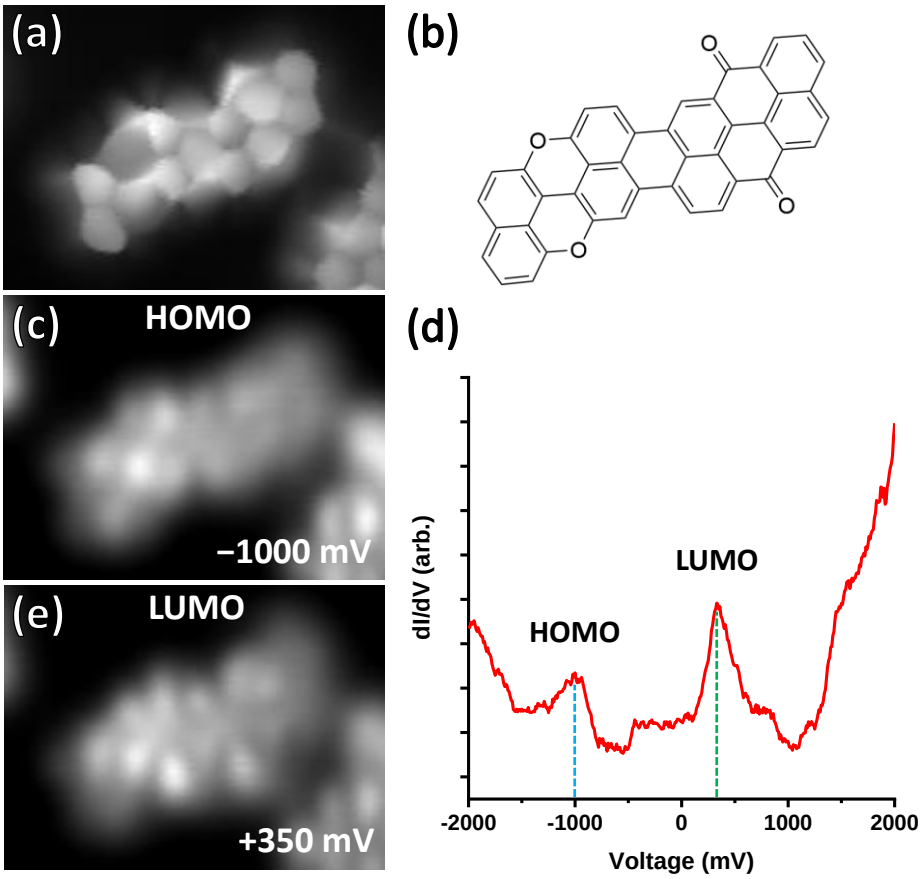

Figure 8.18. *(a) CO tip HR-STM (30 mV) of a VO3-PXX dimer, with a corresponding molecular model in (b). (c) and (e) Constant height STM images (CO tip) of the dimer, at voltages corresponding to the peaks seen in the dI/dV spectrum in (d).*

Examining trimers of all the possible permutations shows a diverse set of properties; in particular, differences were found between alternating and block type co-polymers. The measured HOMO and LUMO positions of all the trimers, along with constant height dI/dV (or current signal) images of the frontier states are presented in **Fig. 8.19** and **Fig. 8.20**. Example dI/dV point spectra that contain the relevant features are also shown alongside the constant height images of the molecules.

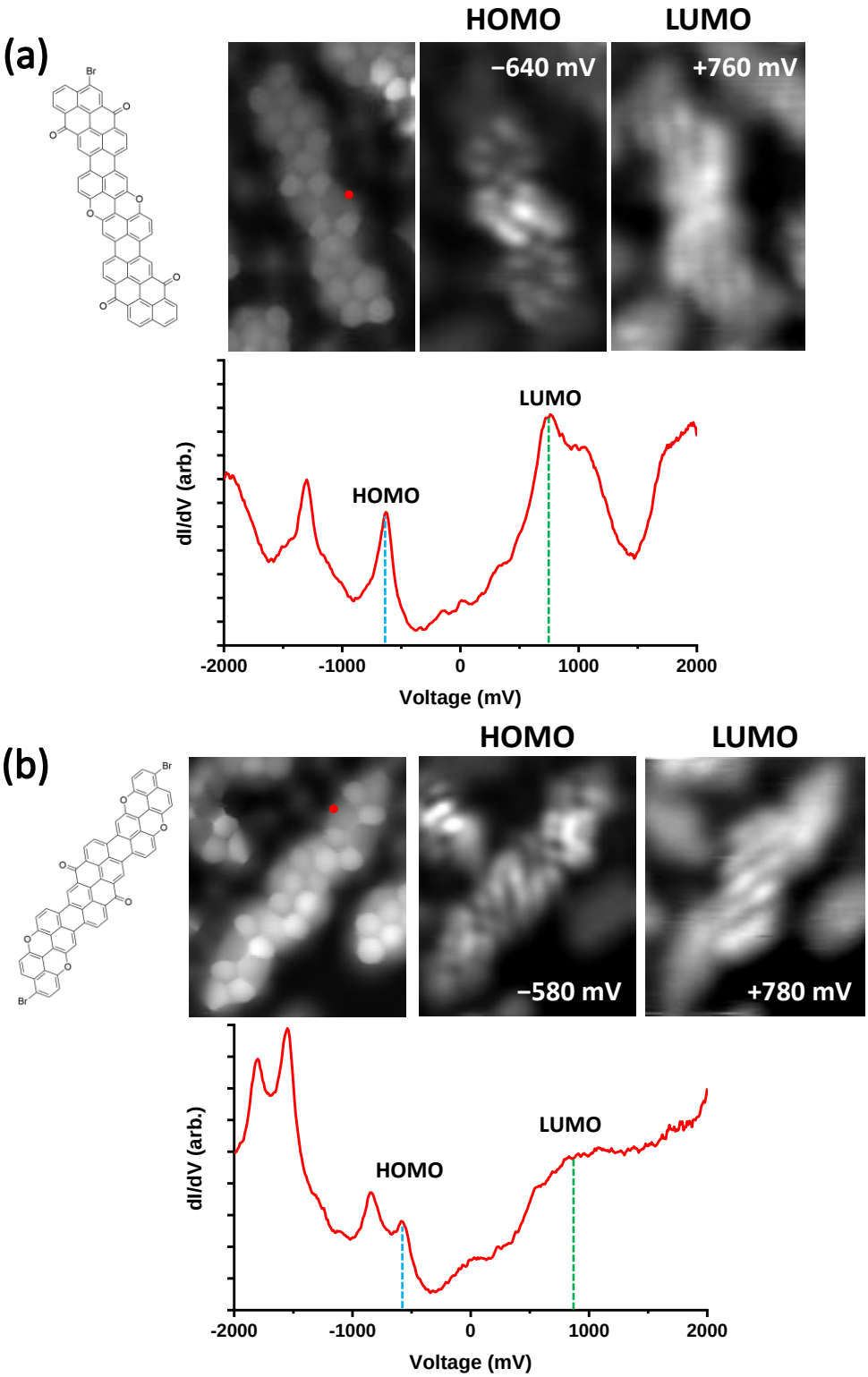

Figure 8.19. *(a) Constant height HR-STM imaging (30 mV), dI/dV imaging and dI/dV spectrum of the VO3-PXX-VO3 alternating trimer, with one end brominated. (b) Constant height HR-STM imaging (30 mV), dI/dV imaging and dI/dV spectrum of the PXX-VO3-PXX alternating trimer, with both ends brominated. All images with a CO tip.*

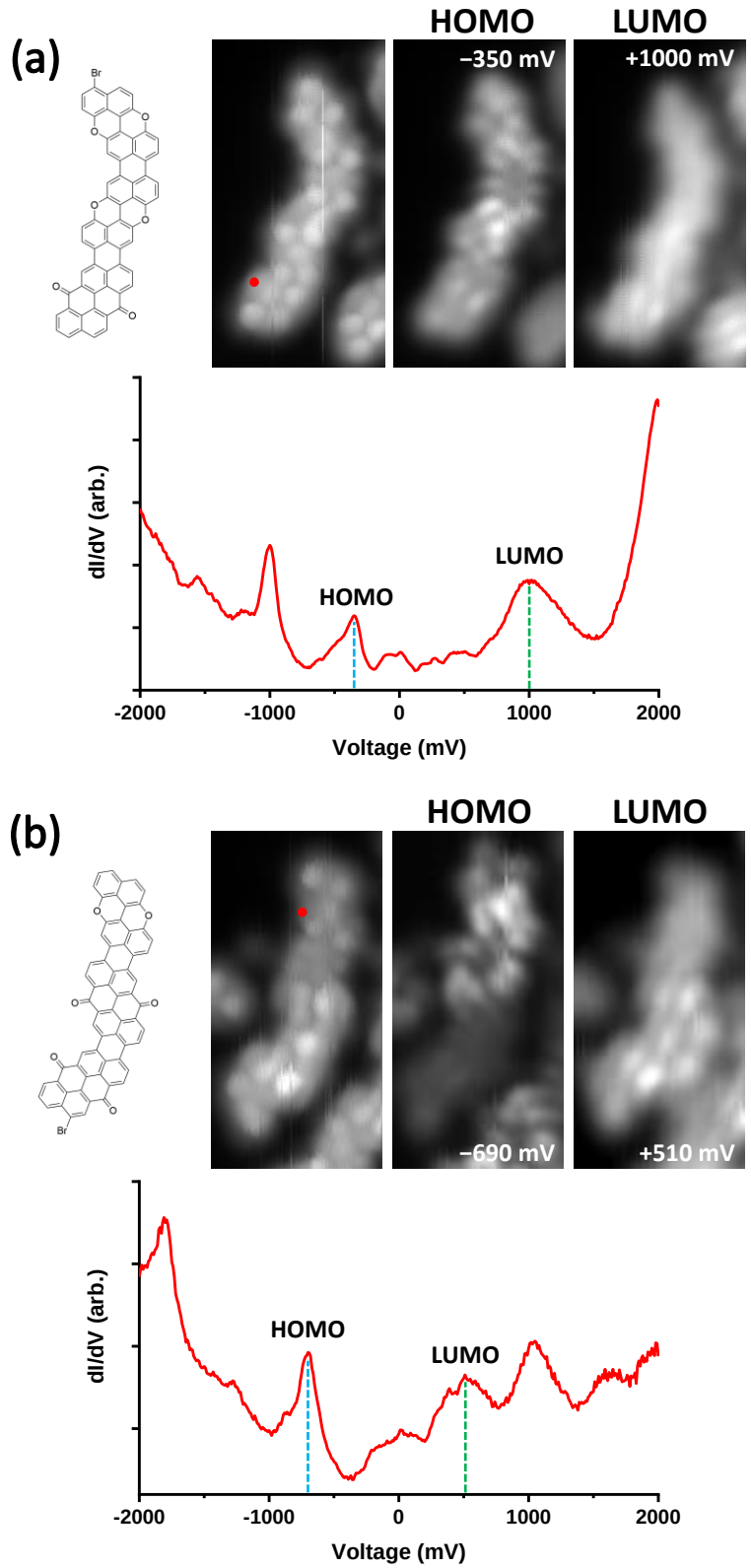

Figure 8.20. *(a) Constant height HR-STM imaging (30 mV), current imaging and dI/dV spectrum of the PXX-PXX-VO3 block trimer, with the PXX end brominated. (b) Constant height HR-STM imaging (30 mV), dI/dV imaging and dI/dV spectrum of the PXX-VO3-VO3 block trimer, with both the VO3 end brominated. All images with a CO tip.*

These results show the influence that the ordering of the sub-units within the nanoribbons can have on their overall electronic properties, and how these may be potentially exploited in order to tune the frontier orbital energies and the HOMO-LUMO gap. In general, though, only relatively small differences are observed. Increasing the number of sequential donor or acceptor units has more of an impact on the position of the HOMO or LUMO states, respectively. For example, three out of the four trimer combinations have a HOMO at approximately −600 mV (with some small variation). However, in the PXX-PXX-VO3 trimer (**Fig. 8.20(a)**), having two PXX units in a block helps to raise the HOMO to approximately −350 mV. In a similar fashion, the VO3-VO3-PXX trimer has a lower LUMO (~ +500 mV) than the rest of the trimer structures (750-1000 mV). In the alternating trimers, the number of each unit (and thus the identity of the end unit) does not seem to have a large impact on the frontier energies, with both in relatively similar positions. There is, however, considerable uncertainty in the exact position of the PXX-VO3-PXX LUMO (**Fig. 8.19(b)**) due to the broadness of the feature observed in the dI/dV spectrum. The features away from the frontier levels, such as the HOMO−1 or LUMO+1, are also very different for the two alternating trimers. More occupied states are observed in the ±2 V range for the alternating trimer with two PXX units; likewise, more unoccupied states are seen in this range for the alternating trimer with two VO3 units. The approximate HOMO-LUMO gaps measured were all fairly similar for the trimers, in the range of 1 – 1.5 eV.

In some cases, the states are also more clearly localised onto specific sections of the polymer. The PXX-VO3-PXX trimer (**Fig. 8.19(b)**) has a LUMO that is clearly positioned around the central VO3 ‘acceptor’ unit. Both block co-polymers in **Fig. 8.20** also have the expected localisation of donor (PXX) HOMO states and acceptor (VO3) LUMO states. It should be noted that this is less obvious for **Fig. 8.20(a)** as the presented images are constant height current signal images rather than dI/dV images; issues with z-drift at the time of the data acquisition for the PXX-PXX-VO3 trimer prevented the slow constant height imaging required for dI/dV images. However, if there are no states between the voltage of the imaged state and the Fermi level, the current signal and dI/dV signal are generally quite similar in appearance.

8.3 Conclusions

It has been demonstrated in this chapter that PXX may be used in donor-acceptor systems at surfaces: in non-covalent 2D co-assemblies with an acceptor molecule and as a component in covalent donor-acceptor polymers

Co-deposition of PXX with TCNQ, a widely used acceptor molecule, yielded the formation of 2D mixed assemblies that resulted in a charge transfer to TCNQ. The source of this charge transfer is not simply the donor molecule, as can be found in 3D co-crystals of donor/acceptor molecules, but rather the underlying surface. The effect of the donor molecule may in fact be more related to the stability of the charged state that it provides when adsorbed locally, via favourable interfacial dipole-dipole interactions, as suggested by Della Pia et al.[84] Effects of the STM tip/bias voltage on the charge state of the TCNQ molecules in the mixed row assembly were also studied, and similar results to those previously seen with TMTTF/TCNQ and TTF/TCNQ were obtained. In particular, two 'ground' charge states for TCNQ were observed, with corresponding differences in dI/dV spectra, such as charging/discharging features and a Kondo peak. Similar assemblies were found when examining the co-assemblies of the PXX nanoribbons with TCNQ; with the exception of a greater tendency towards the formation of core-shell type islands with doubly charged TCNQ molecules contained within. Whilst this might suggest that this is due to the stronger donor character (higher-lying HOMO) of the nanoribbons as they increase in length, it may be related to a number of factors. In particular, the stabilities of mixed row and core-shell type assemblies may be considerably different when involving PXX or nanoribbons in a way that does not necessarily relate to their donor strength, but also other intermolecular interactions (e.g. the number/strength of H-bonds).

In the second half of this chapter, it was shown that PXX and VO3 may be combined via on-surface Ullmann coupling/dehydrogenation into covalent donor-acceptor nanoribbon polymers. The resulting effects on the electronic properties were examined via STS, with the positions of the frontier orbitals determined. Changing the order of the monomer units within short PXX-VO3 co-polymers was proven to be a way of precisely tweaking the energies of the HOMO and LUMO orbitals, and the resulting amount of localisation of these states was shown via dI/dV imaging of the states.

This work paves the way to future work in which PXX-VO3 polymers may be synthesised using methods that allow a larger scale production for more practical applications that may in turn exploit their tweaked electronic properties. Reactions could be tailored around the formation of certain lengths or compositions of co-polymers via careful selection of molecular precursors in order to aim for select HOMO/LUMO energies.

9 Overall Conclusions & Outlook

In this thesis, the properties of peri-xanthenoxanthene and related compounds have been studied at surfaces via scanning tunnelling microscopy and x-ray photoelectron spectroscopy, with the aim of tuning its frontier energy levels for potential future use in optoelectronic devices. In particular, the formation of polymers from a brominated derivative via on-surface synthetic methods was used to attempt to raise the highest occupied molecular orbital in energy to make the molecule a stronger electron donor. A comparison to nanoribbons of an acceptor analogue (Vat Orange 3) was also made, and the two components were mixed to investigate whether the energy and localisation of frontier molecular orbitals could be tweaked further via co-polymer formation. An attempt was also undertaken to access an on-surface metal-catalysed analogue of the solution-based synthesis of PXX, via the molecule binol. Finally, a brief examination of PXX as part of an on-surface donor-acceptor assembly was made, in order to form a comparison with similar assemblies with other traditionally used electron donors, such as tetrathiafulvalene (TTF).

A key motivation behind this work was not just to examine the properties of these systems at surfaces, but also to investigate on-surface methods as an alternative to solution-based synthesis. The synthesis used to form similar PXX-like nanoribbons has previously limited their length due to issues with their solubility and also required side-groups to try to counteract these issues. In another line of investigation, the conversion of binol to PXX was also examined to try and replicate and understand this copper-catalysed reaction with an idealised system; i.e. the binol molecule on a metallic surface.

To form an idealised system for this reaction, binol was deposited onto metallic surfaces in vacuum, with both Cu(111) and Au(111) used to compare substrates of significantly different reactivity. On the copper surface, the molecule was found to deprotonate and cluster, forming metal-organic chains upon annealing that eventually formed disordered covalent polymer structures at high temperatures. When instead deposited on Au(111), the molecule did not react, instead requiring the deposition of iron to initiate the deprotonation and reaction of the molecule at the surface, eventually

leading to a product containing a fused furan ring at higher annealing temperatures. This product was found to be similar to structures seen in related studies on a brominated derivative of the molecule[102]. Potential future work for this system may lie in the deposition of binol on a surface of intermediate reactivity, such as Ag(111), which may catalyse ring-closing reactions in a more controllable way than Cu(111), but more readily than Au(111).

As PXX could not be formed from binol on Cu(111) or Au(111), the synthesised molecule was instead deposited via sublimation and examined via STM/STS on Au(111) and Cu(111). A high level of mobility at 77 K, along with a relatively dispersed assembly on both Au and Cu(111) may be indicative of dipole-dipole repulsion upon adsorption, in a similar manner to that seen previously with TTF[76]. A slightly less repulsive assembly was observed on Au(111), with the formation of more H-bonded molecular chains. The greater level of dispersion on Cu(111) could be attributed to dipoles associated with increased levels of molecule-metal binding/hybridisation in comparison to Au(111). STS measurements of PXX on Au(111) revealed a clear signal corresponding to the HOMO of the molecule, as confirmed by the distinctive shape also seen in STM images recorded at that voltage. The position of this peak well below the Fermi level also implies that there may not be any significant level of charge transfer from the molecule to the metal. Similar measurements were not successfully performed on Cu(111), paving the way for further investigation in future studies that may help to clarify its higher level of dispersion. DFT calculations of the adsorbed molecule could also aid in the understanding of the PXX-metal interface.

The addition of a C-Br moiety to the *peri* positions of PXX allows the possibility of nanoribbon structures formed via on-surface Ullmann coupling/dehydrogenation. The halogen groups also offer the possibility of different forms of self-assembly when adsorbed at surfaces – in particular, halogen bonding. After synthesis by our collaborators in the Bonifazi group, Br_2PXX was studied on the Au(111) and Cu(111) surfaces. A clear contrast with PXX emerged, as Br_2PXX was found to more readily self-assemble into 2D islands due to stronger intermolecular interactions. The structure of the islands observed in STM imaging could not be easily identified by standard STM or free-standing monolayer DFT calculations. HR-STM, performed with a CO tip, solved this problem, and allowed easy identification of the internal

structure (and thus orientation) of the molecules. As a result, the structure was identified as halogen bonded. This method was also used to identify contaminant products from the synthesis of the molecule with C-Br groups on different positions. The electronic structure of these species was determined via STS, with a HOMO state slightly downshifted from PXX due to the addition of C-Br groups.

When Br_2PXX was instead adsorbed onto Cu(111) at room temperature, chain structures were observed, and further revealed by HR-STM to be metal-organic in nature. As has been seen before many times in the literature, the more reactive nature of Cu(111) (in comparison to Au(111)) resulted in the debromination of the molecule upon adsorption at room temperature, with the resulting radicals combining with Cu atoms to form MO structures.

In order to understand the effect of PXX nanoribbon formation on the molecule's donor strength, NRs were formed by annealing the brominated molecule after adsorption on the Au(111) surface. Isolated nanoribbons of increasing length were studied via STS and showed a clear shift of the HOMO upwards in energy towards the Fermi level with increasing ribbon length, as predicted by DFT calculations. The HOMO energy of longer ribbons could not reliably be measured, as they most probably were donating charge to the substrate with a corresponding Fermi level pinning effect. NR lengths were also achieved that were not possible in the solution-based synthesis of similar PXX-type NRs. Future work may involve the more controlled on-surface synthesis of these nanoribbons, using precursors (such as singly brominated PXX dimers or trimers) that may combine and form NRs of a set length that all have the same properties.

As the objective of forming PXX NRs with a stronger donor character had been achieved, an analogous system for a similar acceptor molecule was also investigated. Changing the structure of the central rings of PXX to contain C=O groups results in a significant lowering of the LUMO energy of the molecule, as shown by DFT optimisations in the gas phase. This molecule, (Vat Orange 3) also containing C-Br groups at each end, provides a simple way of forming a comparison to PXX and PXX NRs. Upon deposition on Au(111), STM imaging revealed that VO3 formed large, compact island assemblies, in contrast to the slightly more repulsive (less extended) behaviour observed with Br_2PXX. HR-STM showed that the structure was halogen

bonded, and STS measurements of the molecule exhibited a clear resonance corresponding to its LUMO in the unoccupied states.

Annealing VO3 led to similar NRs to those seen with PXX, and STS measurements also showed a general trend downward in energy of the LUMO, as predicted by DFT. A similar alternating structure was revealed by HR-STM measurements, and indications of the molecular states were seen in STM imaging, with a good fit to the calculated gas phase orbitals. Junctions between the ends of adjacent nanoribbons were observed and rationalised through HR-STM imaging and DFT calculations of gas phase structures as single bonds in a position that could not result in dehydrogenation and thus continuation of the NRs.

The behaviour of PXX and VO3 in donor-acceptor systems was also investigated. Depositing PXX with a commonly used electron acceptor, TCNQ, resulted in large extended islands of a majority mixed row type phase and a minority core-shell phase. Both phases exhibited signs of charge transfer to the TCNQ, in a very similar fashion to other donor/TCNQ systems seen in the literature. A rationalisation of the observed behaviour in these systems is to consider the PXX as a stabiliser for the charging of TCNQ by the Au(111) surface; the presence of PXX makes the charged state of TCNQ more favourable and thus lowers its effective LUMO. Both singly charged (row assembly) and doubly charged (core-shell assembly) TCNQ molecules were observed, with a corresponding Kondo feature on singly charged molecules. A similar tip-induced charging/discharging behaviour to the TMTTF/TCNQ system[87] was also seen in the row assembly. Utilising the PXX NRs as electron donors resulted in similar assemblies, with a larger proportion of core-shell islands involving doubly charged TCNQ in MO structures. This is not necessarily an indication of their performance as stronger electron donors but may instead be related to the different stability of the resulting assemblies when compared to those formed with PXX. Investigations into the dependence of these systems on the relative coverage of each component could provide a pathway towards a more detailed understanding of these systems; similarly, utilising NRs of a set length, rather than a mixture of lengths, could show how the behaviour of the TCNQ molecules varies with donor strength and structure.

Finally, the mixing and reaction of Br_2PXX and VO3 led to the formation of mixed nanoribbons consisting of donor/acceptor units. STS investigations revealed a

dependence of the frontier molecular orbital energies on the internal structure of these ribbons, allowing further tuning of the frontier energies. In future work, on-surface synthetic methods could be utilised to form co-polymers of certain lengths via the careful control of precursor structure.

Although general conclusions could be made from STM, STS and XPS for all of these systems, a significant limitation in these studies lies in the lack of theoretical backing from DFT calculations of adsorbed systems. In particular, modelling of the binol systems with DFT could enable more precise conclusions about the structure of the various clusters and chains that were observed in STM measurements. Similarly, the level of interaction between the nanoribbons and Au(111) substrates could be investigated with DFT calculations that elucidate the LDOS and level of hybridisation/bonding with the surface – any effect of this on the measured STS spectra and imaging is not clear from the experimental evidence.

Bibliography

1 N. Sakai, R. Bhosale, D. Emery, J. Mareda and S. Matile, *J. Am. Chem. Soc.*, 2010, **132**, 6923–6925.

2 J. Wu, W. Pisula and K. Müllen, *Chem. Rev.*, 2007, **107**, 718–747.

3 L. Rocard, A. Berezin, F. De Leo and D. Bonifazi, *Angew. Chemie - Int. Ed.*, 2015, **54**, 15739–15743.

4 V. Balzani, G. Bergamini, P. Ceroni and E. Marchi, *New J. Chem.*, 2011, **35**, 1944–1954.

5 L. Maggini and D. Bonifazi, *Chem. Soc. Rev.*, 2012, **41**, 211–241.

6 A. Fermi, I. Orfanos, A. Avramopoulos, M. G. Papadopoulos, S. Couris and D. Bonifazi, *Chem. - A Eur. J.*, 2017, **23**, 2363–2378.

7 A. Sciutto, A. Fermi, A. Folli, T. Battisti, J. M. Beames, D. M. Murphy and D. Bonifazi, *Chem. - A Eur. J.*, 2018, **24**, 4382–4389.

8 E. Carbonell-Sanromà, J. Hieulle, M. Vilas-Varela, P. Brandimarte, M. Iraola, A. Barragán, J. Li, M. Abadia, M. Corso, D. Sánchez-Portal, D. Peña and J. I. Pascual, *ACS Nano*, 2017, **11**, 7355–7361.

9 X. Wang, G. Sun, P. Routh, D.-H. Kim, W. Huang and P. Chen, *Chem. Soc. Rev.*, 2014, **43**, 7067–7098.

10 U. N. Maiti, W. J. Lee, J. M. Lee, Y. Oh, J. Y. Kim, J. E. Kim, J. Shim, T. H. Han and S. O. Kim, *Adv. Mater.*, 2014, **26**, 40–67.

11 G. D. Nguyen, F. M. Toma, T. Cao, Z. Pedramrazi, C. Chen, D. J. Rizzo, T. Joshi, C. Bronner, Y. C. Chen, M. Favaro, S. G. Louie, F. R. Fischer and M. F. Crommie, *J. Phys. Chem. C*, 2016, **120**, 2684–2687.

12 M. Stępień, E. Gońka, M. Żyła and N. Sprutta, *Chem. Rev.*, 2017, **117**, 3479–3716.

13 Q. Shen, H. Y. Gao and H. Fuchs, *Nano Today*, 2017, **13**, 77–96.

14 K. S. Mali, N. Pearce, S. De Feyter and N. R. Champness, *Chem. Soc. Rev.*,

2017, **46**, 2520–2542.

15 X. Zhang, Q. Zeng and C. Wang, *Nanoscale*, 2013, **5**, 8269.

16 J. V Barth, *Annu. Rev. Phys. Chem.*, 2007, **58**, 375–407.

17 P. A. Held, H. Fuchs and A. Studer, *Chem. - A Eur. J.*, 2017, **23**, 5874–5892.

18 R. Otero, J. M. Gallego, A. L. V. de Parga, N. Martín and R. Miranda, *Adv. Mater.*, 2011, **23**, 5148–76.

19 N. Koch, *J. Phys. Condens. Matter*, 2008, **20**, 184008.

20 M. Fahlman, A. Crispin, X. Crispin, S. K. M. Henze, M. P. De Jong, W. Osikowicz, C. Tengstedt and W. R. Salaneck, *J. Phys. Condens. Matter*, 2007, **19**, 183202.

21 E. Goiri, P. Borghetti, A. El-Sayed, J. E. Ortega and D. G. De Oteyza, *Adv. Mater.*, 2016, **28**, 1340–1368.

22 R. W. Strayer, W. Mackie and L. W. Swanson, *Surf. Sci.*, 1973, **34**, 225–248.

23 R. M. Eastment and C. H. B. Mee, *J. Phys. F Met. Phys.*, 1973, **3**, 1738–1745.

24 H. Ishii, K. Sugiyama, E. Ito and K. Seki, *Adv. Mater.*, 1999, **11**, 605–625.

25 R. L. Gerlach and T. N. Rhodin, *Surf. Sci.*, 1970, **19**, 403–426.

26 S. Braun, W. R. Salaneck and M. Fahlman, *Adv. Mater.*, 2009, **21**, 1450–1472.

27 N. Koch, S. Duhm, J. P. Rabe, A. Vollmer and R. L. Johnson, *Phys. Rev. Lett.*, 2005, **95**, 4–7.

28 Y. Zou, L. Kilian, A. Schöll, T. Schmidt, R. Fink and E. Umbach, *Surf. Sci.*, 2006, **600**, 1240–1251.

29 I. Kröger, B. Stadtmüller, C. Stadler, J. Ziroff, M. Kochler, A. Stahl, F. Pollinger, T. L. Lee, J. Zegenhagen, F. Reinert and C. Kumpf, *New J. Phys.*, 2010, **12**, 083038.

30 M. N. Faraggi, N. Jiang, N. Gonzalez-lakunza, S. Stepanow, K. Kern and A. Arnau, *J. Phys. Chem. C*, 2012, **116**, 24558–24565.

31 G. Heimel, S. Duhm, I. Salzmann, A. Gerlach, A. Strozecka, J. Niederhausen,

C. Bürker, T. Hosokai, I. Fernandez-Torrente, G. Schulze, S. Winkler, A. Wilke, R. Schlesinger, J. Frisch, B. Bröker, A. Vollmer, B. Detlefs, J. Pflaum, S. Kera, K. J. Franke, N. Ueno, J. I. Pascual, F. Schreiber and N. Koch, *Nat. Chem.*, 2013, **5**, 187–94.

32 A. Della Pia, M. Riello, J. Lawrence, D. Stassen, T. S. Jones, D. Bonifazi, A. De Vita and G. Costantini, *Chem. - A Eur. J.*, 2016, **22**, 8105–8112.

33 T.-C. Tseng, C. Urban, Y. Wang, R. Otero, S. L. Tait, M. Alcamí, D. Ecija, M. Trelka, J. M. Gallego, N. Lin, M. Konuma, U. Starke, A. Nefedov, A. Langner, C. Wöll, M. A. Herranz, F. Martín, N. Martín, K. Kern and R. Miranda, *Nat. Chem.*, 2010, **2**, 374–9.

34 T. Classen, G. Fratesi, G. Costantini, S. Fabris, F. L. Stadler, C. Kim, S. de Gironcoli, S. Baroni and K. Kern, *Angew. Chem. Int. Ed. Engl.*, 2005, **44**, 6142–5.

35 H. Walch, R. Gutzler, T. Sirtl, G. Eder and M. Lackinger, *J. Phys. Chem. C*, 2010, **114**, 12604–12609.

36 H. Wang, C. Wang, Q. Zeng, S. Xu, S. Yin, B. Xu and C. Bai, *Surf. Interface Anal.*, 2001, **32**, 266–270.

37 X. Qiu, C. Wang, S. Yin, Q. Zeng, B. Xu and C. Bai, *J. Phys. Chem. B*, 2000, **104**, 3570–3574.

38 A. Della Pia, University of Warwick, 2014.

39 G. A. Jeffrey, *An Introduction to Hydrogen Bonding*, Oxford University Press, 1997.

40 G. Cavallo, P. Metrangolo, R. Milani, T. Pilati, A. Priimagi, G. Resnati and G. Terraneo, *Chem. Rev.*, 2016, **116**, 2478–2601.

41 M. T. Rodgers and P. B. Armentrout, *Mass Spectrom. Rev.*, 2000, **19**, 215–247.

42 A. G. Slater, P. H. Beton and N. R. Champness, *Chem. Sci.*, 2011, **2**, 1440–1448.

43 J. V Barth, J. Weckesser, C. Cai, P. Günter, L. Bürgi, O. Jeandupeux and K. Kern, *Angew. Chem. Int. Ed. Engl.*, 2000, **39**, 1230–1234.

44 S. Griessl, M. Lackinger, M. Edelwirth, M. Hietschold and W. M. Heckl, *Single Mol.*, 2002, **3**, 25–31.

45 H. Zhou, H. Dang, J. H. Yi, A. Nanci, A. Rochefort and J. D. Wuest, *J. Am. Chem. Soc.*, 2007, **129**, 13774–13775.

46 R. Gutzler, L. Cardenas and F. Rosei, *Chem. Sci.*, 2011, **2**, 2290–2300.

47 A. G. Slater, L. M. A. Perdigão, P. H. Beton and N. R. Champness, *Acc. Chem. Res.*, 2014, **47**, 3417–3427.

48 L. M. A. Perdigão, E. W. Perking, J. Ma, P. A. Staniec, B. L. Rogers, N. R. Champness and P. H. Beton, *J. Phys. Chem. B*, 2006, **110**, 12539–12542.

49 P. A. Staniec, L. M. A. Perdigão, A. Saywell, N. R. Champness and P. H. Beton, *ChemPhysChem*, 2007, **8**, 2177–2181.

50 R. Otero, M. Schöck, L. M. Molina, E. Lœgsgaard, I. Stensgaard, B. Hammer and F. Besenbacher, *Angew. Chemie - Int. Ed.*, 2005, **44**, 2270–2275.

51 A. M. Sweetman, S. P. Jarvis, H. Sang, I. Lekkas, P. Rahe, Y. Wang, J. Wang, N. R. Champness, L. Kantorovich and P. Moriarty, *Nat. Commun.*, 2014, **5**, 1–7.

52 C. L. Chiang, C. Xu, Z. Han and W. Ho, *Science*, 2014, **344**, 885–888.

53 C. Meier, U. Ziener, K. Landfester and P. Weihrich, *J. Phys. Chem. B*, 2005, **109**, 21015–21027.

54 Y. Gu, T. Kar and S. Scheiner, *J. Am. Chem. Soc.*, 1999, **121**, 9411–9422.

55 A. Mukherjee, J. Teyssandier, G. Hennrich, S. De Feyter and K. S. Mali, *Chem. Sci.*, 2017, **8**, 3759–3769.

56 L. Dong, Z. A. Gao and N. Lin, *Prog. Surf. Sci.*, 2016, **91**, 101–135.

57 C. Copÿret, M. Chabanas, R. P. Saint-arroman and J. Basset, *Angew. Chem. Int. Ed. Engl.*, 2003, **42**, 156–181.

58 M. Ruben, J. Rojo, F. J. Romero-Salguero, L. H. Uppadine and J.-M. Lehn, *Angew. Chem. Int. Ed. Engl.*, 2004, **43**, 3644–62.

59 Z. F. Wang, Z. Liu and F. Liu, *Nat. Commun.*, 2013, **4**, 1–5.

60 J. Lee, J. Li and J. Jagiello, *J. Solid State Chem.*, 2005, **178**, 2527–2532.

61 H. Walch, J. Dienstmaier, G. Eder, R. Gutzler, S. Schlögl, T. Sirtl, K. Das, M. Schmittel and M. Lackinger, *J. Am. Chem. Soc.*, 2011, **133**, 7909–15.

62 D. Wegner, R. Yamachika, Y. Wang, V. W. Brar, B. M. Bartlett, J. R. Long and M. F. Crommie, *Nano Lett.*, 2008, **8**, 131–5.

63 J. V. Barth, *Surf. Sci.*, 2009, **603**, 1533–1541.

64 N. Lin, D. Payer, A. Dmitriev, T. Strunskus, C. Wöll, J. V Barth and K. Kern, *Angew. Chem. Int. Ed. Engl.*, 2005, **44**, 1488–91.

65 A. Dmitriev, N. Lin and J. Weckesser, *J. Phys. Chem. B*, 2002, **106**, 6907–6912.

66 S. Clair, S. Pons, H. Brune, K. Kern and J. V Barth, *Angew. Chem. Int. Ed. Engl.*, 2005, **44**, 7294–7.

67 N. Lin, A. Dmitriev, J. Weckesser, J. V Barth and K. Kern, *Angew. Chem. Int. Ed. Engl.*, 2002, **41**, 4779–4783.

68 A. Dmitriev, H. Spillmann, M. Lingenfelder, N. Lin, J. V Barth and K. Kern, *Langmuir*, 2004, **20**, 4799–801.

69 S. Stepanow, M. Lingenfelder, A. Dmitriev, H. Spillmann, E. Delvigne, N. Lin, X. Deng, C. Cai, J. V Barth and K. Kern, *Nat. Mater.*, 2004, **3**, 229–33.

70 S. Stepanow, N. Lin, D. Payer, U. Schlickum, F. Klappenberger, G. Zoppellaro, M. Ruben, H. Brune, J. V. Barth and K. Kern, *Angew. Chemie - Int. Ed.*, 2007, **46**, 710–713.

71 S. L. Tait, A. Langner, N. Lin, R. Chandrasekar, O. Fuhr, M. Ruben and K. Kern, *ChemPhysChem*, 2008, **9**, 2495–2499.

72 G. S. McCarty and P. S. Weiss, *J. Am. Chem. Soc.*, 2004, **126**, 16772–16776.

73 L. Dong, P. N. Liu and N. Lin, *Acc. Chem. Res.*, 2015, **48**, 2765–2774.

74 M. Lackinger, *Chem. Commun.*, 2017, **53**, 7872–7885.

75 M. Di Giovannantonio, M. El Garah, J. Lipton-Duffin, V. Meunier, L. Cardenas, Y. Fagot Revurat, A. Cossaro, A. Verdini, D. F. Perepichka, F. Rosei and G. Contini, *ACS Nano*, 2013, **7**, 8190–8198.

76 I. Fernandez-Torrente, S. Monturet, K. J. Franke, J. Fraxedas, N. Lorente and J. I. Pascual, *Phys. Rev. Lett.*, 2007, **99**, 1–4.

77 J. Fraxedas and S. García-Gil, *J. Phys. Chem. C*, 2011, **115**, 18640–18648.

78 G. Tomba, M. Stengel, W. D. Schneider, A. Baldereschi and A. De Vita, *ACS Nano*, 2010, **4**, 7545–7551.

79 F. Bischoff, K. Seufert, W. Auwärter, S. Joshi, S. Vijayaraghavan, D. Écija, K. Diller, A. C. Papageorgiou, S. Fischer, F. Allegretti, D. A. Duncan, F. Klappenberger, F. Blobner, R. Han and J. V. Barth, *ACS Nano*, 2013, **7**, 3139–3149.

80 G. Rojas, S. Simpson, X. Chen, D. A. Kunkel, J. Nitz, J. Xiao, P. A. Dowben, E. Zurek and A. Enders, *Phys. Chem. Chem. Phys.*, 2012, **14**, 4971–4976.

81 C. Stadler, S. Hansen, I. Kröger, C. Kumpf and E. Umbach, *Nat. Phys.*, 2009, **5**, 153–158.

82 A. Della Pia, M. Riello, A. Floris, D. Stassen, T. S. Jones, D. Bonifazi, A. De Vita and G. Costantini, *ACS Nano*, 2014, **8**, 12356–12364.

83 M. De Wild, S. Berner and H. Suzuki, 2002, 881–885.

84 A. Della Pia, M. Riello, D. Stassen, T. S. Jones, D. Bonifazi, A. De Vita and G. Costantini, *Nanoscale*, 2016, **8**, 19004–19013.

85 I. Fernández-Torrente, K. J. Franke and J. I. Pascual, *Phys. Rev. Lett.*, 2008, **101**, 2–5.

86 N. Gonzalez-Lakunza, I. Fernández-Torrente, K. J. Franke, N. Lorente, a. Arnau and J. I. Pascual, *Phys. Rev. Lett.*, 2008, **100**, 1–4.

87 I. Fernández-Torrente, D. Kreikemeyer-Lorenzo, A. Strózecka, K. J. Franke and J. I. Pascual, *Phys. Rev. Lett.*, 2012, **108**, 1–5.

88 T. R. Umbach, I. Fernandez-Torrente, J. N. Ladenthin, J. I. Pascual and K. J. Franke, *J. Phys. Condens. Matter*, 2012, **24**, 354003.

89 T. R. Umbach, I. Fernández-Torrente, M. Ruby, F. Schulz, C. Lotze, R. Rurali, M. Persson, J. I. Pascual and K. J. Franke, *New J. Phys.*, 2013, **15**, 083048.

90 D. G. De Oteyza, E. Barrena, H. Dosch, J. E. Ortega and Y. Wakayama, *Phys. Chem. Chem. Phys.*, 2011, **13**, 4220–4223.

91 D. F. Perepichka and F. Rosei, *Science*, 2009, **323**, 216–217.

92 F. Ullmann and J. Bielecki, *Ber. Dtsch. Chem. Ges.*, 1901, **34**, 2174–2185.

93 M. Xi and B. E. Bent, *Surf. Sci.*, 1992, **278**, 19–32.

94 M. Xi and B. E. Bent, *J. Am. Chem. Soc.*, 1993, **115**, 7426–7433.

95 S.-W. Hla, L. Bartels, G. Meyer and K.-H. Rieder, *Phys. Rev. Lett.*, 2000, **85**, 2777–2780.

96 L. Grill, M. Dyer, L. Lafferentz, M. Persson, M. V Peters and S. Hecht, *Nat. Nanotechnol.*, 2007, **2**, 687–691.

97 J. Cai, P. Ruffieux, R. Jaafar, M. Bieri, T. Braun, S. Blankenburg, M. Muoth, A. P. Seitsonen, M. Saleh, X. Feng, K. Müllen and R. Fasel, *Nature*, 2010, **466**, 470–3.

98 T. A. Pham, F. Song, M. T. Nguyen, Z. Li, F. Studener and M. StÃ¶hr, *Chem. - A Eur. J.*, 2016, **22**, 5937–5944.

99 M. Bieri, M. T. Nguyen, O. Gröning, J. Cai, M. Treier, K. Aït-Mansour, P. Ruffieux, C. a. Pignedoli, D. Passerone, M. Kastler, K. Müllen and R. Fasel, *J. Am. Chem. Soc.*, 2010, **132**, 16669–16676.

100 L. Lafferentz, V. Eberhardt, C. Dri, C. Africh, G. Comelli, F. Esch, S. Hecht and L. Grill, *Nat. Chem.*, 2012, **4**, 215–220.

101 N. Merino-Díez, J. Lobo-Checa, P. Nita, A. Garcia-Lekue, A. Basagni, G. Vasseur, F. Tiso, F. Sedona, P. K. Das, J. Fujii, I. Vobornik, M. Sambi, J. I. Pascual, J. E. Ortega and D. G. De Oteyza, *J. Phys. Chem. Lett.*, 2018, **9**, 2510–2517.

102 H. Kong, S. Yang, H. Gao, A. Timmer, J. P. Hill, O. D??az Arado, H. M??nig, X. Huang, Q. Tang, Q. Ji, W. Liu and H. Fuchs, *J. Am. Chem. Soc.*, 2017, **139**, 3669–3675.

103 M. In't Veld, P. Iavicoli, S. Haq, D. B. Amabilino and R. Raval, *Chem.*

Commun., 2008, 1536–1538.

104 Y.-Q. Zhang, N. Kepčija, M. Kleinschrodt, K. Diller, S. Fischer, A. C. Papageorgiou, F. Allegretti, J. Björk, S. Klyatskaya, F. Klappenberger, M. Ruben and J. V. Barth, *Nat. Commun.*, 2012, **3**, 1286.

105 H. Y. Gao, H. Wagner, D. Zhong, J.-H. Franke, A. Studer and H. Fuchs, *Angew. Chemie (Int. Ed.)*, 2013, **52**, 4024–4028.

106 J. Eichhorn, W. M. Heckl and M. Lackinger, *Chem. Commun.*, 2013, **49**, 2900–2902.

107 V. K. Kanuru, G. Kyriakou, S. K. Beaumont, A. C. Papageorgiou, D. J. Watson and R. M. Lambert, *J. Am. Chem. Soc.*, 2010, **132**, 8081–8086.

108 N. a a Zwaneveld, R. Pawlak, M. Abel, D. Catalin, D. Gigmes, D. Bertin and L. Porte, *J. Am. Chem. Soc.*, 2008, **130**, 6678–6679.

109 S. Schlögl, T. Sirtl, J. Eichhorn, W. M. Heckl and M. Lackinger, *Chem. Commun.*, 2011, **47**, 12355.

110 S. Weigelt, C. Busse, C. Bombis, M. M. Knudsen, K. V. Gothelf, T. Strunskus, C. Wöll, M. Dahlbom, B. Hammer, E. Lægsgaard, F. Besenbacher and T. R. Linderoth, *Angew. Chemie - Int. Ed.*, 2007, **46**, 9227–9230.

111 M. Treier, N. V. Richardson and R. Fasel, *J. Am. Chem. Soc.*, 2008, **130**, 14054–14055.

112 N. Kobayashi, M. Sasaki and K. Nomoto, *Chem. Mater.*, 2009, **21**, 552–556.

113 8399288B2, 2013.

114 L. Wang, G. Duan, Y. Ji and H. Zhang, *J. Phys. Chem. C*, 2012, **116**, 22679–22686.

115 N. Lv, M. Xie, W. Gu, H. Ruan, S. Qiu, C. Zhou and Z. Cui, *Org. Lett.*, 2013, **15**, 2382–2385.

116 A. Berezin, N. Biot, T. Battisti and D. Bonifazi, *Angew. Chemie - Int. Ed.*, 2018, **57**, 8942–8946.

117 X. Y. Wang, M. Richter, Y. He, J. Björk, A. Riss, R. Rajesh, M. Garnica, F.

Hennersdorf, J. J. Weigand, A. Narita, R. Berger, X. Feng, W. Auwärter, J. V. Barth, C. A. Palma and K. Müllen, *Nat. Commun.*, 2017, **8**, 4–10.

118 D. Stassen, N. Demitri and D. Bonifazi, *Angew. Chemie - Int. Ed.*, 2016, **55**, 5947–5951.

119 X. Zhu, H. Tsuji, J. T. L. Navarrete, J. Casado and E. Nakamura, *J. Am. Chem. Soc.*, 2012, **134**, 19254–19259.

120 M. Morales-Vidal, P. G. Boj, J. M. Villalvilla, J. A. Quintana, Q. Yan, N. T. Lin, X. Zhu, N. Ruangsupapichat, J. Casado, H. Tsuji, E. Nakamura and M. A. Diáz-Garciá, *Nat. Commun.*, 2015, **6**, 1–8.

121 X. Zhao, Y. Xiong, J. Ma and Z. Yuan, *J. Phys. Chem. A*, 2016, **120**, 7554–7560.

122 M. Koch, M. Gille, A. Viertel, S. Hecht and L. Grill, *Surf. Sci.*, 2014, **627**, 70–74.

123 H. B. Michaelson, *J. Appl. Phys.*, 1977, **48**, 4729–4733.

124 Q. Fan, T. Wang, L. Liu, J. Zhao, J. Zhu and J. M. Gottfried, *J. Chem. Phys.*, 2015, **142**, 101906.

125 Q. Fan, C. Wang, L. Liu, Y. Han, J. Zhao, J. Zhu, J. Kuttner, G. Hilt and J. M. Gottfried, *J. Phys. Chem. C*, 2014, **118**, 13018–13025.

126 D. Barton, H. Y. Gao, P. A. Held, A. Studer, H. Fuchs, N. L. Doltsinis and J. Neugebauer, *Chem. - A Eur. J.*, 2017, **23**, 6190–6197.

127 J. V. V. Barth, H. Brune, G. Ertl and R. J. Behm, *Phys. Rev. B*, 1990, **42**, 9307–9318.

128 M. Böhringer, K. Morgenstern, W. D. Schneider and R. Berndt, *J. Phys. Condens. Matter*, 1999, **11**, 9871–9878.

129 F. Rossel, P. Brodard, F. Patthey, N. V. Richardson and W.-D. Schneider, *Surf. Sci.*, 2008, **602**, L115–L117.

130 S. M. Driver, T. Zhang and D. A. King, *Angew. Chemie - Int. Ed.*, 2007, **46**, 700–703.

131 C. Urban, D. Écija, Y. Wang, M. Trelka, I. Preda, A. Vollmer, N. Lorente, A. Arnau, M. Alcamí, L. Soriano, N. Martín, F. Martín, R. Otero, J. M. Gallego and R. Miranda, *J. Phys. Chem. C*, 2010, **114**, 6503–6510.

132 G. Binning, H. Rohrer, C. Gerber and E. Weibel, *Phys. Rev. Lett.*, 1982, **49**, 57–61.

133 D. M. Eigler and E. K. Schweizer, *Nature*, 1990, **344**, 524–525.

134 M. F. Crommie, C. P. Lutz and D. M. Eigler, *Nature*, 1993, **363**, 524–527.

135 R. J. Stroscio, J. A.; Celotta, *Science*, 2004, **306**, 242–247.

136 R. J. Celotta, S. B. Balakirsky, A. P. Fein, F. M. Hess, G. M. Rutter and J. A. Stroscio, *Rev. Sci. Instrum.*, 2014, **85**, 121301.

137 R. Feynman, *Eng. Sci.*, 1960, 22–36.

138 G. Binnig, H. Rohrer, C. Gerber and E. Weibel, *Appl. Phys. Lett.*, 1982, **40**, 178–180.

139 A. Della Pia and G. Costantini, in *Surface Science Techniques*, 2013, pp. 565–597.

140 J. Bardeen, *Phys. Rev. Lett.*, 1961, **6**, 6–8.

141 A. D. Gottlieb and L. Wesoloski, *Nanotechnology*, 2006, **17**, R57.

142 N. Lang, *Phys. Rev. B*, 1986, **34**, 2–5.

143 T. Zambelli, J. V. Barth, J. Wintterlin and G. Erti, *Nature*, 1997, **390**, 495–497.

144 L. Bartels, G. Meyer and K.-H. Rieder, *Appl. Phys. Lett.*, 1997, **71**, 213.

145 C. Klink, L. Olesen, F. Besenbacher, I. Stensgaard, E. Laegsgaard and N. D. Lang, *Phys. Rev. Lett.*, 1993, **71**, 4350–4353.

146 R. Temirov, S. Soubatch, O. Neucheva, A. C. Lassise and F. S. Tautz, *New J. Phys.*, 2008, **10**, 053012.

147 L. Gross, Z. L. Wang, D. Ugarte, F. Mohn, N. Moll, W. a Heer, P. Vincent, P. Liljeroth, C. Journet, G. Meyer, V. T. Binh, M. Poot, H. S. J. Van Der Zant, A. Aguasca, A. Bachtold, K. Kim, A. Zettl, P. Hung, H. W. C. Postma, M.

Bockrath, X. Blase and S. Roche, *Science*, 2009, **325**, 1110–4.

148 C. Weiss, C. Wagner, C. Kleimann, M. Rohlfing, F. S. Tautz and R. Temirov, *Phys. Rev. Lett.*, 2010, **105**, 2–5.

149 G. Kichin, C. Weiss, C. Wagner, F. S. Tautz and R. Temirov, *J. Am. Chem. Soc.*, 2011, **133**, 16847–16851.

150 F. Mohn, B. Schuler, L. Gross and G. Meyer, *Appl. Phys. Lett.*, 2013, **102**, 1–5.

151 H. Mönig, S. Amirjalayer, A. Timmer, Z. Hu, L. Liu, O. Díaz Arado, M. Cnudde, C. A. Strassert, W. Ji, M. Rohlfing and H. Fuchs, *Nat. Nanotechnol.*, 2018, 1–5.

152 L. Gross, F. Mohn, N. Moll, G. Meyer, R. Ebel, W. M. Abdel-Mageed and M. Jaspars, *Nat. Chem.*, 2010, **2**, 821–825.

153 K. O. Hanssen, B. Schuler, A. J. Williams, T. B. Demissie, E. Hansen, J. H. Andersen, J. Svenson, K. Blinov, M. Repisky, F. Mohn, G. Meyer, J. S. Svendsen, K. Ruud, M. Elyashberg, L. Gross, M. Jaspars and J. Isaksson, *Angew. Chemie - Int. Ed.*, 2012, **51**, 12238–12241.

154 B. Schuler, G. Meyer, D. Peña, O. C. Mullins and L. Gross, *J. Am. Chem. Soc.*, 2015, **137**, 9870–9876.

155 A. Riss, A. P. Paz, S. Wickenburg, H. Z. Tsai, D. G. De Oteyza, A. J. Bradley, M. M. Ugeda, P. Gorman, H. S. Jung, M. F. Crommie, A. Rubio and F. R. Fischer, *Nat. Chem.*, 2016, **8**, 678–683.

156 D. G. de Oteyza, P. Gorman, Y.-C. Chen, S. Wickenburg, A. Riss, D. J. Mowbray, G. Etkin, Z. Pedramrazi, H.-Z. Tsai, A. Rubio, M. F. Crommie and F. R. Fischer, *Science*, 2013, **340**, 1434–1437.

157 A. Riss, S. Wickenburg, P. Gorman, L. Z. Tan, H. Z. Tsai, D. G. De Oteyza, Y. C. Chen, A. J. Bradley, M. M. Ugeda, G. Etkin, S. G. Louie, F. R. Fischer and M. F. Crommie, *Nano Lett.*, 2014, **14**, 2251–2255.

158 J. Hieulle, E. Carbonell-Sanromà, M. Vilas-Varela, A. Garcia-Lekue, E. Guitián, D. Peña and J. I. Pascual, *Nano Lett.*, 2018, **18**, 418–423.

159 G. D. Nguyen, H.-Z. Tsai, A. A. Omrani, T. Marangoni, M. Wu, D. J. Rizzo, G. F. Rodgers, R. R. Cloke, R. A. Durr, Y. Sakai, F. Liou, A. S. Aikawa, J. R. Chelikowsky, S. G. Louie, F. R. Fischer and M. F. Crommie, *Nat. Nanotechnol.*, 2017, **12**, 1077–1082.

160 C. Sánchez-Sánchez, T. Dienel, O. Deniz, P. Ruffieux, R. Berger, X. Feng, K. Müllen and R. Fasel, *ACS Nano*, 2016, **10**, 8006–8011.

161 M. Liu, M. Liu, L. She, Z. Zha, J. Pan, S. Li, T. Li, Y. He, Z. Cai, J. Wang, Y. Zheng, X. Qiu and D. Zhong, *Nat. Commun.*, 2017, **8**, 14924.

162 C. Weiss, C. Wagner, R. Temirov and F. S. Tautz, *J. Am. Chem. Soc.*, 2010, **132**, 11864–11865.

163 S. K. Hämäläinen, N. Van Der Heijden, J. Van Der Lit, S. Den Hartog, P. Liljeroth and I. Swart, *Phys. Rev. Lett.*, 2014, **113**, 1–5.

164 S. Kawai, A. Sadeghi, F. Xu, L. Peng, A. Orita, J. Otera, S. Goedecker and E. Meyer, *ACS Nano*, 2015, **9**, 2574–2583.

165 S. P. Jarvis, *Int. J. Mol. Sci.*, 2015, **16**, 19936–19959.

166 P. Hapala, G. Kichin, C. Wagner, F. S. Tautz, R. Temirov and P. Jelínek, *Phys. Rev. B - Condens. Matter Mater. Phys.*, 2014, **90**, 1–9.

167 O. Krejčí, P. Hapala, M. Ondráček and P. Jelínek, *Phys. Rev. B*, 2017, **95**, 1–9.

168 J. Van Der Lit, F. Di Cicco, P. Hapala, P. Jelinek and I. Swart, *Phys. Rev. Lett.*, 2016, **116**, 2–6.

169 P. Hapala, M. Švec, O. Stetsovych, N. J. Van Der Heijden, M. Ondráčk, J. Van Der Lit, P. Mutombo, I. Swart and P. Jelínek, *Nat. Commun.*, 2016, **7**, 1–8.

170 P. Hapala, R. Temirov, F. S. Tautz and P. Jelínek, *Phys. Rev. Lett.*, 2014, **113**, 1–5.

171 L. Gross, F. Mohn, N. Moll, B. Schuler, A. Criado, E. Guitian, D. Pena, A. Gourdon and G. Meyer, *Science*, 2012, **337**, 1326–1329.

172 J. Repp, G. Meyer, S. M. Stojković, A. Gourdon and C. Joachim, *Phys. Rev. Lett.*, 2005, **94**, 1–4.

173 P. Liljeroth, J. Repp and G. Meyer, *Science*, 2007, **317**, 1203–1206.

174 L. Gross, N. Moll, F. Mohn, A. Curioni, G. Meyer, F. Hanke and M. Persson, *Phys. Rev. Lett.*, 2011, **107**, 1–4.

175 C. J. Chen, *Oxford Univ. Press*, 2008, (2008).

176 I. Horcas, R. Fernández, J. M. Gómez-Rodríguez, J. Colchero, J. Gómez-Herrero and a M. Baro, *Rev. Sci. Instrum.*, 2007, **78**, 013705.

177 D. Nečas and P. Klapetek, *Cent. Eur. J. Phys.*, 2012, **10**, 181–188.

178 A. Einstein, *Ann. Phys.*, 1905, **322**, 132–148.

179 H. Hertz, *Ann. Phys.*, 1887, **267**, 983–1000.

180 C. S. Fadley, *Surf. Interface Anal.*, 2008, **40**, 1579–1605.

181 D. P. Woodruff, *Modern Techniques of Surface Science*, Cambridge University Press, 3rd edn., 2016.

182 J. M. Brunel, *Chem. Rev.*, 2007, **107**, PR1-PR45.

183 M. Giesen and S. Baier, *J. Phys. Condens. Matter*, 2001, **13**, 5009–5026.

184 L.-A. Fendt, M. Stöhr, N. Wintjes, M. Enache, T. a Jung and F. Diederich, *Chemistry*, 2009, **15**, 11139–50.

185 S. L. Tait, Y. Wang, G. Costantini, N. Lin, A. Baraldi, F. Esch, L. Petaccia, S. Lizzit and K. Kern, *J. Am. Chem. Soc.*, 2008, **130**, 2108–13.

186 S. Fischer, A. C. Papageorgiou, J. A. Lloyd, S. C. Oh, K. Diller, F. Allegretti, F. Klappenberger, A. P. Seitsonen, J. Reichert and J. V. Barth, *ACS Nano*, 2014, **8**, 207–215.

187 M. Bowker and R. J. Madix, *Surf. Sci.*, 1980, **95**, 190–206.

188 X. C. Guo and R. J. Madix, *Surf. Sci.*, 1995, **341**, L1065–L1071.

189 C. J. Villagómez, T. Sasaki, J. M. Tour and L. Grill, *J. Am. Chem. Soc.*, 2010, **132**, 16848–16854.

190 F. Schulz, P. H. Jacobse, F. F. Canova, J. Van Der Lit, D. Z. Gao, A. Van Den Hoogenband, P. Han, R. J. M. Klein Gebbink, M. E. Moret, P. M. Joensuu, I.

Swart and P. Liljeroth, *J. Phys. Chem. C*, 2017, **121**, 2896–2904.

191 B. J. Hinch and L. H. Dubois, *J. Chem. Phys.*, 1992, **96**, 3262–3268.

192 Z. Shi, J. Liu, T. Lin, F. Xia, P. N. Liu and N. Lin, *J. Am. Chem. Soc.*, 2011, **133**, 6150–6153.

193 A. Brodde, K. Dreps, J. Binder, C. Lunau and H. Neddermeyer, *Phys. Rev. B*, 1993, **47**, 6609–6616.

194 H. Jenniches, M. Klaua, H. Höche and J. Kirschner, *Appl. Phys. Lett.*, 1996, **69**, 3339–3341.

195 M. Klaua, H. Höche, H. Jenniches, J. Barthel and J. Kischner, *Surf. Sci.*, 1997, **381**, 106–116.

196 C. Ruby and J. Fusy, *Appl. Surf. Sci.*, 1996, **99**, 393–400.

197 L. R. Merte, J. Knudsen, L. C. Grabow, R. T. Vang, E. Lægsgaard, M. Mavrikakis and F. Besenbacher, *Surf. Sci.*, 2009, **603**, 1–4.

198 N. A. Khan and C. Matranga, *Surf. Sci.*, 2008, **602**, 932–942.

199 L. Álvarez, S. Peláez, R. Caillard, P. A. Serena, J. A. Martín-Gago and J. Méndez, *Nanotechnology*, 2010, **21**, 305703.

200 U. Schlickum, R. Decker, F. Klappenberger, G. Zoppellaro, S. Klyatskaya, M. Ruben, I. Silanes, K. Kern, H. Brune and J. V. Barth, *Nano*, 2007, **12**, 3813–3817.

201 A. Delga, J. Lagoute, V. Repain, C. Chacon, Y. Girard, M. Marathe, S. Narasimhan and S. Rousset, *Phys. Rev. B*, 2011, **84**, 035416.

202 B. Voigtländer, G. Meyer and N. M. Amer, *Surf. Sci. Lett.*, 1991, **255**, L529–L535.

203 Patent 0013381A1, 2010.

204 P. Maksymovych, D. C. Sorescu, D. Dougherty and J. T. Yates, *J. Phys. Chem. B*, 2005, **109**, 22463–22468.

205 F. Hanke and J. Björk, *Phys. Rev. B*, 2013, **87**, 235422.

206 G. Witte, S. Lukas, P. S. Bagus and C. Wöll, *Appl. Phys. Lett.*, 2005, **87**, 1–3.

207 P. Han and P. S. Weiss, *Surf. Sci. Rep.*, 2012, **67**, 19–81.

208 S. Blankenburg, J. Cai, P. Ruffieux, R. Jaafar, D. Passerone, X. Feng, K. Müllen, R. Fasel and C. a. Pignedoli, *ACS Nano*, 2012, **6**, 2020–2025.

209 C. A. Talirz, L., Shinde, P., Passerone, D., Pignedoli, in *On-Surface Synthesis*, ed. A. Gourdon, Springer, 2016, pp. 269–287.

210 S. M. Clarke, T. Friščić, W. Jones, A. Mandal, C. Sun and J. E. Parker, *Chem. Commun.*, 2011, **47**, 2526–2528.

211 F. Silly, *J. Phys. Chem. C*, 2017, **121**, 10413–10418.

212 M. Sacchi, A. Y. Brewer, S. J. Jenkins, J. E. Parker, T. Friščić and S. M. Clarke, *Langmuir*, 2013, **29**, 14903–14911.

213 U. S. Jeon, M. H. Chang, W. J. Jang, S. H. Lee, S. Han and S. J. Kahng, *Appl. Surf. Sci.*, 2018, **432**, 332–336.

214 W. J. Jang, K. H. Chung, M. W. Lee, H. Kim, S. Lee and S. J. Kahng, *Appl. Surf. Sci.*, 2014, **309**, 74–78.

215 J. K. Yoon, W. J. Son, K. H. Chung, H. Kim, S. Han and S. J. Kahng, *J. Phys. Chem. C*, 2011, **115**, 2297–2301.

216 W. Song, N. Martsinovich, W. M. Heckl and M. Lackinger, *Chem. Commun.*, 2014, **50**, 13465–13468.

217 A. Y. Brewer, M. Sacchi, J. E. Parker, C. L. Truscott, S. J. Jenkins and S. M. Clarke, *Phys. Chem. Chem. Phys.*, 2014, **16**, 19608–19617.

218 S. K. Noh, J. H. Jeon, W. J. Jang, H. Kim, S. H. Lee, M. W. Lee, J. Lee, S. Han and S. J. Kahng, *ChemPhysChem*, 2013, **14**, 1177–1181.

219 Z. Han, G. Czap, C. lun Chiang, C. Xu, P. J. Wagner, X. Wei, Y. Zhang, R. Wu and W. Ho, *Science*, 2017, **358**, 206–210.

220 H. Huang, Z. Tan, Y. He, J. Liu, J. Sun, K. Zhao, Z. Zhou, G. Tian, S. L. Wong and A. T. S. Wee, *ACS Nano*, 2016, **10**, 3198–3205.

221 S. Yasuda, A. Furuya and K. Murakoshi, *RSC Adv.*, 2014, **4**, 58567–58572.

222 Z. Guo, P. Yu, K. Sun, S. Lei, Y. Yi and Z. Li, *Phys. Chem. Chem. Phys.*, 2017, **19**, 31540–31544.

223 Q. Chen, T. Chen, X. Zhang, L. J. Wan, H. B. Liu, Y. L. Li and P. Stang, *Chem. Commun.*, 2009, 3765–3767.

224 M. Matena, M. Stöhr, T. Riehm, J. Björk, S. Martens, M. S. Dyer, M. Persson, J. Lobo-Checa, K. Müller, M. Enache, H. Wadepohl, J. Zegenhagen, T. a Jung and L. H. Gade, *Chemistry*, 2010, **16**, 2079–91.

225 U. Schlickum, R. Decker, F. Klappenberger, G. Zoppellaro, S. Klyatskaya, W. Auwärter, S. Neppl, K. Kern, H. Brune, M. Ruben and J. V. Barth, *J. Am. Chem. Soc.*, 2008, **130**, 11778–11782.

226 T. Wang, Q. Fan, L. Feng, Z. Tao, J. Huang, H. Ju, Q. Xu, S. Hu and J. Zhu, *ChemPhysChem*, 2017, **18**, 3329–3333.

227 J. Vandevondele, M. Krack, F. Mohamed, M. Parrinello, T. Chassaing and J. Hutter, *Comput. Phys. Commun.*, 2005, **167**, 103–128.

228 M. Dion, H. Rydberg, E. Schröder, D. C. Langreth and B. I. Lundqvist, *Phys. Rev. Lett.*, 2004, **92**, 22–25.

229 J. Klimeš, D. R. Bowler and A. Michaelides, *J. Phys. Condens. Matter*, 2010, **22**, 022201.

230 A. Mukherjee, S. Tothadi and G. R. Desiraju, *Acc. Chem. Res.*, 2014, **47**, 2514–2524.

231 I. F. Torrente, K. J. Franke and J. I. Pascual, *Int. J. Mass Spectrom.*, 2008, **277**, 269–273.

232 M. Garnica, D. Stradi, S. Barja, F. Calleja, C. Díaz, M. Alcamí, N. Martín, A. L. Vázquez de Parga, F. Martín and R. Miranda, *Nat. Phys.*, 2013, **9**, 368–374.

233 T. Kreuch, S. Meierott, N. Néel, W. J. D. Beenken and J. Kröger, *J. Phys. Chem. C*, 2014, **118**, 30162–30169.

234 Q. Fan, C. Wang, Y. Han, J. Zhu, J. Kuttner, G. Hilt and J. M. Gottfried, *ACS Nano*, 2014, **8**, 709–718.

235 P. B. Bennett, Z. Pedramrazi, A. Madani, Y. C. Chen, D. G. De Oteyza, C. Chen, F. R. Fischer, M. F. Crommie and J. Bokor, *Appl. Phys. Lett.*, 2013, **103**, 1–5.

236 N. Abdurakhmanova, N. Amsharov, S. Stepanow, M. Jansen, K. Kern and K. Amsharov, *Carbon N. Y.*, 2014, **77**, 1187–1190.

237 J. Cai, C. Pignedoli, L. Talirz, P. Ruffieux, H. Söde, L. Liang, V. Meunier, R. Berger, R. Li, X. Feng, K. Müllen and R. Fasel, *Nat. Nanotechnol.*, 2014, **9**, 896–900.

238 A. Kimouche, M. M. Ervasti, R. Drost, S. Halonen, A. Harju, P. M. Joensuu, J. Sainio and P. Liljeroth, *Nat. Commun.*, 2015, **6**, 1–6.

239 H. Zhang, H. Lin, K. Sun, L. Chen, Y. Zagranyarski, N. Aghdassi, S. Duhm, Q. Li, D. Zhong, Y. Li, K. Müllen, H. Fuchs and L. Chi, *J. Am. Chem. Soc.*, 2015, **137**, 4022–4025.

240 P. Han, K. Akagi, F. Federici Canova, R. Shimizu, H. Oguchi, S. Shiraki, P. S. Weiss, N. Asao and T. Hitosugi, *ACS Nano*, 2015, **9**, 12035–12044.

241 L. Talirz, P. Ruffieux and R. Fasel, *Adv. Mater.*, 2016, 6222–6231.

242 C. Sánchez-Sánchez, T. Dienel, O. Deniz, P. Ruffieux, R. Berger, X. Feng, K. M??llen and R. Fasel, *ACS Nano*, 2016, **10**, 8006–8011.

243 A. Batra, D. Cvetko, G. Kladnik, O. Adak, C. Cardoso, A. Ferretti, D. Prezzi, E. Molinari, A. Morgante and L. Venkataraman, *Chem. Sci.*, 2014, **5**, 4419–4423.

244 V. Y. Kutsenko, Y. Y. Lopatina, L. Bossard-Giannesini, O. A. Marchenko, O. Pluchery and S. V. Snegir, *Nanotechnology*, 2017, **28**, 235603.

245 K. A. Simonov, N. A. Vinogradov, A. S. Vinogradov, A. V. Generalov, E. M. Zagrebina, N. Mårtensson, A. A. Cafolla, T. Carpy, J. P. Cunniffe and A. B. Preobrajenski, *J. Phys. Chem. C*, 2014, **118**, 12532–12540.

246 L. Talirz, H. Söde, J. Cai, P. Ruffieux, S. Blankenburg, R. Jafaar, R. Berger, X. Feng, K. Müllen, D. Passerone, R. Fasel and C. a. Pignedoli, *J. Am. Chem. Soc.*, 2013, **135**, 2060–2063.

247 M. Chen, J. Xiao, H. P. Steinrück, S. Wang, W. Wang, N. Lin, W. Hieringer and J. M. Gottfried, *J. Phys. Chem. C*, 2014, **118**, 6820–6830.

248 S. Turton, M. Kadodwala and R. G. Jones, *Surf. Sci.*, 1999, **442**, 517–530.

249 D. G. De Oteyza, A. García-Lekue, M. Vilas-Varela, N. Merino-Díez, E. Carbonell-Sanromà, M. Corso, G. Vasseur, C. Rogero, E. Guitián, J. I. Pascual, J. E. Ortega, Y. Wakayama and D. Peña, *ACS Nano*, 2016, **10**, 9000–9008.

250 F. Flores, J. Ortega and H. Vázquez, *Phys. Chem. Chem. Phys.*, 2009, **11**, 8658–8675.

251 R. R. Cloke, T. Marangoni, G. D. Nguyen, T. Joshi, D. J. Rizzo, C. Bronner, T. Cao, S. G. Louie, M. F. Crommie and F. R. Fischer, *J. Am. Chem. Soc.*, 2015, **137**, 8872–8875.

252 S. Kawai, S. Saito, S. Osumi, S. Yamaguchi, A. S. Foster, P. Spijker and E. Meyer, *Nat. Commun.*, 2015, **6**, 8098.

253 R. A. Durr, D. Haberer, Y. L. Lee, R. Blackwell, A. M. Kalayjian, T. Marangoni, J. Ihm, S. G. Louie and F. R. Fischer, *J. Am. Chem. Soc.*, 2018, **140**, 807–813.

254 M. Smerieri, I. Píš, L. Ferrighi, S. Nappini, A. Lusuan, C. Di Valentin, L. Vaghi, A. Papagni, M. Cattelan, S. Agnoli, E. Magnano, F. Bondino and L. Savio, *Nanoscale*, 2016, **8**, 17843–17853.

255 T. Maki and H. Hashimoto, *Bull. Chem. Soc. Jpn.*, 1953, **26**, 348–351.

256 M. U. Schmidt, E. F. Paulus, N. Rademacher and G. M. Day, *Acta Crystallogr. Sect. B Struct. Sci.*, 2010, **66**, 515–526.

257 S. I. Kawano, M. Baumgarten, D. Chercka, V. Enkelmann and K. Müllen, *Chem. Commun.*, 2013, **49**, 5058–5060.

258 Y. Lin, J. Wang, Z.-G. Zhang, H. Bai, Y. Li, D. Zhu and X. Zhan, *Adv. Mater.*, 2015, **27**, 1170–1174.

259 C. Zhan, X. Zhang and J. Yao, *RSC Adv.*, 2015, **5**, 93002–93026.

260 M. Irimia-Vladu, P. A. Troshin, M. Reisinger, L. Shmygleva, Y. Kanbur, G.

Schwabegger, M. Bodea, R. Schwödiauer, A. Mumyatov, J. W. Fergus, V. F. Razumov, H. Sitter, N. S. Sariciftci and S. Bauer, *Adv. Funct. Mater.*, 2010, **20**, 4069–4076.

261 M. Irimia-Vladu, N. S. Sariciftci and S. Bauer, *J. Mater. Chem.*, 2011, **21**, 1350–1361.

262 M. Irimia-Vladu, P. A. Troshin, M. Reisinger, G. Schwabegger, M. Ullah, R. Schwoediauer, A. Mumyatov, M. Bodea, J. W. Fergus, V. F. Razumov, H. Sitter, S. Bauer and N. S. Sariciftci, *Org. Electron.*, 2010, **11**, 1974–1990.

263 K. H. Chung, J. Park, K. Y. Kim, J. K. Yoon, H. Kim, S. Han and S. J. Kahng, *Chem. Commun.*, 2011, **47**, 11492–11494.

264 K. H. Chung, H. Kim, W. J. Jang, J. K. Yoon, S. J. Kahng, J. Lee and S. Han, *J. Phys. Chem. C*, 2013, **117**, 302–306.

265 K. E. Wilson, H. a Früchtl, F. Grillo and C. J. Baddeley, *Chem. Commun. (Camb).*, 2011, **47**, 10365–10367.

266 A. Kirakosian, M. J. Comstock, J. Cho and M. F. Crommie, *Phys. Rev. B - Condens. Matter Mater. Phys.*, 2005, **71**, 1–4.

267 L. Gross, B. Schuler, N. Pavliček, S. Fatayer, Z. Majzik, N. Moll, D. Peña and G. Meyer, *Angew. Chemie - Int. Ed.*, 2018, **57**, 3888–3908.

268 J. Ferraris, D. O. Cowan, V. Walatka and J. H. Perlstein, *J. Am. Chem. Soc.*, 1973, **95**, 948–949.

269 I. Fernández-Torrente, D. Kreikemeyer-Lorenzo, a. Strózecka, K. J. Franke and J. I. Pascual, *Phys. Rev. Lett.*, 2012, **108**, 1–5.

270 B. Fiedler, W. Reckien, T. Bredow, J. Beck and M. Sokolowski, *J. Phys. Chem. C*, 2014, **118**, 3035–3048.

271 K. F. Braun and S. W. Hla, *J. Chem. Phys.*, 2008, **129**, 064707.

272 P. J. Blowey, L. A. Rochford, D. A. Duncan, D. A. Warr, T. L. Lee, D. P. Woodruff and G. Costantini, *Faraday Discuss.*, 2017, **204**, 97–110.

273 M. Hjorth, N. Thorup, P. Frederiksen, K. Bechgaard, A. Undén, G. B. Paulsen,

R. I. Nielsen, C. E. Olsen, C. Pedersen and C. E. Stidsen, *Acta Chem. Scand.*, 1994, 48, 139–143.

274 S. Yokokura, Y. Takahashi, H. Hasegawa, J. Harada, T. Inabe, M. M. Matsushita and K. Awaga, *J. Nanosci. Nanotechnol.*, 2016, **16**, 3355–3359.

275 T. Asari, N. Kobayashi, T. Naito and T. Inabe, *Bull. Chem. Soc. Jpn.*, 2001, **74**, 53–58.

276 K. Müllen and W. Pisula, *J. Am. Chem. Soc.*, 2015, **137**, 9503–9505.

277 Y.-C. Chen, T. Cao, C. Chen, Z. Pedramrazi, D. Haberer, D. G. de Oteyza, F. R. Fischer, S. G. Louie and M. F. Crommie, *Nat. Nanotechnol.*, 2015, **10**, 156–60.

278 S. Kawai, S. Nakatsuka, T. Hatakeyama, R. Pawlak, T. Meier, J. Tracey, E. Meyer and A. S. Foster, *Sci. Adv.*, 2018, **4**, 1–8.

279 S. Wickenburg, J. Lu, J. Lischner, H. Z. Tsai, A. A. Omrani, A. Riss, C. Karrasch, A. Bradley, H. S. Jung, R. Khajeh, D. Wong, K. Watanabe, T. Taniguchi, A. Zettl, A. H. C. Neto, S. G. Louie and M. F. Crommie, *Nat. Commun.*, 2016, **7**, 1–7.

280 H. Z. Tsai, A. A. Omrani, S. Coh, H. Oh, S. Wickenburg, Y. W. Son, D. Wong, A. Riss, H. S. Jung, G. D. Nguyen, G. F. Rodgers, A. S. Aikawa, T. Taniguchi, K. Watanabe, A. Zettl, S. G. Louie, J. Lu, M. L. Cohen and M. F. Crommie, *ACS Nano*, 2015, **9**, 12168–12173.

281 M. N. Faraggi, N. Jiang, N. Gonzalez-Lakunza, A. Langner, S. Stepanow, K. Kern and A. Arnau, *J. Phys. Chem. C*, 2012, **116**, 24558–24565.